

UNIVERSITÀ DEGLI STUDI DI PADOVA

DIPARTIMENTO DI FISICA E ASTRONOMIA

SCUOLA DI DOTTORATO DI RICERCA IN ASTRONOMIA  
CICLO XXVII°

TESI DI DOTTORATO

MULTIWAVELENGTH ANALYSIS OF  
HIGH-REDSHIFT FAR-IR GALAXIES  
DETECTED BY  
THE HERSCHEL SPACE OBSERVATORY  
IN THE SOUTH ECLIPTIC POLE FIELD

DIRETTORE DELLA SCUOLA Prof. Giampaolo Piotto  
RELATORE: Prof. Alberto Franceschini  
CORRELATRICE: Dott.ssa Giulia Rodighiero

Dottorando: Ivano Baronchelli  
Matricola: 1038868

2015



# Sommario

Negli ultimi anni, sempre più studi hanno dimostrato l'esistenza di una co-evoluzione tra nuclei galattici attivi e galassie ospiti. Fenomeni di starburst sono spesso accompagnati da una incrementata attività nucleare e le proprietà dei due meccanismi fisici sembrano essere correlate. Data la natura polverosa delle regioni nelle quali questi meccanismi si manifestano, l'osservazione diretta è fortemente influenzata dall'estinzione. L'emissione UV ed ottica nascosta ha costituito per lungo tempo una grande limitazione a questi studi sia per la difficoltà nella rilevazione di una frazione consistente di queste sorgenti, sia per per la stima della loro estinzione intrinseca. Comunque, l'energia assorbita a lunghezze d'onda minori è riemessa dalla polvere riscaldata, nel medio e lontano infrarosso (MIR e FIR).

In questo contesto, le osservazioni ottenute con gli osservatori spaziali *Herschel* e *Spitzer* giocano un ruolo predominante. Esplorando le regioni spettrali tra il picco di emissione stellare ed il picco di emissione delle polveri, essi permettono di stimare la quantità totale di energia emessa dai meccanismi fisici coinvolti e, conseguentemente, la loro importanza relativa ed assoluta. Le osservazioni *Herschel* e *Spitzer* sono comunque necessarie ma non sufficienti per questo tipo di studi. Redshift fotometrici affidabili possono essere calcolati solo con una buona copertura spettrale alle lunghezze d'onda dell'ottico. Inoltre, nello studio dell'attività AGN, tenere in considerazione la regione spettrale del medio IR, dove domina l'emissione del toro di polveri, diventa cruciale. La regione spettrale del medio IR può essere indagata e.g. dall'osservatorio spaziale *Akari*.

Con il lavoro sintetizzato in questa tesi, abbiamo contribuito allo studio della connessione tra AGN e galassia ospite sotto vari aspetti. La nostra analisi si focalizza nell'area del polo sud eclittico (SEP), che data la sua posizione, è soggetta ad una bassa emissione da cirri. Per prima cosa, abbiamo ridotto un vasto set di immagini ottiche riprese nel campo SEP. I mosaici risultanti sono ora disponibili per ulteriori studi relativi allo stesso argomento o ad altri. In secondo luogo, a partire dalle nostre immagini ottiche e da altre immagini e cataloghi sia pubblici che privati, abbiamo costruito un catalogo di sorgenti all'interno di  $\sim 7$  gradi quadrati nell'area SEP. La copertura fotometrica va dall'ottico al lontano infrarosso delle bande *Herschel*–SPIRE. Misurazioni *Spitzer*–IRAC e MIPS, insieme ad osservazioni *Akari*–IRC sono inoltre incluse. Questo catalogo è ora disponibile per la comunità scientifica. Il nostro terzo contributo alla ricerca in questo campo è rappresentato dall'analisi condotta su un sottocampione di sorgenti selezionate nel lontano IR. Usando tecniche di SED fitting, abbiamo analizzato le principali proprietà di queste galassie (redshift, massa in stelle, attività di formazione stellare e di AGN). Quindi, abbiamo studiato il contributo di ciascun singolo meccanismo fisico (stelle, AGN, formazione stellare) all'emissione a differenze lunghezze d'onda. Per ultimo, abbiamo discusso le relazioni tra queste proprietà. La nostra analisi multi-banda è complementare ad analisi di letteratura condotte nel dominio dei raggi X, le quali puntano verso l'esistenza di una doppia “sequenza principale”, una nel piano massa stellare ( $M^*$ ) contro tasso

di formazione stellare (SFR), e l'altra nel piano  $M^*$  contro tasso di accrescimento del buco nero (BHAR). Per ultimo abbiamo stimato la pendenza della sequenza principale  $M^*$ -BHAR a redshift  $z < 0.5$

# Abstract

In the last years, more and more studies demonstrated the existence of a coevolution between active galactic nuclei and host galaxies. Starbursts are often accompanied by an enhanced nucleus activity and the physical properties of the two physical mechanisms seems to be correlated. Given the dusty nature of the region in which such mechanisms take place, their direct observation is strongly affected by extinction. The hidden UV and optical emission has been for a long time a big limitation to these studies for both the difficulty in detecting a consistent fraction of such sources and for the estimation of their intrinsic emission. However, the energy absorbed at shorter wavelengths is re-emitted by the heated dust, in the mid and far infrared (MIR and FIR).

In this picture, the observations obtained with the *Herschel* and *Spitzer* space observatories play a major role. Exploring the spectral region spanning from the peak of stellar emission to the peak of dust emission, they allow to constrain the total amount of energy emitted by the underlying physical mechanisms and, consequently, their relative and absolute strength. *Herschel* and *Spitzer* observations are however necessary but not sufficient for these kind of studies. Reliable photometric redshifts can only be computed with a good spectra coverage at optical wavelengths. Moreover, when studying the AGN activity, keeping into account the mid-IR spectral region, where the dusty torus emission dominates, become crucial. The mid-IR spectral region can be explored, e.g. by the *Akari* space observatory

With the work summarized in this thesis, we contributed to the study of the connection between AGN and host galaxy under different aspects. Our analysis focuses on the south ecliptic pole (SEP) area, that given its position, is subject to a low cirrus emission. First, we reduced a large dataset of optical images taken in the SEP field. The resulting mosaics are now available for further studies both in the same and different topics. Second, starting from our optical images, and other publicly and private available images and catalogs, we built a multiwavelength catalog of sources covering  $\sim 7$  square degrees in the SEP area. The photometric coverage of this catalog spans from the optical to the far-IR of the *Herschel*-SPIRE bands. *Spitzer*-IRAC and MIPS bands, beside *Akari*-IRC observations are also included. This catalog is already available for the scientific community. Our third contribution to the research in this field is represented by our analysis on a sub-sample of far-IR selected sources. Using SED fitting techniques, we analyzed the main properties of these galaxies (redshifts, stellar masses, star formation and AGN activity). Then we studied the contribution of each single physical mechanism (stars, AGN, star formation) to the total emission at different wavelengths. Finally we discussed the relations among these properties. Our multiwavelength results complement literature analysis undertaken in the X-rays, pointing toward the existence of a double “main sequence”, one in the stellar mass ( $M^*$ ) versus SFR space and the other in the  $M^*$  versus black hole accretion rate (BHAR) space. We conclude with the estimation of the  $M^*$ -BHAR main sequence slope at  $z < 0.5$ .



# Contents

<b>Sommario</b>	<b>i</b>
<b>Abstract</b>	<b>iii</b>
<b>Introduction</b>	<b>1</b>
<b>1 Star formation and AGN activity</b>	<b>5</b>
1.1 Stellar masses and star formation rates . . . . .	6
1.2 Normal star forming galaxies, starbursts and main sequence of star forming galaxies . . . . .	8
1.3 SFR indicators . . . . .	11
1.3.1 UV light . . . . .	12
1.3.2 IR emission . . . . .	13
1.3.3 Other SFR indicators . . . . .	15
1.3.4 SFR indicators and analysis comparison . . . . .	15
1.4 AGN Activity . . . . .	16
1.4.1 AGN properties . . . . .	16
1.4.2 AGN taxonomy and unified model . . . . .	19
1.5 Interplay between AGN and SF activity . . . . .	22
1.6 The South Ecliptic Pole field (SEP) . . . . .	24
<b>2 The multi-wavelength catalog</b>	<b>27</b>
2.1 IRAC-1 catalog . . . . .	27
2.1.1 Survey sensitivity . . . . .	31
2.1.2 Survey completeness and number counts . . . . .	34
2.2 Multi-wavelength catalog merging . . . . .	40
2.2.1 IRAC-2 . . . . .	41
2.2.2 MIPS 24 and 70 . . . . .	42
2.2.3 SPIRE 250, 350, 500 $\mu$ m . . . . .	46
2.2.4 MIPS and SPIRE counterparts reliability . . . . .	48
2.2.5 WISE and 2MASS . . . . .	50
2.2.6 Akari IRC bands . . . . .	52
2.2.7 Optical bands . . . . .	56
2.2.8 VISTA J, H, K <sub>S</sub> . . . . .	64
2.3 Multi-wavelength catalog characteristics and columns description . . . . .	66

<b>3</b>	<b>Optical–based photometric redshifts</b>	<b>77</b>
3.1	Aperture fluxes on smoothed images . . . . .	77
3.2	Redshift from the SED fitting technique . . . . .	78
3.3	Fluxes recalibration . . . . .	80
3.4	Redshift from total optical flux: an alternative technique . . . . .	81
3.5	Redshift computation methods: comparison and final photometric redshifts . . . . .	84
3.6	Outliers treatment . . . . .	89
<b>4</b>	<b>Infrared–based photometric redshifts in the extended area</b>	<b>93</b>
4.1	Hyperz photometric redshifts . . . . .	93
4.2	IRAC1 versus z relation . . . . .	95
4.3	Final IR–based redshifts and reliability . . . . .	96
<b>5</b>	<b>Multiwavelength analysis through SED fitting</b>	<b>103</b>
5.1	Sample selection . . . . .	103
5.2	SED fitting . . . . .	106
5.2.1	The DC08 MAGPHYS version . . . . .	107
5.2.2	The BE13 MAGPHYS version . . . . .	107
5.3	Resulting SEDs, physical quantities and reliabilities . . . . .	109
5.3.1	SEDs . . . . .	109
5.3.2	AGN fraction . . . . .	110
5.3.3	AGN fraction and the Fadda & Rodighiero (2014) diagnostic . . . . .	110
5.3.4	AGN fraction evolution . . . . .	111
5.3.5	Black hole accretion rate . . . . .	111
5.3.6	Stellar mass $M^*$ . . . . .	120
5.3.7	Star formation rate . . . . .	121
5.3.8	AGN fraction and main sequence . . . . .	121
5.3.9	Black hole accretion rate and main sequence . . . . .	124
5.3.10	BHAR/SFR ratio and main sequence . . . . .	136
5.3.11	Starbursts in our sample . . . . .	137
<b>6</b>	<b>Discussion and conclusions</b>	<b>147</b>
	<b>Bibliografia</b>	<b>151</b>

# Introduction

The life of a galaxy is often subject to transient starburst and Active Galactic Nuclei (AGN) activity, during which, an high amount of energy is produced. During the “starburst phase”, stars are formed at very high rates, while supermassive black holes (SMBH), residing at the centers of galaxies, accrete mass during the “AGN phase”. While in the past years, the two phenomena were studied separatly, recently, an apparent co-evolution between the properties of supermassive black holes and the host galaxies has been observed (e.g. Kormendy & Ho 2013, for a recent review). AGNs and Starbursts are found to co-exist in galaxies at all redshifts (Farrah et al. 2003; Alexander et al. 2005), with the global star formation rate density (SFRD) showing an evolution (Lilly et al. 1996; Madau et al. 1996; Hopkins & Beacom 2006) similar to that of the cosmic black hole accretion rate density (Hopkins et al. 2007a; Merloni & Heinz 2008), with a peak of SFRD at  $z \sim 2$ . The mass of the SMBH shows a tight relation with the mass of the bulge (e.g. Marconi & Hunt 2003) and deep surveys results suggest that the presence of a very energetic AGN is able to quench the star formation (e.g. Page et al. 2012). Again, the black hole accretion rate shows a correlation with the stellar mass  $M^*$  (Mullaney et al. 2012), similar to the so called “*Main Sequence*” of star forming galaxies (Brinchmann et al. 2004; Elbaz et al. 2007; Daddi et al. 2007; Noeske et al. 2007a), between the star formation rate (SFR) and the stellar masses  $M^*$ . Moreover, at a given stellar mass  $M^*$ , the black hole accretion rate increases with the specific star formation rate (i.e.  $SSFR = SFR/M^*$ ) of a galaxy (Rodighiero et al. submitted). Finally, from the theoretical point of view, models of galaxy formation shows that quasar-mode feedback is responsible for terminating the star formation (e.g. Granato et al. 2004; Springel et al. 2005)

As seen above, the most recent results suggest that the super massive black hole accretion happens very often concomitantly with intense star formation. Under the point of view of the spectral energy distributions (SED) analysis, quantify the relative importance of these two emission mechanisms was, till recently, an extremely difficult task. This was mainly due to the dusty nature of the physical environments in which these mechanisms take place. The absorbtion of the ultraviolet and optical light and its re-emission at longer wavelengths by the dust, make the infrared (IR) region of the spectra the crucial regime at which these two phenomena should be studied. Nowadays, the large amount of high quality data available from space observatories, such as *Herschel*, *Spitzer* and *Akari*, provide an unprecedented IR coverage of the extragalactic sources. Thanks to the IRAC instrument on board of *Spitzer*, we are able to sample the peak of the stellar emission of distant galaxies. At the same time, the *Spitzer*-MIPS detectors allow to sample the peak of the hot dust, AGN heated, emission. Thanks to its unprecedented angular resolution, the *Herschel*-PACS and SPIRE instruments are able to sample the far-infrared (FIR) peak of the cold dust emission, which is a powerful tracer of star formation. These two observatories can be considered a fundamental tool for the study of AGNs and starburst emission. Obscured AGNs can be detected in the infrared,

## Introduction

---

whereas for example, only 50 per cent of the sources in the hard X-ray band 5–10 keV are currently resolved (Worsley et al. 2005; Shi et al. 2013). However, it is sometimes difficult to separate AGN from star-forming dominated systems (Feltre et al. 2013; Delvecchio et al. 2014), mostly because of the undersampled region among the IRAC and MIPS bands. At these wavelengths, the physical modeling through SED fitting or color–color diagnostics techniques are often affected by highly variable spectral features that prevent from a clear distinction among different classes of galaxies and a precise AGN fraction computation. Covering the mid-infrared (MIR) spectral region between the IRAC and MIPS bands, The *Akari*–IRC observations allow for a fundamental improvement of the capability of these techniques.

In the context of the *Spitzer*-IRAC/MIPS Extragalactic survey (SIMES), the *Spitzer* space telescope carried out extensive observations at 3.6 and 4.5  $\mu\text{m}$  in the South Ecliptic Pole (SEP) area. This field has already been the target of numerous other optical, mid and far-IR surveys. A large part of this thesis focuses on the detailed description of the multiwavelength *Spitzer*-IRAC 1 (3.6 $\mu\text{m}$ ) based catalog that we built using data that we personally elaborated together with publicly available data. The data that we collected in the multiwavelength catalog represent the fundamental starting point for any successive analysis.

Our analysis starts with the computation of photometric redshifts, that we calculated, for our SPIRE selected sample, through a combination between SED-fitting results obtained through the *hyperz* code Bolzonella et al. (2000) and optical and IRAC flux priors that we empirically determined using SEP and COSMOS field data.

From cosmological simulations, that require AGN feedback to suppress star formation, to the correlation found between the mass of the black hole and that of the host galaxy, we saw before that there is mounting evidence that the super-massive black hole accretion is related to enhanced star formation rates. The problem that we try to address is if these correlations are the result of a direct causal relation between the two mechanisms, or if, for example, they are two physically separated consequences of the same underlying physics. More in general, knowing how the two mechanisms are connected each other will provide important information on how AGNs and host galaxies evolve.

The strong IR emission of both AGN and starbursts bring us to the problem of quantifying the relative contribution of the two mechanisms at these wavelengths. In order to study the relative importance of the emission due to the SFR and to the AGN, we applied a different SED fitting technique using a modified version of the *Magphys* code (da Cunha et al. 2008), developed for this precise purpose (Berta et al. 2013). We then reproduced the optical-to-FIR emission accounting for the stellar, AGN and starburst emission. This allowed us to estimate stellar masses  $M^*$ , star formation rates SFRs and AGN accretion. The outlined procedure has been already applied in already published works such as Berta et al. (2013) and Delvecchio et al. (2014), but for the first time we explore the possibilities allowed by this technique with crucial *Akari* mid-IR data.

The summary of this thesis follows:

- **First chapter - Star formation and AGN activity:** We describe the physical context in which our analysis is inserted. A general overview of the most important arguments that we will treat in the following discussion is given. Starting from the description of some fundamental physical quantities such as the stellar mass ( $M^*$ ) and the star formation rate (SFR), we discuss the important relation between them, referred as “main sequence of star forming galaxies”. The most important SFR tracers are here outlined. In the second part, we discuss the properties of different AGN classes in the

picture of the unified model. Finally, we report a brief discussion of the principal issues treated in literature concerning the interactions between AGN and starburst activity and, more in general, between AGN and host galaxy.

- **Second chapter - The multi-wavelength catalog:** starting from a description of the IRAC-channel 1 mosaic, its depth and coverage, we describe in detail the source extraction and the IRAC catalog upon which the rest of the multi-catalog is based. We compute  $3.6\mu\text{m}$  number counts calculating the completeness at various fluxes. We present the images at different wavelengths that we reduced and from which we extracted sources and computed fluxes. The catalogs that we searched for the IRAC detections counterparts and other characteristics are also described. We define how we matched the sources in the various catalogs, computing reliability indicators for the MIPS-SPIRE, IRAC-MIPS and IRAC-SPIRE correlations, and finally how we studied the counterpart distances improving our matches.
- **Third chapter - Optical-based photometric redshifts:** we describe the procedure applied to calculate photometric redshifts from the aperture fluxes computed on optical and near-IR images that we smoothed to obtain the homogeneous PSF. We outline how we refined the flux calibration through the fit of galaxy template SEDs (obtained from Bruzual & Charlot 2003, SSPs). Then, we define the combined technique, that we developed and tested, used to improve the precision of the redshifts resulting from the SED-fitting. This technique implies the use of an IR selection at  $24\mu\text{m}$  and the use of combined optical fluxes as redshift priors. Finally we describe how we identify and treat the probable outliers (i.e. sources with completely wrong photometric redshifts) in our sample. The precision of our estimates is computed using spectroscopic and photometric data taken both in the SEP and COSMOS fields.
- **Fourth chapter - Infrared-based photometric redshifts in the extended area:** The combined technique that we used to compute photometric redshift for the sources not covered in the optical bands is here explained. We describe how we obtained approximate redshift estimates using only IR photometric data and an IRAC flux prior. A MIPS selection of the sources is required in this case as for the optical-based combined technique used in Chapter 3. The precision of our estimates is computed using spectroscopic and photometric data taken both in the SEP and COSMOS fields.
- **Fifth chapter - Multiwavelength analysis through SED fitting:** We describe the multiwavelength analysis that we undertook on a far-IR selected sample of galaxies, in the central square degree of the SEP field. The properties and peculiarities of the SED fitting tool that we exploited are here highlighted. This tool allows to estimate the AGN contribution to the overall emission at different wavelengths. We discuss the reliability of such estimates and compare our approach with a diagnostic methods presented in literature. We also computed stellar masses  $M^*$ , star formation rates (SFR) and black hole accretion rates (BHAR). Finally, these properties are analyzed in order to study how they relate each other. In particular, we estimate the  $M^*$ -BHAR “main sequence” slope at  $z < 0.5$ .
- **Sixth chapter - Discussion and conclusion:** We briefly summarize the results obtained in the different sections, with a particular attention for the catalog that we built and for the multi-wavelength analysis described in the fifth chapter.

## Chapter 0: CONTENTS

---

# Chapter 1

## Star formation and AGN activity

In this section we focus on the star formation and on the AGN activity, that represent two important aspects of the galaxy evolution. When the central super-massive black hole accretion and the star formation rate (SFR) of a galaxy reach appreciable values, then we are in the realm of the so called “*active galaxies*”.

The rapid accretion of the super massive black holes in the cores of the galaxy centers, that define an active galactic nucleus (AGN) is usually observable at various wavelengths, since it involves, directly or indirectly, a large number of physical mechanisms. Nowadays, the differences among AGNs showing different observational characteristics are explained in the context of the unified model (Rowan-Robinson 1977; Antonucci 1984; Antonucci & Miller 1985; Antonucci 1993; Urry & Padovani 1995), as due to the orientation with respect to the observer. This thesis mostly focuses on the infrared (IR) emission that, as widely accepted in literature, comes from the dusty torus surrounding the central engine. This dusty torus absorbs the high energy and optical radiation emitted by the accretion disk of the central black hole and is responsible for the successive black-body-like emission that peak at IR wavelengths.

During the secular evolution of a galaxy, the SFR of a galaxy seems to be regulated by a simple law: the bigger is the galaxy, in terms of stellar mass  $M^*$ , the higher is the SFR. This law, usually referred as *main sequence* (MS) of star forming galaxies (Brinchmann et al. 2004; Elbaz et al. 2007; Daddi et al. 2007; Noeske et al. 2007a; Rodighiero et al. 2014), seems to be valid for local as well as for distant galaxies, for a wide range of stellar masses, and considering different SFR tracers. A galaxy can be considered “*active*” under the point of view of the star formation, when its SFR is consistent with or higher than that of the main sequence. A galaxy is then “*passive*” when the SFR is very low or absent. This is a common case among red elliptical galaxies. At the opposite side of the main sequence, a special class of star forming galaxies is represented by the so called “*starbursts*”, that shows SFRs even ten times or more higher than those in the main sequence. These rare objects, represent a very peculiar and still not well known phase of the galaxy evolution. Their role in the star formation rate density (SFRD), at the peak of the cosmic star formation ( $z \sim 2$ ) seems to be secondary (Rodighiero et al. 2011). This means that the majority of the stars were formed during the secular evolution of the galaxies. However, this doesn't clarify how and why a phase of enhanced SFR can appear during the lifetime of a galaxy. What is the role played by the AGN activity during this phase? Is it responsible for the successive quenching of the star formation activity? These questions bring us to the contents of this chapter, that is a review

of the main issues concerning the star formation, the AGN activity and their interconnections

## 1.1 Stellar masses and star formation rates

The study of star formation properties, such as the star formation rate (SFR), the relation between SFR and stellar masses  $M^*$  and the specific SFR (SSFR=SFR/ $M^*$ ) is fundamental to understand the process of galaxy formation and evolution.

We will better describe the observed relation between stellar masses and star formation rates below. Before going on, we need to better clarify the meaning of stellar mass. The total mass of gas burned into stars from the the epoch of its formation to its age correspond to the integration of the SFR over these two extremes:

$$M_{\text{SFR}}(t) = \int_0^{t_z} \dot{M}^*(t') dt' \quad (1.1)$$

To obtain the mass contained at any epoch into still surviving stars and dead remnants, it is necessary to subtract the mass of gas  $M_{\text{loss}}(t')$  returned to the interstellar medium from stars at any epoch  $t'$ .

$$M^*(t) \equiv M_{\text{star}}(t) = \int_0^{t_z} \dot{M}^*(t') dt' - \int_0^{t_z} M_{\text{loss}}(t') dt' \quad (1.2)$$

Finally, to obtain the mass that at any epoch is contained into still surviving stars, we have to subtract the mass of the remnants  $M_r(t)$ :

$$M_{\text{alive}}(t) = \int_0^{t_z} \dot{M}^*(t') dt' - \int_0^{t_z} M_{\text{loss}}(t') dt' - M_r(t) \quad (1.3)$$

The stellar mass  $M^*$  expressed in Equation 1.2 is the most common definition adopted in literature and in the following we always refer to this definition. The stellar mass  $M^*$  of a galaxy is often computed through a SED fitting procedures. The photometric data are in these cases fitted using template spectra derived from stellar synthesis population models (SSPs, e.g. Bruzual & Charlot 2003; Maraston 2005; Maraston et al. 2009). Given the previous definitions, when modeling photometric data through SED fitting, using SSP models, a star formation history (SFH) is chosen among a set of possibilities. The modeled spectrum of a single stellar population model (SSP) can be expressed as follows:

$$f_\lambda(T, Z) = \int_{m_0}^{m_T} h_\lambda(T, Z, m) \phi(m) dm \quad (1.4)$$

where  $m_T$  represents the mass of the star that is directly relate to its lifetime  $T$ . The function  $f_\lambda(T, Z)$  is the spectrum of a population of age  $T$  and metallicity  $Z$ ,  $h_\lambda(T, Z, m)$  is the spectrum of a star along an isochrone with age  $T$ , metallicity  $Z$  and mass  $m$ . Finally  $\phi(m)$  is the stellar IMF. The total galactic synthetic spectra at time  $T$ ,  $F_\lambda(T)$ , can be obtained simply adding the light of all the single stellar spectra:

$$F_\lambda(T) = \int_0^T \Psi(t) f_\lambda(T-t, Z(t)) dt \quad (1.5)$$

In the previous equation,  $\Psi(t)$  represent the instantaneous SFR at time  $t$ . The dust diffuse in the galaxy or concentrated in star forming regions has also to be considered. Its effect determines a differential absorption that can be parametrized as follows:

$$f_{\text{obs}} = f_{\text{int}}^{-0.4A_\lambda} \quad (1.6)$$

with the extinction  $A_\lambda$  that can be written as:

$$A_\lambda = k(\lambda)E(B - V) = \frac{k(\lambda)A_V}{R_V} \quad (1.7)$$

For a star forming galaxy, the Calzetti et al. (2000) parametrization can be used. In this case, then:

$$K(\lambda) = \begin{cases} 2.659 \left( -2.156 + \frac{1.509}{\lambda} - \frac{0.198}{\lambda^2} + \frac{0.011}{\lambda^3} \right) + R_V & 0.12\mu\text{m} \leq \lambda \leq 0.63\mu\text{m} \\ 2.659 \left( -1.857 + \frac{1.040}{\lambda} \right) + R_V & 0.63\mu\text{m} \leq \lambda \leq 2.20\mu\text{m} \end{cases} \quad (1.8)$$

The stellar mass resulting from a SED fitting also depends on the initial mass function (IMF), that specifies the mass distribution of the newly formed stars:

$$\xi(\log m) = \frac{d(N/V)}{d \log m} = \frac{dn}{d \log m} \quad (1.9)$$

where  $n$  represents the stellar numerical density and is expressed in units of [ $\text{pc}^{-3}$ ]. The IMF is usually represented as a power law:

$$\xi(m) = \xi_0 M^{-(1+x)} \quad (1.10)$$

This power law is usually defined in a specified range of mass, such as e.g.  $M_1=0.1M_\odot$  and  $M_2=125M_\odot$  for the (SA55, Salpeter 1955) IMF, for which  $x=1.35$ . The IMF has a rapidly decreasing cut above the characteristic mass  $M_2$ . Other commonly used IMFs are the (CH03, Chabrier 2003), and the (KR01, Kroupa 2001). While using KR01 and CH03 IMFs, the resulting stellar masses and SFRs are similar,

The effects of using a SA55 or a CH03 IMF on the computed stellar masses and SFR can be quantified through a constant correction of 0.24 dex (Santini et al. 2012; Béthermin et al. 2013)

$$\log(M_{\text{Chab}}^*) = \log(M_{\text{Salp}}^*) - 0.24 \quad (1.11)$$

$$M_{\text{Chab}}^* = M_{\text{Salp}}^*/1.74 \quad (1.12)$$

$$\log(\text{SFR}_{\text{Chab}}^*) = \log(\text{SFR}_{\text{Salp}}^*) - 0.24 \quad (1.13)$$

$$\text{SFR}_{\text{Chab}}^* = \text{SFR}_{\text{Salp}}^*/1.74 \quad (1.14)$$

## 1.2 Normal star forming galaxies, starbursts and main sequence of star forming galaxies

Approaching the observed relation between stellar masses and star formation rates from an historical point of view can help to understand why, for example, a simple classification based on the luminosity of the galaxies is not enough to describe the physics behind the galaxy evolution. This approach also helps to define some general properties that allow to better understand the overall physical picture. The first identification of starburst sources dates back to the studies of Rieke & Lebofsky (1979) and Weedman et al. (1981). The interest in these sources increased during the 80s thanks to the discovery of a large population of IR ultra luminous starburst galaxies by the Infrared astronomical satellite (IRAS). We can refer to starburst galaxies as those systems with a so high SFR that it can not be sustained for their entire lifetime (Weedman et al. 1981; Harwit & Pacini 1975). Compared with a common spiral galaxy, starburst galaxies show SFR even two or three order of magnitude higher. Given their mass and this such high rate of star formation, they would be able to sustain it for only  $10^7 - 10^8$  years. In the local universe, starbursts may be the result of major mergers (Sanders & Mirabel 1996) and the starburst activity seems to take place in the few Kpc surrounding the nuclear region. Starbursts are commonly associated with gas-rich disc galaxies with a concentration of molecular gas in the central Kpc that can be compared to the stellar densities in ellipticals (Bryant & Scoville 1999; Downes & Solomon 1998).

At high redshifts, it is quite common to observe galaxies, actively forming stars, with SFRs of the order of hundreds of  $M_{\odot}/\text{yr}$ . These galaxies are caught during their secular evolution. In the local Universe, galaxies with such high SFRs are instead quite rare and represent a transitory starburst phase. Following the definition of Sanders et al. (1988), both the local starbursts and the distant secularly evolving galaxies can be classified as “ultra-luminous infrared galaxies” (ULIRGs), having luminosities  $L_{\text{IR}} > 10^{12}$ . This simple definition can’t then represent the overall evolutionary picture in which galaxies evolve. For analogy with the local galaxies, the distant ULIRGs were first classified as starburst as well, until new studies begun to delineate the new physical evolutionary properties of the cosmic star formation. The major growth of galaxies, in terms of stellar masses, is observed between  $z \sim 1$  and  $z \sim 3$  (Dickinson et al. 2003; Rudnick et al. 2003). Using K20 survey spectroscopic data (Mignoli et al. 2005), Daddi et al. (2004) found that a reddening independent and relatively clean selection of massive galaxies at  $z \sim 2$  can be obtained by selecting outliers in the (B-z) versus (z-K) diagram. Following this selection criterium, Daddi et al. (2005) found that more than the 80% of a “BzK” mass selected sample of  $z \sim 2$  galaxies have to be considered ULIRGs. Despite their luminosities,  $z \sim 2$  galaxies couldn’t be at the same time and altogether in the transient starburst phase. As resulting from the observations, the high SFRs measured were not an exception at high redshifts and, for this reason, their values were more probably related to the secular evolution than to a transient phase.

This picture was indeed confirmed when the existence of a tight correlation between SFR and stellar mass  $M^*$  was discovered both at low (Brinchmann et al. 2004) and at high redshifts (Elbaz et al. 2007; Daddi et al. 2007; Noeske et al. 2007a). This relation represents the so called *Main sequence* of the star forming galaxies, mathematically expressed as:

$$\text{SFR} = f(t)M_*^{1+\beta} \quad (1.15)$$

The observed dispersion is around 0.3 dex. In the previous equation,  $1 + \beta$  represents the slope of the relation in the logarithmic plane, at a given redshift, while  $f(t)$  is an increasing

function of the redshift that following Sargent et al. (2012), can be described with the following equation:

$$f(t) = (1 + z)^{2.8} \quad (1.16)$$

Thanks to the previous equations, the preponderant fraction of high redshift galaxies with high SFRs can be explained in the context of a secular evolution regime rather than by a transitory phase. In Figure 1.1 we report the main sequence computed at  $z \sim 2$  using different SFR indicators (Rodighiero et al. 2014).

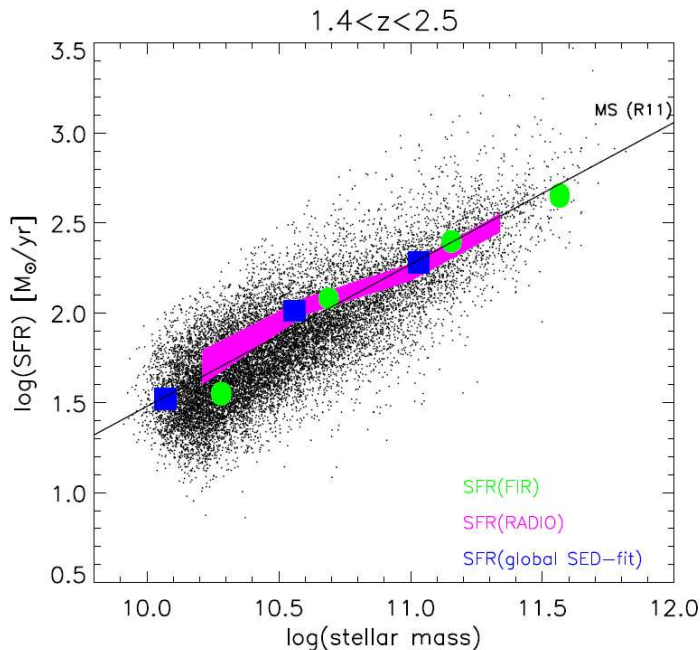


Figure 1.1: *Main sequence of star forming galaxies as computed at  $z \sim 2$ , using different SFR indicators. Black points represent SFRs computed using the UV emission as SFR indicator Rodighiero et al. (2014), the magenta shaded region corresponds to SFRs from stacked radio data Karim et al. (2011), the green data points refer to stacked far-IR based SFRs (sBzK selection) and the blue squares results from a global SED fit applied to sBzK selected data (Magdis et al. 2012). This image is taken from Rodighiero et al. (2014).*

The existence of this main sequence has several implications on the cosmic evolutive picture. First of all, it allows to better define the starburst phase: the observed high SFR, high redshift galaxies are not starbursts but normal galaxies in a steady evolution. At any redshift, the starburst phase is better identified by the SFR/ $M^*$  ratio (SSFR) than by the total luminosity, as it is for the ULIRG definition. The logarithmic distribution of galaxy SFRs at fixed  $M^*$ , can be described by a gaussian curve, with starbursts representing a deviation, visible at high SFRs, from this behaviour. At the peak of the cosmic star formation ( $z \sim 2$ ), considering SFRs above 4 times the main sequence value, the starbursts represent the 2% of a total mass selected sample of galaxies and the 10-15% of the cosmic SFR density (SFRD). Again, the numerical fraction of these outliers seems to be more or less stable between  $0 < z < 2$  (Rodighiero et al. 2011; Sargent et al. 2012). The cosmic star formation is mainly fueled by a steady accretion of material (Dekel & Birnboim 2006; Daddi et al. 2007; Dekel et al. 2009; Lilly et al. 2013), rather than by catastrophic major mergers of gas-rich galaxies that represent very vigorous but short-lived episodes of star formation.

This SSFR based definition of the starburst systems complements the differences in the IR ( $\sim 3\text{-}500\mu\text{m}$ ) spectral energy distributions (SEDs) between secularly evolving and starburst galaxies observed at  $0 < z < 2.5$  (Elbaz et al. 2011), and the different efficiency with which the two classes of objects convert molecular gas into stars Daddi et al. (2010); Genzel et al. (2010). All these peculiarities give rise to the notion of “*bimodal*” star formation.

The inclination  $1+\beta$  of the main sequence is indeed an important factor in the evolutionary context. With  $\beta = 0$ , all star-forming galaxies have the same SSFR, meaning a star formation rate directly proportional to the stellar content of a galaxy; in this case the fractional growth of galaxies would not depend on the stellar mass. The observed value of  $\beta$  ranges from shallow slopes such as  $\beta \sim 0.1$  (Elbaz et al. 2007; Daddi et al. 2007; Dunne et al. 2009; Peng et al. 2010) or  $\beta \sim 0.2$  (Rodighiero et al. 2011), to steeper values as  $\beta \sim 0.4$  (Noeske et al. 2007b; Karim et al. 2011). This inclination parameter regulates the differential growth of high mass galaxies versus low mass ones and then the galaxy mass (in stars) function. This can be appreciate looking at Figure 1.2, from Peng et al. (2014). However, the importance of this parameter is even deeper since it is responsible for the slope of the stellar mass function inside single galaxies (Peng et al. 2014; Lilly et al. 2013).

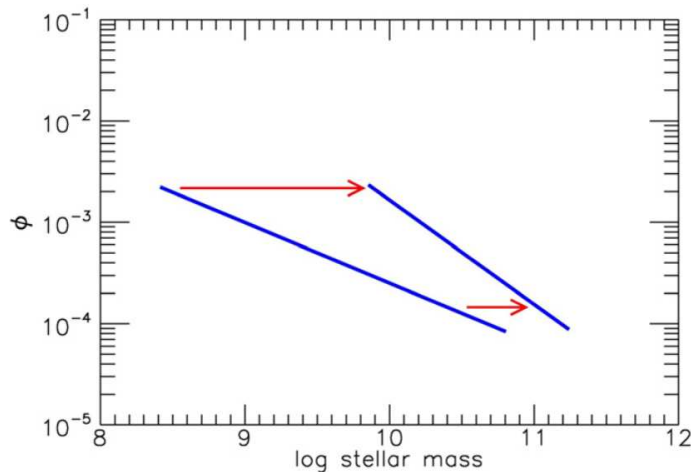


Figure 1.2: *This scheme, taken from Peng et al. (2014), shows the steepening of the star-forming mass function slope consequence of a differential stellar mass increase of galaxies and considering a negative  $\beta$  slope of the SSFR- $M^*$  relation. The power law part of the mass function is represented with blue lines, while the red arrows represents the increase in stellar mass during the time. Because of the negative  $\beta$  value, this increase is proportional to the SSFR and then it is smaller for higher masses.*

A small stellar mass difference (and then a small SFR difference) at early cosmic time would be dramatically amplified as time passes. This results in a quasi-exponential  $M^*$  and SFR growth in case of galaxies with above average SFR, while such evolution is avoided when the SFR is below the average. For the high redshift most actively star forming galaxies, a quenching mechanisms is then required in order to stop the exponential growth, that is not sustainable all way to the present (Renzini 2009). An empirical description of such possible quenching mechanisms is given in Peng et al. (2010) where, using SDSS and zCOSMOS data, they demonstrate the separability of the differential effects of stellar mass and environment on the fraction of actively star forming galaxies up to  $z \sim 1$ . While the mass effect depends on the intrinsic characteristics of each single galaxy, the “environmental” effect, that depends on both the galaxy neighborhoods and on its intrinsic characteristics (through the mass ratios,

for example), can be confined to the “satellite” galaxies, i.e., galaxies in the halo of a central, dominant galaxy (Peng et al. 2012)

Nowadays, the existence of the main sequence is widely accepted. There remain however some differences in the slope (as we saw above) and width values reported in literature. These differences can depend on many issues. First of all, the sample selection. Given the direct relation between far infrared luminosity (FIR) and SFR (Kennicutt 1998), selecting galaxies in a FIR band introduces a malmquist bias, so that at the lowest masses, only those galaxies with above average SFRs are observable. The resulting effect is a flattening of the main sequence. This is indeed observed when using *Herschel* selected samples, as in Rodighiero et al. (2010, 2011); Reddy et al. (2012a). The same flattening effect is observed when the selection is performed in a UV band. As for the FIR selection, the UV luminosity, at the neat of the extinction, is directly correleated to the SFR (Kennicutt 1998). The result of an UV/optical selection is an almost SFR selection. This is what happens for example in Reddy et al. (2006) or in Erb et al. (2006) where no correlation between stellar mass and SFR was found ( $1+\beta=0$ ), for a spectroscopic sample of UV-selected galaxies at  $z\sim 2$ . With a similar selection, but correcting the effects of the biased selection through appropriate simulations, Reddy et al. (2012a) found instead a perfectly linear correlation ( $\beta=0$ ). A spectroscopically selected sample, as seen before, doesn’t ensure a complete sample, even when the original photometric selection can be considered mass selected. This happens because, when getting spectroscopic redshifts, the success rate is higher for higher SFRs. A deeper description of the different SFR indicators and their effects can be found in Section 1.3.

The MS parametrization differences observed among various literature works can also depend on the SFR estimator used (see Section 1.3). As demonstrated in Stringer et al. (2011), little errors in the conversion from observables to physical quantities (physical scatter), and no corrections for the selection biases are responsible for misrepresentations of the main computed parameters ( $M^*$  and SFRs) and finally, of the main sequence. Whitaker et al. (2012) found differences in the slope of the main sequence, when considering a whole sample of star forming galaxies and when selecting blue galaxies only. A selection like this second one, removes the red, dusty star forming galaxies causing a steepening of the main sequence’s slope.

### 1.3 SFR indicators

There are many ways in which the SFR can be inferred from the integrated light emitted by a galaxy. Extensive reviews of this topic are reported in Kennicutt (1998) and in Kennicutt & Evans (2012). We do not analyze here, the physical mechanisms that determine how molecular clouds contract and fragment into clumps, cores, clusters to finally form stars. These observations can be carried out only in our Galaxy or in the neighborhoods. We consider here, a brief review of the collective observational effects of such star formation, considering the compexive contribution of the star forming regions to the total light emitted by a galaxy. We report a description of the SFR indicators, reserving particular attention to the UV and the far infrared (FIR) total emission. The FIR emission is the tracer that we exploited in our analysis, using *Herschel* data, to compute the SFRs for the galaxies in our sample. Given the physical connection between the FIR and the UV emission in a galaxy, the first beeing the dust reprocessed UV light emitted in the star forming regions, explaining the UV mission in its physical origin, and as a SFR tracer, will allow to better understand the peculiarity of the FIR as SFR indicator as well. Other important SFR tracers are here described in a separate

section in order to give a general overview on this vast topic.

### 1.3.1 UV light

The IMF of a newly formed population of stars is numerically dominated by the low mass stars. Also the fraction of integrated mass represented by high mass stars is marginal. However, massive stars dominates the emission at UV wavelengths. This remains true for the whole lifetime of this class of stars, i.e. for less than 1 Gyr. The 1500Å luminosity of a simple stellar population (a group of stars formed at the same time with a characteristic IMF) with a Salpeter (1955) IMF, metallicity between 0.1 and 1  $Z_{\odot}$  decreases by a factor of 100 after  $10^8$  yrs and by a factor of  $10^3$ - $10^6$  depending on the metallicity, after  $10^9$  yrs. For a simple stellar population, an half of the bolometric luminosity emitted during its lifetime, is produced in the first 100 Myrs and mostly in the UV region of the spectra Madau & Dickinson (2014). This values show why the UV light is one of the most important SFR indicators.

Assuming a constant SFR, the 1500Å luminosity stabilizes after about  $10^{7.5}$  yrs. The UV luminosity at this wavelength is then a good tracer of the ongoing star formation rate, provided that the timescale for significant SFR variations is longer than some  $10^{7.5}$  yrs years.

At longer UV wavelengths, as 2300Å and 2800Å, that are commonly used in literature as SFR tracer, the contribution of lower masses to the luminosity begin to become important. The average lifetime of the stars that most contribute at these wavelengths (A and B) is longer than at 1500Å (dominated by the O type), and correspondently, the measure of the *instantaneous* SFR become less precise. The advantage is however that the dust attenuation is lower at longer wavelengths making these bands more suitable for deeper observations. The obscuration is, in general, the principle drawback for the SFR measurements based on all the UV emission. Extinction is stronger in the UV range of the spectra and even small amounts of dust can suppress the UV emission. The SFR can then be determined only after correcting for the absorbtion effects.

The UV emission strongly depends on the metallicity so that metal rich stars emit lower amounts of UV light. Considering a metallicity range between  $Z=0.0003$  and 0.03, the far-UV (FUV) luminosity variation is 70% or less, but this value increases with larger metallicity ranges or older ages. The SFR value can be obtained from the FUV luminosity using a direct correlation:

$$\text{SFR} = K_{\text{FUV}} \times L_{\nu}(\text{FUV}) \quad (1.17)$$

with  $K_{\text{FUV}}$  depending on the IMF, metal enrichment and star formation histories. The wavelength (e.g. 1500Å, 2300Å or 2800Å) has in this case less importance. Considering a Salpeter (1955) IMF in the range  $0.1 \div 100 M_{\odot}$  an age  $t > 300$  Myrs and a constant SFR, the values of  $K_{\text{FUV}}$  obtained for a  $L_{\nu}(\text{FUV})$  in units of [ $\text{erg s}^{-1} \text{Hz}^{-1}$ ] and a SFR in [ $M_{\odot} \text{y}^{-1}$ ] are:  $K_{\text{FUV}} = (1.55, 1.3, 1.1, 1.0) \times 10^{-28}$  for metallicities of  $\log(Z/Z_{\odot}) = 0.2, 0, -0.5, -1.0$  Conroy et al. (2009) or 5% less using the Bruzual & Charlot (2003) values. The original and widely used conversion factor proposed by Kennicutt (1998) is instead  $K_{\text{FUV}} 1.4 \times 10^{-28}$ . Given the lower metallicity at higher redshifts, and the younger ages of the galaxies, a variation of  $K_{\text{FUV}}$  with the distance is expected as a consequence. This redshift dependence is higher in the near-UV (2300Å or 2800Å) than in the FIR (1500Å). The scaling factor to convert  $K_{\text{FUV}}$  to a Kroupa (2001) or Chabrier (2003) IMF is variable and depending on the age and metallicity, but for ages  $> 10^8$  yrs approximable as follows (Madau & Dickinson 2014):

$$K_{\text{FUV}}^{\text{Chab}} / K_{\text{FUV}}^{\text{Salp}} \sim 0.64 \quad (1.18)$$

$$K_{\text{FUV}}^{\text{Krou}}/K_{\text{FUV}}^{\text{Salp}} \sim 0.68 \quad (1.19)$$

$$(1.20)$$

In order to correct for the dust extinction, the UV spectral slope can be used. For example, the Calzetti et al. (2000) extinction law can be used to derive such attenuation when considering optically bright star forming galaxies. The Meurer et al. (1999) method, can alternatively be used. In that work, they locally calibrated the relation between the UV reddening and the UV extinction ( $\text{IRX}=\text{L}_{\text{IR}}/\text{L}_{\text{FUV}}$ ), that can be directly related to  $A_{\text{FUV}}$ .

### 1.3.2 IR emission

The UV light absorbed by the dust in the star forming regions and in the diffuse gas is re-radiated at longer wavelengths, in the mid and far-IR. Since the contribution of wavelengths longer than the UV, to the total light absorbed by the dust is secondary, especially at high SFRs and in younger populations, the total infrared emission (usually considered between 8 and  $1000\mu$ ) can be considered important tracer of ongoing SFR. In this picture, the total IR luminosity is interpreted as the re-processed UV light emission coming from star forming regions. Beside the older stellar populations, that mostly contributes in older galaxies with lower SFRs (and then especially in the near universe), another source of contamination is represented by the AGN torus emission. As we will see in section 1.4, the dusty torus surrounding the accretion disk is responsible for a light reprocessing similar to that involving the SF activity. The high energy radiation emitted by the inner regions of an AGN are absorbed by the dusty torus and re-emitted at MIR and FIR wavelengths. For the most star forming galaxies, with emissions not dominated by the AGN contribution, the total IR light can be assumed, with good approximation, as directly related to the SFR.

Apart for low mass stars and AGN contamination, the total IR emission between is the result of different components. For the most part, the dust in a galaxy is cold (15-60 K). This dust component is responsible for the emission between 30 and  $1000\mu$ . Other components with lower temperatures, as in the interstellar medium (ISM) or with higher temperature as in the SF regions are also present. Below  $30\mu\text{m}$ , the IR emission is dominated by the warm component in the star forming regions. This is a complicate range of the spectrum, since spectral features due to polycyclic aromatic hydrocarbons (PAH) emission and silicate absorptions are also present. The silicate absorption is observed both in presence of AGN and in nuclear starburst regions, while the strength of the PAH features strongly depend on the ISM metallicity and field intensity (Smith et al. 2007; Engelbracht et al. 2005, 2008). The AGN contamination in this region is higher than elsewhere and can dominate over the SF component. This spectral region is well sampled, through cosmological distances, by instruments such as *Spitzer*-MIPS, at  $24\mu\text{m}$  or the IRC instruments of the *Akari* space observatory. Given the complexity of this spectral region, the SFR can't simply be deduced from the total MIR luminosity, since more information about the type of the galaxy are needed for this conversion. The FIR emission, at longer wavelengths doesn't present such problems and it is more directly related to the SFR. This region has been explored until recently by the *Herschel space observatory*, thanks to its instruments, PACS and SPIRE, that cover the spectral range between 100 and  $500\mu\text{m}$ . The *Herschel*-FIR sensitivity is however shallower than the *Spitzer*  $24\mu\text{m}$  one and deep observations in this band detect galaxies with SFRs several times lower. For the reasons explained above, the SFR deduced from the MIR luminosity still remains an important tool for the study of distant galaxies, even if the FIR luminosity has a simpler correlation with the SFR.

The total FIR emission deduced from  $24\mu\text{m}$  measures and the consequent SFR have however proved to be substantially consistent with those derived using other SFR tracer, including radio emission and *Spitzer*  $70\mu\text{m}$  measurements Papovich et al. (2007); Magnelli et al. (2009); Daddi et al. (2007); Magnelli et al. (2011). At higher redshifts, using locally derived SEDs, the FIR luminosity deduced from  $24\mu\text{m}$  measurements seems to be overestimated, when compared with *Herschel* estimates (Elbaz et al. 2010; Nordon et al. 2010). These observations can be explained in the context of the main sequence of star forming galaxies and its evolution (see Section 1.2). While the local ULIRGs are merger-driven starbursts, at  $z\sim 2$ , they are main sequence star forming galaxies, and their SED is more similar to the local main sequence galaxies with lower IR luminosity, than to the starbursts with similar IR luminosity. With this in mind, is now possible to use the appropriate SEDs when computing the total IR luminosity, from the MIR observations.

The total IR luminosity can be constrained, beyond the peak of dust emission, by observations that can be carried out with instruments and observatories such as the SCUBA camera, on the *JCMT* or the ALMA interferometer. These observations can also be useful for the detection of high redshift galaxies, where the FIR peak moves to submillimetric bands (e.g. Smail et al. 1997; Hughes et al. 1998; Barger et al. 1998)

As for the UV derivation, the SFR can be derived from the total IR emission using a direct correlation:

$$\text{SFR}_{\text{IR}} = K_{\text{IR}} \times L_{\text{IR}} \quad (1.21)$$

where  $L_{\text{IR}}$  is the total IR luminosity, integrated over the 8–1000 $\mu\text{m}$  range, expressed in units of [ $\text{erg s}^{-1}$ ]. Following Kennicutt (1998) and considering a Salpeter (1955) IMF,  $K_{\text{IR}} = 4.5 \times 10^{-44} \text{M}_{\odot} \text{yr}^{-1} \text{erg}^{-1} \text{s}$ . In this equation, as described above, the total IR luminosity is completely ascribed to the dust reprocessed light originally emitted by young massive stars and then to the instantaneous star formation activity. The contribution of a possible AGN torus emission or the light emitted by less massive stars is not kept into account. Another drawback of this equation is that all the UV emission is considered as absorbed by the dust. This is however a good approximation for starburst galaxies, for which this formula was presented by Kennicutt (1998). In these cases, the fraction of escaping UV light is only marginal. Using *Herschel* data, Reddy et al. (2012b) estimates that for Lyman break galaxies (LBG), a class of UV-selected star forming and high redshift galaxies, the fraction of FUV light typically absorbed by the dust is the 80% of the entire emission. For the other cases, alternative equations were presented, for example in Papovich et al. (2007) or in Santini et al. (2009), where the UV light and the FIR total emission were complementary considered as follows:

$$\text{SFR}_{\text{tot}} = K_{\text{IR}} \times L_{\text{IR}} + K_{\text{FUV}} \times L_{\text{FUV}} \quad (1.22)$$

In this case,  $L_{\text{FUV}}$  is the total FUV luminosity without an absorption correction, expressed in [ $L_{\odot}$ ] or in [ $\text{erg s}^{-1} \text{Hz}^{-1}$ ]. The values computed in Madau & Dickinson (2014) for the proportionality constants are  $K_{\text{FUV}} = 1.3 \times 10^{-28} \text{M}_{\odot} \text{yr}^{-1} \text{erg}^{-1} \text{s Hz}$  or equivalently  $2.5 \times 10^{-10} \text{M}_{\odot} \text{yr}^{-1} L_{\odot}^{-1}$ , and  $K_{\text{IR}}$  is the value proposed by Kennicutt (1998) of  $K_{\text{IR}} = 4.5 \times 10^{-44} \text{M}_{\odot} \text{yr}^{-1} \text{erg}^{-1} \text{s}$  or equivalently,  $K_{\text{IR}} = 41.73 \times 10^{-10} \text{M}_{\odot} \text{yr}^{-1} L_{\odot}^{-1}$ . In order to obtain the correspondent SFR for a Chabrier (2003) or for a Kroupa (2001) IMF, the SFR obtained above for a Salpeter (1955) IMF can be simply divided for a constant factor of 1.7 (Santini et al. 2012; Béthermin et al. 2013), similarly to the value used to convert the stellar masses, (see Section 1.1).

### 1.3.3 Other SFR indicators

The SFR of a galaxy can be measured quantifying the emission in some particular nebular lines such as the recombination  $H_\alpha$  and  $Ly_\alpha$  lines. The strength of these two emission lines is closely related to the gas photoionization rates and then to the UV radiation field. This last one, as we saw before, is assumed to be the result of the emission of mainly O and B stars. As for the MIR and FIR emission, the AGN contamination can be not negligible, since black hole accretion disks are responsible for similar emission lines. Emission lines are also subject to dust absorption in the star forming regions. The resonant  $Ly_\alpha$  line is particularly subject to this kind of extinction since it is easily scattered by neutral hydrogen atoms. Scattering increases the average path length of the  $Ly_\alpha$  photons, and consequently, the probability of encounters with dust grains able to absorb them. The NIR Paschen  $\alpha$  line is less absorbed but intrinsically weaker than the other hydrogen lines. Its use as SFR tracer is however limited to the local Universe. In this sense, the JWST telescope will allow for deeper observations at cosmological distances. Emission lines of heavier elements (e.g. [OII] at  $3727\text{\AA}$  or [OIII] at  $5007\text{\AA}$ ) can also be used, but the dependency from other ISM characteristics, such as the metallicity or the excitation make these indicators more complicated. For these reasons,  $H_\alpha$  emission is considered the most reliable SFR tracer among the nebular lines Moustakas et al. (2006), in particular at lower redshifts Domínguez Sánchez et al. (2012). Following the Kennicutt (1998) review, based on previous Madau et al. (1998) calibrations, the SFR can be obtained using a linear correlation with the total emitted light:

$$\text{SFR}_{H_\alpha} = K_{H_\alpha} \times L_{H_\alpha} \quad (1.23)$$

Where, for a Salpeter (1955) IMF, and a  $L_{H_\alpha}$  in units of  $\text{erg s}^{-1}$ , the corresponding conversion factor is  $K_{H_\alpha} = 7.9^{-42} \text{ M}_\odot \text{ yr}^{-1} \text{ erg}^{-1} \text{ s}$ .

A tight correlation is observed between Radio and FIR emission Condon (1992); Yun et al. (2001). This correlation makes the Radio region a suitable indicator of SFR. The underlying physics is not entirely understood, but the main causes of this correlation are: 1) non thermal emission from super novae accelerated electrons; 2) free free emission from electrons in HII regions ( $>5\text{GHz}$ ). The great advantage of radio observations is the insensitivity to dust extinction but, as for the FIR observations, it is difficult to detect ordinary star forming galaxies at high redshifts. This spectral region can be contaminated, in rare cases, by the emission of radio-loud AGNs, that are however a minority population.

### 1.3.4 SFR indicators and analysis comparison

In this section, we briefly compare the results obtained in literature, in the context of the main sequence analysis (see Section 1.1), by different authors. As stated in Section 1.3.3, one of the most reliable SFR indicators at low redshifts is the  $H_\alpha$  emission. Measures at these wavelengths are largely available as a result of the SDSS survey. Using this data sample and the  $H_\alpha$  SFR tracer, Brinchmann et al. (2004) and Peng et al. (2010) determined a slope of  $\beta \sim -0.1$  for the main sequence. Noeske et al. (2007b) combined the  $24\mu\text{m}$  based SFR indicator (see Section 1.3.2) with the less reliable [OII] tracer (see Section 1.3.3), obtaining a slope  $\beta \sim -0.3$  in the redshift range  $0.2 < z < 0.7$ . Using the  $24\mu\text{m}$  emission in combination with a SED fitting technique, Santini et al. (2009) calculated a slope of  $\beta \sim -0.15$  for a star forming selected sample at  $z \sim 2$ . Using the  $24\mu\text{m}$  emission alone and for a sample of galaxies at  $z \sim 1$ , the slope computed by Elbaz et al. (2007) resulted  $\beta \sim -0.1$ , similar to that found

by Daddi et al. (2007) for galaxies at  $z \sim 2$ , exploiting the absorption corrected UV emission (see Section 1.3.1). The main sequence slope was measured using the SFR derived from radio emission, by Pannella et al. (2009), obtaining  $\beta \sim -0$  for galaxies at  $z \sim 2$ . With a stacking technique applied to the same radio data, Karim et al. (2011) found  $\beta \sim -0.4$  for a selection of star forming galaxies (rest frame color  $\text{NUV-r}^+ < 3.5$ ), and  $-0.2 < \beta < -0$  for a sample of active galaxies (rest frame color  $\text{NUV-r}^+ < 1.2$ ). Comparing the techniques described above, Rodighiero et al. (2014) found a good agreement among different SFR indicators, with a slope  $\beta$  in the range  $0 \div -0.2$  for galaxies in the redshift range  $1.4 < z < 2.5$ . The agreement among SFRs obtained using different tracers such as the emission in the UV, MIR, FIR, radio (1.4GHz) and  $\text{H}\alpha$  luminosity, is the result of accurate selections, adopted to be as close as possible to mass selected data samples.

### 1.4 AGN Activity

In this section we briefly describe the main characteristics of active galactic nuclei (AGNs), in order to present the final and, for our purposes, most important introductory section, that refers to the interaction and co-evolution between AGNs and actively star forming galaxies.

Active galactic nuclei are those ensemble of physical and observative phenomena that occur at the very center of galaxies and ascribable to the presence of a super massive black hole (SMBH) accreting matter at high rates. Their emission, that encompasses the whole electromagnetic spectrum, can not be explained by stars, gas and dust alone, and the presence of a SMBH is then required. Luminosity variability measurements allow to determine the maximum size of these sources that are not bigger than few parsecs. AGNs are the most powerful emitting sources in the universe and for quite long time, they were the only kind of source that was possible to detect at high redshifts. Nowadays, they represent one of the important mechanisms, together with the star formation that seem to drive the evolution of galaxies and the environment in which they evolve.

An overall explanation of such objects required almost a century, from the first spectroscopic observation of the “NGC 1068 spiral nebula“, carried out by Fath (1909), that showed a peculiar spectrum with both emission and absorption lines, to the unified model presented by Urry & Padovani (1995), widely accepted today. The wide taxonomy used to describe AGNs is indicative of the vast amount of observational differences that these objects present. Many of them are now well represented by inclination effects in the context of the unified model, but it took long time before being able to relate Seyfert galaxies and quasars as the same type of objects. Nowadays, while the nature of AGNs and the unified model used to explain them as the same physical mechanisms are widely accepted, the structure of the emitting regions and the reasons for which the AGN phenomenon appears in some galaxies rather than others are still debated.

#### 1.4.1 AGN properties

In this section we summarize the common peculiarities that characterize the majority of the AGNs. This will allow to introduce the differences, that we will present in the following section, as different expressions of the same underlying mechanism. The common characteristics will be presented in a schematic list, in order to give a more clear overview of the physical and observational picture.

### High bolometric luminosity

The bolometric luminosity of an AGN is not an easy physical quantity to be computed. Many AGNs are strongly obscured by the dust in the surrounding toroidal structure and they can be sometimes fainter than the host galaxy, making their detection extremely difficult. It seems however that the most luminous sources are as bright as  $10^{48} \text{erg s}^{-1}$ , while for the faintest, a minimum of  $10^{42} \text{erg s}^{-1}$  is observed. The total luminosity is the combination of a “primary” emission, that is directly observed, and a “secondary” emission, represented by the light absorbed by the toroidal dusty structure and then re-emitted in the infrared.

### Small physical size compared to the host galaxy

AGNs represent, as the name says, the nuclei of their host galaxies, occupying the few inner parsecs of these last ones. For optically resolved galaxies, this result in a correspondent small angular size, compared to the extension of the outer parts of the galaxy. In some cases, the brightest nuclei can overwhelm the surface brightness of the galaxy that would not be detected, being below the flux limit of the observations.

### Emission lines

AGN spectra are characterized by intense emission lines, among which the  $\text{Ly}\alpha$ , line, the Balmer series, the CIV pair at  $1549\text{\AA}$  the [OIII] line at  $5007\text{\AA}$  the  $\text{K}\alpha$  Fe line at  $6.4\text{KeV}$  (Padmanabhan 2002). The most important distinction is based on the line width, that correspond to a different velocity field of the emitting region. Broad lines are emitted in the inner regions and given the high velocity field ( $\sim 10^3 \div 10^4 \text{Km/s}$ ) they present an important doppler effect enlargement. Narrow lines are emitted in regions characterized by lower velocity fields ( $\sim 10^2 \text{Km/s}$ ). Both permitted and prohibited lines are observed, but these last ones are more commonly observed with a narrow profile.

### Wide multi–band emission

In an AGN, many thermal and non–thermal mechanisms interplay to create the final observed spectrum of these sources. The continuum emission spans from the gamma domain to the radio bands and sometimes without strong discontinuities. A typical galactic spectrum is instead the result of combined black bodies emissions at different characteristic temperatures. However, stars are not responsible for emission in a range wider than an order of magnitude in frequency Padmanabhan (2002) and dusty environments doesn’t emit in larger frequency ranges.

In the **radio** wavelengths, AGN taxonomy refers to radio “quiet” and radio “loud” sources. In the first case, the radio spectrum is the continuation, at longer wavelengths, of the FIR thermal emission peak due to the dust (sub–mm break). Only  $\sim 10\%$  of AGNs own to the second category. In this case, the strong radio emission observed is emitted by a compact radio source and by an extended structure, referred as “radio lobes“ that depart from the compact object. In both cases, the radio luminosity is due to synchrotron emission of accelerated charges (Beckmann & Shrader 2012). The synchrotron emission by an homogeneous source with a constant magnetic field can be described by a power law:

$$F_\nu \propto \nu^{-\alpha} \tag{1.24}$$

with  $F_\nu$  in units of  $\text{erg s}^{-1}\text{cm}^{-2}\text{Hz}^{-1}$  and  $\alpha = (s - 1)/2$  derived from the electron energy distribution:

$$N(E)dE = N_0E^s dE \quad (1.25)$$

Typically, for the lobe emission and at high frequencies,  $\alpha \sim 0.7$ , while at lower frequencies  $\alpha \sim 5/2$  (Peterson 1997). For the compact source,  $\alpha < 0.5$ .

In the **infrared**, the AGN's spectrum is dominated by dust emission between 1 and  $300\mu\text{m}$ . This thermal emission is due to the dusty torus surrounding the central engine that, being heated by the high energy radiation, re-emits at longer wavelengths causing the observed black body type emission. In the radio loud sources, this wavelength range can be still dominated by synchrotron emission. The dusty torus, is also responsible for the PAH and silicate emission and absorption lines that contribute to the spectral shape between 5 and  $24\mu\text{m}$ .

In the **optical** bands, the observed spectrum strongly depends on the inclination of the object (following the unified model of Urry & Padovani 1995). If the dusty torus inclination allows to observe the inner regions, the optical continuum shows a power law spectrum and an emission that increases toward the UV. The Fe emission line and the Balmer continuum creates the so called "small blue bump", in contraposition with the more important "big blue bump" observed in the UV. This spectral shape makes AGNs "bluer" than inactive galaxies. Important emission lines such as the Ly $\alpha$ , Balmer series, Helium, Carbon and Magnesium lines, are emitted in regions spatially close to the central engine, where the doppler effects due to the strong velocity field make them broad. Other narrow lines are instead emitted in more distant and colder regions, where the doppler effects are less effective. No important variability is observed in these regions.

The **UV** emission is characterized by the continuation of the increasing optical spectrum. The emission presents a peak, the so called "big blue bump" thought to be associated with the thermal emission of the accretion disk at the very center of the AGN structure (Shields 1978), where the temperature reaches temperatures of  $10^4 \div 10^5\text{K}$  (Beckmann & Shrader 2012). The measured emission lines provide an high precision measure of the inner region dynamics.

At the **X-ray** wavelengths, between  $10^2$  to  $10^5\text{eV}$ , the physical mechanism responsible for the emission is the black hole accretion process. The UV photons emitted in the accretion disk gain energy through inverse Compton effect, during scattering processes with highly energetic particles (Haardt & Maraschi 1993). The particles combined emission generates the so called "soft X-ray excess". Given the high velocity variation observed for this emission, in the order of the day, the emitting region has to be very small. Broad Fe emission lines are observed in the spectra at these wavelengths and another small "hump" of emission is observed in the hard X-ray region, between 20 and  $30\text{KeV}$  (Beckmann & Shrader 2012).

In the  **$\gamma$ -ray** spectral region, the emission is a peculiarity of a certain class of AGNs called "BLAZARS". At  $\sim\text{MeV}$  energetic scales, the inverse Compton effect dominates the photon-matter interaction, while above  $100\text{MeV}$ , the pair production interactions become predominant. The high energy jets observed in the BLAZARS are the responsible for such an emission. In this case, electrons are more energetic than those in the accretion disk. The relativistic motion of these particles in the direction of the observer can further amplify the observed energy.

### High variability

The optical luminosity of an AGN is highly variable (10% in a year following Krolik 1999), with an increasing variability at shorter wavelengths. Using variability timescales, it is possible to

quantify the maximum size of the inner emitting regions, that results smaller than a parsec. In the IR continuum, the variability is due to the dust surrounding the inner accretion disk. Since the dust can't stay closer than a certain distance, called "sublimation radius", due to the high temperatures of the inner regions, the time difference between the optical/UV and the IR luminosity variations allows to measure the inner radius of the dusty torus. Following for example the results of Clavel et al. (1989) this distance resulted  $R_i \sim 400$  light days.

### 1.4.2 AGN taxonomy and unified model

The classification here reported is the result of mainly observational characteristics that each class of AGN shows. Before the advent of the unified model of Urry & Padovani (1995), all these differences were interpreted as intrinsic physical differences of the various objects. Nowadays it is possible to re-interpret the classification and explain the main differences as a consequence of the inclination between the AGN structure and the observer. In this section we present the taxonomy of AGNs. This classification has not to be intended in a restrictive way since there is not a clean distinction among the different classes of objects here described.

#### Radio galaxies

AGN identified as radio sources are usually associated with giant elliptical galaxies. The radio emission is concentrated in a compact nuclear region but radio emitting jets and extended "lobes" are also present. These components extend to the outer galactic regions, from tens of Kpc, to 1Mpc from the central source. There exist more than one classification method, each of which is based on a different observative parameter.

On the basis of their 1.4GHz luminosity, they can be classified as "*Weak*" ( $L_{1.4} < 10^{25}$  W/Hz) or "*Powerful*" ( $L_{1.4} > 10^{25}$  W/Hz) radio sources. The weak sources are associated to optically luminous elliptical galaxies and with strong emission lines. The powerful sources show lower optical luminosities and fainter or absent emission lines.

Using the  $\alpha$  spectral index at 1GHz (see Equation 1.24), radio galaxies can be classified as "*steep*" ( $\alpha > 0.4$ ) or "*flat*" ( $\alpha < 0.4$ ) spectrum sources. The steep spectrum sources present larger extension and appear optically thin, while the "flat" look more compact, variable and optically thick.

Considering the ratio  $q$  between the the lobes separation and the total source's size, measured at 178MHz, radio galaxies can be classified as "*Faranoff-Riley I*" (FRI) when  $q < 0.5$  and "*Faranoff-Riley II*" (FRII) when  $q > 0.5$ . While FRI shows edge darkening effects and radio lobes with a smoothed surface brightness, FRII are edge-bright with lobes characterized by high surface brightness extremes.

#### Quasars

The quasi stellar radio sources, as they were indicated in the first observations, present a very high luminosity and compact emission. Their extragalactic nature was clarified only after the identification of highly redshifted emission lines. Quasars are classified using the loudness parameter  $R = F_r / F_o$  (Kellermann et al. 1994), that represents the ratio between the luminosities measured at 5GHz and in the B band (4400Å).

The "*radio-loud* quasars" ( $R > 10$ ) presents a strong unresolved radio emission and an optically luminous nucleus ( $M_V > -23$ ). The radio emission is associated with relativistic jets.

The “*radio-quiet* quasars” ( $R < 10$ ) represent the 90% of the entire population. Their radio emission is weaker and with an unclear physical nature, although the most likely explanation is the synchrotron emission from accelerated electrons in shocks (Ishibashi & Courvoisier 2011).

### Seyfert galaxies

Seyfert galaxies show quasar-like nuclei, with very high nuclear luminosities but with a detectable host galaxy. Their optical spectra present strong emission lines due to both hydrogen recombination and other prohibited transitions, such as oxygen, iron, nitrogen and sulphur.

Seyfert galaxies can be classified on the basis of their optical spectra: while “*type 1*” Seyfert galaxies shows broad permitted and narrow forbidden lines, “*type 2*” are characterized by the presence of only narrow emission lines. Most of the spiral galaxies own to the first typology.

The permitted broad emission lines shows widths with values up to  $10^4$  Km/s. Instead, narrow lines widths are in the order of several hundreds of Km/s and are emitted in low density ionized regions ( $n_e \sim 10^3 \div 10^6 \text{cm}^{-3}$ ), where both permitted and prohibited emissions are allowed. Basing its classification on the optical spectra appearance Osterbrock (1981) introduced new Seyfert typologies as: 1.5, 1.8, 1.9, where higher number correspond to stronger narrow lines.

### Blazars

This class of AGN is characterized by fast optical, X-ray and radio variability and high polarization levels in the continuum. This class is usually associated with elliptical galaxies and the typical variability timescale is on the order of the day. In the optical, the polarization degree ranges between 5% and 40%.

Two sub-classes are recognized: the “*BL Lacertae*” type, with strong radio emission, as radio loud quasars, but without strong emission and absorption lines in their spectra, and the “*optically violent variables*”, that show some broad emission lines (weaker than those of quasars).

### LINERS

Low ionization nuclear emission-line regions (LINERs) represent a low nuclear luminosity class of AGNs. These sources are the most commonly observed class of AGNs. Emission lines due to the Balmer series and to low ionization levels of oxygen and sulphur are observed in the spectra. This last characteristics makes this class different from Seyfert galaxies, that show instead higher ionization levels. Veilleux & Osterbrock (1987) proposed a diagnostic method to separate Seyferts from LINERs based on the ratio among different lines close in wavelength but due to different elements. The  $[\text{OIII}/\text{H}\beta]$  ratio can define for example such a distinction among Seyfert-2 ( $[\text{OIII}(5007\text{\AA})/\text{H}\beta(5861\text{\AA})] > 3$ ) and LINERs ( $[\text{OIII}/\text{H}\beta] < 3$ ). From  $[\text{OIII}]$  measures ( $4363\text{\AA}$ ), the electronic temperature resulted  $\sim 40000\text{K}$ , with a width of  $200 \div 400\text{Km/s}$ .

### Unified model and AGN components

Comparing the IR continuum of Seyfert-1 and Seyfert-2 classes, Rowan-Robinson (1977) found an excess of emission of the Sy2 galaxies with respect to the Sy1. Considering also the differences in the emission lines widths, these effects were interpreted as due to the presence

of a dusty structure surrounding the central engine of the Sy2 class. In the same work, the possibility of an inclination effect was also argued. Analyzing the Sy2 prototype NGC1068, Antonucci & Miller (1985) observed polarized broad lines in its spectrum. This was possible since, thanks to reflection by the dust, broad lines can be *indirectly* observed. Broad lines can't be *directly* observable since a dusty structure is interposed between the central engine and the observer. Reflection instead, polarizes the light making possible the observed effect (Antonucci 1984; Antonucci & Miller 1985; Antonucci 1993). In the representation given by Urry & Padovani (1995), the dusty structure surrounding the central black hole has a toroidal shape. This would explain the observed differences between type 1 and type 2 AGNs (or Seyfert galaxies), through an inclination effect: the broad lines, emitted in the very inner regions close to the accretion disk, are absorbed for some inclination values, when the circular structure is seen edge-on, and are directly observable when the dusty torus is observed face-on. Narrow lines are emitted above the accretion disk but at higher distances. In this case, the probability to observe this kind of emission lines is higher. The famous representation of the Urry & Padovani (1995) is represented in Figure 1.3.

On the basis of the UV spectra, following the explained unified scheme, all the AGN typologies can be summarized in two simpler classes:

- **Type 1 AGN:** characterized by luminous continuum with both narrow and broad lines. The AGN structure is observed “face-on”
- **Type 2 AGN:** characterized by faint continuum with only narrow lines. The AGN structure is observed “edge-on”

In the unified model picture, almost all the AGNs present similar physical characteristics and components. All of them contain a **super massive black hole** (SMBH) at their very center. Its mass can vary in the range  $10^6 \div 10^9 M_{\odot}$  and can be measured using for example the rotational curves of circumnuclear medium. This can be achieved thanks to high resolution HST images (Marconi et al. 2006), or ground based adaptive adaptive optic systems (Häring-Neumayer et al. 2006). The AGN mass can also be measured through masers techniques Miyoshi et al. (1995).

Surrounding the close vicinity of the black hole, an **accretion disk** is responsible of the AGN primary emission. The matter lying in the disk loses angular momentum through viscous and turbulent processes emitting UV radiation in the energetic spectral regions. The accretion disk is geometrically thin and optically thick (Shakura & Sunyaev 1973)

Close to the accretion disk, the **hot corona** of highly energetic particles emits in the X-rays through inverse comptonization of the UV photons emitted by the primary source Haardt & Maraschi (1993).

**Broad lines regions** (BLR) are clouds of gas ( $N \sim 10^7 \div 10^8$  Arav et al. 1998) in rapid rotation at a distance of about 0.1 to 1 pc from the center and with a density  $n_e \sim 10^9 \div 10^{10} \text{cm}^{-3}$ .

At higher distances ( $\sim 100 \text{pc}$ ) from the center, the **narrow lines regions** (NLR) are characterized by the presence of ionized gas with lower densities than those in the BLRs ( $n_e \sim 10^4 \div 10^{5.5} \text{cm}^{-3}$ ). This allows the production of forbidden lines. Compared with the BLRs, the lower velocity of the NLRs ( $< 1000 \text{km/s}$  Antonucci 1993) determines their narrower width. Their spatial distribution seems to form axisymmetric cones that depart from the inner region towards opposite directions

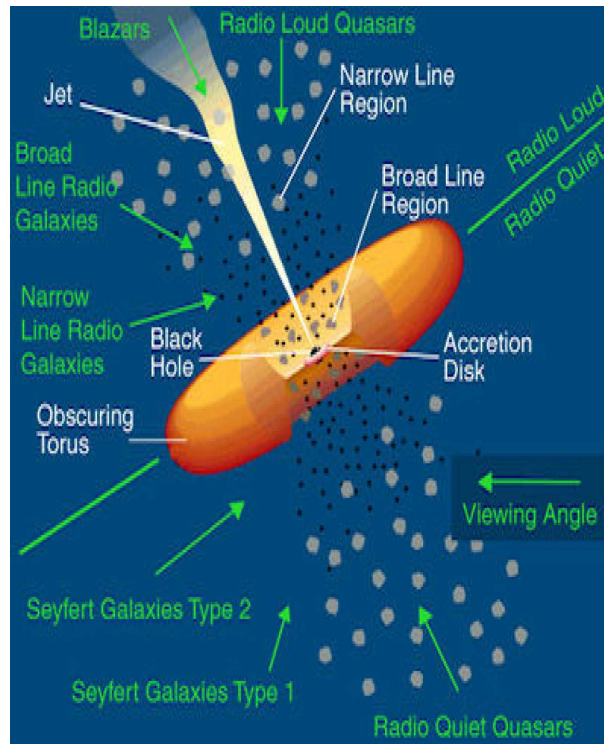


Figure 1.3: *Schematic diagram of the AGN paradigm. AGN observative taxonomy does not correspond to physical differences but it is the consequence of the inclination between the dusty torus structure surrounding the accretion disk and the observer. This image is taken from Urry & Padovani (1995).*

The **toroidal dusty torus** that occupy the outer regions of the AGN is responsible for the absorption of the primary emission and for the occultation of the radiation emitted from narrow line regions but it is also responsible for the thermal emission in the FIR spectral region. The presence of this structure was proven for the first time by Antonucci & Miller (1985) through the observation of polarized broad lines in a Seyfert–2 galaxy. The origin of the polarization is the reflection from the dust that prevent from the direct observation of such lines.

**Relativistic Jets** are observed in radio loud AGNs. The reason for which jets are present in some AGNs and absent in others is probably related to the collimation of these structures with the angular momentum of the accretion disk, together with the prominence of this last one. Some radiogalaxies shows one only outflowing jet. These structures departs from the central black hole and extend to  $\sim 10^5 \div 10^6$ pc where they possibly form extended **radio lobes**.

## 1.5 Interplay between AGN and SF activity

AGN and star formation activity coexist in galaxies at all redshifts (Farrah et al. 2003; Alexander et al. 2005). While the small dimensions of an AGN seem to prevent from possible strong interactions between the few inner parsecs and the rest of the host galaxy, various observations suggest a different scenario. In this section we briefly explore the various clues on the coevolution of the two mechanisms and the possible physical connection that relate them.

One of the most important relations between AGNs and host galaxies is the observed correlation between the mass of the super massive black hole (SMBH) and the mass of the galaxy bulge (e.g. Marconi & Hunt 2003).

The evolution of the global star formation rate density (i.e. the SFR per unit of comoving space) looks similar to that characterizing the black hole accretion rate density (BHARD). In particular, both the SFRD and the BHARD shows a peak of activity at  $z \sim 2$  (Lilly et al. 1996; Madau et al. 1996; Hopkins & Beacom 2006; Hopkins et al. 2007a; Merloni & Heinz 2008).

The observed main sequence of star forming galaxies (see Section 1.2) has a counterpart when considering the BHAR (Mullaney et al. 2012): both the star formation rate and the central black hole accretion rate are correlated to the mass in stars of the host galaxy ( $M^*$ ). An even more direct relation between the star formation and the black hole accretion is observed for example in Rodighiero et al. (2015), where fixed the stellar mass  $M^*$ , the black hole accretion rate increases with the specific star formation rate (i.e.  $SSFR = SFR/M^*$ ).

Physically, one important issue concerning the interaction between AGN and star formation is the concept of “AGN feedback”. The AGN role in the star formation activity can be both positive and negative depending on the evolutionary stage. While at the beginning the presence of an AGN can possibly trigger the star formation, at later stages, it is one of the responsible of its quenching. This is indeed observed in deep surveys (e.g. Page et al. 2012). A luminous AGN causes the heating and photo-ionization of the surrounding medium, and the radiation pressure can push the gas to outer galactic regions with a resulting lack of fuel for further star formation (Springel et al. 2005; Farrah et al. 2012; Cano-Díaz et al. 2012; Pope et al. 2012). A negative feedback is also required by semi-analytical models and cosmological simulations, in order to suppress the star formation activity (Granato et al. 2004; Springel et al. 2005; Bower et al. 2006; Croton et al. 2006; Booth & Schaye 2009). On the other hand, a positive feedback would explain the circumnuclear starburst observed in local AGNs (Genzel et al. 1998; Schweitzer et al. 2006).

One of the most popular explanation of the AGN–starburst connection is given by Hopkins et al. (2008). In this scenario, the connection between the two mechanisms is found in major mergers between galaxies. These drive new fuel to the inner regions, enhancing both the star formation and the black hole accretion. After a rapid growth, the central black hole begin to dominate the total luminosity. Gas and dust are heated, ionized and then removed by radiation pressure, quenching the star formation. The picture here summarized is well represented by Figure 1.4, taken from Hopkins et al. (2008).

Given the relations observed, and here discussed, between AGNs and host galaxies, it becomes crucial to quantify the relative importance of the two mechanisms. This can be obtained, for example, through the ratio between the emission of AGN and the rest of the galaxy, at different wavelengths. Both mechanisms emits in the MIR and FIR. In one case this emission is due to the diffuse dust and to the dust surrounding the star forming regions, while in the other case, the responsible for such an emission is the dusty torus surrounding the central black hole. In both cases, the total IR energy emitted correspond to a similar amount of energy absorbed at shorter wavelengths. Thanks to the high resolution and depth of the images taken at these wavelengths by the *Herschel* and *Spitzer* space observatories, both the AGN and SF emission peaks in the FIR can be sampled. In this sense, the SPIRE bands (250, 350 and  $500\mu\text{m}$ ) for *Herschel*, and the MIPS bands (24 and  $70\mu\text{m}$ ) for *Spitzer* are a fundamental tool to constrain the IR spectra of such sources. the *Spitzer* IRAC bands, at the same time, are located at the peak of the stellar emission (3.5 and  $4.5\mu\text{m}$ ), allowing for deep detections and precise stellar masses computations. The *Akari* IRC bands are crucial to compute the precise

energy distribution in those spectral regions affected by PAH emission, between IRAC and MIPS. Thanks to this multi-wavelength analysis, it is possible to constrain the emission due to AGN and star formation, computing at the same time the relative importance of these mechanisms at different SFR levels and for different masses. This is exactly what we will do in the analysis described in this thesis.

## 1.6 The South Ecliptic Pole field (SEP)

The South Ecliptic Pole field (SEP), also referred as AKARI Deep Field South (ADF-S), covers, in the *spitzer*-IRAC bands, a rectangular area of  $\sim 7 \text{ deg}^2$ . IRAC observations were undertaken as a part of the Spitzer IRAC-MIPS Extragalactic Survey (SIMES), designed to “statistically” cover up to 28 square degrees in up to 557 MIPS- $24\mu\text{m}$ -only independent fields. The most prominent advantage of this field is its position with respect to the ecliptic plane, that makes it less affected from cirrus and zodiacal dust contamination. The SEP field is then the ideal field where extragalactic multiwavelength surveys can be undertaken, since both the extinction is minimized in the optical/UV spectral region, and the dust emission in the mid and far-IR is lower than elsewhere.

The IRAC covered area, upon which this thesis focuses, is centered at RA 04:47:00 and dec -52:15:00 (J2000). This field is one of the prime targets of many infrared, sub-mm, and mm telescopes, accompanied by ancillary data in the optical and ultraviolet. The IRAC-covered SEP field presents the advantage of an elongated geometry (4:1) that substantially reduces the cosmic variance bias (Trenti & Stiavelli 2008), given the high variety of different density environments probed when compared to a square sky region.

Originally, the field was explored by the *Akari* space telescope within the Far Infrared Survey (FIS, Matsuhara et al. 2006; Matsuura et al. 2011), covering a total of  $\sim 12 \text{ deg}^2$  at 65 and  $160\mu\text{m}$ . The  $7 \text{ deg}^2$  imaged by IRAC are also covered by *Spitzer*-MIPS (24- $70\mu\text{m}$ , Clements et al. 2011) and *Herschel*-PACS (100- $160\mu\text{m}$ ) and SPIRE (250, 350,  $500\mu\text{m}$ ) in the context of the Herschel Multi-tiered Extragalactic Survey (HerMES). Radio observations were taken in the submm regime with the South Pole Telescope and the Atacama Cosmology Telescope. A small but very deep area was observed by AzTEC at 1.1mm. Optical coverage of the central square degree is now available in the CTIO-u, B, V, I, VST-g, i, z and VISTA-J, H, Ks bands, while the coverage of the entire field in the g, r, i, and z bands will be obtained as part of the Dark Energy Survey (DES).

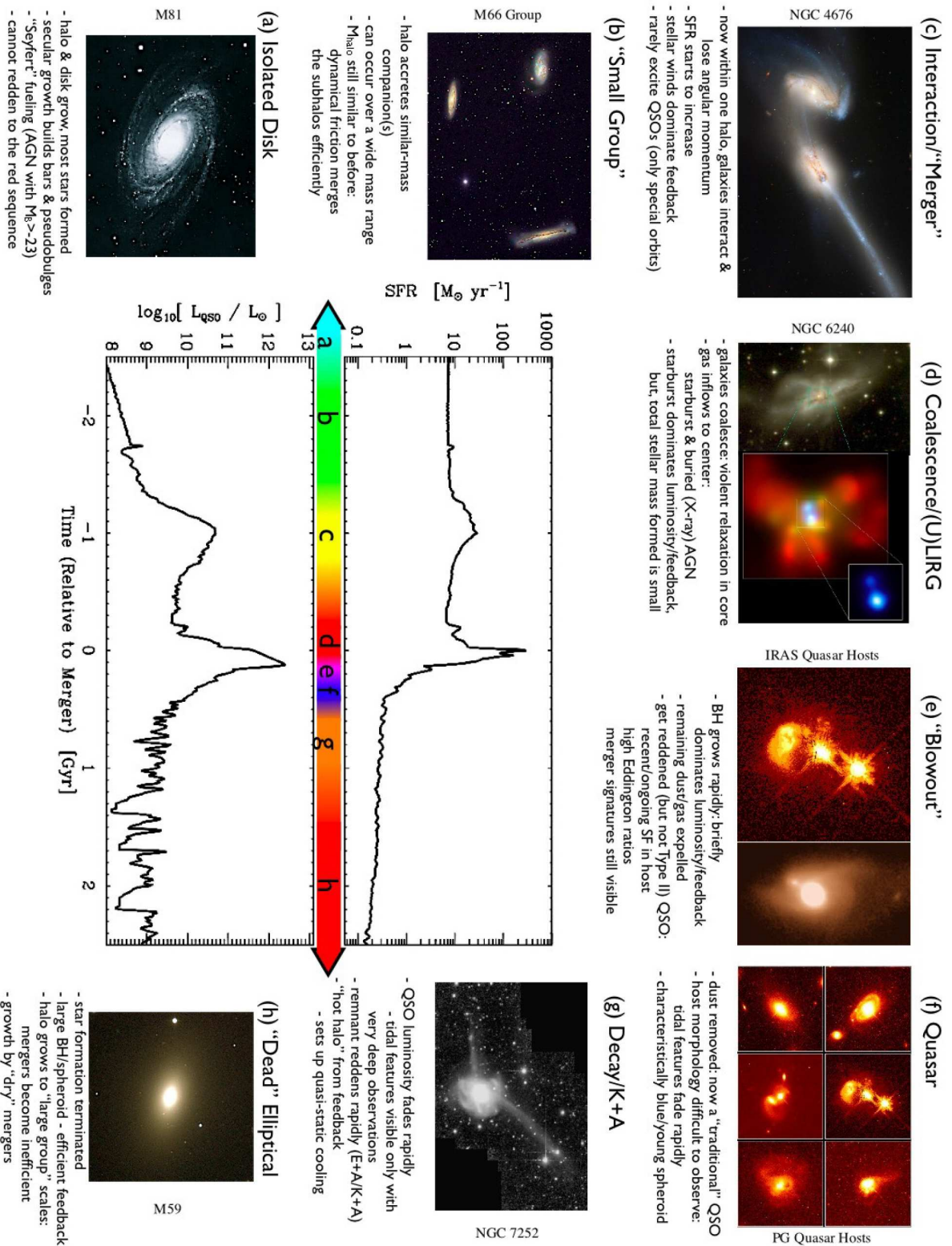


Figure 1.4: Schematic representation of the AGN–starburst connection through a major merging scenario of Hopkins et al. (2008). This image is taken from the same work.



## Chapter 2

# The multi-wavelength catalog

In this chapter we describe the characteristics of the multi-wavelength catalog of sources detected in the SEP field. The catalog contains the positions of the sources computed using different photometric bands, their fluxes with the associated uncertainties and other information useful to determine the reliability of the reported values, such as the identified associations at the different wavelengths. For some photometric bands, the fluxes were computed from SEP images that we personally reduced or that are not publicly available. In these case, we present the images along with their main characteristics. For other bands, the fluxes were taken from publicly available catalogs. The catalog is based on the IRAC-1 ( $3.6\mu\text{m}$ ) identifications above the  $3\sigma$  S/N level. We do not use in the following analysis, and we do not report the fluxes of any of the sources below the  $3\sigma$  threshold in the IRAC-1 band. We will describe the source extraction that we undertook in the different bands, giving a particular importance to the IRAC-1 channel upon which our catalog is based. We will discuss also the completeness and the numer counts obtained at  $3.6\mu\text{m}$ . In Figure-2.1 we report the final IRAC-1 mosaic of images taken in the SEP field. The  $\sim 7\text{ deg}^2$  of the SEP filed are fully covered (see Figure-2.2) by the following instruments and bands: IRAC-1 and IRAC-2, MIPS 24 and  $70\mu\text{m}$ , SPIRE 250, 350,  $500\mu\text{m}$ , WISE W1, W2, W3, W4 ( $3.35, 4.60, 11.56, 22.09\mu\text{m}$ ), 2MASS-J, H, Ks, VISTA-J, H, Ks. The central  $\text{deg}^2$  is covered in the optical wavelengths by CTIO-.u, B, V, I, VST-g, i, z, WFI- $R_C$ . A fraction of the optically covered areas is also covered in the AKARI 3.3, 4.6, 7, 11, 15,  $24\mu\text{m}$  bands.

### 2.1 IRAC-1 catalog

For the detection and extraction of sources we used the *SExtractor* software (Bertin & Arnouts 1996) in dual image mode, using IRAC channel 1 as detection image and computing the fluxes in the IRAC-2 image in the same sky positions. The IRAC-1 image is represented in Figure 2.1 and its coverage in Figure 2.2

The extraction and the photometry performed with *SExtractor*, take place in two separate phases. The detection of the sources is performed over a filtered map. The dimension (FWHM) of the filter is set through the FILTER parameter. As specified in the *SExtractor* user manual<sup>1</sup> a gaussian filter improve the faint object detections and the best choise is to set its value to the FWHM of the filter similar to the seeing FWHM of the observations. Since the FWHM of the IRAC images is  $1.66''$ , corresponding to 2.77 pixels, we used a 2.5 pixels gaussian filter. During

---

<sup>1</sup>Sources Extractor for dummies, by Dr. Benne W. Holwerda

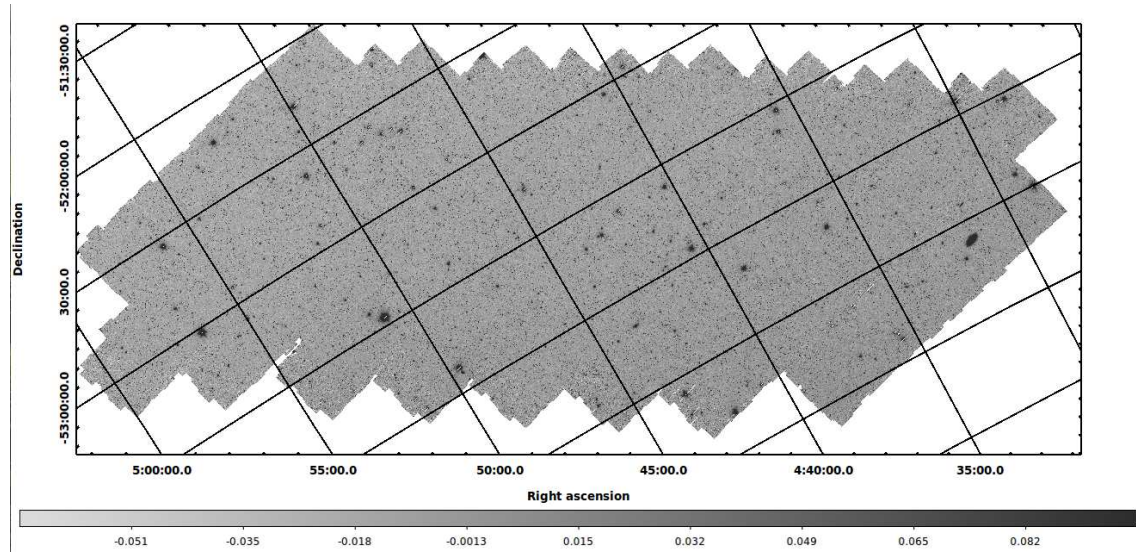


Figure 2.1: Image of the SEP field in the IRAC 1 band. Darker colors correspond to higher fluxes. The color scale is expressed in units of MJy/str.

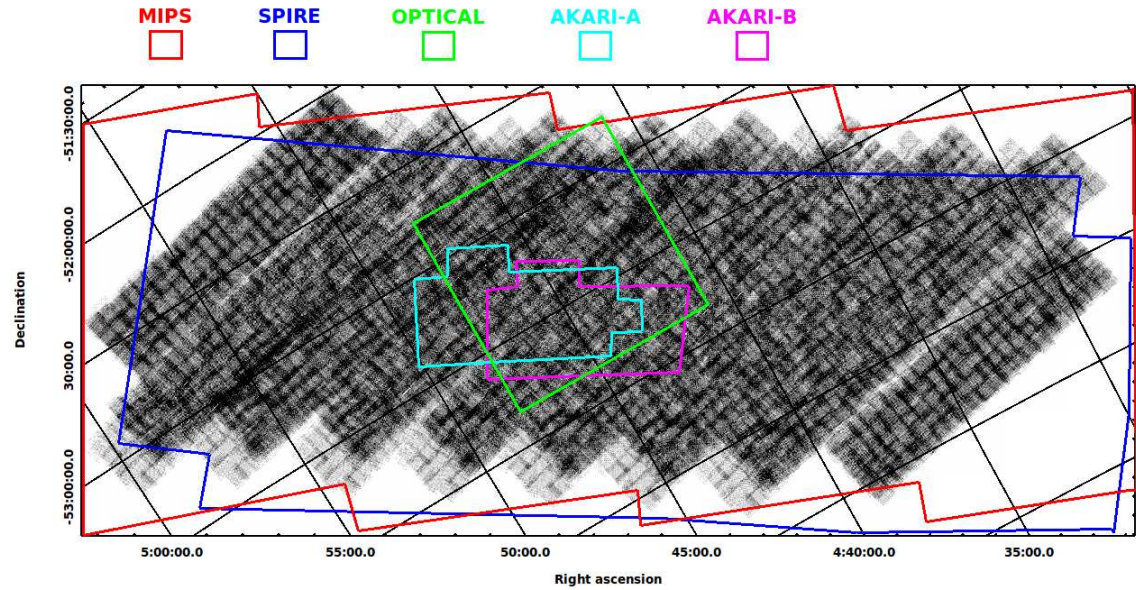


Figure 2.2: Coverage of the SEP field in the IRAC 1 band. Darker colors correspond to higher coverages. Superimposed, the coverages in the MIPS (red) and in the SPIRE (blue) bands, that cover almost the whole field. The coverage in the WISE, 2MASS and VISTA bands is not reported, since the field is completely covered in these bands. The central square degree (green) is covered by the optical bands (CTIO- $u$ ,  $B$ ,  $V$ ,  $I$ , VST- $g$ ,  $i$ ,  $z$ , WFI- $R_C$ ), while the AKARI bands  $N_3$ ,  $N_4$ ,  $S_7$  and  $S_{11}$  cover the cyan area (Akari-A) and the AKARI- $L_{15}$  and  $L_{24}$  cover the magenta area (Akari-B).

the same phase, for a first background estimation, the original image is filtered with a different filter, the size of which is chosen through the BACK\_FILTERSIZE parameter. We set this parameter equal to 3. This naive background estimation is computed over an area of  $32 \times 32$  pixels (set using the BACK\_SIZE parameter), through a bi-cubic-spline interpolation over all

the areas of size BACK\_SIZE. We set the BACK\_SIZE parameter greater than the average dimension of the sources, in order to prevent from the contamination of the background with the source's light. For the photometry, a more precise value of background is estimated as follows. First, the isophotal boundaries of the object, computed at the detection level, define a rectangular box in the image, centered in each source. This box is then symmetrically enlarged on both axes by 50%. This sets the inner boundaries of the background annulus. Adding BACKPHOTO\_THICK more pixels on both sides of each axis the outer limits of the background annulus can be obtained.

We set the *SExtractor* parameters that rule the background computation to privilege a good background estimation for the faintest sources. In Figure 2.3 we show a restricted area of the IRAC image with the background that we computed in the same region. It is possible to notice that the background is not affected by the source's light in the majority of the cases, while there is a residual contamination for the brightest sources with a flux close to the saturation value.

For the detection, we set a  $1.5\sigma$  threshold, with a minimum of 5 connected pixels above this level. For each object we computed AUTO fluxes, as well as total fluxes within  $4''8$ ,  $7''2$  and  $12''0$  diameter apertures (pixel-scale= $0.6''/\text{pix}$ ). In the detection, we used the uncertainty map as a weight image. The main parameters set in the *SExtractor* configuration file are listed in table 5.4.

Parameter	Setting
DETECT_MINAREA [pixels]	5
DETECT_THRESH [sigma]	1.5
ANALYSIS_THRESH [sigma]	1.5
FILTER (type, FWHM [pixels])	gauss, 2.5
size [pixels]	5x5
DEBLEND_NTHRESH	32
DEBLEND_MINCONT	0.005
BACK_SIZE	32
BACKPHOTO_TYPE	LOCAL
BACK_FILTERSIZE	3
BACKPHOTO_THICK	15
PHOT_APERTURES [pixels]	8, 12, 20
PHOT_AUTOPARAMS	2.5, 3.5
SEEING_FWHM [arcsec]	1.66
PIXEL_SCALE [arcsec]	0.6

Table 2.1: Parameters used to extract the sources and compute the fluxes in the IRAC-1 channel. The fluxes were computed from the the IRAC-2 image using the IRAC-1 prior positions, through the the dual-mode technique.

*SExtractor* AUTO fluxes are an estimate of the total flux of a source in an elliptical aperture with semi-major axis ( $a$ ) proportional to the Kron radius of the object ( $R_K$  Kron 1980). We chose  $a = 2.5 \times R_K$ , by setting the *SExtractor* parameter Kron\_fact= $2.5^2$ . A Kron\_fact= $2$  would theoretically ensure that, for any Sersic index  $n$  (Sérsic 1963), the aperture includes

<sup>2</sup>In *SExtractor* nomenclature,  $a[\text{pixels}] = \text{KRON\_RADIUS} \times \text{A\_IMAGE}$ , where A\_IMAGE is the luminosity profile RMS, in pixels, along the major axis direction while  $\text{KRON\_RADIUS} = \text{Kron\_fact} \times R_K$ . Both KRON\_RADIUS and A\_IMAGE are available as *SExtractor* output parameters, while Kron\_fact is an input parameter and  $R_K$  is the Kron radius computed by *SExtractor* and expressed in units of semi-major axis A\_IMAGE

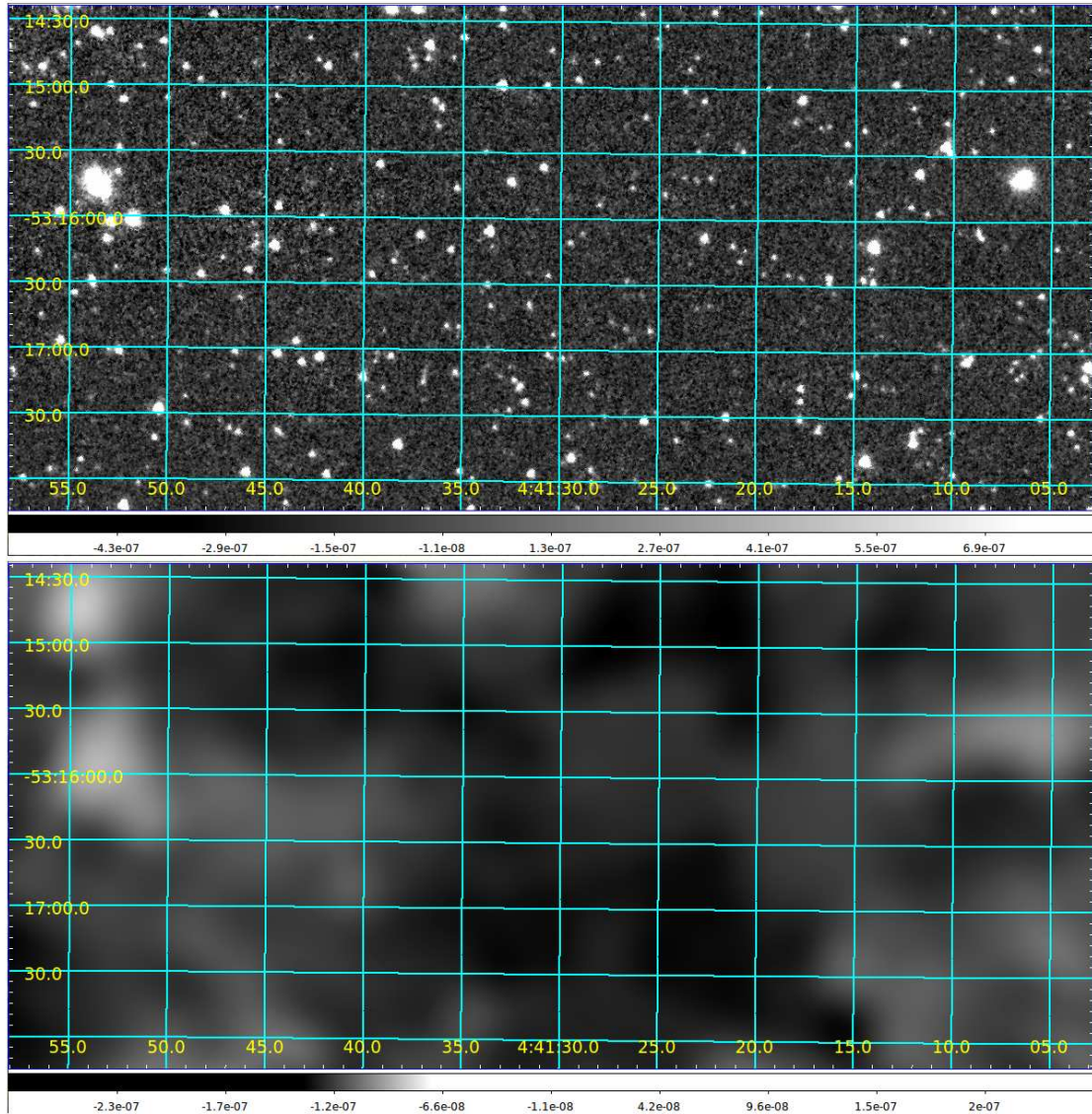


Figure 2.3: **Upper panel:** Zoom in a central region of the IRAC-1 image. **Lower panel:** Background computed in the same area. The color scales are in Jy.

more than the  $\sim 90\%$  of the galaxy flux (Kron 1980; Graham & Driver 2005). Since, however, the observationally derived Kron radii  $R_K$  result smaller than the theoretical ones, especially at higher  $n$  values, in the practical case this fraction can reduce to about the 50% for some extreme cases, such as bright cluster galaxies and concentrated systems (Graham & Driver 2005). When  $a < 3.5$  pixels ( $2''1$ ), then the AUTO flux is computed within a circular aperture of 3.5 pixel radius. We chose to report AUTO fluxes in the catalog because these take into account the real apparent dimension of the sources, the elliptical shape of the observed isophotes and the radial profile of the sources. The constant aperture correction that has to be applied to the APERTURE fluxes, computed inside fixed circular apertures doesn't take into account these effects. For objects with a point-like surface brightness profiles, the ratio  $R$  between the AUTO flux and the APERTURE flux should be constant with the total apparent luminosity

of the sources, since the semi-major axis ( $a$ ) used to compute the Kron fluxes does not depend on the total flux, but only on the luminosity profile. This can be understood in the simple example of PSFs with perfect Gaussian profiles. An aperture with radius equal to one  $\sigma$  will always include the 68.27% of the total flux, regardless of the total intensity of the galaxy.

In Figure 2.4 we report the median radii  $\langle R \rangle$  computed in bins of semi-major axis. The ratio  $R$  is computed for three different apertures (4"8 in black, 7"2 in red, 12"0 in blue). We note that when the semi-major axis computed for the elliptical aperture is the same as the radius used for the circular aperture taken as referent,  $\langle R \rangle$  should be equal to unity, since the flux is computed in apertures with similar dimensions. This is verified for all the three apertures used. When the semimajor axis of the elliptical aperture become smaller than the dimension of the fixed circular aperture, the APERTURE fluxes seem to be smaller than the AUTO fluxes. This effect is invisible at the smallest fixed aperture (4"8), while it becomes more important when considering the biggest aperture (12"0). This behaviour is probably due to a little overestimation of the background that becomes appreciable when considering point-like sources (more likely faint), and the largest circular aperture, more prone to this kind of contamination.

Figure 2.4 shows a strong linear correlation between  $\log(\langle R \rangle)$  and  $a$  (with different slopes depending on the size of the aperture used):

$$\log(\langle R \rangle) = m \times a + q \quad (2.1)$$

The coefficients of the linear fit are reported in table 2.2. For these objects a constant cor-

Aperture [arcsec]	m	q
4.8	0.0214	-0.0831
7.2	0.0148	-0.100
12	0.0085	-0.100

Table 2.2: *Coefficients of the linear interpolation (equation 2.1). The  $m$  and  $q$  coefficients were computed for the three referent apertures, excluding the points that evidently deviate from the linear behaviour.*

rection (as measured from point sources, and provided in the IRAC data handbook) to the aperture fluxes provide the wrong total flux. Thus, hereafter, all fluxes reported are total fluxes measured within the Kron SExtractor apertures.

The average  $\langle R \rangle$  that we computed considering the whole set of data was  $1.213 \pm 0.002$  for the 4.8" aperture,  $1.063 \pm 0.001$  for the 7.2" aperture and  $1.030 \pm 0.006$  for the 12" aperture. These values are consistent with the aperture corrections reported in the IRAC IRS Data handbook (Reach et al. 2005) that are:  $1.213 \pm 2\%$ ,  $1.124 \pm 2\%$  and  $1.061 \pm 2\%$  for the three apertures. It has to be considered, however, that in this computation we considered all the sources, independently from their extension, while in the IRAC handbook, only the point-like sources are considered.

### 2.1.1 Survey sensitivity

We include in the final catalogs only sources with significant flux measurement ( $> 3\sigma$ ). As seen before, the AUTO flux is computed within a variable elliptical aperture that depends on the extension of the source. To compute the signal-to-noise ratio we instead used the APERTURE fluxes of the sources computed in the smallest aperture, and compare them with the noise measured in apertures with the same size.

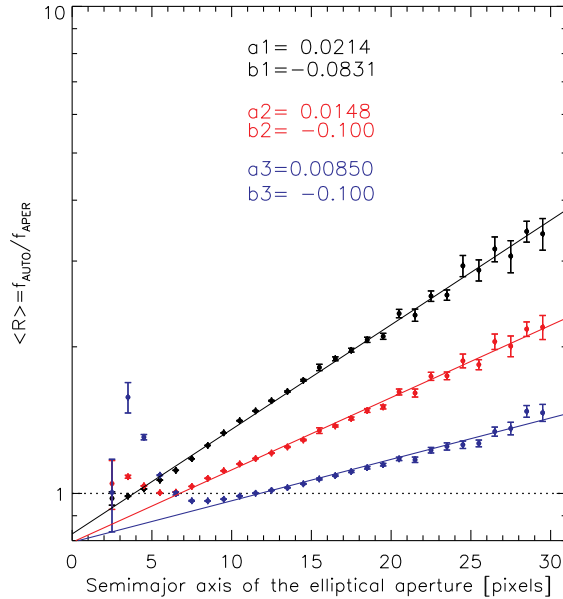


Figure 2.4: Average ratio between AUTO fluxes and uncorrected aperture fluxes (4''8 in black, 7''2 in red, 12''0 in blue), as a function of the semi-major axis of the Kron elliptical aperture, together with the best linear fit. A logarithmic ordinate scale is used, with values coincident with those expressed in the shown y axis.

The standard procedure to derive the signal-to-noise ratio in variable-depth mosaics is to compute the  $\sigma_{mc}$  corresponding to the mean coverage value ( $\langle C \rangle$ ) and then scale it by a factor  $f$  to account for the specific coverage,  $C$ , of each point in the mosaic, i.e.,  $f = \sqrt{\langle C \rangle / C}$  (see e.g., Surace et al. 2005). This procedure assumes that the noise scales as the square root of the exposure time, which is true only if the noise is dominated by the sky background. In our data, we found that this is not the case, and the noise contribution of faint unresolved sources is substantial.

Thus, we derive the noise properties of the image empirically, as a function of the actual coverage of the mosaic. We proceed as follows: first, we divide the mosaic into a grid of square apertures, each with an area of 49 pixels, corresponding to the number of pixels in the smallest circular aperture considered (i.e.,  $\pi \times 4^2 \text{ pixels} \simeq 50 \text{ pixels}$ ). Then, we assign to each square the total flux computed from all pixels within it. This is equivalent to measuring fluxes inside randomly distributed circular apertures, but with the advantage of maximizing their number and minimizing overlap. The situation is visually described in Figure ??.

Next, we divide all square apertures into six groups, according to the median coverage of the 49 pixels that contributed to the total flux. In Figure 2.6, we show the cumulative coverage distribution in the pixels of the original mosaic, as well as the coverage distribution of the square apertures in the binned mosaic, compared with that in the pixels of the original mosaic.

In each coverage bin, we compute the standard deviation of the background apertures, by fitting a Gaussian function to the symmetrized<sup>3</sup> distribution of the fluxes within the square apertures. Symmetrization is necessary to exclude those apertures falling on sources. The fits

<sup>3</sup>The flux distributions were symmetrized with respect to the value corresponding to the median of the distributions.

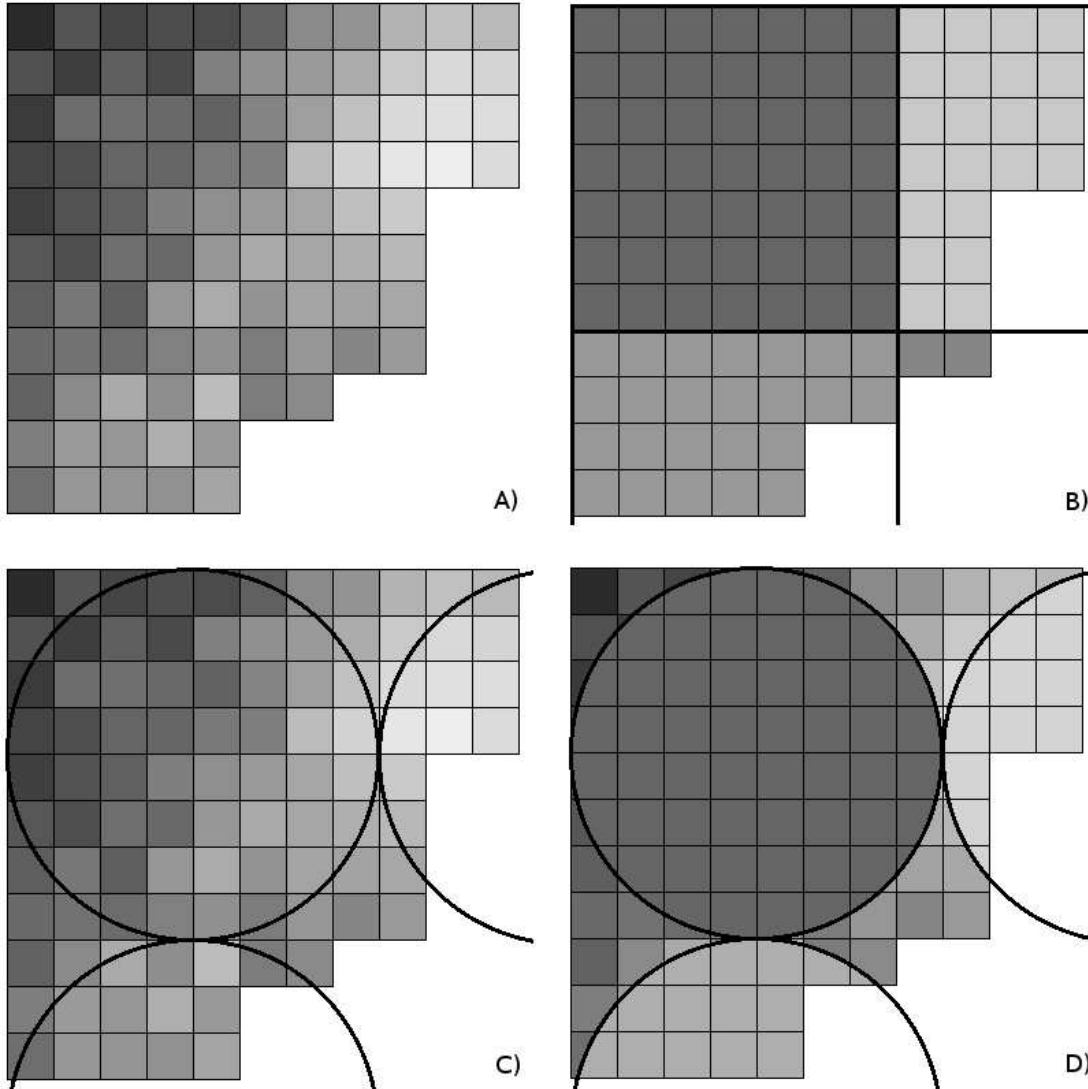


Figure 2.5: Procedure applied to compute the signal-to-noise ratio in our IRAC image. First, we divided the original image (A) in squared areas containing 49 pixels each, then we compute the total flux inside the square apertures (B). This is equivalent (with a 2% difference) to compute the flux inside circular apertures with 4 pixel radii (B and C), but with the advantage that the number of the number of aperture is maximized, improving the statistic, without overlaps.

are reported in Figure 2.7.

In Figure 2.8, we show the resulting  $\sigma$  as a function of average coverage in each of the six bins. Clearly the dependency with  $C$  is shallower than expected for the simple Poissonian approximation ( $\sigma \propto C^{-0.5}$ ; shown with a continuous red line). The theoretical curve is normalized to reproduce  $\sigma$  at the average coverage of the survey ( $\langle C \rangle = 6$ ).

We found that the trend between  $\sigma$  and coverage is well reproduced by a shallower relation, with  $\sigma \propto C^{-\alpha}$ , and  $\alpha = 0.224$  (black solid line in Figure 2.8).

Finally, for each source in the catalog we computed its average coverage within the  $4''8$  aperture, and compared the aperture flux to the  $3\sigma$  value of the corresponding coverage. We

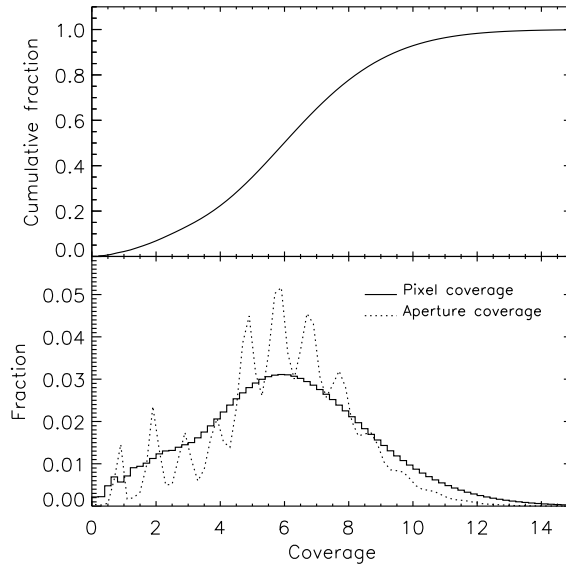


Figure 2.6: **Top** Cumulative distribution of the pixel coverage. **Bottom** Distribution of average coverage in the  $7 \times 7$  square apertures (dotted line), compared with the coverage distribution for all pixels in the original IRAC mosaic.

retain in the final catalog only sources with IRAC-ch1 flux above  $3\sigma$ .

The typical aperture corrected (Aperture correction=1.213)  $\sigma$  gives the depth of the IRAC-1 observations, that is  $3.54\mu\text{Jy}$ . Since we cut the catalog at a  $3\sigma$  level, for the sources close to the  $3\sigma$  limit, we expect a total flux of  $3 \times 3.54\mu\text{Jy} = 10.62\mu\text{Jy}$ . The real distribution of the total fluxes in the proximity of this cut is shown in Figure 2.9. The total flux of the sources at the cut limit ( $F < 3.1$ ) is  $9.7 \div 10.5\mu\text{Jy}$  (peak  $\div$  median). The flux corresponding to the 90% of completeness, computed as described in section 2.1.2 is  $13.5\mu\text{Jy}$ . The final IRAC-based catalog includes 255232 sources.

### 2.1.2 Survey completeness and number counts

We determine the completeness of the IRAC survey by comparing the number counts observed in IRAC-ch1 with those published in (Fazio et al. 2004, FA04) and in (Franceschini et al. 2006, FR06). We perform the analysis using galaxies+stars in the entire SEP field as well as using galaxy only in the central square degree, where we use the optical WFI- $R_C$  band for the star/galaxy separation.

#### Galaxy/star separation

In order to separate galaxies from stars, we proceed applying multiple diagnostics, based on the available multiwavelength data. Because of the need of the optical data, we limit the selection to the central  $1.13\text{deg}^2$  area covered by the R/WFI band. This area is larger than the value reported in table 2.7 ( $1.08^2$ ). In table 2.7, for the “OPTICAL” bands as R/WFI, we are considering only the sources included in the final multi-wavelength catalog for having at least two optical detections (see section 2.2.7). In this section and for the completeness computations we consider instead a direct IRAC- $R_C$  correlation that we performed without

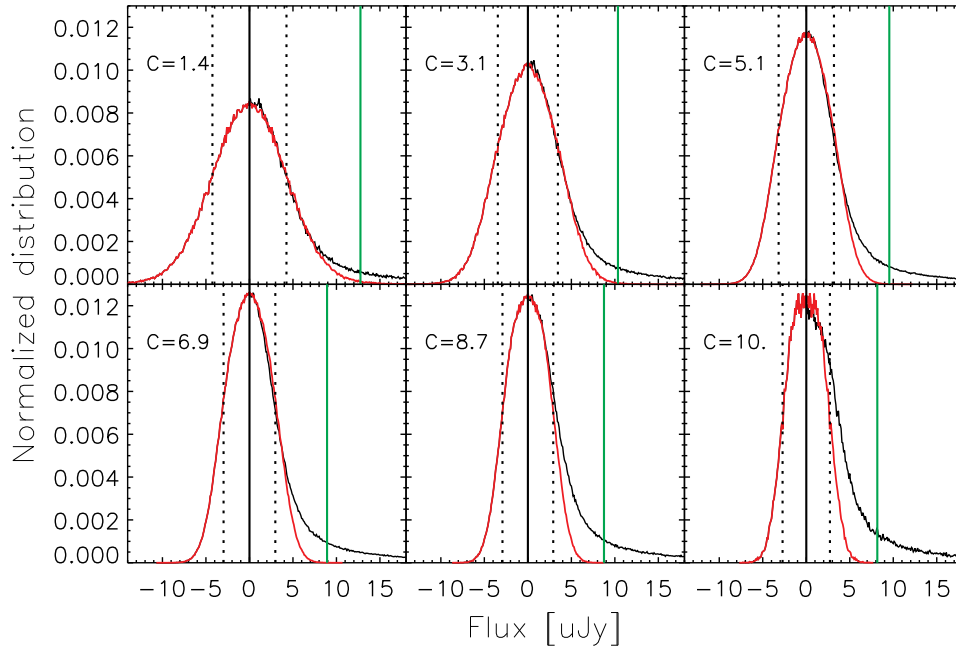


Figure 2.7: Normalized original (black line) and symmetrized (red) histograms of the fluxes inside the  $7 \times 7$  pixels square apertures, for the 6 bins of coverage. The median coverages in each bin are indicated. The pointed black lines represent the values of  $\pm 1\sigma$  and the continue green line is the  $3\sigma$  level above the sky that we used as a threshold to select the IRAC 1 sources in the final catalog. The distributions are symmetrized with respect to the flux value of the median bin found between those with number values above the 85% of peak values of the distributions.

the two-detection limitation. The use of the IRAC- $R_C$  direct or indirect (through the optical catalog) correlation doesn't substantially affect the number counts and the completeness levels computed. We chose the R/WFI band among the other optical ones for the following reasons: 1) the large area covered; 2) the depth of the  $R_C$  mosaic; 3) the high detection rate (for points 1, 2 and 3, see Table 2.6); 4) The clear separation between stars and galaxies that can be achieved using the  $F_{R_C}$  versus  $F_{I1}$  diagram (see middle panel of Figure 2.10).

In order to separate the contribution of stars and galaxies in the number counts, we first classify as galaxy any object detected in the SPIRE-250 $\mu\text{m}$  band. The stellar emission at these wavelengths is very low even for the coldest stars, while the dust in the star-forming galaxies is more probably the responsible for such an emission. A SPIRE detected source is more probably a distant star forming galaxy than a very local cold star. Then, we identified stars in the IRAC-ch1 versus MIPS-24 plane (Figure 2.10, top panel). All the sources with MIPS-24 below  $\log(F_{24}) = a_1 \times \log(F_{3.6}) + b_1$  ( $a_1=1.33$  and  $b_1=0.33$ ), are classified as stars. Because of the bright MIPS-24 flux limit, this selection misses fainter IRAC-detected stars. We thus implement two additional constraints, based on the  $R_C - 3.6\mu\text{m}$  color (middle panel in Figure 2.10) and the *SExtractor* CLASS\_STAR parameter measured in the IRAC-ch1 image (bottom panel in Figure 2.10). The *SExtractor* CLASS\_STAR<sup>4</sup> parameter's reliability worsens at the faintest and at brightest fluxes. At low fluxes galaxies look more and more like

<sup>4</sup>CLASS\_STAR = 0 for galaxies, = 1 for stars.

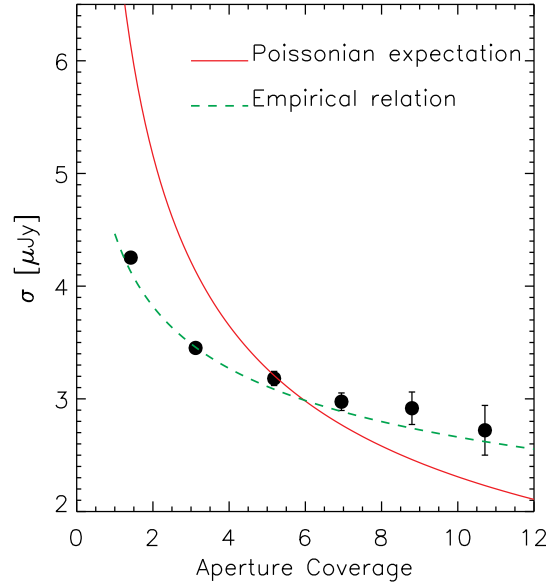


Figure 2.8: Sky background noise,  $\sigma$ , as a function of coverage,  $C$ , for the IRAC-1 image. The expected Poissonian trend is shown with a red solid line, while the observed best fit relation is shown with a green dashed line. Clearly, the observed trend is shallower than the theoretical one.

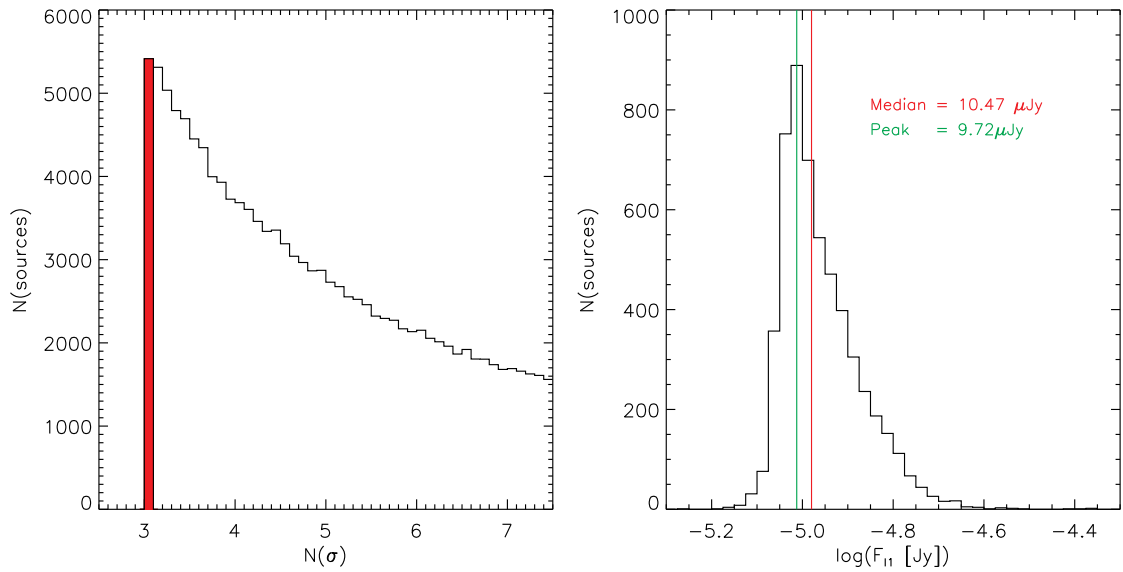


Figure 2.9: Distribution of the sources in the proximity of the  $3\sigma$  cut of the IRAC catalog. On the left, the histogram of the ratio  $N(\sigma)$  between aperture fluxes and underlying noise. No sources with IRAC flux below  $3\sigma$  are included in the final catalog. The distribution of fluxes for the sources with  $N(\sigma) < 3.1$  is represented on the right panel.

point sources with the IRAC PSF, while for bright objects the wings of the PSF are wrongly interpreted as due to an extended galaxy by *SExtractor*. We classify as stars sources with

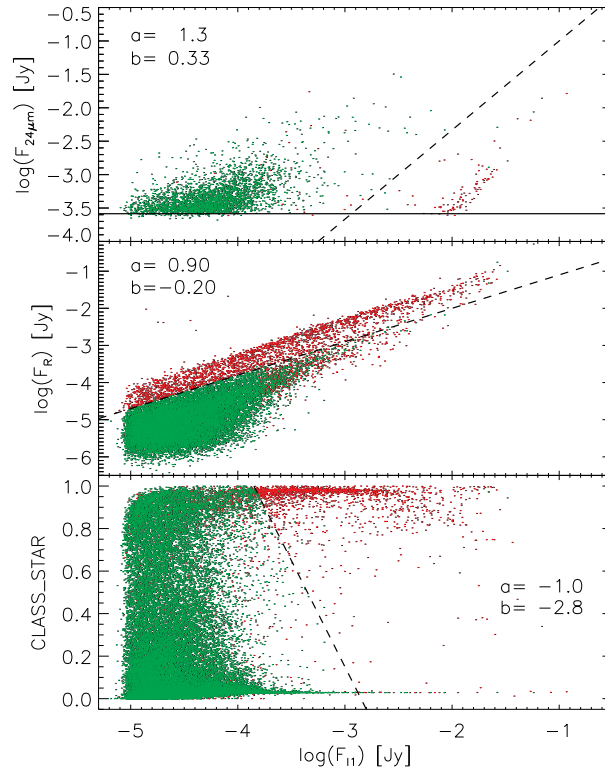


Figure 2.10: Galaxy selection. **Upper panel:** in the  $3.6\mu\text{m}$  Vs  $24\mu\text{m}$  fluxes plot (IRAC1-MIPS24), the stars are located below the line with coefficients  $a=1.33$  and  $b=0.33$ . **Middle panel:** in the  $3.6\mu\text{m}$  Vs  $R_c(\text{WFI})$  fluxes plot, the stars stay below the line with coefficients  $a=0.90$  and  $b=-0.20$ . **Lower panel:** in the  $3.6\mu\text{m}$  flux Vs CLASS STAR parameter we considered galaxies all the sources in the left of the line with coefficients  $a=-1.0$  and  $b=-2.85$ , but also the ones in the right of the same line with a SPIRE  $250\mu\text{m}$  identification. In all the three plots, the sources in the  $R_c$  area used for the completeness computation have been highlighted in red.

$\log(F_{R_c}) > a_2 \times \log(F_{3.6}) + b_2$  ( $a_2=0.90$ ,  $b_2=-0.20$ ) and with  $\text{CLASS\_STAR} = a_3 \times \log(F_{3.6}) + b_3$  ( $a_3=-1.0$ ,  $b_3=-2.8$ ). The latter condition implies that all objects with  $F_{11} < 141\mu\text{Jy}$  are classified as galaxies, unless they were classified as stars by the other two conditions. Below this flux limit, however, the number of galaxies greatly exceeds the number of stars and the number counts are only weakly affected by a possible contamination from stars. At the bright end, the unlikely misidentification of galaxies as stars is mitigated by the fact that such  $3.6\mu\text{m}$ -bright galaxies will be detected at both  $24\mu\text{m}$  and  $250\mu\text{m}$ , and thus properly identified as galaxies.

### Cumulative number counts

In table 2.3 we report the SIMES IRAC ch1 cumulative number counts (both for galaxies+stars, and galaxies only), with associated Poissonian uncertainties. The comparison between the cu-

mulative SIMES number counts and those in FA04 and FR06 are shown in Figure 2.11. Out of the three fields presented in FA04, we only compare to their intermediate depth field, i.e., the  $0.17 \times 2.0$  area in the EGS field. The FA04 *galaxy* number counts are presented in differential form, starting at the highest flux of  $178 \mu\text{Jy}$ . To convert them from differential to cumulative, we use the cumulative galaxy number counts at  $178 \mu\text{m}$  from FR06. FR06 does not present *total* number counts, so in this case we use the SIMES value as a starting point. We note that given the small contribution of the brightest bins to those at fainter fluxes in the cumulative distributions, the results do not change with or without the small correction for the very bright objects. Figure 2.11 shows that the cumulative number counts of FR06 and FA04 differ both at low and high fluxes. At the brightest fluxes, these differences are likely due to cosmic variance and small number statistics. At the faintest fluxes, the differences can be due to both cosmic variance and the assumed correction we performed to the FA04 cumulative number counts.

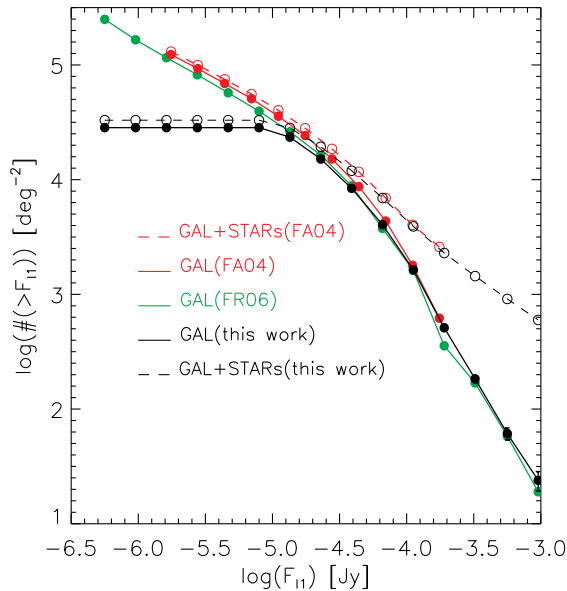


Figure 2.11: *IRAC 1* integral number counts for galaxies only (continue lines) and for galaxies and stars (dashed lines). Our counts are reported in black, FA04 counts in red and FR06 in green. For FR06, only galaxy counts are available. FA04 counts tend to stay somewhat higher than FR06 counts. Our counts are more similar to FR06 than to FA04.

As Figure 2.11 shows, the cumulative number counts in the SEP field start to depart from the deeper FR04 and FA04 number counts around  $F_{I1} \sim 10^{-4.5} - 10^{-5} \text{Jy}$ . To estimate the completeness quantitatively, we use the ratio between our cumulative number counts and those in FR06 and FA04. We are clearly complete above  $\sim 50 \mu\text{Jy}$ , where the counts are dominated by statistical fluctuations due to small number statistics. As already noticed, the FR06 and FA04 number counts disagree with each other, likely due to cosmic variance. We therefore proceed as follows: we assume that all surveys are complete above  $55 \mu\text{Jy}$ , and normalize the cumulative number counts to one above that flux level. We then compute completeness as a function of IRAC flux from the average between the ratio of our number counts and FR06

Flux log[Jy]	$N_{\text{GAL}}$ ( $> S_{3.6}$ ) [deg $^{-2}$ ]	$N_{\text{TOT}}$ ( $> S_{3.6}$ ) [deg $^{-2}$ ]	Corr. fact.
-3.020	24 ± 5	598 ± 24	1.0
-3.250	61 ± 8	912 ± 30	1.0
-3.490	183 ± 14	1443 ± 38	1.0
-3.720	511 ± 23	2292 ± 48	1.0
-3.756*	599 ± 24	2477 ± 50	1.0
-3.950	1636 ± 40	3911 ± 63	1.0
-3.956*	1687 ± 41	3967 ± 63	1.0
-4.156*	3715 ± 61	6518 ± 81	1.0
-4.180	4050 ± 64	6920 ± 83	1.0
-4.356*	7181 ± 85	10583 ± 103	0.981
-4.410	8395 ± 92	11959 ± 109	0.972
-4.556*	12420 ± 111	16376 ± 128	0.963
-4.640	15129 ± 123	19337 ± 139	0.946
-4.756*	19258 ± 139	23762 ± 154	0.933
-4.870	23482 ± 153	28234 ± 168	0.918
-4.956*	26349 ± 162	31110 ± 176	0.855
-5.100	28387 ± 168	32962 ± 182	0.734
-5.156*	28400 ± 169	32974 ± 182	0.677
-5.330	28401 ± 169	32975 ± 182	0.508
-5.356*	28402 ± 169	32975 ± 182	0.489

Table 2.3: Integral number counts for IRAC-1 sources and completeness. The counts are reported for the same flux bin intervals as in FA04 (indicated with an asterisk) and in FR06. We calculated the completeness as the normalized mean ratio between our number counts and the number counts in FA04 and FR06. The integral number counts corrected for completeness can be obtained dividing the first column for the third column, but the result is dependent from the FA04 and FR06 when the correction is lower than 1.0. The associated error is the poissonian noise  $\sqrt{N}$ .

and FA04. Figure 2.12 shows the completeness as a function of IRAC flux. We report the final values in Table 2.4.

Compleat. level	Flux I1 [log(Jy)]
50	-5.37
90	-4.82
95	-4.67
97	-4.54
99	-4.41

Table 2.4: Significant completeness levels for I1 detected sources, linearly interpolated from the normalized completeness curves.

## Differential number counts

We computed IRAC-1 differential number counts separating galaxies from stars in the way already described in section 2.1.2. We considered the *total* number counts obtained both in the whole IRAC-1 area and in the R/WFI area (used to separate the contribution from stars and galaxies). The raw differential counts are reported in table 2.5 for galaxies and stars together (*total* counts) and for galaxies only. The associated poissonian error is also reported.

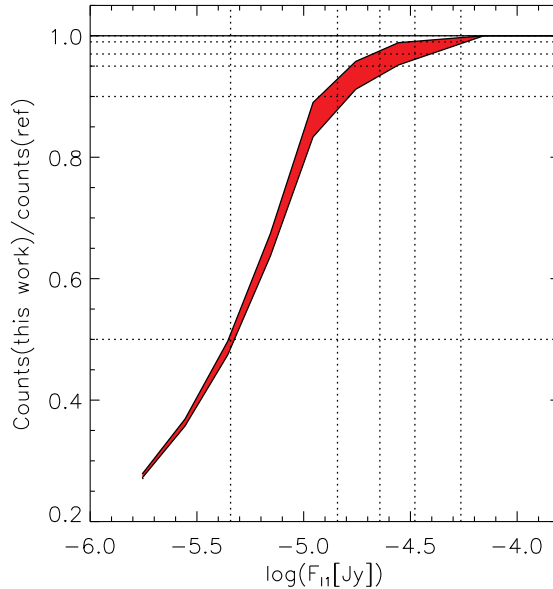


Figure 2.12: Normalized completeness curve derived from the ratios between our (total and galaxy) and referent number counts (FR06 galaxy counts, FA04 total and FA04 galaxy counts), the area include the minimum and the maximum values obtained. The dashed lines represent the 50, 90, 95 and 97% completeness levels of the average curve and the correspondent  $F_{11}$ .

In figure 2.13 we compare our results with FR06 and FA04 number counts. In this case, besides the FA04 counts in the EGS field, we also show the FA04 counts in the Bootes field (the shallower data points). The FA04 measures in the EGS field and in the shallower Bootes field are clearly separable at about  $10^{-4.6}$  Jy, where a little step in the counts is visible.

Comparing with FA04 counts, we observe an excess of number counts above 1mJy. This excess is mostly due to the stars. On the contrary, the *galaxy* differential number counts stay a little below the FA04 results, at least for what concern the counts in the Bootes field. In the same range of fluxes, our *galaxy* number counts result more similar to FR06.

## 2.2 Multi-wavelength catalog merging

We merged the IRAC 1 catalog with the catalogs obtained in different photometric bands. Basically, for each IRAC-1 source we search each of the catalogs obtained at different wavelengths, for the geometrically closest counterpart. This procedure, simple in principle, is in reality a little bit more complicated in reality. We adopted different strategy for the different instruments used and for this reason, there are more detailed descriptions of the procedures adopted in the following sections. For example, the IRAC-2 counterparts are not “searched”; thanks to the dual-mode technique, the flux in the IRAC-2 band is measured in the original image, at the same positions where the IRAC-1 sources where found. Again, the SPIRE counterparts are not identify trough a direct search in the IRAC catalog. We instead exploited the known MIPS position to find the counterparts in the tree bands. In order to increase the precision of our search, we performed an initial run that we used to find the baricenter position of the

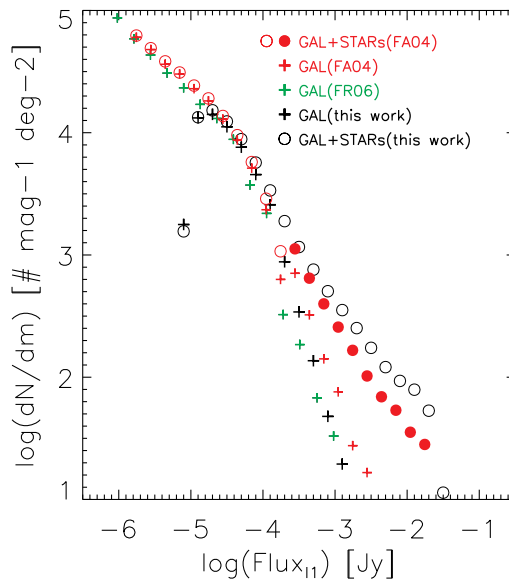


Figure 2.13: *IRAC 1 differential number counts.* Galaxy counts are represented by crosses, while total (galaxies+stars) number counts by circles. The colors used are: black for our results, green for FR06 and red for FA04. The filled red circles represents counts in the Bootes field, while the open red circles correspond to the EGS field (the red crosses represent galaxy counts in the corresponding fields). Our total counts are represented by filled circles when referring to the  $\sim 1 \text{ deg}^2$  covered by R-WFI, and by open circles when representative of the whole area covered by IRAC 1.

geometrical counterparts. Then we re-center all the catalogs to the IRAC-1 positions and we performed a new search. This allowed us, in some cases, to include in the multi-wavelength catalog a small fraction of counterparts wrongly excluded before, and to exclude some counterparts inappropriately included. The results of the recentering technique are summarized in table 2.6. The number of counterparts that we identified in each band and that we included in the final multi-wavelength catalog are summarized in table 2.7. The MIPS and SPIRE detected counterparts are highlighted. In the same table, we report the depth reached in the different bands. Unless differently specified, we computed the depth as described in Section 2.1.1, and visually represented in figure 2.4, for the IRAC-1 band. As aperture corrections, we used the average  $\text{FLUX\_AUTO}/\text{FLUX\_APER}$  ratios that we computed in each filter for unsaturated and not-too-faint sources.

### 2.2.1 IRAC-2

The IRAC-2 band covers about the 94% of the IRAC-1 area, with a depth of  $1.87 \mu\text{Jy}$  ( $1\sigma$ ). The noise level was computed as already described for the IRAC-1 band, computing the flux in square apertures each of which with an area similar to the  $4''8$  aperture. The sigma of the symmetrized distribution is finally multiplied for the aperture correction (1.234) to obtain the final depth. As it can be noted from Figure 2.14, in this case the noise level inside the square apertures is more similar to the expected Poissonian behaviour. The mean coverage is 5.9.

We measured the fluxes using the IRAC-1 prior positions, exploiting the dual-image mode

Flux log[Jy]	$N_{\text{GAL}}$ [mag <sup>-1</sup> deg <sup>-2</sup> ] R+I1 area	$N_{\text{TOT}}$ [mag <sup>-1</sup> deg <sup>-2</sup> ] R+I1 area	$N_{\text{TOT}}$ [mag <sup>-1</sup> deg <sup>-2</sup> ] Whole I1 area
-0.9	0.0 ± 0	1.8 ± 1	3.1 ± 2
-1.1	0.0 ± 0	3.5 ± 2	2.3 ± 2
-1.3	0.0 ± 0	5.3 ± 2	7.2 ± 3
-1.5	0.0 ± 0	11 ± 3	11 ± 3
-1.7	0.0 ± 0	58 ± 8	53 ± 7
-1.9	0.0 ± 0	67 ± 8	79 ± 9
-2.1	1.8 ± 1	71 ± 8	93 ± 10
-2.3	3.5 ± 2	135 ± 12	121 ± 11
-2.5	3.5 ± 2	179 ± 13	174 ± 13
-2.7	7.1 ± 3	264 ± 16	252 ± 16
-2.9	19 ± 4	337 ± 18	354 ± 19
-3.1	48 ± 7	436 ± 21	505 ± 22
-3.3	136 ± 12	668 ± 26	759 ± 28
-3.5	342 ± 18	960 ± 31	1161 ± 34
-3.7	879 ± 30	1655 ± 41	1891 ± 43
-3.9	2576 ± 51	3027 ± 55	3372 ± 58
-4.1	4546 ± 67	4941 ± 70	5695 ± 75
-4.3	7607 ± 87	8039 ± 90	8859 ± 94
-4.5	11175 ± 106	11601 ± 108	12366 ± 111
-4.7	14121 ± 119	14562 ± 121	15245 ± 123
-4.9	13214 ± 115	13639 ± 117	13383 ± 116
-5.1	1775 ± 42	1851 ± 43	1560 ± 39

Table 2.5: *Differential number counts for IRAC-1 sources. We computed the galaxy number counts removing the stars as explained in the text. To do this we used also the R-WFI fluxes and the computation is consequently limited to this area. The total counts (galaxies+stars) are computed in the whole area. The associated poissonian error is computed as  $\sqrt{N}$ .*

technique allowed by *SExtractor*. This technique allows to use one image as a reference for the detection and position of the sources, and the other to measure the fluxes. If the wavelengths of the two bands are close enough, the same “auto” apertures (in which the flux is computed), can be used for both the images<sup>5</sup>. We found 405 sources with a null IRAC 2 flux, the majority of which (~80%) are located in areas poorly covered even in the I1 band (COVERAGE less than 2). We considered as “undetected” (F=0) this kind of sources. The IRAC-1 sources not covered in the IRAC-2 band are set to F=-99. The positions of the sources are those of the IRAC 1 priors, and for this reason they are not reported in the multiwavelength catalog.

## 2.2.2 MIPS 24 and 70

We merge the IRAC catalog with the MIPS 24 and 70 $\mu$ m catalog described in Clements et al. (2011). As described in that work, the sources were extracted using *SExtractor* with a  $2\sigma$  threshold and a minimum of 5 connected pixels above this threshold. A combined set of aperture and “AUTO” fluxes were used as described in Shupe et al. (2008). Basically the fluxes are computed in automatic elliptical apertures if the sources have extended profiles (more than 100 pixels) while aperture fluxes are considered for point-like surces. The Clements et al. (2011) catalog already include the 70 $\mu$ m counterparts of the 24 $\mu$ m sources, so we limit the analysis to

---

<sup>5</sup>This means that the parameters A\_IMAGE, B\_IMAGE, and KRON\_RADIUS that we report in the catalog for IRAC 1 channel, are the same that were used for IRAC 2 extraction.

Band	Search radius	Mean distance		Baricenter position (RA, DEC)		$\Delta N$
		before r.	after r.	before r.	after r.	
MIPS	2.60	1.01	0.86	0.099, 0.49	0.0098, 0.069	+125 (0.5%)
SPIRE *	8.04	3.02	3.02	0.018, -0.020	0.0046, -0.0029	+1 (0.01%)
CTIO u**	1.16	0.35	0.30	-0.030, -0.18	$1.05 \times 10^{-5}$ , -0.0068	/
CTIO B**	1.02	0.31	0.28	-0.079, -0.14	-0.0020, -0.0060	/
CTIO V**	0.91	0.29	0.25	-0.078, -0.13	-0.0026, -0.0071	/
CTIO I**	0.93	0.29	0.26	-0.11, -0.10	-0.0049, -0.0052	/
WFI R <sub>C</sub> **	0.82	0.34	0.28	-0.086, -0.17	-0.0064, -0.015	/
VST i**	0.80	0.28	0.26	0.034, -0.11	0.0022, -0.0088	/
VST g**	0.90	0.30	0.27	0.040, -0.11	0.0029, -0.0080	/
VST z**	0.78	0.27	0.25	0.039, -0.12	0.0023, -0.0081	/
OPTICAL**	0.82	0.24	0.24	-0.0037, -0.015	$-5.76 \times 10^{-5}$ , -0.0011	-8 (-0.03%)
VISTA (J,H,K <sub>S</sub> )	0.82	0.26	0.24	0.0123, -0.0947	0.00049, -0.0053	+155 (0.1%)
AKARI N3	3.73	1.059	1.054	0.047, -0.051	0.012, -0.0087	-5 (-0.06%)
AKARI N4	3.73	1.082	1.071	0.067, -0.11	0.011, -0.016	+1 (0.01%)
AKARI S7	5.20	1.61	1.59	-0.049, -0.18	-0.0028, -0.037	0 (0.01%)
AKARI S11	5.66	1.51	1.49	-0.17, -0.12	-0.028, -0.010	-2 (0.08%)
AKARI L15	5.68	2.044	1.99	-0.24, -0.38	-0.030, -0.072	+4 (0.2%)
AKARI L24	6.90	2.44	2.42	-0.087, -0.35	-0.028, -0.077	+3 (0.4%)
WISE & 2MASS	2.68	0.52	0.50	-0.0012, -0.10	$5.4 \times 10^{-4}$ , -0.0072	-2 (0.001%)

\* In this case, the recentering and the indicated distances refers to the MIPS 24 position.

\*\* For the optical bands we proceeded as follows:

- 1) The catalogs were singularly recentered to the IRAC coordinates.
- 2) Then we made an optical catalog, with coordinates averaged among the various optical catalogs.
- 3) Finally we recentered the optical catalog average coordinates to the IRAC catalog.

Table 2.6: Counterpart searching radii and recentering effects. The quantities are indicated in arcseconds. We report the radii used for the search, the mean distance of the counterparts and the position of their baricenter (RA, dec). The 2MASS positions indicate the good agreement with the IRAC coordinates.

the cross-correlation between IRAC and MIPS-24, and report the  $70\mu\text{m}$  association identified in the original MIPS catalog. Clements et al. (2011) estimate that the  $24\mu\text{m}$  catalog is 50% complete at 0.26mJy and 80% complete at 0.32mJy, while the sources reliability is 96% at 0.285mJy.

In order to identify the most likely IRAC counterpart to the detected MIPS source, we proceed as follows. For each MIPS- $24\mu\text{m}$  source, we searched the IRAC catalog for the nearest source inside a radius equal to the quadratic sum of the  $\sigma$  of the PSF of the two instruments (i.e., given  $\sigma_{I1}=0.705$  and  $\sigma_{24\mu\text{m}}=2.505$ , a search radius of  $2''6$ ). In the matching process, we corrected the small systematic shift<sup>6</sup> (of the order of  $\Delta RA = 0''099$ ,  $\Delta DEC = 0''49$ ) between the two catalogs. Thus, we corrected the MIPS positions before searching for the nearest IRAC counterpart. We report in the final catalog both the corrected and the original coordinates of the sources in each band. In table 2.6 we report the distance and the average RA and DEC shifts of all sources matched in the catalog. The MIPS-IRAC distance distribution is represented in Figure 2.15 for the sources in the multiwavelength catalog. When multiple IRAC sources are found within the search area, we associate the closest IRAC object. However, we do flag the object as a possible misidentification. Out of all MIPS sources (24531 objects), 99.8% have an unique IRAC counterpart within a region of  $2''6$  radius. The reliability of the identifications is discussed in section 2.2.4. In the multi-wavelength catalog, the fluxes of

<sup>6</sup>We verified that the shift did not depend on the position in the large mosaic, thus indicating that any distortion in the IRAC mosaic was properly accounted for.

## Chapter 2: The multi-wavelength catalog

Band	Area [deg <sup>2</sup> ]	Depth	Detection rate [%]	Number of detections in the catalog			
				All	MIPS	SPIRE	MIPS & SPIRE
IRAC				255232	24531	12296	8500
1	7.74	3.54μJy <sup>[1]</sup>	100.00	255232	24531	12296	8500
2	7.26	1.9μJy	99.83	238958	23115	12152	8399
MIPS	7.66		9.71	24531	24531	8500	8500
24μm		0.26mJy <sup>[2]</sup>	9.71	24531	24531	8500	8500
70μm		24mJy <sup>[2]</sup>	0.35	882	882	711	711
SPIRE	6.52		5.72	12296	8500	12296	8500
250μm		5.2mJy <sup>[3]</sup>	4.95	10640	7649	10640	7649
350μm		4.24mJy <sup>[3]</sup>	5.54	11911	8307	11911	8307
500μm		6.16mJy <sup>[3]</sup>	4.77	10265	7147	10265	7147
OPTICAL <sup>[4]</sup>	1.28		68.28	28381	2819	1416	1080
CTIO u	0.67	0.37μJy (AB=25.0)	14.43	3085	573	262	235
CTIO B	0.67	0.37μJy (AB=25.0)	28.08	6008	809	393	328
CTIO V	0.66	0.42μJy (AB=24.9)	41.13	8707	1032	508	418
CTIO I	0.66	0.21μJy (AB=25.6)	61.25	13020	1364	729	558
WFI R <sub>C</sub>	1.08	0.13μJy (AB=26.2)	60.76	21971	2273	1117	864
VST g	1.20	0.075μJy (AB=26.7)	57.05	22887	2510	1222	950
VST i	1.17	0.26μJy (AB=25.3)	69.66	26660	2647	1314	1008
VST z	1.20	0.44μJy (AB=24.8)	68.61	27526	2732	1360	1043
VISTA	7.74		45.15	115245	15003	6257	5259
VISTA J	7.74	1.76μJy (AB=23.3) <sup>[5]</sup>	40.75	104016	13080	5357	4567
VISTA H	7.74	2.44μJy (AB=22.9) <sup>[5]</sup>	35.83	91437	12060	5006	4330
VISTA Ks	6.01	5.31μJy (AB=22.1) <sup>[5]</sup>	39.70	78457	11182	4427	3775
AKARI	0.64 (A+B)		57.85	12240	1845	1124	828
AKARI N3	0.46 (A)	5.53μJy	57.86	8826	1044	656	461
AKARI N4	0.47 (A)	4.59μJy	60.65	9336	1155	733	504
AKARI S7	0.44 (A)	33.07μJy	16.80	2445	721	397	345
AKARI S11	0.44 (A)	41.80μJy	17.67	2560	945	489	423
AKARI L15	0.41 (B)	74.1μJy	15.50	2070	958	536	442
AKARI L24	0.40 (B)	155.8μJy	6.11	810	558	319	306
WISE	7.74		55.90	142687	19622	9212	6903
WISE W1		3.15μJy	55.90	142687	19622	9212	6903
WISE W2		6.2μJy	55.90	142687	19622	9212	6903
WISE W3		54μJy	55.90	142687	19622	9212	6903
WISE W4		450μJy	55.90	142687	19622	9212	6903

NOTE:

<sup>[1]</sup> IRAC 1 catalog is cut at a  $3\sigma$  level, as described in the text, keeping into account the underlying coverage for each source. Sources with fluxes below this value can consequently be found in the catalog.

<sup>[2]</sup> 50% completeness from Clements et al. (2011). Minimum 24μm flux in the catalog: 0.20mJy. Minimum for MIPS identified sources with a SPIRE counterpart: 0.31mJy.

<sup>[3]</sup> From Oliver et al. (2012).

<sup>[4]</sup> Sources detected in at least 2 optical bands among u, B, V, I, i, g, z, R<sub>C</sub>.

<sup>[5]</sup> From McMahon et al. (2013); Vista Hemisphere survey data release 2 expected depths.

Table 2.7: Area covered and  $1\sigma$  depth (unless differently specified in the notes) in the bands of the catalog. An IRAC-1 identification and the correspondent measured flux is always present. We also report the number of counterparts with a MIPS 24, SPIRE or with both MIPS and SPIRE counterpart. The detection rate is computed as the ratio between the number of IRAC sources covered and the number of sources with a detection in each band.

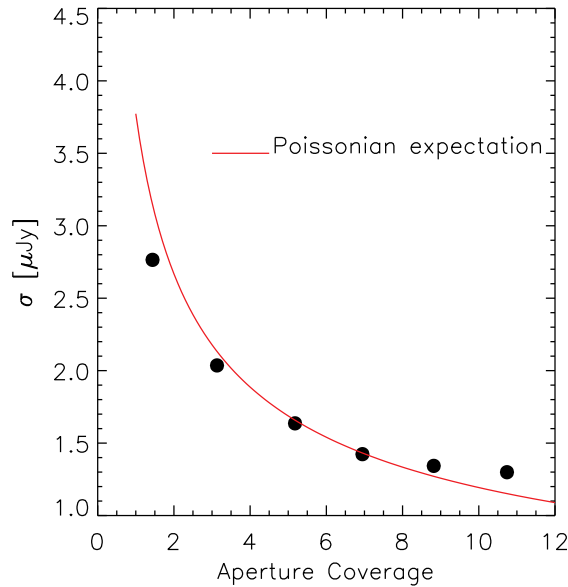


Figure 2.14: Sky background noise,  $\sigma$ , as a function of coverage,  $C$ , for the IRAC-2 image. The expected Poissonian trend is shown with a red solid line.

the sources covered by the MIPS survey are set to  $F=0$  when undetected. The sources not covered in this band have fluxes set to -99.

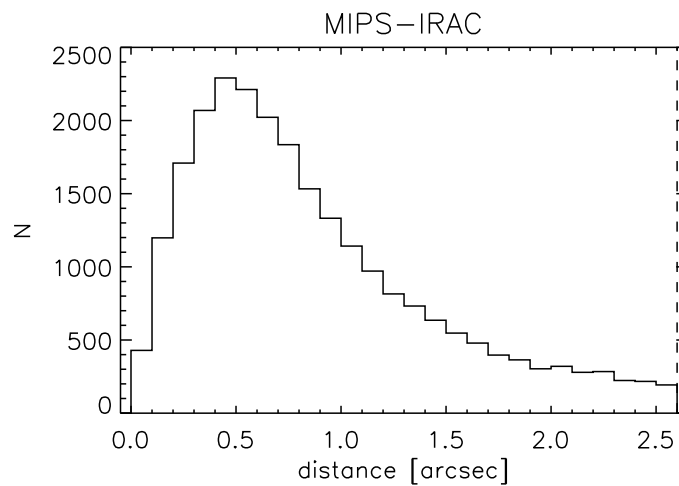


Figure 2.15: MIPS-IRAC distance distribution for the MIPS sources in the multiwavelength catalog. The coordinates of the MIPS sources are corrected for the average shift with the IRAC (ra, dec) positions.

### 2.2.3 SPIRE 250, 350, 500 $\mu$ m

The SEP field was observed as part of the *Herschel* Multi-tiered Extragalactic Survey (HerMES, Oliver et al. 2012). The SPIRE survey in the SEP field covers approximately the 84% of the whole SIMES field. The second data release (DR2) of the SPIRE catalog includes all sources identified at  $1\sigma$  level at least in one band among the 250, 350 or 500 $\mu$ m. In our multi-wavelength catalog, we included the SPIRE counterparts identified in the band-merged catalog (“*xID250*”). In the HerMES nomenclature, these catalogs contains the fluxes in the three spire bands extracted on the *Starfinder* Diolaiti et al. (2000) 250 $\mu$ m positions. A Gaussian shaped PSF is used, with the FWHM set to 18.15, 25.15 and 36.3 arcsecs at 250, 350 and 500 micron respectively.

The large size of the SPIRE PSF (18”0 at 250 $\mu$ m) prevents us from directly cross-correlate the SPIRE and IRAC catalogs. Instead, we exploited the MIPS 24 $\mu$ m detections as a “bridge” between the two wavelengths, using a direct SPIRE-IRAC correlation only when the MIPS detection was not available. Given the extreme low S/N cut applied to the original SPIRE catalog, and the not trascurable possibility of introducing spurious SPIRE detections, we serched the SPIRE counterparts given the MIPS-24 prior position as illustrated in the left panel of Figure 2.16. In the search for SPIRE counterparts, we used a radius of 8”04 (quadratic sum of the MIPS and SPIRE-250 $\mu$ m PSF’s  $\sigma$ ), centered in the MIPS source position. For the IRAC-SPIRE direct correlation we used a searching radius of 7.675”, quadratic sum of the IRAC and SPIRE-250 $\mu$ m PSF’s  $\sigma$ . As we did for the MIPS-IRAC correlation, we corrected the small systematic shift between the MIPS and SPIRE original catalogs. Thus, we corrected the SPIRE positions before searching for the nearest MIPS counterpart. In table 2.6 we report the distance and the average RA and DEC shifts. When a single SPIRE detection resulted as the possible counterpart for two or more different MIPS sources, we associate a fraction of the total SPIRE fluxes to each MIPS counterpart. The correpondent fraction of flux is proportional to the 24 $\mu$  flux. We do not include in the multi-wavelength catalog those SPIRE-MIPS sources for which we couldn’t find a MIPS-IRAC correlation, unless a direct SPIRE-IRAC correlation is found. We include in the catalog the original SPIRE coordinates together with the IRAC-recentered ones<sup>7</sup>.

We found 8047 SPIRE sources having a single MIPS counterpart, 440 with a double counterpart and 3 with more than 2 counterparts (see Figure 2.18). The sum of these sources, 8490, is not the total number of sources with both a SPIRE and a MIPS counterpart (that is instead 8500), since we found an indipendent SPIRE-IRAC and a MIPS-SPIRE correlation for 10 sources without a MIPS-IRAC correlation (see right panel of Figure 2.16). The SPIRE sources with more than a single MIPS counterpart, or with only a direct SPIRE-IRAC association are flagged in the catalog ( $N\_MIPS\_IRAC > 1$  and  $N\_MIPS\_IRAC \leq 0$ ). Considering the 8490 sources with a SPIRE-IRAC association through the MIPS position and the 3806 sources with a direct SPIRE-IRAC association, we included a total of 12296 SPIRE sources in the multi-wavelength catalog. The reliability of the association with the IRAC counterpart is discussed in section 2.2.4. The SPIRE-MIPS and the SPIRE-IRAC distance distributions are represented in Figure 2.17 for the sources included in the multiwavelength catalog. The distance of the counterparts can exceed the SPIRE-IRAC and SPIRE-MIPS searching radii. In the first case, this effect is due to the SPIRE sources with a MIPS counterpart correlated to an IRAC source, but with the SPIRE center more distant to the IRAC center then the IRAC-

---

<sup>7</sup>To recenter the SPIRE coordinates to the IRAC positions, we summed up the SPIRE-MIPS and MIPS-IRAC average shifts reported in table 2.6

SPIRE searching radius. In the second case, the effect is described above and illustrated in the right panel of Figure 2.16. For these sources we found both a MIPS-IRAC correlation and a SPIRE-IRAC direct correlation, but the SPIRE and MIPS centers are more distant than a SPIRE-MIPS searching radius. As for the MIPS sources, in the multi-wavelength catalog, the fluxes of the sources covered by the SPIRE survey are set to F=0 when undetected. The sources not covered in this band instead, have fluxes set to -99.

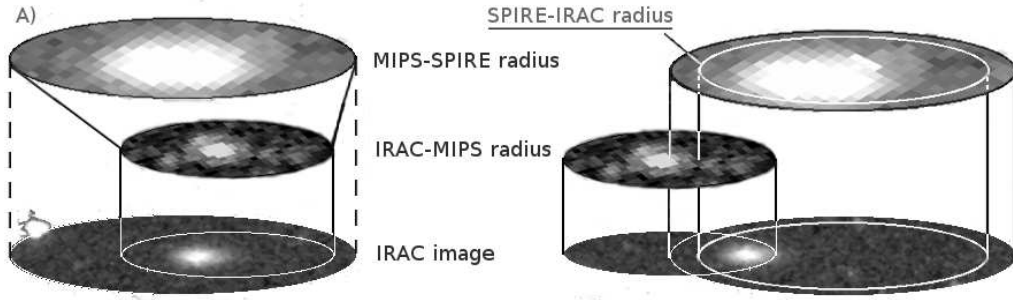


Figure 2.16: On the left (A), the typical association of the SPIRE sources to the IRAC sources: We find a SPIRE counterpart for a MIPS source and then we look for an IRAC counterpart for the MIPS detection. On the right (B), a rare case (10 sources in the final catalog) in which we find a MIPS-IRAC and a SPIRE-IRAC correlation without a MIPS-SPIRE association. The center of the MIPS counterpart is just outside the MIPS-SPIRE search radius. The MIPS-SPIRE association is however established since there are both a direct IRAC-MIPS and an IRAC-SPIRE association. The IRAC-SPIRE associations are considered also in those cases in which the MIPS counterpart is not detected (they are easily identifiable in the catalog).

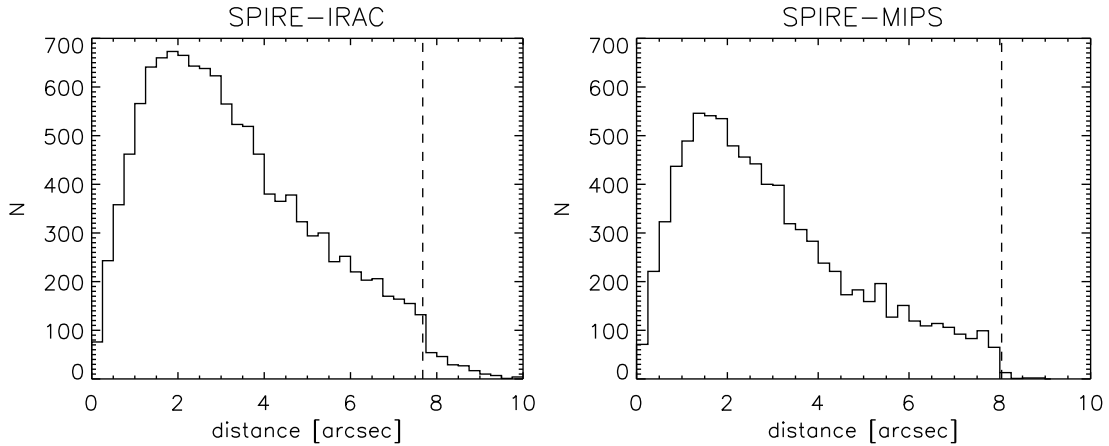


Figure 2.17: SPIRE-IRAC and SPIRE-MIPS distance distribution for the SPIRE sources in the multiwavelength catalog. The vertical dashed lines represent the searching radii used. In rare cases, the counterparts distance can exceed these thresholds as a consequence of the SPIRE-MIPS-IRAC and the direct SPIRE-IRAC correlations that we searched. The coordinates of the SPIRE sources are corrected for the average shift with the IRAC ( $ra$ ,  $dec$ ) positions, through two passages: first they are recentered to the average MIPS positions, then they are corrected for the average MIPS-IRAC shift.

### 2.2.4 MIPS and SPIRE counterparts reliability

Quantify the probability of having associated the right MIPS (IRAC) counterpart to the SPIRE (MIPS) source depends on both the number of galaxies found within the searching area, as well as the distance to the identified counterpart(s). We therefore develop a parameter  $P$  to assess the reliability of the matched counterparts, that accounts for both effects.

As mentioned earlier, we define the searching area by the radius  $r_s$  equal to the the quadratic sum of the PSF's  $\sigma$  of the two instruments involved (e.g.,  $r_s = \sqrt{\sigma_{\text{IRAC}}^2 + \sigma_{\text{MIPS}}^2}$ , for IRAC–MIPS correlation). We consider a normalized 2D Gaussian function with  $\sigma = r_s$ . For a counterpart at a distance  $d_i$  ( $\leq r_s$ ), we compute the quantity  $A_i$  as the probability of the galaxy being at a distance greater than  $d_i$ , for the given Gaussian function. For a single counterpart, centered on the coordinates of the starting objects,  $A_i = 1$ ; in general,  $A_i$  decreases as the distance of the counterpart increases. We then account for the presence of multiple counterparts (at different  $d_i$ ), by defining the parameter  $P$  as follows:

$$P = A_1 \times \frac{A_1}{\sum_i A_i}, \quad (2.2)$$

where  $A_1$  is defined as  $A_i$  corresponding to the closest counterpart. For multiple counterparts the factor  $A_1/\sum A_i$  is less than one, and decreases with the number of counterparts. For example, if we have two counterparts located at similar distances from the geometrical center, then  $A_1 \sim A_2$ , and  $P \sim A_1/2$ , meaning that the probability of one of the two geometrical counterpart to be the real and unique physical counterpart is shared with the other geometrical counterpart. If, instead, one of the two counterparts is close to the geometrical center ( $A_1 \sim 1$ ) and the other is at the border of the spot ( $A_1 \sim 0.3173^8$ ), then  $P_1 \sim 0.76$ , that is still an value close to one, indicating that the first geometrical counterpart remains the most likely unique physical counterpart, despite the presence of the second geometrical counterpart in the spot.

We computed the values  $P$  for the SPIRE-MIPS ( $P1$ ), MIPS-IRAC ( $P2$ ) and SPIRE-IRAC ( $P3$ ) correlations. The distribution of the  $P$  values is represented in Figure 2.19. The direct SPIRE-IRAC correlation is studied for the whole SPIRE sample in our catalog, considering also the sources for which we found a correlation trough the MIPS position.

The MIPS-IRAC and SPIRE-MIPS association reliability is usually high, as demonstrated by the distribution of  $P1$  and  $P2$ . As a consequence, the association of the SPIRE sources to the IRAC counterparts, trough the MIPS position is still reliable, even if the  $P3$  distribution is not as good as the previous ones. However, since we included in the final catalog also the SPIRE sources with a direct IRAC association, we assessed the value of  $P3$  that can be used to separate “reliable” and unreliable associations, trough a Monte Carlo Simulation (MCS). The simulation is performed by shifting the positions of the SPIRE sources within an area of 10, 20, 30, and 50  $\sigma$ , and then looking for potential IRAC counterparts. We found a detection rate of 38.89<sup>39.0</sup><sub>38.6</sub>%. We computed the  $P$  indicator for these false detections considering only the first counterpart, in order to obtain an upper limit for the value of  $P$  that they could have if they where in our catalog. The resulting distribution is represented with a green area in Figure 2.20, where it is normalized to represent the fraction of the SPIRE counterparts, found trough a direct IRAC-SPIRE association, and with a single IRAC counterpart (filled black area), that we expect to be wrong associations. The distribution of  $P$  for the whole

---

<sup>8</sup>This value correspond to  $1-0.6827$ , where 0.6827 is the unitary fraction included inside a gaussian function in the  $[-\sigma; +sigma]$  range.

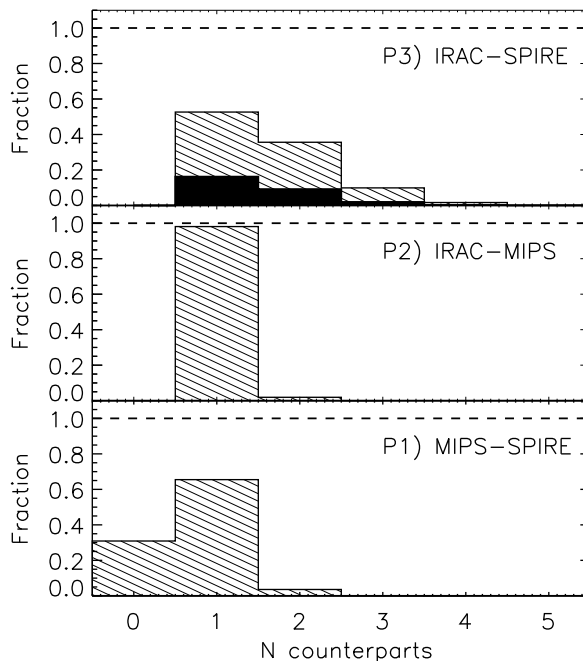


Figure 2.18: Fraction of sources with one or multiple “potential” counterparts inside the searching radius for the SPIRE-MIPS, MIPS-IRAC and SPIRE-IRAC positional correlations. The black filled distribution in the top panel represents the fraction of SPIRE sources without any MIPS counterpart (SPIRE sources with no MIPS counterparts in the bottom panel) and for which the IRAC counterpart is found through a direct IRAC-SPIRE positional correlation. The number of potential IRAC counterparts inside the SPIRE-IRAC spots is computed for the whole sample of SPIRE sources in the catalog, even when the correlation is found through the MIPS-24 positions.

SPIRE sample with a single IRAC counterpart is also represented (black dashed area). When considering the SPIRE-IRAC direct correlations, assuming as real the SPIRE sources in the original catalog, from the Monte Carlo simulation, we expect the wrong identification rates reported in Table 2.8.

P	Wrong identification rate at $P3=P$	Wrong identification rate above P	$N_{\text{SPIRE-IRAC}}^{\text{direct}}(P)$
0.35	0.75	0.39	3063
0.45	0.64	0.34	2265
0.55	0.46	0.27	1596
0.65	0.32	0.22	1097
0.75	0.21	0.18	659
0.85	0.15	0.15	268
0.95	0.14	0.14	31

Table 2.8: Expected rate of wrong direct SPIRE-IRAC identifications as a function of  $P$ .  $N_{\text{SPIRE-IRAC}}^{\text{direct}}(P)$  is the number of sources in our catalog, with  $P3>P$ , for which only a direct SPIRE-IRAC association, without MIPS, is found. For  $P=0$ ,  $N_{\text{SPIRE-IRAC}}^{\text{direct}}=3806$ . The wrong identification rates here reported have to be considered as superior limit, since we did not consider multiple potential IRAC counterparts in the simulation.

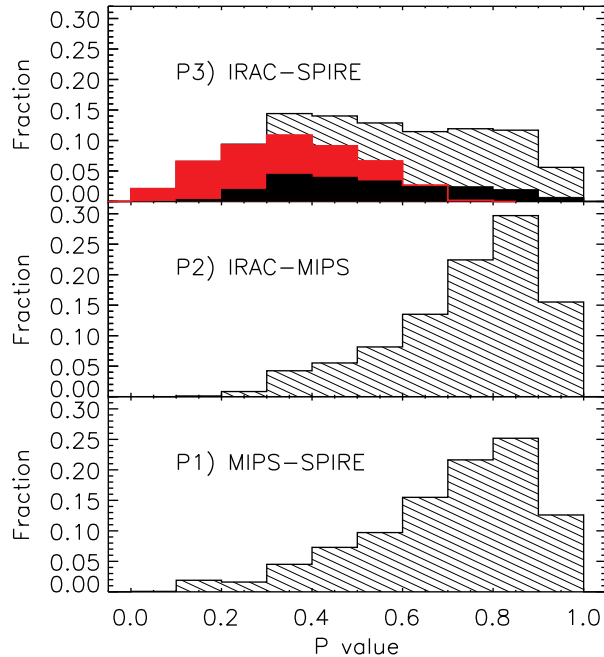


Figure 2.19: Correlation reliability indicator  $P$  computed for the SPIRE-MIPS ( $P1$ ), MIPS-IRAC ( $P2$ ) and SPIRE-IRAC ( $P3$ ) positional correlations. This last one was computed for all the SPIRE sources in our catalog, even when the correlation with IRAC is found through the MIPS position. The black filled distribution in the top panel represents the fraction of SPIRE sources without any MIPS counterpart. The red filled distribution represent the fraction of SPIRE with multiple IRAC potential counterparts inside the IRAC-SPIRE radius.

### 2.2.5 WISE and 2MASS

The ADF-S area is covered, as a part of the whole sky survey, in the WISE W1, W2, W3, W4 bands at 3.35, 4.60, 11.56, 22.09  $\mu\text{m}$  respectively (Wright et al. 2010) and in the 2MASS survey in the bands J, H and  $K_S$  at 1.25  $\mu\text{m}$ , 1.65  $\mu\text{m}$  and 2.16  $\mu\text{m}$  (Skrutskie et al. 2006). The public “AllWISE” catalog is superior to the older WISE “All-Sky” release catalog, with the exception of sources brighter than the saturation limits in bands W1 and W2, that were observed during the Post-Cryo survey phase. The WISE survey scanning strategy resulted in frameset depth-of-coverage that increased with increasing ecliptic latitude. Moreover, sensitivity improves toward the ecliptic poles due to lower zodiacal background. In terms of depth, the southern and the northern ecliptic pole are then privileged fields.

The reported depths in the four bands are 7.4  $\mu\text{Jy}$ , 15.8  $\mu\text{Jy}$ , 0.134 mJy, 1.02 mJy for the 95% of the covered field. However, using the publicly available tables of noise modeled for the WISE survey as a function of the coverage, we could estimate the average depths ( $1\sigma$ ), at the south ecliptic pole coordinates. They resulted 3.15  $\mu\text{Jy}$ , 6.2  $\mu\text{Jy}$ , 54  $\mu\text{Jy}$ , 450  $\mu\text{Jy}$ . We note that in the WISE 1 band, the theoretical depth in the SEP field is compatible with that of the IRAC-1 channel (3.54  $\mu\text{Jy}$ ), and in the W3 band it is comparable with that of the *Akari*-S11 band (46  $\mu\text{Jy}$ ). Anyway, it has to be kept into account that the WISE fluxes shows systematic offsets with the IRAC measures, at the smallest fluxes (Jarrett et al. 2011). This increases the value of  $\sigma$  for W1 of about the 40%.

The measures included in the multi-wavelength catalog are the “W1(2,3,4)MPRO” Vega

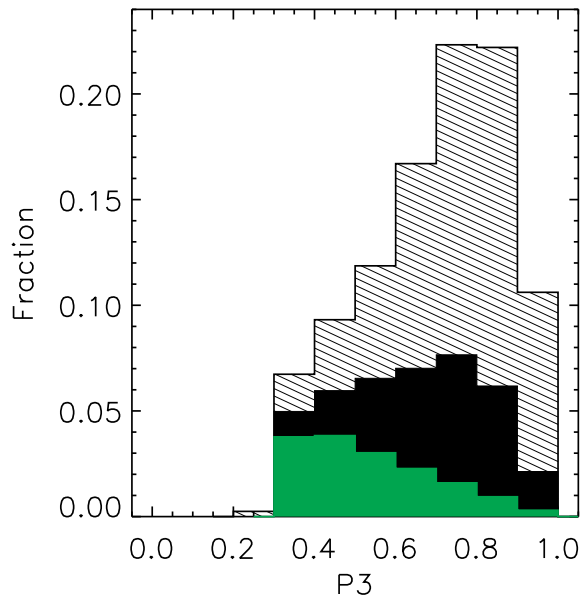


Figure 2.20: *Distribution of  $P3$  resulting from a Monte Carlo simulation (green). The distribution is here normalized to represent the fraction of SPIRE-IRAC direct associations, with a single IRAC counterpart, present in our catalog (black filled area). The distribution of  $P3$  for the whole sample of SPIRE sources with a single IRAC counterpart is also represented (black shaded area).*

magnitudes of the original release, converted to AB magnitudes and Jy fluxes in our catalog. These magnitudes are the result of a profile-fitting photometry, or the 95% confidence brightness upper limit if the flux measurement has  $\text{SNR} < 2$ .

The AllWISE Source Catalog is positionally cross-correlated with the 2MASS Point and Extended Source Catalogs (PSC and XSC). A search radius of 3 arcsec was used for the AllWISE/2MASS PSC correlation. If more than one 2MASS PSC object was found within 3 arcsec, the closest association was considered. Associations between AllWISE Catalog and the 2MASS XSC were searched using a matching radius equal to 1.1 times the Ks isophotal radius size of the 2MASS XSC source. We include the 2MASS J, H, and Ks fluxes in our catalog

We found the closest IRAC 1 geometrical counterparts to the WISE positions recentered to the IRAC coordinates, as described in section 2.2.2 for the MIPS band. The average shift applied to the WISE coordinates is reported in Table 2.6. The searching radius used in the counterpart search (i.e.  $2.68''$ ) is the quadratic sum of the PSF’s sigmas of the IRAC ( $0.705''$ ) and WISE W1 ( $2.59''$ ) PSFs. The counterpart distance distribution is represented in Figure 2.21. In the original WISE-2MASS catalog there are some sources with a not specified (“null” values) associated error. In our multiwavelength catalog, we set the associated error of these sources to -99. Since the whole field is covered by the WISE survey, differently from the other bands, there are no sources with fluxes set to -99 values. We set the fluxes of the undetected sources to 0.0

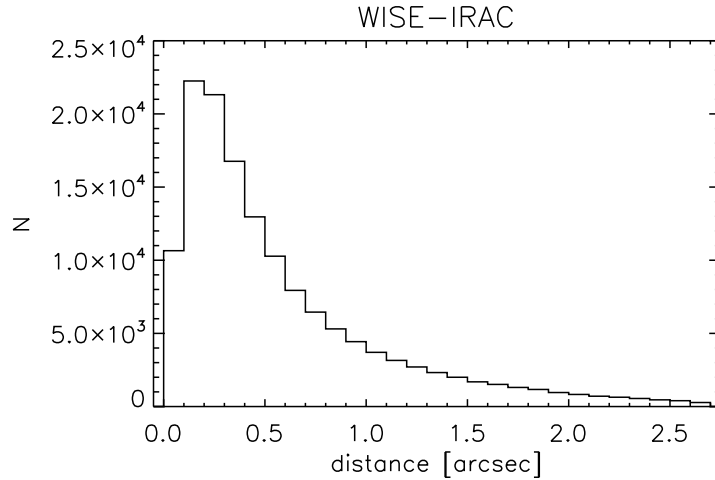


Figure 2.21: *WISE-IRAC* distance distribution for the *WISE/2MASS* sources in the multiwavelength catalog. The coordinates of the *WISE* sources are corrected for the average shift with the *IRAC* (*ra*, *dec*) positions.

### 2.2.6 Akari IRC bands

The SEP field is covered in the 3-24 $\mu\text{m}$  spectral range by the *Akari*-IRC filters (Onaka et al. 2007) N3, N4, S7, S11, L15 and L24 bands (3.2, 4.6, 7, 11  $\mu\text{m}$ ). The area covered in each band is  $\sim 0.5 \text{ deg}^2$  (see Table 2.7), but the N3, N4, S7 and S11 coverage is a little bit shifted from the L15 and L24 pointings (see Figure 2.2). The images taken in the Akari bands are represented in Figures 2.26,2.27,2.28,2.29,2.30,2.31.

As in the other cases, we computed the depth reached in each Akari image as the width ( $\sigma$ ) of the symmetrized distribution of the fluxes calculated on 7x7 pixels apertures. The value obtained is finally multiplied for the aperture correction, that we computed as the average ratio between 8 pixel aperture fluxes and *SExtractor*-“AUTO” fluxes.

We computed the fluxes in the Akari bands through a blind extraction that we performed using the *SExtractor* code. In the multi-wavelength catalog we include the “AUTO” fluxes. These values are computed, as for the *IRAC*-1 band, inside elliptical apertures with semi-major axis ( $a$ ) equal to 2.5 the Kron radius of the object ( $R_K$  Kron 1980). The *SExtractor* parameters that we used for the extractions are summarized in table 2.9. In the same table, we report the conversion factors that we used to convert the extracted fluxes, expressed in ADU, to Jy fluxes.

The S/N threshold of an extraction is ruled by the parameters `DETECT_THRESH` and `ANALYSIS_THRESH`. We selected these parameters in order to obtain the deepest possible extraction, minimizing at the same time the number of spurious sources in the final multi-wavelength catalog. This result is obtained simulating void (i.e. without sources) IRC images and performing an extraction for each different values of the `DETECT_THRESH` and `ANALYSIS_THRESH` parameters in our simulation. The sources extracted from these simulated maps are spurious by definition, but not all of them would be included in the multi-wavelength catalog, since only a fraction is casually found in correspondence of an *IRAC* position, upon which the multi-wavelength catalog is based. Then, matching the extracted (spurious) sources with the *IRAC* catalog, we estimated the fraction of spurious detections that can influence

Parameter	Setting					
	N3	N4	S7	S11	L15	L24
DETECT_MINAREA [pixels]			5			
DETECT_THRESH [sigma]			1.0			
ANALYSIS_THRESH [sigma]			1.0			
FILTER (gauss) FWHM [pixels]	3.0	3.0	2.0	2.5	2.5	3.0
size [pixels]	7x7	7x7	5x5	5x5	5x5	7x7
DEBLEND_NTHRESH			32			
DEBLEND_MINCONT			0.005			
BACK_SIZE			32			
BACKPHOTO_TYPE			LOCAL			
BACK_FILTERSIZE			3			
BACKPHOTO_THICK			15			
PHOT_APERTURES [pixels]			8			
PHOT_AUTOPARAMS			2.5, 3.5			
SEEING_FWHM [arcsec]	4.234	4.234	5.148	5.616	5.635	6.86
PIXEL_SCALE [arcsec]	1.46	1.46	2.34	2.34	2.45	2.45
Jy/ADU conversion factor ( $\times 10^{-7}$ )	3.394	2.584	10.22	7.732	16.91	48.92

Table 2.9: Parameters used to extract the sources and compute the fluxes in the Akari bands.

the final multi-wavelength catalog. The value that we obtain is a superior limit to the fraction of spurious Akari detections present in our catalog since during the IRAC counterpart search, each IRAC source close to a spurious Akari detection could have another closer and *real* Akari counterpart that is then associated to the IRAC detection. This probability is not negligible, since the detection rate for the Akari sources spans from  $\sim 6\%$  to  $\sim 60\%$  (see Table 2.7).

In order to simulate pure-noise images, an image with inverted fluxes can be used. Assuming a symmetrical distribution of the noise, while the sources will assume negative fluxes, preventing them from being extracted, the average noise will remain inalterate. In our case, this method brings to an overestimation of spurious sources surrounding the bright sources. This image defect result from the peculiar PSF profile of the sources. For this reason we did not consider this method. The situation is represented in Figure 2.22.

The pure-noise simulated images were built using the following procedure. First, we computed the distribution (histogram) of the fluxes inside each single pixel of the original image. Then, we symmetrized the distribution (with respect to the peak) eliminating those pixels falling on the source's positions. Using a linear y-axis representation, the distribution appear gaussian. Analyzing it with a logarithmic scale, it is possible to notice that the wings of the distribution appears usually higher then in a gaussian distribution. This is not a negligible effect in our computation, since the wings of the noise distribution are the major responsible for the spurious detections. For this reason we re-created a similar non-gaussian distribution of fluxes that we randomly copied in a simulated void-image with dimensions similar to those of the original image. The distribution of the fluxes inside each single pixel is represented in Figure 2.23 for the Akari-N3 image, with a linear and with a logarithmic y-axis scale.

For exemplificative purposes, in the left panel of Figure 2.24, we graphically represent the number of detected sources in the original Akari-N3 image, as a function of the SExtractor detection threshold set (in black). In the same plot, we also represent the number of sources extracted from the simulated pure-noise image (blue) and the number of them for which we found an IRAC counterpart (green). In the right panel we represent the unitary fraction of spurious detections and spurious detections with an IRAC association. In the Akari-N3 case

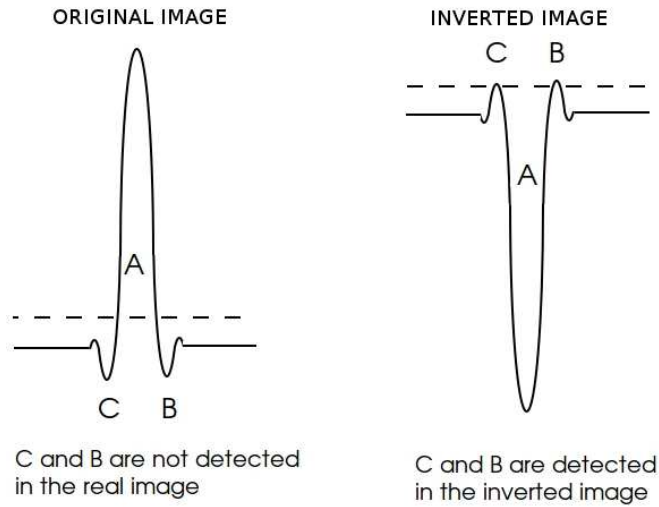


Figure 2.22: Typical PSF profile of bright sources in the Akari-IRC images. The inverted images are not assimilable to a pure-noise map, since the PSF profiles produce an overestimation of spurious detections in the regions surrounding bright sources.

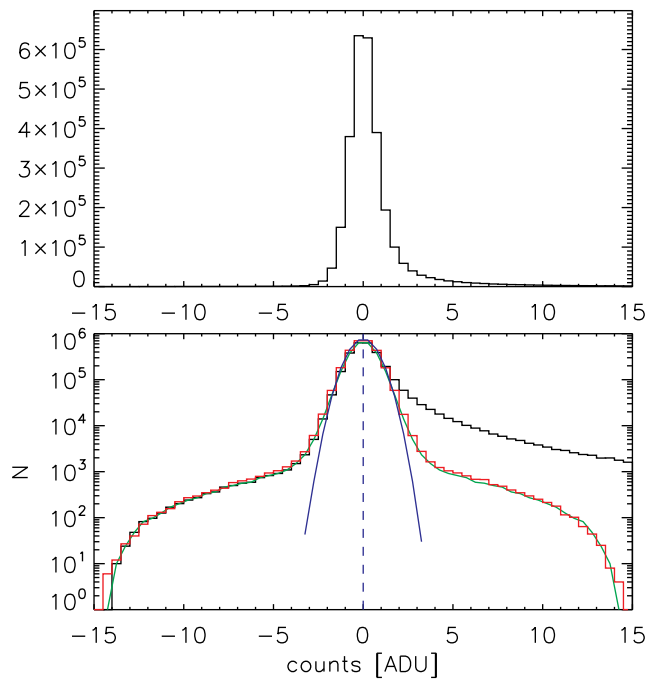


Figure 2.23: Flux distribution in the Akari-N3 image. **Upper panel:** distribution of the fluxes inside each single pixel in a linear y-axis representation. The number of pixels with fluxes above and below 5 ADUs seems to be negligible. **Lower panel:** distribution of the fluxes inside each single pixel in a logarithmic y-axis representation (in black). The symmetrized distribution (in green) deviates from the random gaussian distribution (in blue) at high fluxes. This behaviour is not appreciable in the linear representation but is responsible for a not-negligible number of false detections. We reproduced this distribution in our pure-noise test image (in red).

here represented, all the detection fractions became smaller and smaller with the increasing threshold. In two cases however (i.e. S7 and L24), the spurious detections rate shows a minimum at about  $1\sigma$ , with an increase at higher values. This is due to the peculiar noise distribution function described before. This not-gaussian distribution creates false sources even at high fluxes. For this reason, while increasing the detection threshold the number of these high-flux spurious sources remains pretty stable, the number of real sources does decrease, creating the observed effect. Since we set a detection threshold of  $1\sigma$ , in our Multiwavelength catalog we expect a fraction of spurious Akari detections smaller than the values reported in Table 2.10.

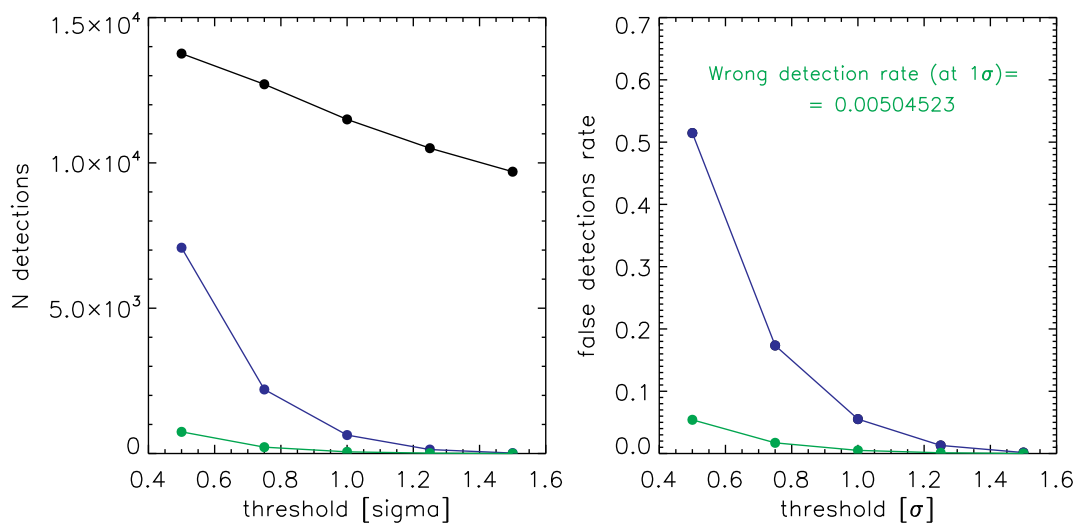


Figure 2.24: **Left panel:** number of detections in the real Akari-N3 image, as a function of the SExtractor detection threshold set (in black). The number of sources extracted from the N3 pure-noise image is represented in blue. In green, the number of them for which a casual IRAC association can be found. **Right panel:** with the same color code, the fraction of extracted spurious sources and the fraction of spurious source with a random IRAC association.

For the Akari-N3 and N4 band, we searched the IRAC catalog for the closest counterpart using a maximum searching radius equal to the quadratic sum of the PSF's  $\sigma$  of the two instruments (i.e. a searching radius of  $3.73''$  in both cases). The Akari-IRAC distance distribution for N3 and N4 is represented in the first two upper panes of Figure 2.25. In the other cases (S7, S11, L15 and L24), we found this choice to much restrictive, since the distance distribution of counterparts (see Figure 2.25) suggests that a consistent fraction of real counterparts wouldn't be considered. This is probably due to an underestimation of the width of the Akari handbook PSF with respect to these images. Then, in the quadratic sum, we considered the FWHM ( $=2.355 \times \sigma$ ) of the Akari instruments PSFs instead of the  $\sigma$  value. This make the distance distribution of counterparts more similar to that found for N3 and N4 and for the other instruments (see Figures 2.15, 2.17, 2.21 and 2.33 for a comparison). For S7, S11, L15 and L24 we used searching radii of  $5.196''$ ,  $5.660''$ ,  $5.679''$  and  $6.896''$  respectively. In the multi-wavelength catalog, the fluxes of the sources covered by the different Akari bands are set to  $F=0$  when undetected. For the sources not covered in these bands, we set flux values of -99.

Threshold [ $\sigma$ ]	Spurious detection rate <sup>[1]</sup>					
	N3	N4	S7	S11	L15	L24
without IRAC random association						
0.5	0.5146	0.3968	0.4956	0.4441	0.5212	0.3725
0.75	0.1735	0.1170	0.1499	0.1647	0.2380	0.1890
1.0	0.0552	0.0564	0.0896	0.1130	0.1560	0.2353
1.25	0.0129	0.0339	0.1068	0.0660	0.1216	0.3060
1.5	0.0015	0.0230	0.1258	0.0143	0.0991	0.3407
with IRAC random association						
0.5	0.0541	0.0416	0.1000	0.1052	0.1154	0.1122
0.75	0.0172	0.0121	0.0311	0.0413	0.0555	0.0510
<b>1.0</b>	<b>0.0050</b>	<b>0.0056</b>	<b>0.0122</b>	<b>0.0283</b>	<b>0.0329</b>	<b>0.0674</b>
1.25	0.0011	0.0036	0.0139	0.0178	0.0267	0.0951
1.5	0.0001	0.0023	0.0180	0.0029	0.0215	0.1053

Table 2.10: *Spurious detection rates computed at various detection thresholds, for the various Akari bands. Only the fraction of sources with a random IRAC association are considered.*

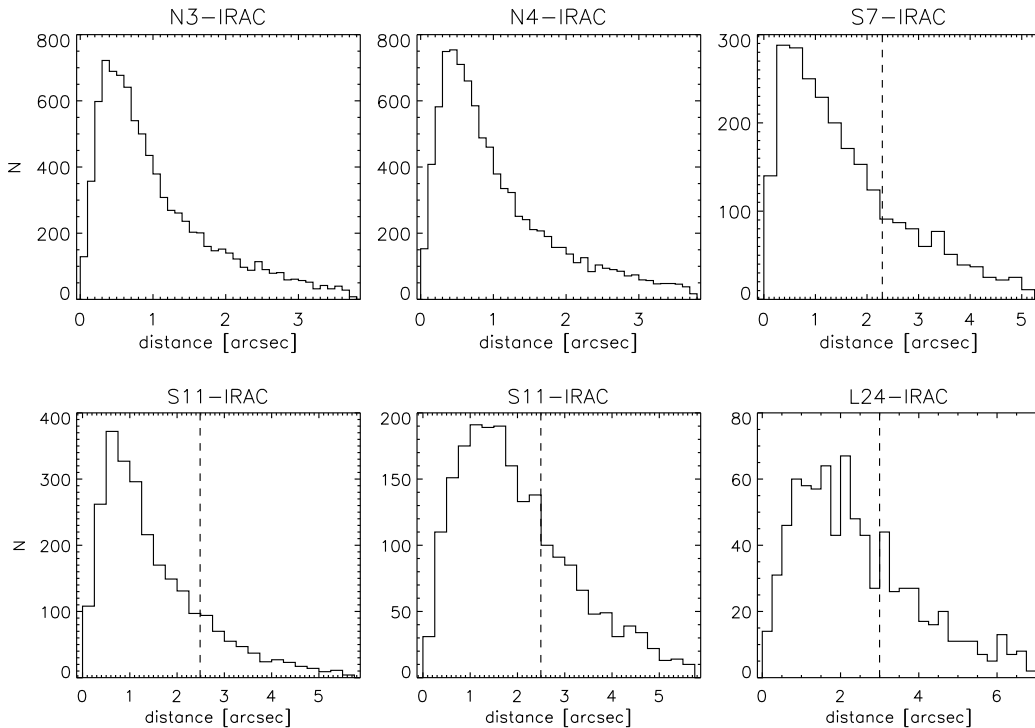


Figure 2.25: *Akari-IRAC distance distribution for the sources in the multiwavelength catalog. While for N3 and N4 the searching radius correspond to the quadratic sum of the PSF's  $\sigma$  of the IRAC and akari N3 and N4 images, for the S7, S11, L15 and L24 bands, a similar threshold, represented with a dashed line in the plots, would eliminate a consistent fraction of real counterparts. For these bands, in the quadratic sum, we used the FWHM instead of the  $\sigma$  value. The coordinates of the Akari sources are corrected for the average shift with the IRAC (ra, dec) positions.*

## 2.2.7 Optical bands

The central square degree of the SEP field is optically covered in various VST, CTIO and MPG/WFI bands. The complete coverage is shown in Figure 2.2 but a more precise indication

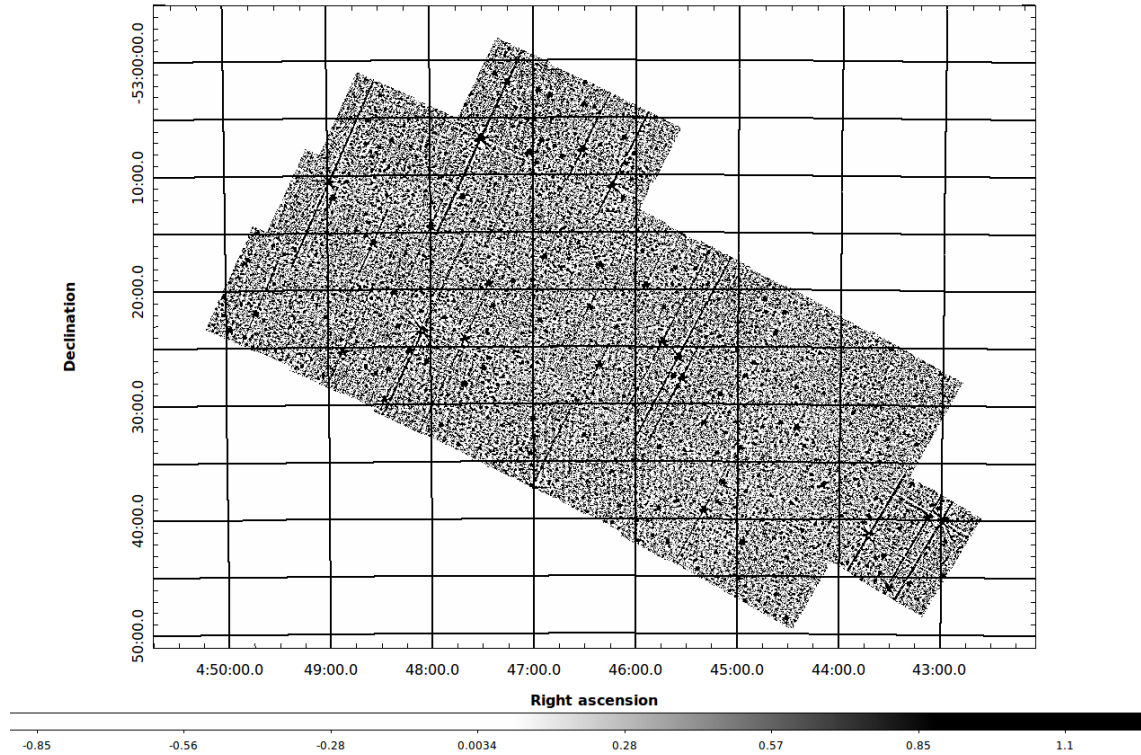


Figure 2.26: Image of the SEP field in the Akari N3 band. Color scale in counts.

of the coverage of each band is represented in Figure 2.32. We reduced a set of images taken in the CTIO-u, B, V, I and WFI- $R_C$  bands, making a mosaic for each band. The images from which we extracted the fluxes are presented in Section 2.2.7. We measured the fluxes, from these images and from a set of VST images taken in the g, i and z bands and reduced with the VST-Tube pipeline (Grado et al. 2012). The SExtractor parameters used to detect the sources and measure their fluxes, are summarized in Table 2.11. Before merging the optical detections with the IRAC catalog, we made an independent optical catalog of sources with average optical coordinates. This catalog and how we made it, is reported in the second part of this section. We searched the IRAC catalog for the closest geometrical counterparts with respect to the average positions reported in the optical catalog. These average optical coordinates were previously recentered to the IRAC positions as already described in section 2.2.2 for the MIPS band and in section 2.2.5 for the WISE bands. The shift applied to the optical coordinates is reported in Table 2.6. The searching radius used (i.e.  $0.823''$ ) is the quadratic sum of the PSF's sigmas of the IRAC-1 image ( $0.705''$ ) and  $0.425''$ . For the optical images, we considered a sigma value smaller than the average PSF's sigmas computed on the optical bands ( $\langle FWHM \rangle / 2.355 = 1,332/2,355 = 0,5657''$ ). We made this choice since we expect the optical average coordinates considered to be more precise than the coordinates in each single optical band. The counterpart distance distribution is represented in Figure 2.33.

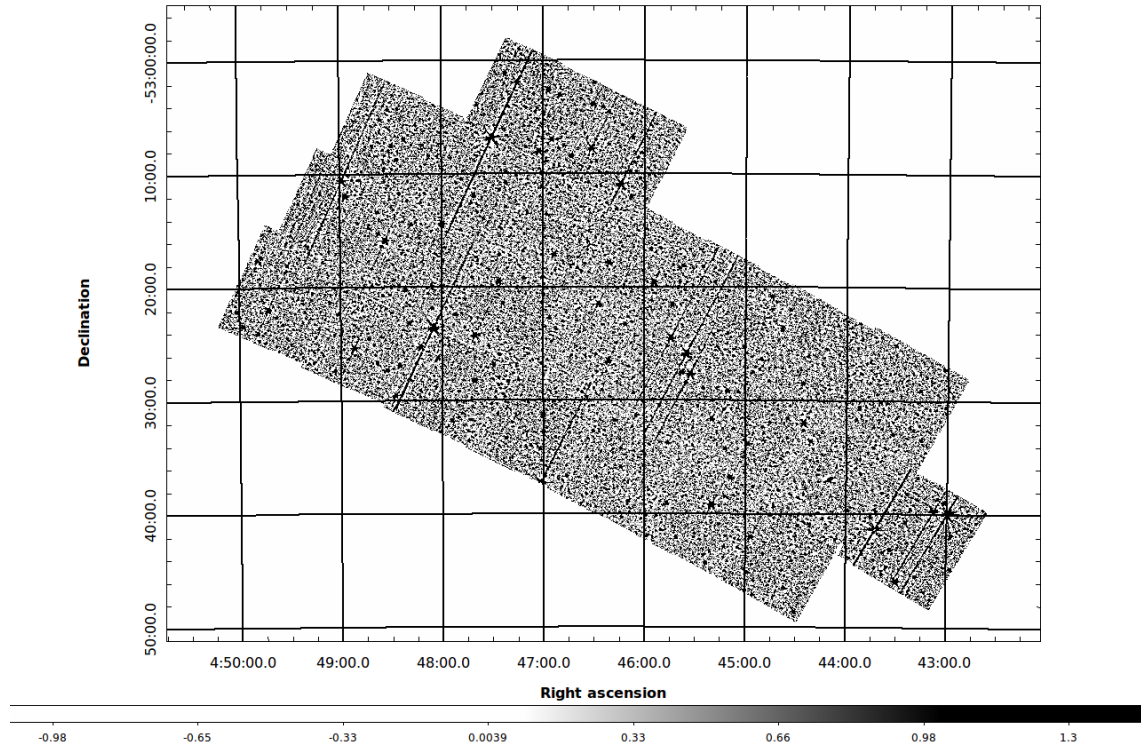


Figure 2.27: Image of the SEP field in the Akari  $N_4$  band. Color scale in counts.

Parameter	Setting							
	u	CTIO		I	WFI	g	VST	
		B	V		$R_C$		i	z
DETECT_MINAREA [pixels]					5			
DETECT_THRESH [sigma]					1.0			
ANALYSIS_THRESH [sigma]					1.0			
FILTER (gauss) [pixels]	5.0	5.0	5.0	5.0	5.0	5.0	4.0	4.0
	9x9	9x9	9x9	9x9	9x9	9x9	7x7	7x7
DEBLEND_NTHRESH					32			
DEBLEND_MINCONT					0.005			
BACK_SIZE	150	170	170	170	250	250	250	250
BACKPHOTO_TYPE					LOCAL			
BACK_FILTERSIZE					3			
BACKPHOTO_THICK	50	45	40	35	50	50	50	50
PHOT_APERTURES [pixels]					8			
PHOT_AUTOPARAMS					2.5, 3.5			
SEEING_FWHM [arcsec]	2.179	1.735	1.345	1.4181	0.9778	0.889	1.335	0.779
PIXEL_SCALE [arcsec]	0.268	0.270	0.268	0.268	0.237	0.210	0.206	0.210

Table 2.11: Parameters used to extract the sources and compute the fluxes in the optical bands.

## Optical catalog

As said above, before merging the optical detections with the IRAC catalog, we made an independent catalog of optical sources. First we recentered the original optical coordinates

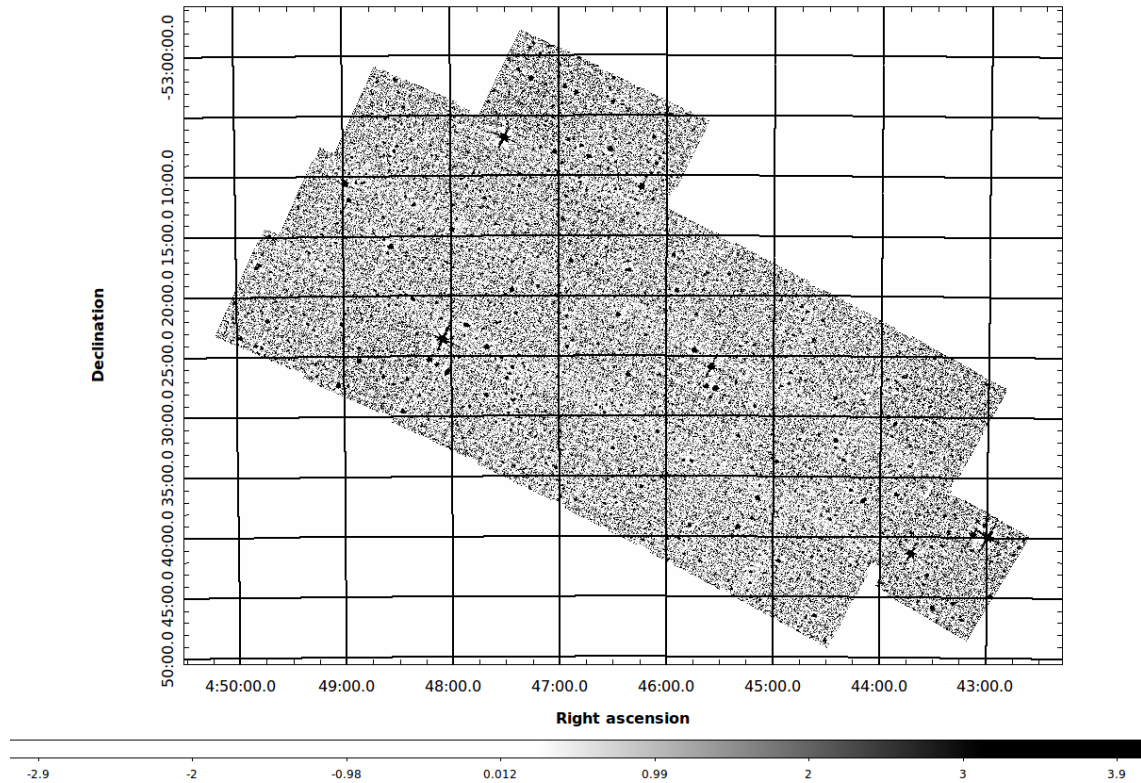


Figure 2.28: *Image of the SEP field in the Akari S7 band. Color scale in counts.*

in each band to the IRAC–1 coordinates, as we did for the other bands. The average shifts found are reported in Table 2.6. Then we merged the single optical bands in a unique optical catalog containing the sources with 2 optical detections at least, found in a common radius of 1". At this purpose, we used a different method from the matching method used for the MIPS, SPIRE, WISE and Akari bands. The optical catalog, at this level, does not take in consideration the IRAC positions (they were only used as referement to correct the average shift among the different optical catalogs). We matched the optical coordinates alone using the stilts<sup>9</sup> function “*tmatchn*“. The *tmatchn* function performs efficient and flexible crossmatching between multiple tables. In particular, it can match rows on the basis of their relative position in the sky. Setting the “*matcher*” parameter to “*sky*“, as we did, the *tmatchn* function compares positions on the celestial sphere with a fixed error radius. The sources are considered to match when the two (ra, dec) positions are within max-error arcseconds of each other along a great circle. We set the “*multimode*” parameter to “*group*“. In this way, groups of objects from all the input tables are identified. The matcher identifies a matched group as the largest possible group of objects in which each is linked to any other object in the group. For any particular pair in a group, there is no guarantee that the two objects match each other, only that it is possible to pass from one to another through a series of pair mathces. The optical catalog is finally merged with the multi-wavelength catalog as described in the first part of

<sup>9</sup>For more information, see  
<http://www.star.bris.ac.uk/~mbt/stilts/sun256/sun256.html>

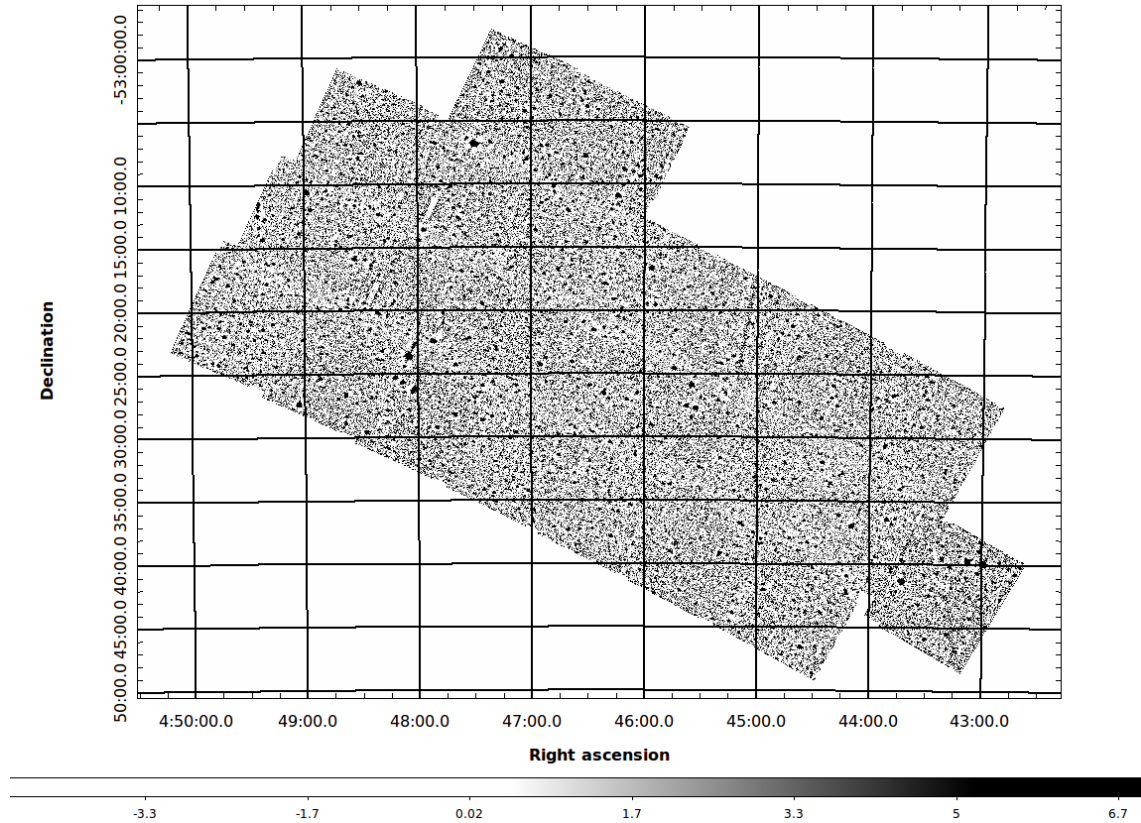


Figure 2.29: Image of the SEP field in the Akari S11 band. Color scale in counts.

this section. To do this, we computed average optical coordinates and we corrected them for the average shift with the IRAC coordinates. Finally we used the average and recentered optical coordinates to search the IRAC catalog for the closest counterpart.

The initial calibration of the fluxes extracted in the  $u$ ,  $B$ ,  $V$ ,  $I$  and  $R_C$  bands can be considered a raw estimation of the real zeropoints. We obtained these zeropoints comparing the extracted fluxes with the fluxes of bright sources in external catalogs (Zacharias et al. 2005), in similar, but not identical, bands. Before including the optical sources in the multi-wavelength catalog, all the optical fluxes were re-calibrated using an iterative SED fitting technique. This procedure is better described in section 3.3. Basically, we fit our fluxes with a set of galaxy templates obtained using the Bruzual & Charlot (2003) stellar synthesis population models (SSP). The average offsets are adjoined to better reproduce the templates and then a new SED fit is performed to compute more precise corrections. The resulting offsets, reported in table 3.3, can assume relevant values in the roughly photometrically calibrated bands ( $u$ ,  $B$ ,  $V$ ,  $I$  and  $R_C$ ), while there are not consistent corrections to be applied to the already photometrically precise VST  $i$ ,  $g$  and  $z$  bands. Again, the optical fluxes of the sources covered by the different optical bands are set to  $F=0$  when undetected. For the sources not covered in these bands, we set flux values of -99.

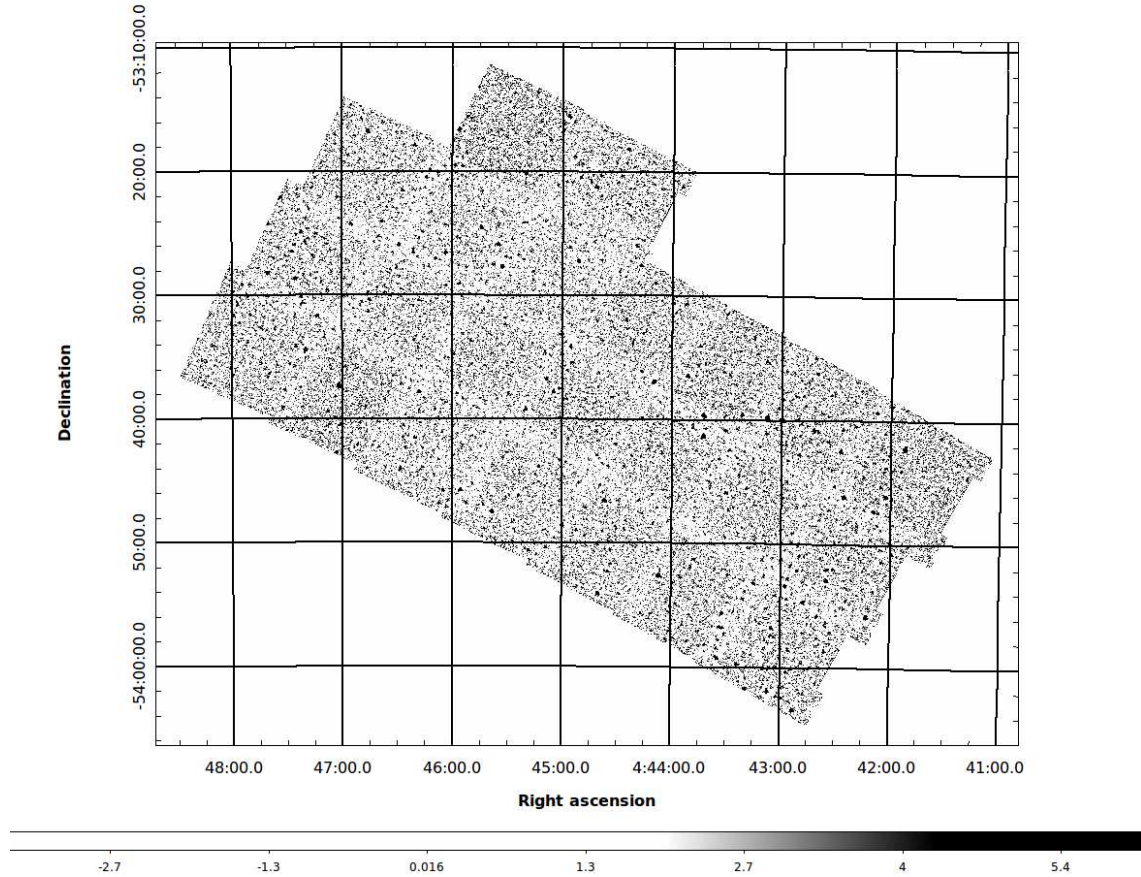


Figure 2.30: Image of the SEP field in the Akari L15 band. Color scale in counts.

## Optical images

In this section we present, and briefly describe, the CTIO-*u*, *B*, *V*, *I* and WFI-*R<sub>C</sub>* bands images that we reduced, as well as the images taken in the VST-*g*, *i* and *z* bands. The coverage of these bands, with respect to the total optically covered area is represented in Figure 2.32.

- The CTIO-*u* mosaic (Figure 2.34) results from the sum of a total of 17 single exposures in two different pointings with a  $\sim 0.25$  square degree area. In the first pointing (RA $\sim$ 4:46:00, dec $\sim$ -53:35:00), we summed up 10 images for a total exposure of 11000 seconds, with an average PSF of 2.18". The PSF computed in the resulting image is however 2.15". In the second pointing (RA $\sim$ 4:42:30, dec $\sim$ -53:35:00) we considered 7 exposures, for a total of 6600 seconds, with an average PSF of 2.17". The PSF computed in the resulting image is however 2.14". We didn't consider 3 images taken in this pointing because of the wider PSF ( $>2.8''$ ), in order to keep an homogeneous PSF along the field. The difference in depth among the two pointings and the area of superimposition is appreciable as a difference in the background noise level.
- The CTIO-*B* mosaic (Figure 2.35) results from the sum of a total of 10 single exposures

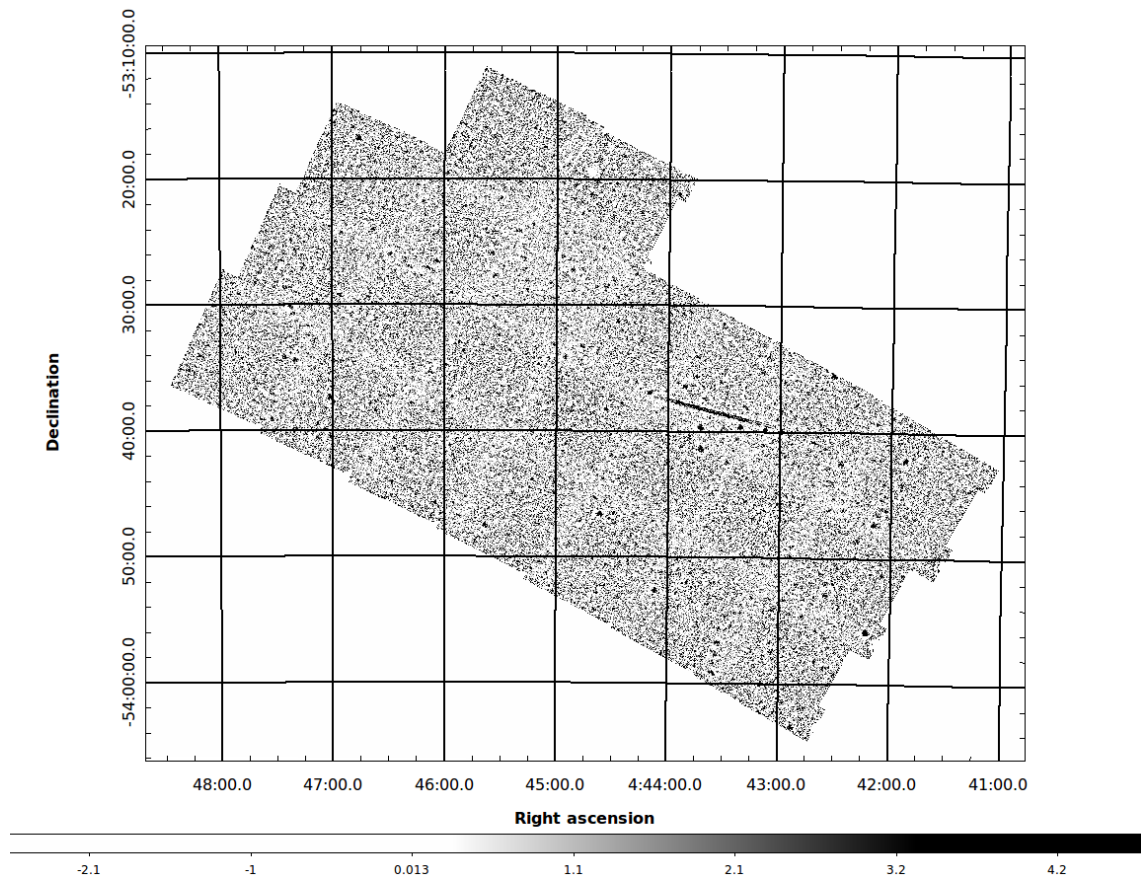


Figure 2.31: Image of the SEP field in the Akari L24 band. Color scale in counts.

in two pointings. Maintaining the same definition of the two pointings given for the u band, in the first we summed 5 images with an average PSF of  $1.81''$ , for a total exposure time of 1800 seconds. In the second pointing we considered again 5 exposures with an average PSF of  $1.66''$  and the same total exposure time.

- The CTIO–V mosaic (Figure 2.36) results from the sum of a total of 10 single exposures in two pointings. With the same pointing definition as above, in the first pointing, we summed 5 images with an average PSF of  $1.48''$ , for a total exposure time of 1800 seconds. In the second pointing we considered 5 exposures with an average PSF of  $1.21''$  and the same total exposure time.
- The CTIO–I mosaic (Figure 2.37) results from the sum of a total of 10 single exposures in two pointings. Keeping the same definition of the pointings, in the first we summed 5 images with an average PSF of  $1.41''$  for a total exposure time of 1800 seconds. In the second pointing we considered again 5 exposures with an average PSF of  $1.43''$  and the same exposure time.
- The WFI–R mosaic (Figure 2.38) results from the sum of 50 single exposures in four different pointings with an area of  $\sim 0.25$  square degree. In the first pointing (RA $\sim$ 4:42:30,

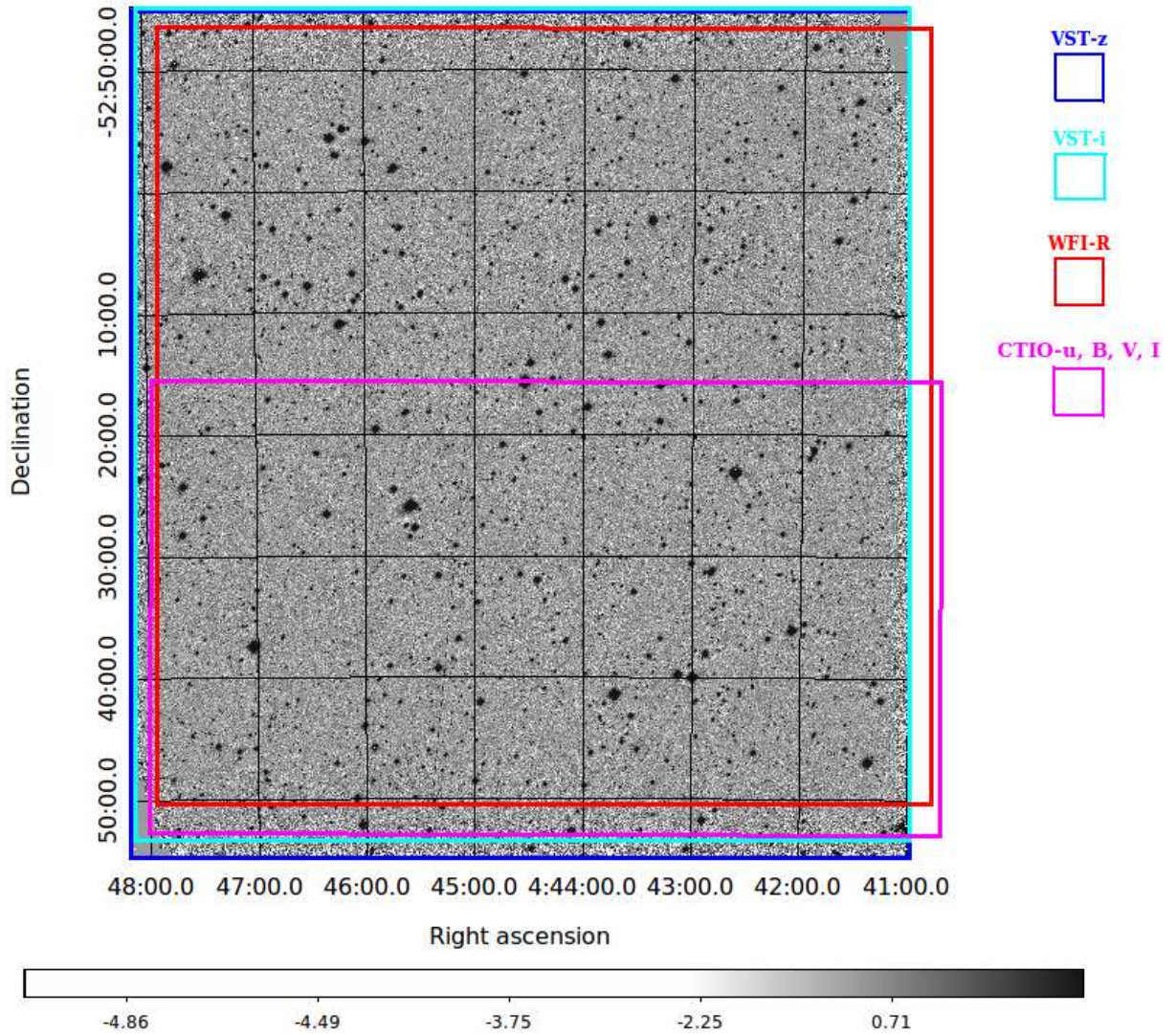


Figure 2.32: *VST-g* image of the *SEP* field with the optical coverage in different bands. The *CTIO* images cover only an half of the total square degree. The color scale is expressed in counts.

dec $\sim$ -53:35:00), we summed 20 images with an average PSF of 1.01". In the second pointing (RA $\sim$ 4:46:00, dec $\sim$ -53:35:00) we considered 13 exposures with an average PSF of 0.95". In the third (RA $\sim$ 4:42:30, dec $\sim$ -53:35:00), 9 images for a PSF of 1.00" and in the fourth (RA $\sim$ 4:46:00, dec $\sim$ -53:35:00), 8 images for 0.95" of PSF width.

- The *VST-g* image, already presented in Figure 2.32, results from the sum of 14 images, for a total exposure time of 5600.0 seconds, with an average PSF of 1.34"
- The *VST-i* image (Figure 2.39), results from the sum of 11 images, for a total exposure time of 4400 seconds, with an average PSF of 0.89"
- The *VST-z* image (Figure 2.40), results from the sum of 15 images, for a total exposure time of 6000 seconds, with an average PSF of 0.78"

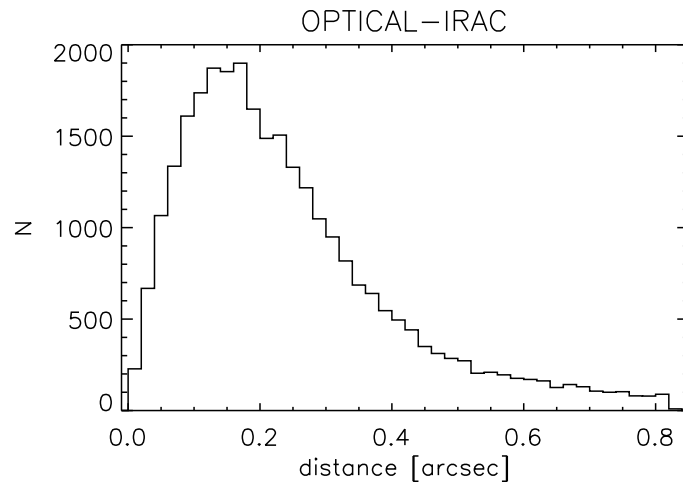


Figure 2.33: *OPTICAL-IRAC* distance distribution for the optical sources in the multiwavelength catalog. The coordinates of the *OPTICAL* sources are the average among the various optical bands, corrected for the average shift with the *IRAC* (*ra*, *dec*) positions.

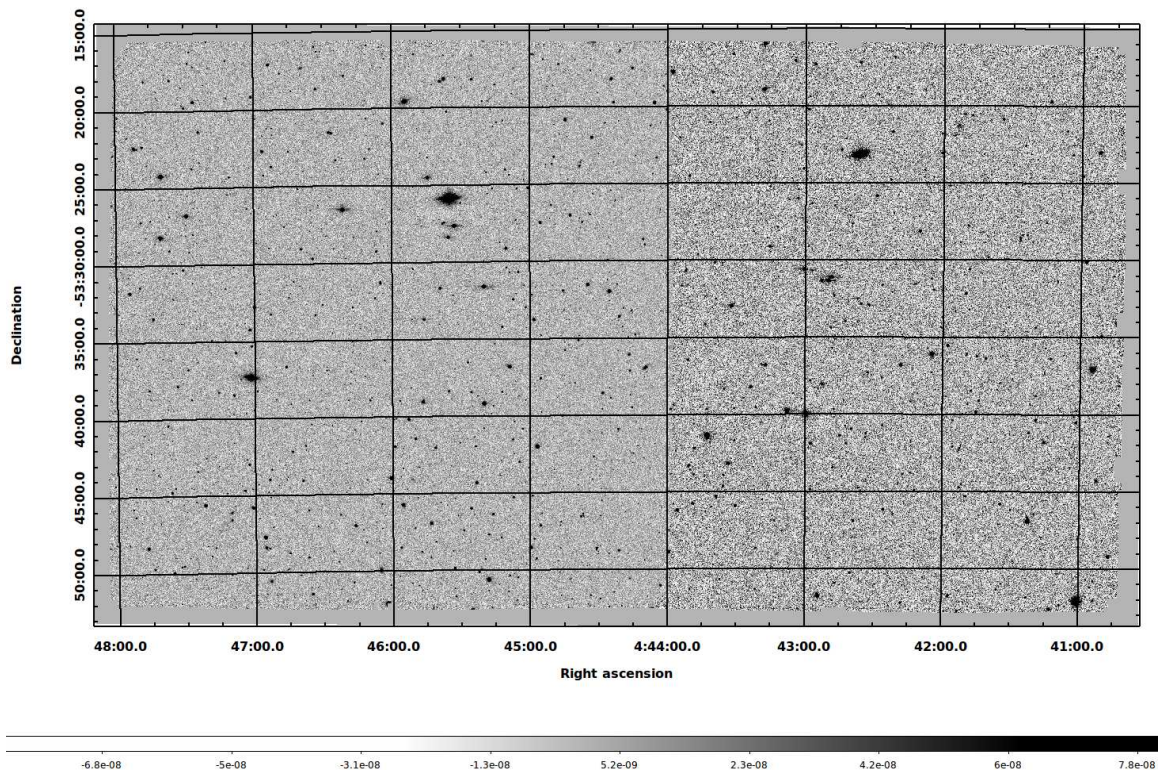


Figure 2.34: *Image of the SEP field in the CTIO-u band. Color scale in Jy.*

## 2.2.8 VISTA J, H, $K_S$

Beside the 2MASS J, H and  $K_S$  observations, the SEP field is also covered by deeper VISTA observations in the same bands. These observations were conducted as a part of the wider

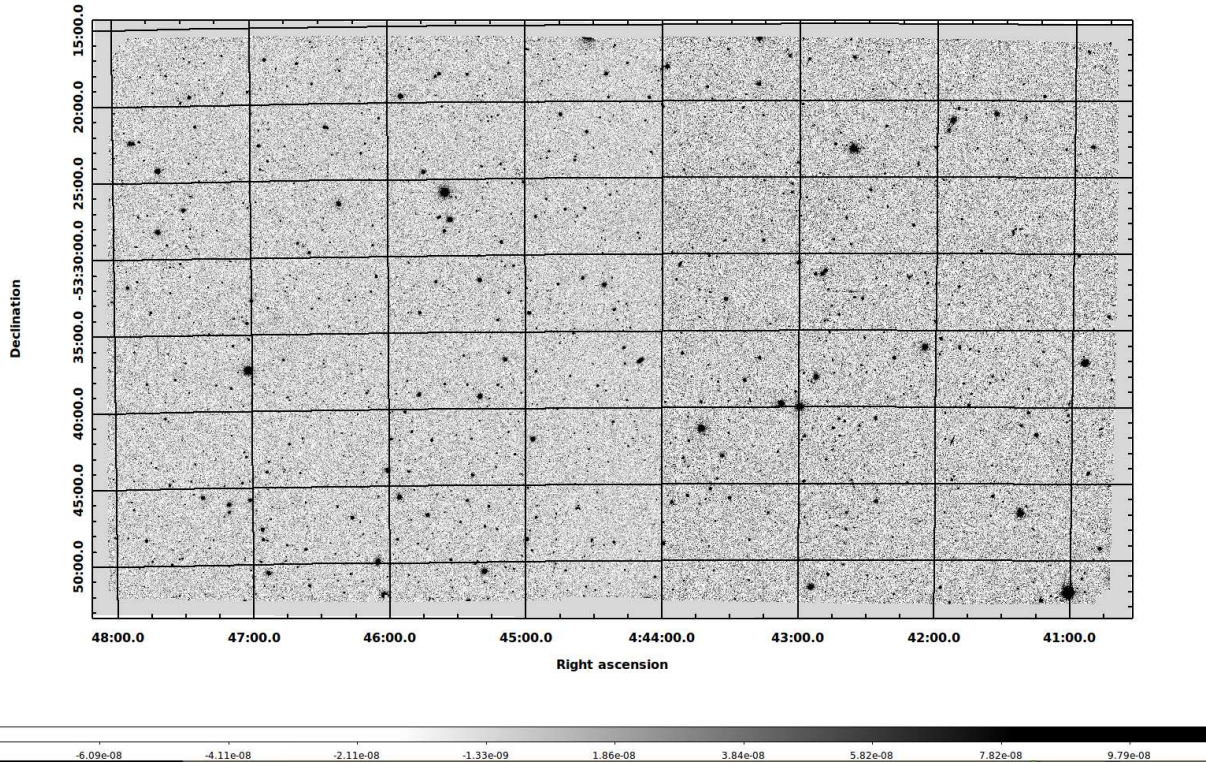


Figure 2.35: *Image of the SEP field in the CTIO-B band. Color scale in Jy.*

VISTA Hemisphere Survey (VHS, McMahon et al. 2013). We exploited both the VISTA public source catalog (second data release, DR2) and the correspondent SEP field images<sup>10</sup>. In order to compute photometric redshifts, we calculated aperture fluxes from the smoothed images, as described in section 3.1. We do not include these fluxes in our multi-wavelength catalog. Instead, we merged our multiwavelength catalog with the publicly available VISTA catalog of sources. We corrected the VISTA coordinates for the average shift with the IRAC source positions, as for the other bands (see Table 2.6). Then we searched the IRAC catalog for the closest geometrical counterpart to the VISTA sources, using a searching radius of  $0.823''$ , similar to that of the other optical bands, that is the quadratic sum of the IRAC and VISTA-J PSF's sigmas ( $0.705''$  and  $0.425''$ ). The distance distribution of the counterparts is represented in Figure 2.41.

The fluxes reported in the public VISTA catalog that we included in our multi-wavelength catalog, are the Petrosian Vega magnitudes (flux inside 2 petrosian radii, as defined in Petrosian 1976) converted to AB magnitudes and then to Jy, using the Vega to AB conversion factors calculated for the VISTA filter set<sup>11</sup> ( $C_{AB \rightarrow Vega} = 0.937, 1.384, 1.839$  for , respectively, J, H, and  $K_s$ , with  $AB = Vega + C_{AB \rightarrow Vega}$ ), that are within a few parts per thousand of the independently computed values in Hewett et al. (2006). The total fluxes computed on variable radii related to the surface brightness ensure the homogeneity with the other fluxes reported in

<sup>10</sup>For a detailed description of these data, see

[https://www.eso.org/sci/observing/phase3/data\\_releases/vhs\\_dr2.pdf](https://www.eso.org/sci/observing/phase3/data_releases/vhs_dr2.pdf)

<sup>11</sup>see <http://casu.ast.cam.ac.uk/surveys-projects/vista/technical/filter-set>

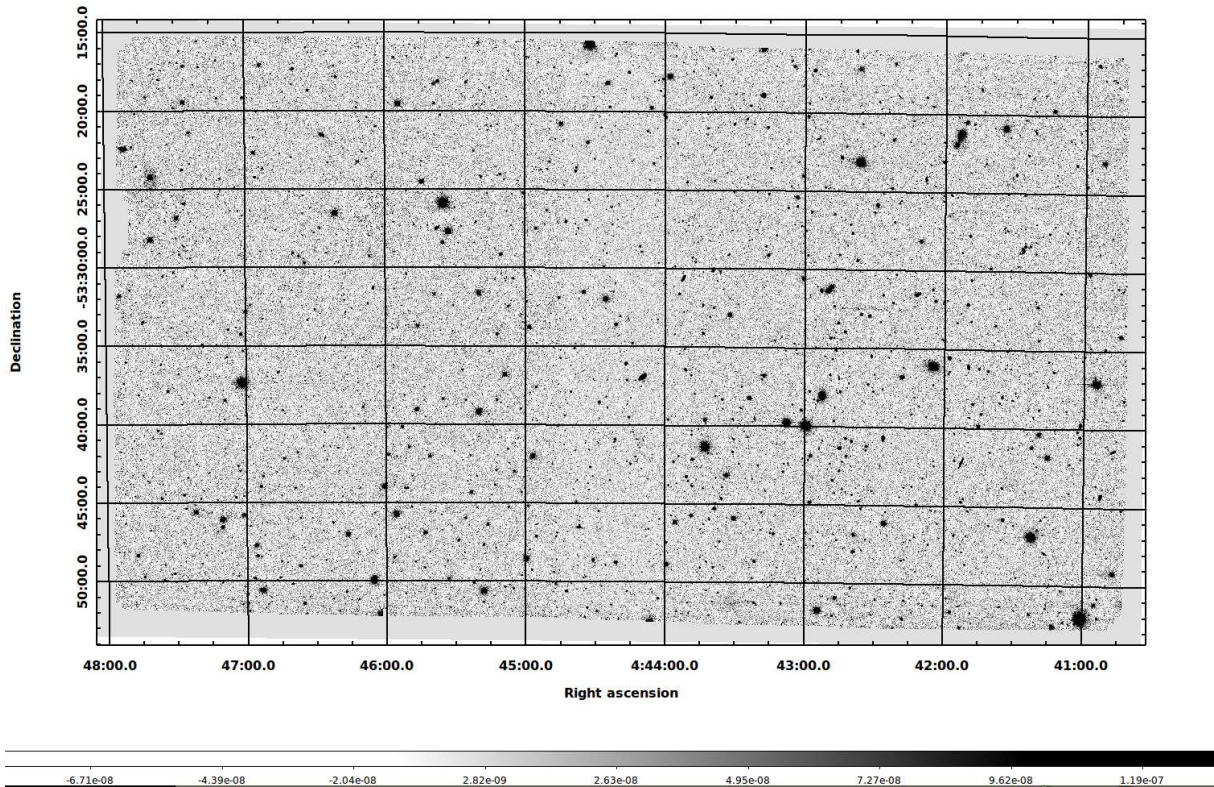


Figure 2.36: Image of the SEP field in the CTIO-V band. Color scale in  $Jy$ .

our multi-wavelength catalog. However, given the expected difference between the Petrosian fluxes included in the VISTA catalog and Krone fluxes (*AUTO* fluxes) given by SExtractor, before including the VISTA sources in the multi-wavelength catalog, we re-calibrated the J, H and K<sub>s</sub> fluxes using the same iterative SED fitting technique applied to the optical bands. This procedure is described with an higher detail in section 3.3, and the offsets obtained are reported in table 3.3. As for the other bands, we set to 0 the fluxes of the undetected sources and to -99 the fluxes of the sources out of coverage. For the VISTA bands, while the J and H bands cover the whole IRAC area, the K<sub>S</sub> band does not. In particular, a small fraction of the optically covered area is not covered by the K<sub>S</sub> observations.

### 2.3 Multi-wavelength catalog characteristics and columns description

In this section, we summarize the main characteristics of the multi-wavelength catalog described in detail in the previous sections. In table 2.12 we analitically report the columns of the multi-wavelength catalog with an example and with a brief description.

- The multi-wavelength catalog is based on the IRAC-1 detections. This means that all the sources have an IRAC-1 flux value higher than 0 and that all the detections in the other bands that we included in the catalog are limited to the IRAC covered area.

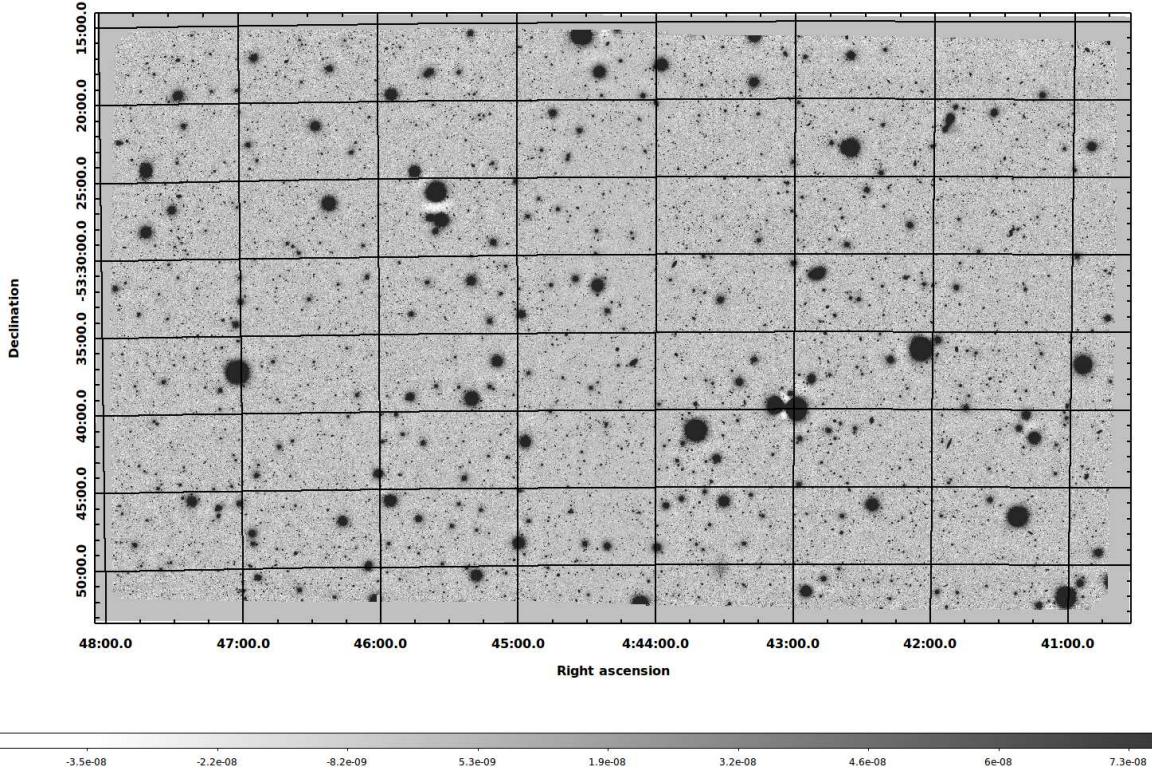


Figure 2.37: Image of the SEP field in the CTIO-I band. Color scale in Jy.

- Given a certain band, we set to -99 the flux of those sources outside the area covered in that specific band. When a source is covered but undetected, its flux in that band is set to 0.
- For the following bands: IRAC-1 and 2, Akari-N3, N4, S7, S11, L15 and L24, CTIO-u, B, V, I, WFI-R, VST-i, g, z, the fluxes considered in the catalog are the *SExtractor* “AUTO” fluxes, based on Krone apertures (Krone-Martins et al. 2014), that we computed using the parameters reported in Table 5.4, 2.9 and 2.11. For VISTA J, H and  $K_S$ , the fluxes are obtained from Petrosian apertures (Petrosian 1976). The MIPS fluxes are taken from the Clements et al. (2011) catalog. *SExtractor* “AUTO” fluxes are considered for extended sources, while aperture fluxes are considered for point-like sources. For the SPIRE bands, the *Starfinder* flux estimates are considered, meaning a flux obtained from a PSF fitting technique. For the WISE fluxes, taken from the allWISE catalog (DR2), a profile fit photometry is considered.
- In the multi-wavelength catalog, we report the original coordinates (as extracted from the images) as well as the recentered ones. The recentered coordinates correspond to the original ones plus the average offset that we computed with respect to the IRAC-1 positions, as described in section 2.2
- We report additive information concerning the reliability of the SPIRE-MIPS, MIPS-IRAC and SPIRE-IRAC correlations that we found. The P value describe how good

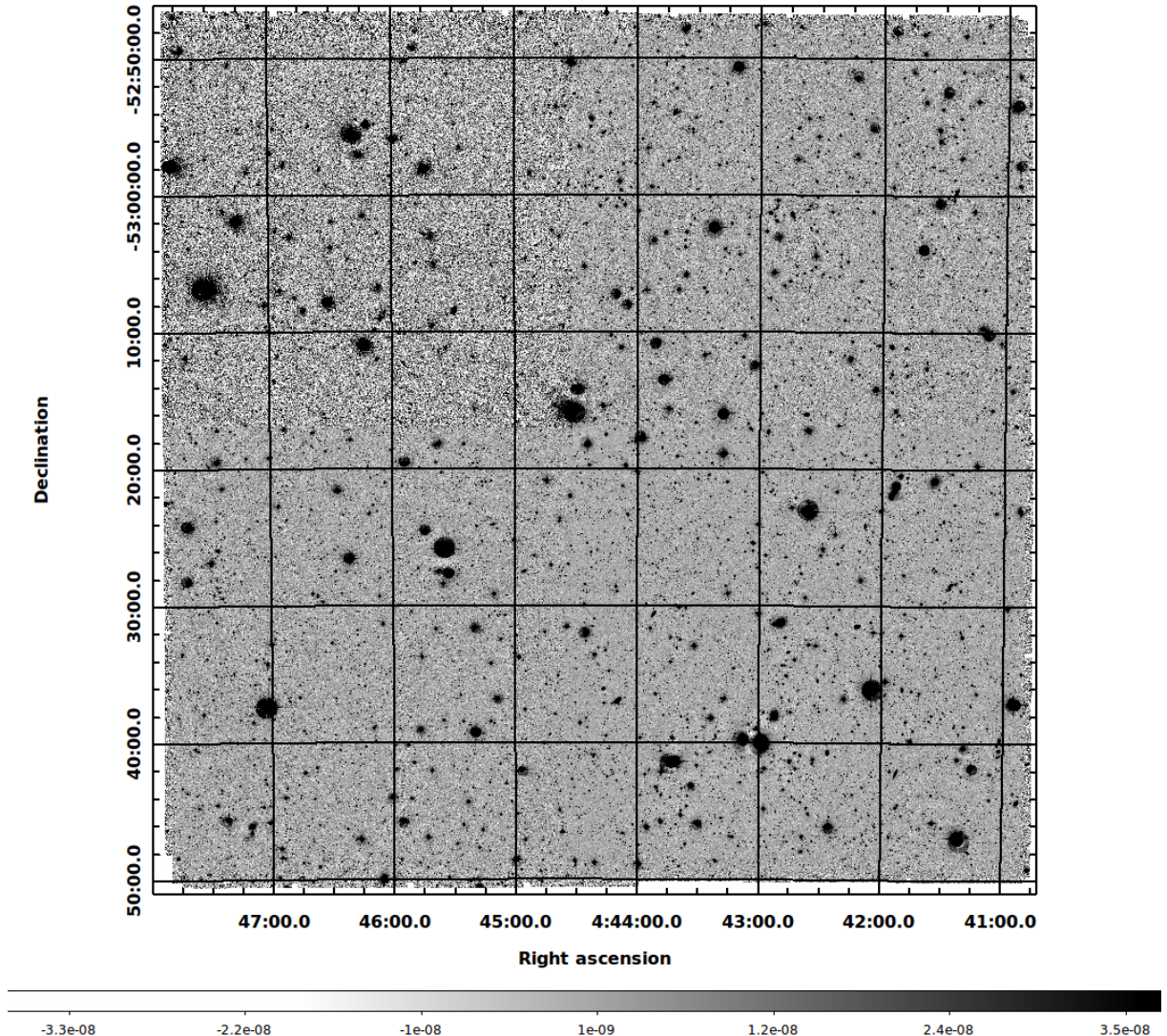


Figure 2.38: Image of the SEP field in the WFI- $R_C$  band. Color scale in Jy.

the correlation is in terms of counterparts distance and number of other possible counterparts in the searching radius. Basically, the higher the P value is, the better is the correlation. However, while the correlation is in general always reliable when both the MIPS and SPIRE counterparts are present, this is not the case when the MIPS counterpart is missing. For this specific case, when a SPIRE-IRAC direct correlation is used, the probability of introducing a spurious correlation is reported in table 2.8. The other important reliability parameters to be considered are  $N\_MIPS\_SPIRE$ ,  $N\_IRAC\_MIPS$  and for the SPIRE-IRAC direct correlation,  $N\_IRAC\_SPIRE$ . These parameters define how many possible counterparts were found in the searching radius.

- In the multiwavelength catalog, we report the redshifts computed using the optical photometry, on the optically covered area ( $FINAL\_Z\_OPTICAL$ ), as well as the redshifts

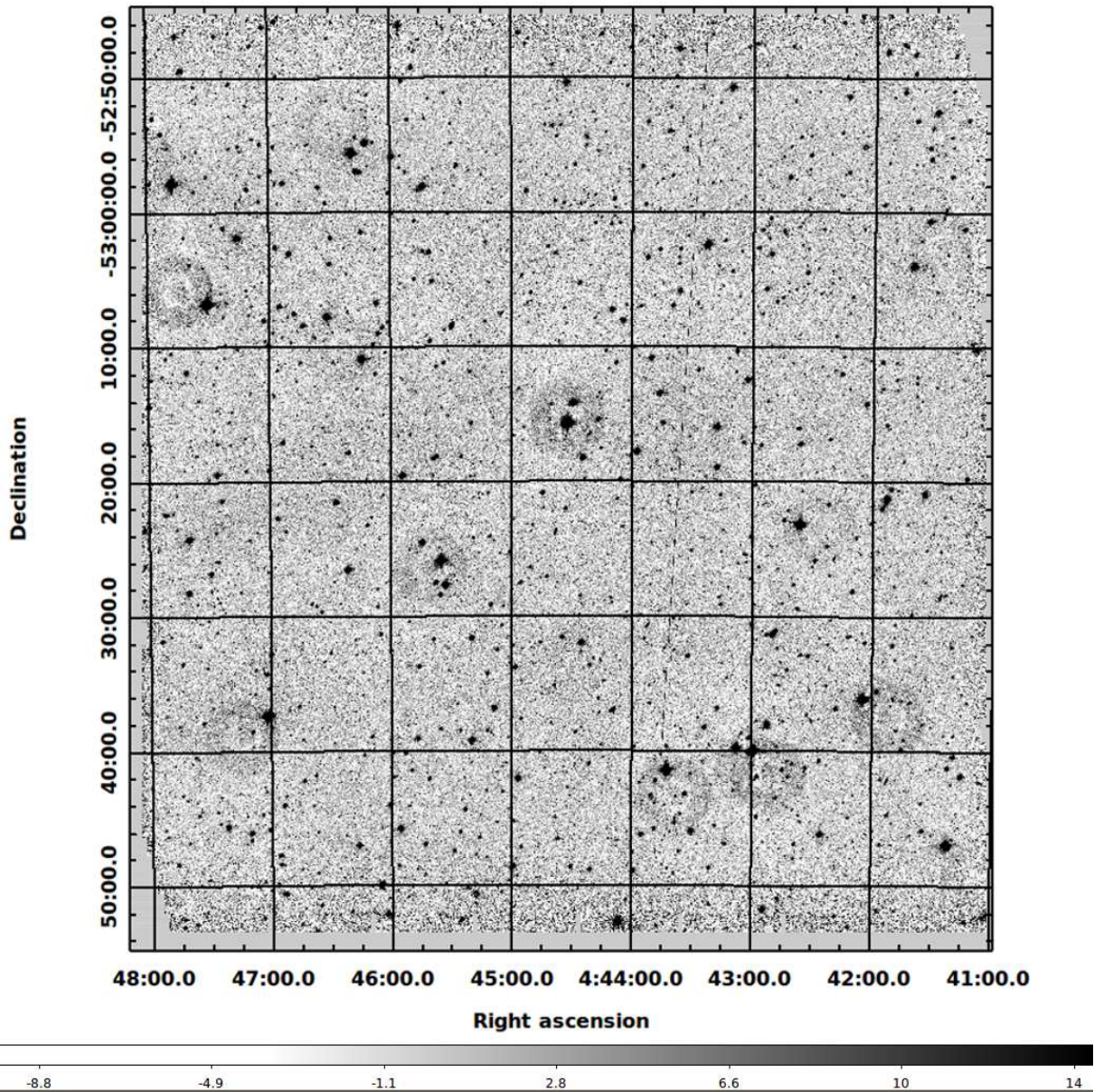


Figure 2.39: Image of the SEP field in the VST-*i* band. Color scale in Counts.

computed in the whole MIPS+SPIRE covered area, and based on the IR and far-IR photometry (FINAL\_Z\_IR). The description of how we computed these estimates can be found in Sections 3 and 4. These estimates result from a combination of different techniques (SED fitting and flux-redshift relations). The intermediate values are also reported in the catalog.

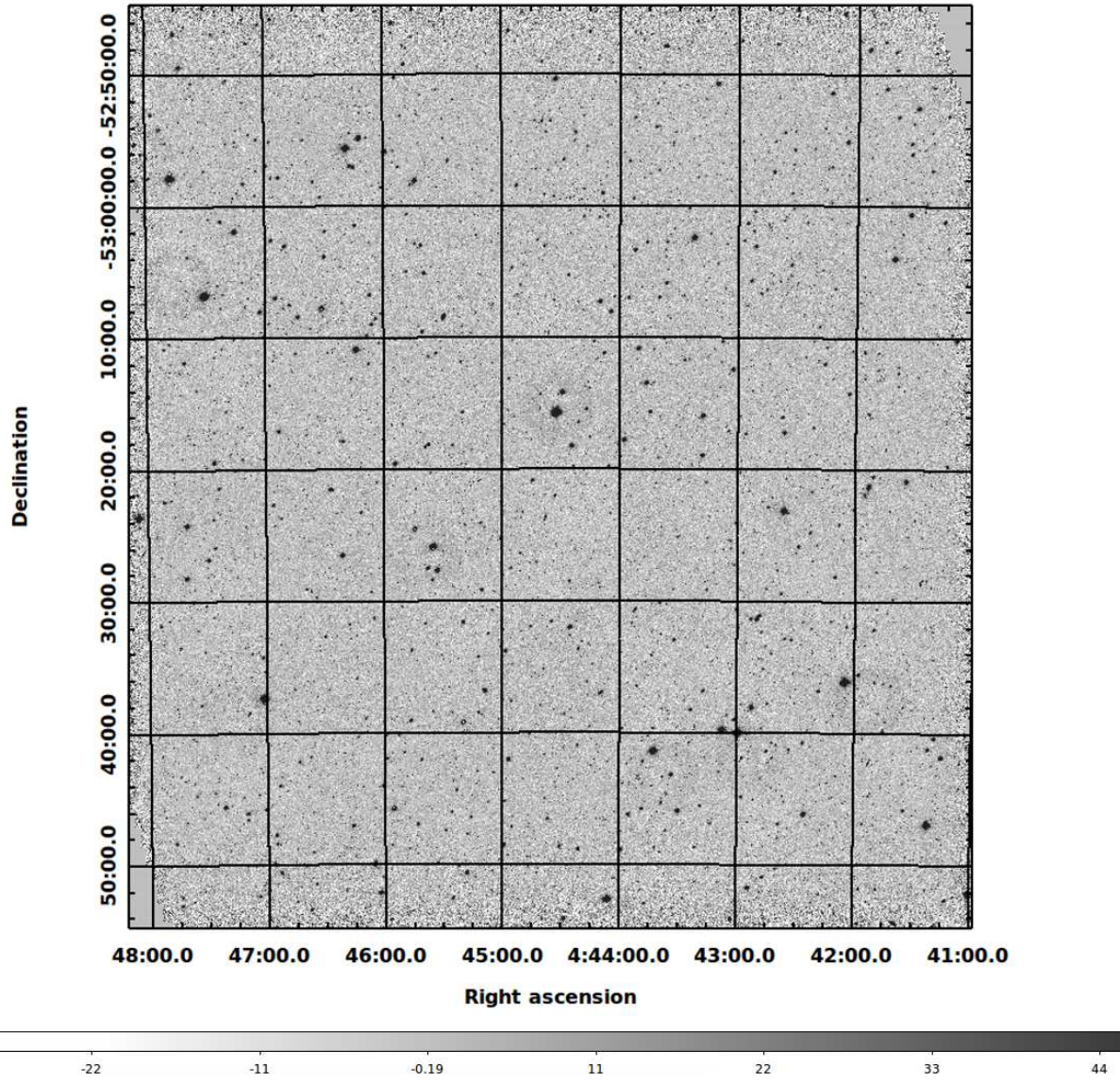


Figure 2.40: *Image of the SEP field in the VST-z band. Color scale in counts.*

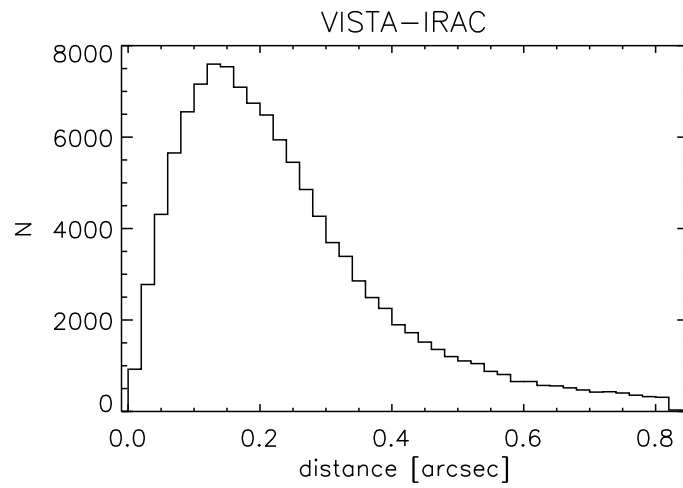


Figure 2.41: *VISTA-IRAC* distance distribution for the optical sources in the multiwavelength catalog. The coordinates of the *VISTA* sources are the those reported in the public catalog of the *VISTA* Hemisphere Survey, corrected for the average shift with the *IRAC* (*ra*, *dec*) positions.

Column	Example	description
ID	122507	Progressive identificative number
RA_I1	70.839699	RA coordinate for the IRAC 1 extracted sources
DEC_I1	-53.659025	DEC coordinate for the IRAC 1 extracted sources
FLUX_I1	0.00117295	IRAC channel 1 ( $3.6\mu\text{m}$ ) <i>SExtractor</i> “AUTO” flux
FLUXERR_I1	4.37397e-06	IRAC channel 1 flux associated uncertainty
FLUX_I1_CORRECTED	0.00112728	FLUX_I1 + correction factor resulting from SED fitting on stellar emission (see Section 3.3). We suggest the use of the original FLUX_I1 because of possible dust contamination.
FLUX_I2	0.000921681	IRAC channel 2 ( $4.5\mu\text{m}$ ) <i>SExtractor</i> “AUTO” flux (computed on I1 prior positions)
FLUXERR_I2	3.98424e-06	IRAC channel 2 flux associated uncertainty
FLUX_I2_CORRECTED	0.000713776	FLUX_I2 + correction factor resulting from SED fitting on stellar emission (see Section 3.3). We suggest the use of the original FLUX_I2 because of possible dust contamination.
RA_24	70.839854	RA coordinate for MIPS 24 sources recentered to the I1 average positions
DEC_24	-53.658936	DEC coordinate for MIPS 24 sources recentered to the I1 average positions
O_RA_24	70.839900	original RA coordinate for MIPS 24 sources *
O_DEC_24	-53.658800	original DEC coordinate for MIPS 24 sources *
FLUX_24	0.00720900	MIPS $24\mu\text{m}$ flux *
FLUXERR_24	4.60000e-05	MIPS $24\mu\text{m}$ flux associated uncertainty *
FLUX_70	0.0510000	MIPS $70\mu\text{m}$ flux *
FLUXERR_70	0.00645570	MIPS $70\mu\text{m}$ flux associated uncertainty *
RA_W	70.839736	RA coordinate for WISE sources recentered to the I1 mean position
DEC_W	-53.659074	DEC coordinate for WISE sources recentered to the I1 mean position
O_RA_W	70.839768	original RA coordinate for WISE sources **
O_DEC_W	-53.659093	original DEC coordinate for WISE sources **
FLUX_W1	0.00098174796	WISE W1 ( $3.35\mu\text{m}$ ) flux **
FLUXERR_W1	2.2347312e-05	WISE W1 flux associated uncertainty **
FLUX_W2	0.00075718131	WISE W2 ( $4.60\mu\text{m}$ ) flux **
FLUXERR_W2	1.7235551e-05	WISE W2 flux associated uncertainty **
FLUX_W3	0.0034705630	WISE W3 ( $11.56\mu\text{m}$ ) flux **
FLUXERR_W3	0.00010699717	WISE W3 flux associated uncertainty **
FLUX_W4	0.0074199308	WISE W4 ( $22.09\mu\text{m}$ ) flux, **
FLUXERR_W4	0.00062789675	WISE W4 flux associated uncertainty **
FLUX_J_2MASS	0.00071186846	2MASS J flux **
FLUXERR_J_2MASS	6.8588901e-05	2MASS J flux associated uncertainty **
FLUX_H_2MASS	0.00092982229	2MASS H flux **
FLUXERR_H_2MASS	0.00010035368	2MASS H flux associated uncertainty **
FLUX_KS_2MASS	0.00093583642	2MASS $K_S$ flux **
FLUXERR_KS_2MASS	9.6376545e-05	2MASS $K_S$ flux associated uncertainty **

\* from Clements et al. (2011)

\*\* from WISE *allWISE* catalog (DR2)

Table 2.12: (A) List of the multiwavelength catalog columns with a brief description of their content. All the fluxes are expressed in Jy and the coordinates in degrees.

Column	Example	description
RA_SPIRE	70.840265	RA coordinate for SPIRE sources recentered to the I1 average position
DEC_SPIRE	-53.658761	DEC coordinate for SPIRE sources recentered to the I1 average position
O_RA_SPIRE	70.840320	original RA SPIRE coordinate ***
O_DEC_SPIRE	-53.658630	original DEC SPIRE coordinate ***
FLUX_250	0.091913074	SPIRE 250 $\mu\text{m}$ flux ***
FLUXERR_250	0.0023182620	SPIRE 250 flux associated uncertainty ***
FLUX_350	0.039603529	SPIRE 350 $\mu\text{m}$ flux ***
FLUXERR_350	0.0026140863	SPIRE 350 flux associated uncertainty ***
FLUX_500	0.0083840684	SPIRE 500 $\mu\text{m}$ flux ***
FLUXERR_500	0.0032940428	SPIRE 500 flux associated uncertainty ***
RA_N3	70.839928	RA coordinate for AKARI N3 sources recentered to the I1 average position
DEC_N3	-53.658989	DEC coordinate for AKARI N3 sources recentered to the I1 average position
O_RA_N3	70.839950	RA coordinate for AKARI N3 extracted sources
O_DEC_N3	-53.659003	DEC coordinate for AKARI N3 extracted sources
FLUX_N3	0.00115753	AKARI N3 ( $3.2\mu\text{m}$ ) <i>SExtractor</i> flux
FLUXERR_N3	5.08719e-06	AKARI N3 flux associated uncertainty
RA_N4	70.839909	RA coordinate for AKARI N4 sources recentered to the I1 average position
DEC_N4	-53.658963	DEC coordinate for AKARI N4 sources recentered to the I1 average position
O_RA_N4	70.839940	RA coordinate for AKARI N4 extracted sources
O_DEC_N4	-53.658994	DEC coordinate for AKARI N4 extracted sources
FLUX_N4	0.000875167	AKARI N4 ( $4.1\mu\text{m}$ ) <i>SExtractor</i> flux
FLUXERR_N4	4.92463e-06	AKARI N4 flux associated uncertainty
RA_S7	70.839974	RA coordinate for AKARI S7 sources recentered to the I1 average position
DEC_S7	-53.659065	DEC coordinate for AKARI S7 sources recentered to the I1 average position
O_RA_S7	70.839951	RA coordinate for AKARI S7 extracted sources
O_DEC_S7	-53.659115	DEC coordinate for AKARI S7 extracted sources
FLUX_S7	0.00238070	AKARI S7 ( $7.0\mu\text{m}$ ) <i>SExtractor</i> flux
FLUXERR_S7	3.32690e-05	AKARI S7 flux associated uncertainty
RA_S11	70.839976	RA coordinate for AKARI S11 sources recentered to the I1 average position
DEC_S11	-53.658947	DEC coordinate for AKARI S11 sources recentered to the I1 average position
O_RA_S11	70.839897	RA coordinate for AKARI S11 extracted sources
O_DEC_S11	-53.658980	DEC coordinate for AKARI S11 extracted sources
FLUX_S11	0.00320643	AKARI S11 ( $11.0\mu\text{m}$ ) <i>SExtractor</i> flux
FLUXERR_S11	4.49318e-05	AKARI S11 flux associated uncertainty
RA_L15	70.839764	RA coordinate for AKARI L15 sources recentered to the I1 average position
DEC_L15	-53.659377	DEC coordinate for AKARI L15 sources recentered to the I1 average position
O_RA_L15	70.839653	RA coordinate for AKARI L15 extracted sources
O_DEC_L15	-53.659482	DEC coordinate for AKARI L15 extracted sources
FLUX_L15	0.00402966	AKARI L15 ( $15.0\mu\text{m}$ ) <i>SExtractor</i> flux
FLUXERR_L15	8.19825e-05	AKARI L15 flux associated uncertainty

\*\*\* from Oliver et al. (2012)

Table 2.12: (B) List of the multiwavelength catalog columns with a brief description of their content. All the fluxes are expressed in Jy and the coordinates in degrees.

Column	Example	description
RA_L24	70.839382	RA coordinate for AKARI L24 sources recentered to the I1 average position
DEC_L24	-53.659655	DEC coordinate for AKARI L24 sources recentered to the I1 average position
O_RA_L24	70.839341	RA coordinate for AKARI L24 extracted sources
O_DEC_L24	-53.659753	DEC coordinate for AKARI L24 extracted sources
FLUX_L24	0.00521725	AKARI L24 (24.0 $\mu$ m) <i>SExtractor</i> flux
FLUXERR_L24	0.000175077	AKARI L24 flux associated uncertainty
RA_OPT	70.839746	RA coordinate for OPTICAL sources recentered to the I1 average position
DEC_OPT	-53.658990	DEC coordinate for OPTICAL sources recentered to the I1 average position
O_RA_OPT	70.839744	average optical RA coordinate
O_DEC_OPT	-53.658994	average optical DEC coordinate
FLUX_U	0.000128362	CTIO-u <i>SExtractor</i> flux
FLUXERR_U	1.31381e-06	CTIO-u flux associated uncertainty
FLUX_B	0.000253157	CTIO-B <i>SExtractor</i> flux
FLUXERR_B	1.84902e-06	CTIO-B flux associated uncertainty
FLUX_V	0.000517036	CTIO-V <i>SExtractor</i> flux
FLUXERR_V	0.000166493	CTIO-V flux associated uncertainty
FLUX_I	0.000988918	CTIO-I <i>SExtractor</i> flux
FLUXERR_I	4.31660e-05	CTIO-I flux associated uncertainty
FLUX_R_WFI	0.000762545	WFI-R <i>SExtractor</i> flux
FLUXERR_R_WFI	2.21666e-06	WFI-R flux associated uncertainty
FLUX_G_VST	0.000357647	VST-g <i>SExtractor</i> flux
FLUXERR_G_VST	3.02272e-07	VST-g flux associated uncertainty
FLUX_I_VST	0.00100435	VST-i <i>SExtractor</i> flux
FLUXERR_I_VST	8.83767e-07	VST-i flux associated uncertainty
FLUX_Z_VST	0.00128068	VST-z <i>SExtractor</i> flux
FLUXERR_Z_VST	1.98721e-06	VST-z flux associated uncertainty
DET_ALL	8	number of optical detections among CTIO-u, B, V, I, WFI-R, VST-g, i, z. Minimum value=2
OPT_ID	1194	Identificative number in the optical catalog
RA_VISTA	70.839741	RA coordinate for VISTA sources recentered to the I1 average position
DEC_VISTA	-53.659095	DEC coordinate for VISTA sources recentered to the I1 average position
O_RA_VISTA	70.839747	RA coordinate from the VISTA catalog****
O_DEC_VISTA	-53.659121	DEC coordinate from the VISTA catalog****
FLUX_J_VISTA	0.00207866	VISTA-J flux
FLUXERR_J_VISTA	2.13354e-05	VISTA-J flux associated uncertainty
FLUX_H_VISTA	0.00246939	VISTA-H flux
FLUXERR_H_VISTA	3.44808e-05	VISTA-H flux associated uncertainty
FLUX_KS_VISTA	0.00225621	VISTA-K <sub>S</sub> flux
FLUXERR_KS_VISTA	4.11302e-05	VISTA-K <sub>S</sub> flux associated uncertainty

\*\*\*\* from (VHS, McMahon et al. 2013, DR2)

Table 2.12: (C) List of the multiwavelength catalog columns with a brief description of their content. the counterpart distances are expressed in arcseconds.

Column	Example	description
P1	0.892983	Reliability indicator for SPIRE-MIPS correlation (0 bad, 1 good)
MIPS_SPIRE_DIST	1.08162	Number of potential MIPS counterparts for the SPIRE source
N_MIPS_SPIRE	1	
FCD_M_S_DIST	1.08162	Nearest MIPS potential counterpart distance from SPIRE source
P2	0.859157	Reliability indicator for MIPS-IRAC correlation (0 bad, 1 good)
IRAC_MIPS_DIST	0.461364	Number of potential IRAC counterparts for the MIPS source
N_IRAC_MIPS	1	
FCD_I_M_DIST	0.461364	Nearest IRAC potential counterpart distance from MIPS source
P3	0.841023	Reliability indicator for SPIRE-IRAC (0 bad, 1 good)
IRAC_SPIRE_DIST	1.53949	Number of potential IRAC counterparts for the SPIRE source
N_IRAC_SPIRE	1	
FCD_I_S_DIST	1.53949	Nearest IRAC potential counterpart distance from SPIRE source
CLASS_STAR_I1	0.0286282	CLASS_STAR parameter for IRAC 1 extraction (0 galaxy, 1 stars)
A_IMAGE_I1	5.46241	<i>SExtractor</i> A_IMAGE parameter for IRAC 1 extraction
B_IMAGE_I1	2.61625	<i>SExtractor</i> B_IMAGE parameter for IRAC 1 extraction
KRON_RADIUS_I1	3.50000	<i>SExtractor</i> KRON_RADIUS parameter for IRAC 1 extraction
N_SIGMA	194.309	Ratio between IRAC 1 FLUX and sky sigma value (depend on the coverage)
SIGMA	3.09314e-06	IRAC1 sky sigma value (depend on the coverage)
COVERAGE	5.93006	Mean coverage in the 49 central pixels underlying the source
AP1_FLUX_I1	0.000601023	IRAC 1 first aperture flux (8pixels-4.8")
AP2_FLUX_I1	0.000845565	IRAC 1 second aperture flux (12pixels-7.2")
AP3_FLUX_I1	0.00106531	IRAC 1 third aperture flux (20pixels-12.0")
AP1_FLUX_I2	0.000484432	IRAC 1 first aperture flux (8pixels-4.8")
AP2_FLUX_I2	0.000672558	IRAC 2 second aperture flux (12pixels-7.2")
AP3_FLUX_I2	0.000833726	IRAC 3 third aperture flux (20pixels-12.0")
FLUX_APER_J_VISTA	0.000499680	VISTA J Aperture fluxes. We suggest the use of the Petrosian fluxes FLUX_J_VISTA, for coherence with the other fluxes in the catalog
FLUXERR_APER_J_VISTA	4.05294e-06	VISTA J Aperture fluxes associated uncertainties
FLUX_APER_H_VISTA	0.000589439	VISTA H Aperture fluxes. We suggest the use of the Petrosian fluxes FLUX_H_VISTA, for coherence with the other fluxes in the catalog
FLUXERR_APER_H_VISTA	5.45138e-06	VISTA H Aperture fluxes associated uncertainties
FLUX_APER_KS_VISTA	0.000618229	VISTA K <sub>S</sub> Aperture fluxes. We suggest the use of the Petrosian fluxes FLUX_Ks_VISTA, for coherence with the other fluxes in the catalog
FLUXERR_APER_KS_VISTA	6.57450e-06	VISTA K <sub>S</sub> Aperture fluxes associated uncertainties

Table 2.12: (D) List of the multiwavelength catalog columns with a brief description of their content. the counterpart distances are expressed in arcseconds.

Column	Example	description
ID_SPC_Z	149	Spectroscopic redshift identificative number *
RA_SPC_Z	70.839668	RA coordinate of spectroscopic sources *
DEC_SPC_Z	-53.659138	DEC coordinate of spectroscopic sources *
SPECT_Z	0.0920000	Spectroscopic redshift *
FLAG_ZSPC	3.00000	Spectroscopic redshift reliability * (1=bad, 2=average, 3=good)
HYPERZ_Z_IR	0.00000	<i>Hyperz</i> output redshift based on IR photometry** see Section 4.1
HYPERZ_COMB_Z_IR	0.00000	<i>Hyperz</i> combined solutions. Computation based on IR photometry** see Section 4.1
FINAL_Z_IR	0.0389425	redshift from <i>Hyperz</i> combined solutions and I1 flux**. Computation based on IR photometry. See Section 4.3
HYPERZ_Z_OPTICAL	0.100000	<i>Hyperz</i> output redshift based on OPTICAL photometry***. See Section 3.2
FLUX_Z_OPTICAL	0.0143676	Redshift from optical flux in R, i and z bands***. See Section 3.4
FINAL_Z_OPTICAL	0.0143676	Photometric redshift based on optical photometry***. Combination of <i>Hyperz</i> output and redshift from optical flux in R <sub>c</sub> , i and z bands. See Section 3.5
SUPERFLUX	0.00145891	Quadratic sum of R <sub>c</sub> , i and z fluxes used to compute the FLUX_Z_OPTICAL value

---

\* from Sedgwick et al. in preparation.

\*\* Computed in the whole MIPS+SPIRE covered area.

\*\*\* Computed in the optically covered area.

Table 2.12: (E) List of the multiwavelength catalog columns with a brief description of their content. the counterpart distances are expressed in arcseconds.

## Chapter 3

# Optical–based photometric redshifts

We computed reliable photometric redshifts using 13 bands in the optical-near-IR region of the spectrum, from the u band to the IRAC 2 channel ( $4.5\mu\text{m}$ ). We exploited both a SED-fitting procedure applied to the photometric data through a  $\chi^2$  minimization, and a technique based on the total observed flux in three optical bands. The combined method used here was tested in the COSMOS field, using a similar set of filters and comparing the results with reliable spectroscopic and photometric redshifts. For the SED-fitting procedure we used the aperture fluxes computed on the images taken in the 13 filters, smoothed to get a similar PSF in each band. We also computed, through an iterative procedure, a set of corrections to be applied to the total fluxes in each filter.

### 3.1 Aperture fluxes on smoothed images

We performed the SED fitting through the  $\chi^2$  minimization, using the fixed-aperture fluxes computed on the smoothed images. The smoothing scale chosen for each image was selected to obtain a similar PSF in all the filters. This is justified by the considerations that follows.

The extraction of the sources from the images and the computation of their fluxes can be performed using fixed or variable (automatic) apertures. In the first case, the size of the aperture is set as an input parameter and it is identical in size for every extracted source. Instead, the shape and the size of the variable aperture basically depends on the axis ratio and on the luminosity profile of each source. We already saw the differences between these two modes when describing the extraction of the sources from the IRAC image.

While the automatic apertures allows for a more precise total flux computation in a given photometric band, they are not the very best solution when a color index has to be determined. Let us consider for example two images with a similar PSF, taken in two different filters, and a faint extended source detected in both the images. Unless one image is used to get the position of the source and the other to compute the flux (dual mode extraction), the size and the position of the variable aperture is independently determined in the two images. For an extended source, the error on the total flux computed inside the variable apertures is smaller than in the case of the fixed ones, but the fraction of light excluded in two filters, can be different. On the contrary, when considering fixed apertures, the total flux in a single band is prone to an higher error, but this fractional error is similar using two different filters. When considering extended sources, the aperture corrected fluxes calculated in fixed apertures are far from being precise, but the same size considered in different filters guarantees that a

similar fraction of light is lost in the two images, if they have a similar PSF. The resulting color indexes will then be more precise when computed in fixed apertures. This solution can even be improved if the position of the fixed apertures is not automatically determined in each image. In this case, the exact position of the aperture’s center depends on the estimated luminosity profile. This is not the best solution, especially when the source is faint and only few counts per pixel are available to estimate the baricenter. Moreover, the luminosity of the different parts of a galaxy can change with the wavelength, determining a shift of the apparent position with  $\lambda$ . This problem can be prevented using the average position determined in the various bands. We stress that this solution does not give the most precise value of the total flux in each filter, but only the most precise relative fluxes (color indexes).

The redshift values computed using a SED fitting technique does not depend on the normalization of the best fit SED. In other words, the total flux does not change the resulting redshift. What is instead important, is the ratio between the fluxes computed in the different filters (i.e. the color indexes). As explained above, this means that when the images have a similar PSF, the best solution from the  $\chi^2$  minimization technique will be obtained using fluxes computed inside fixed apertures (for the same reason, not applying the aperture corrections would not change the results).

The PSFs of the images in the filters that we used for the SED fitting weren’t characterized by an identical full width half maximum (FWHM). The values that we computed in the original images are reported in table 3.1. In order to use all the available bands between CTIO-u and IRAC 2, we used the worst FWHM among these bands as a referement (u band). We smoothed all the other images obtaininig a similar value of FWHM as that of the worst image. Some images, being the result of a mosaic, showed a not negligible variation of the PSF in the field. For these images we smoothed the images using a different scale in the different regions, in order to obtain the most uniform PSF along the field. An initial guess of the smoothing scale, corresponding to the  $\sigma$  of the gaussian filter used ( $\sigma = \text{FWHM}/2.355$ ), was computed from the inverse of the following equation:

$$\sigma_{\text{ref}}^2 = \sigma_{\text{image}}^2 + \sigma_{\text{filter}}^2, \quad (3.1)$$

where  $\sigma_{\text{ref}} = \sigma_{\text{u}} = 0.91''$  is the  $\sigma$  of the PSF that we want to obtain, and  $\sigma_{\text{image}}$  is the original sigma of the image. Since the PSF shapes are not perfectly gaussian, the final result can differ from what expected. We check our results measuring the resulting PSF values on the smoothed images, finding better results when the used smoothing scale is the  $1/0.92$  of the  $\sigma_{\text{filter}}$  computed. The results and the actual smoothing scales are shown in table 3.1.

We computed the fluxes in different fixed apertures (1'', 2'', 3''). We found a better agreement between our photometric and spectroscopic redshifts (from Sedgwick et al. in preparation) when using the 1'' aperture. We centered the fixed apertures in the mean RA, dec position of the sources determined in the different bands. To do this, we converted the sky coordinates to the corresponding (x,y) positions in the images. The recentering corrections that we applied when we were looking for the counterparts in the different bands where here considered.

## 3.2 Redshift from the SED fitting technique

The technique here described, allows to obtain photometric redshifts from the model fitting of the observed fluxes. The results obtained using this technique are not, however, the final

Filter/region	Original FWHM [arcsec]	Final FWHM [arcsec]	Smoothing scale $\sigma_{\text{filter}}$ [arcsec]
CTIO-u region1	2.15	2.15	/
region 2	2.14	2.14	/
CTIO-B region1	1.81	2.13	0,45
region 2	1.66	"	0,53
CTIO-V region 1	1.48	2.13	0,60
region2	1.21	"	0,69
region 3	1.35	"	0,65
CTIO-I region 1	1.41	2.06	0,63
region2	1.43	"	0,63
WFI-R <sub>c</sub> region1	1.01	2.18	0,68
region 2	0.95	"	0,68
region 3	1.00	"	0,68
region 4	0.95	"	0,68
VST- $g_{\text{sdss}}$	1.34	2.24	0,62
VST- $i_{\text{sdss}}$	0.89	2.20	0,76
VST- $z_{\text{sdss}}$	0.78	2.18	0,77
VISTA-J image 1	1.00	2.16	0,74
image 2	1.33	2.21	0,66
VISTA-H image 1	1.25	2.22	0,68
image 2	1.09	2.15	0,72
VISTA-K <sub>s</sub>	1.08	2.14	0,73
IRAC 1	1.66	2.20	0,39
IRAC 2	1.72	2.33	0,48

Table 3.1: *FWHM values of the PSFs, computed on the original images and in the smoothed images, in the different filters. The smoothing factor used is also reported.*

redshifts that we used in our analysis. We instead combined these results with those obtained using another method that is based on the observed relation between the total observed fluxes in three optical bands and the redshift of the source.

Using the *Hyperz* software (Bolzonella et al. 2000), we fitted the photometric aperture magnitudes with a set of 8 templates from the Bruzual & Charlot (2003) collection. The templated models ranged from  $\tau=0.3$  to 30 Gyrs, with an implicit SFR given by:

$$\text{SFR} \propto \exp(t/\tau) \quad (3.2)$$

We assumed a Calzetti et al. (2000) extinction law with  $A_V$  ranging from 0.0 to 4.0 and a solar metallicity. The list of templates and the other most important parameters adopted for the SED fitting procedure are summarized in table 3.2. We assumed a constant uncertainty of 0.1 magnitudes for each band. The use of the actual photometric uncertainties can give very good fits in those parts of the spectrum where the uncertainty is low, and completely wrong fits where the uncertainty is higher. For this reason, this is not always the best approach, since the color indexes in some bands, in particular those with a  $\lambda$  position close to the major breaks in the spectra, have a more tight correlation with the redshift, even when the associated uncertainties are higher. This fact become more and more important when the number of filters used to perform the fit is lower. A good solution, when the effective wavelengths of the filters used are well distributed along the spectrum, is to use similar uncertainties. This allow to balance the importance of the various parts of the spectra during the best fit determination.

We tested the precision of the SED-fitting method here described using spectroscopic data taken in both the SEP and the COSMOS filed, where we could use a similar set of photometric bands. The results of this analysis are reported in section 3.5.

Parameter	value
Code	<i>Hyperz</i>
Bands	CTIO u, B, V, I VST g, i, z WFI R <sub>C</sub> VISTA J, H, K <sub>s</sub> IRAC I1, I2
Extinction law	Calzetti et al. (2000)
Extinction range	$A_V^{min} = 0.0$ , $A_V^{max} = 4.0$ , $A_{step} = 0.3$
BC03 Models ( $\tau$ )	0.3, 1, 2, 3, 5, 10, 15, 30
IMF	Chabrier (2003)
Metallicity	$Z=0.02$ ( $=Z_{\odot}$ )
Cosmological parameters	$\Omega_M=0.3$ , $\Omega_{\Lambda}=0.7$ , $H_0=70$

Table 3.2: *Hyperz* configuration for the  $\chi^2$  minimization technique. This SED fitting represented the first step in the redshift determination.

The SED fitting method performed and its results are only an intermediate step. The redshifts used in our analysis are the result of a combination with those obtained with the technique explained in section 3.4.

### 3.3 Fluxes recalibration

The original photometric calibrations of the images in the CTIO-B, V and WFI-R<sub>C</sub> correspond to the ratio between the measured number counts in the automatic elliptical apertures and the fluxes in the shallower referent catalog of Zacharias et al. (2005). For the CTIO-I and u bands we used the fits of a set of unsaturated and not too faint star SEDs to obtain the calibration factor needed. The calibrations here described have an high associated error. First, they are the result of a comparison between fluxes measured in not identical filters. Second, the calibration is obtained using star fluxes, while our analysis concerns galaxies. Third, the calibration of some bands (CTIO-I and u) depends on the fit of not precisely calibrated bands, performed with few bands (the bands that have to be calibrated with an SED fitting can't be considered during the calibration itself).

In order to refine the original calibrations, we applied an iterative procedure that involves the best fits obtained using *Hyperz*. The first time we run *Hyperz* we used the extracted magnitudes roughly calibrated as described here above. We compared the best fitting SEDs with our fluxes at the effective wavelengths and then we computed, for each filter, an average correction. At this purpose, we considered only the best fits (smallest  $\chi^2$ ) and only the sources with resulting photometric redshifts more similar to the referent spectroscopic redshifts. We iterated this computation calculating at every run, a more precise set of correction factors. The final corrections used are reported in table 3.3. Note that this recalibration, computed for the fixed aperture magnitudes (aperture corrected), can be directly applied to the fluxes computed in the variable (AUTO) apertures. The calibration on the IRAC 1 band was applied only in the last two iterations, in order to prevent any possible runaway of the corrections during the iterations. More in general, the offsets computed for the IRAC bands were used during the SED fitting procedure but, differently from the offsets that we computed for the other optical bands, they were not further applied in the following analysis. The primary purpose of our recalibration was to correct the originally roughly calibrated fluxes in the optical bands. The

Filter	$\Delta m$
CTIO-u	-0.356
CTIO-B	0.348
CTIO-V	0.685
CTIO-I	-0.152
WFI-R <sub>c</sub>	0.123
VST-g	0.043
VST-i	-0.061
VST-z	-0.043
VISTA-J	-0.244
VISTA-H	-0.219
VISTA-Ks	-0.126
IRAC-I1*	0.043*
IRAC-I2*	0.278*
NOTE:	
* The offsets on the IRAC bands were used only during the iterative SED fitting, while they are not kept into account in the following analysis.	

Table 3.3: *Recalibration results. Here  $\Delta m = \langle m_{\text{SED}} - m_{\text{original}} \rangle$ .*

fluxes in the IRAC bands were instead extracted using the precise parameters reported in the IRAC handbook and theoretically they wouldn't need any further correction. Moreover, the corrections are calculated using the Bruzual & Charlot (2003) SSP models, that describe only the stellar components of the galaxies. Since the dust component could affect the two IRAC bands, and in particular the IRAC-2 flux, the offset here could be the result of the models used and not a real systematic error on the computed fluxes.

### 3.4 Redshift from total optical flux: an alternative technique

In order to improve the results obtained through the  $\chi^2$  minimization technique, we integrated the information from the SED fitting with the information from the total flux observed in three optical bands.

The  $\chi^2$  minimization technique allows to find the modelized SED that better fit the measured fluxes. The observed shift in  $\lambda$  of the best fitting SED, with respect to the rest frame one, is the only information used to obtain the redshift  $z$ . In the SED fitting method, the normalization of the SED (the total observed flux) is not used to get supplementary information on the redshift of the source. This information is anyway important, especially considering those cases in which the  $\chi^2$  minimization bring to wrong solutions (outliers) or to a degeneracy between high redshifts and low redshifts solutions, with similar resulting probabilities in the probability distribution function (PDF).

We performed an analysis on the correlation between optical fluxes and redshifts, for far-IR selected sources, in the COSMOS field, where a similar set of filters and reliable photometric and spectroscopic redshifts are available. The simple idea at the basis of this method is that the more distant a galaxy is, the fainter it appears. A relation similar to what we are discussing here can be found for example in Cowie et al. (1996), where they correlated the apparent magnitude in the k band with the redshift of the sources. Here we show how this kind of relations improves when the sources are detected in the far-IR.

If we consider the mass in stars  $M^*$ , that is responsible for the optical emission, we can

roughly say that there are massive and small galaxies. For this reason, the same observed flux could be emitted by a massive and distant or by a small and close galaxy. This degeneracy is mitigated by the existence of a superior physical limit to  $M^*$ . In the redshift versus observed flux plane, this means that, fixed the redshift, there is a superior limit to the observed flux and that this limit decreases with the redshift. This simple observation give us an important information: the sources with, at the same time, an high redshift resulting from the SED fitting, and an high observed flux (possibly beyond the identified superior limit at that redshift) are probably outliers. The low redshift solution (possible secondary peak in the probability distribution function), if present, has to be considered in place of the first solution.

A consistent improvement of these kind of relations is however achieved when the far-IR selected sources are considered. As we demonstrate here for the COSMOS field, the far-IR selected sources show a better defined relation between the redshift and the observed optical flux. In figure 3.1 we report, for the sources in the COSMOS field, the optical fluxes in three optical bands (Subaru r+, i+, z+). The sources with a MIPS  $24\mu\text{m}$  detection above  $0.3\text{mJy}$  are highlighted with bigger and colored dots. From the distribution of the small black dots, it appears evident that a relation between the optical flux and the redshift does already exist even without a selection in the far IR. The same relation is however better correlated if we consider only the sources with some kind of FIR detection<sup>1</sup>. In the y axis of figure 3.1 we express the redshift in a form that shows a linear correlation with the logarithm of the flux.

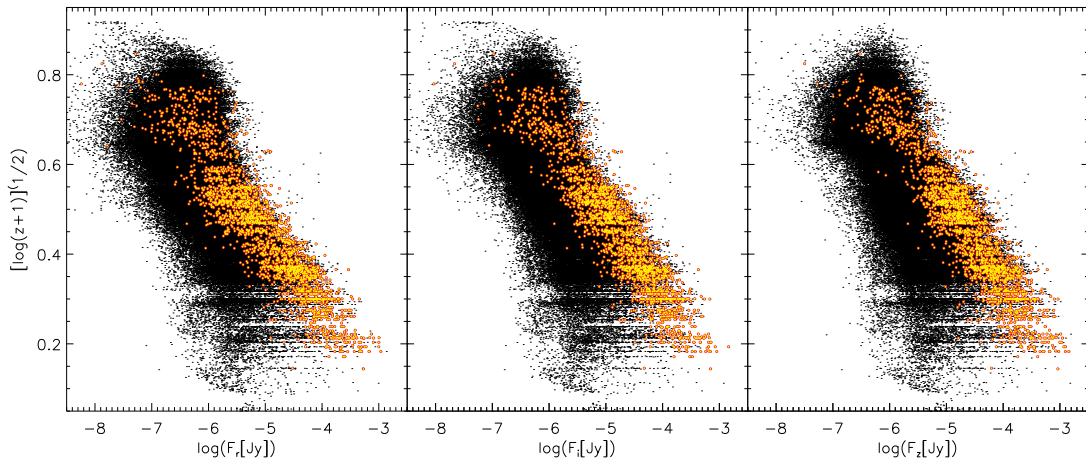


Figure 3.1: Fluxes in three different optical bands in the COSMOS field. The redshift is expressed in the y axis in a form that we found to be linearly correlated with the logarithm of the flux. With black dots, the sources without a MIPS  $24\mu\text{m}$  detection or with a  $24\mu\text{m}$  flux below  $0.3\text{mJy}$ . With colored and bigger dots, the sources with  $F_{24} > 0.3\text{mJy}$ .

We used the fluxes in the z band as a reference: first we computed the median ratio  $R_{rz}$  between the fluxes in the z band and those in the r band. We did the same also for the i band ( $R_{iz}$ ). Then we computed a “super-flux”  $F_{r,i,z}$  as the quadratic sum of the three fluxes:

$$F_{r,i,z} = \sqrt{\frac{F_z^2 + (R_{iz}F_i)^2 + (R_{rz}F_r)^2}{3}} \quad (3.3)$$

<sup>1</sup>We found a similar behaviour when selecting the sources using the PACS 100 or  $160\mu\text{m}$  bands. The results are not reported here

To compute more precise coefficients for the relation, we considered only the sources with a detection in all the three bands. We found the best linearity when the redshift was expressed as  $[\log(z+1)]^{1/2}$ . In figure 3.2 we show the behaviour of the *super-flux*  $F_{r,i,z}$  with the photometric redshift: the sources used to determine the best fit are highlighted.

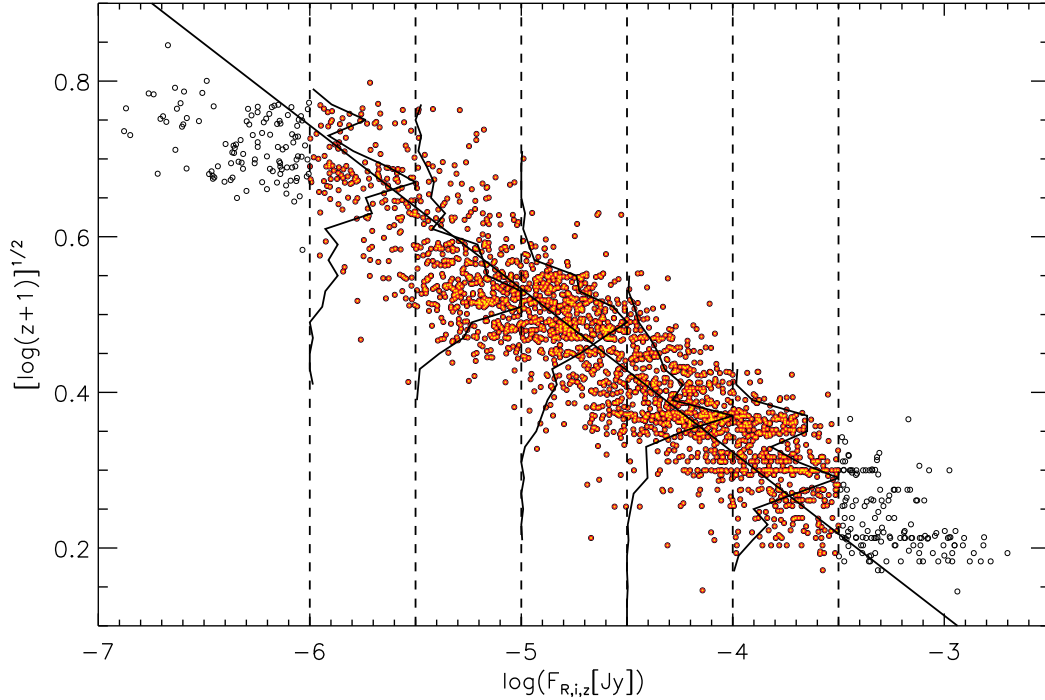


Figure 3.2: “Super-flux”  $F_{r,i,z}$  computed as described in the text, versus redshift. The sources used to compute the best fit, highlighted with filled dots, are selected at  $F_{24} > 0.3mJy$ . We excluded the brightest ( $F_{r,i,z} > 10^{-3.5} Jy$ ) and the faintest ( $F_{r,i,z} < 10^{-6} Jy$ ) sources.

The relation can be expressed as:

$$V_z = [\log(z+1)]^{1/2} = a + b \times \log(F_{r,i,z}), \quad (3.4)$$

In other words, we can estimate the redshift from  $F_{r,i,z}$ , using the following relation:

$$z_{F-z} = 10^{(a+b \times \log(F_{r,i,z}))^2} - 1 = 10^{V_z^2} - 1, \quad (3.5)$$

with  $a=-0.51677$  and  $b=-0.20997$ . In order to compute the best fit, the  $\sigma$  that we used in the two axis are the horizontal dispersion that we computed in the range  $0.47 < [\log(z+1)]^{1/2} < 0.53$  and the vertical dispersion calculated in the range  $10^{-5.1} < F_{r,i,z} < 10^{-4.9}$ . The mean vertical dispersion obtained in five isotropic bins of flux between  $F_{r,i,z} = 10^{-3.5} Jy$  and  $F_{r,i,z} = 10^{-6} Jy$  is  $\langle \sigma_{V_z} \rangle = 0.04$ , whereas the bin with the maximum dispersion had  $\sigma_{V_z}(max) = 0.07$ .

After calibrating this relation in the COSMOS field using the photometric redshifts, we tested it trying to compute the redshift of a sample of sources with available spectroscopic redshifts. We also computed the redshifts of the sources in the SEP filed, using the same method and comparing again with spectroscopic redshifts (Sedgwick et al. in preparation).

Since there exists a maximum value of  $F_{r,i,z}$  for which  $z=0$ , given by:

$$F_{r,i,z}(z_{F-z} = 0) = 10^{-a/b} = 0.00346\text{Jy} \quad (3.6)$$

we fixed  $z_{F-z} = \min(z_{\text{hyperz}}) = 0.01$  when  $F_{r,i,z} > F_{r,i,z}(z_{F-z} = 0)$ , but we discourage the use of these sources, being probable stars. The precision reported in table 3.5 doesn't consider these sources.

The resulting precisions are discussed in section 3.5. In the case of the SEP field, we used the fluxes in the WFI- $R_c$ , VST- $z$ , and VST- $i$  bands to compute  $F_{r,i,z}$ , as shown in the equation 3.3. When the fluxes in one or two bands were not available, we used the other available filters: in the equation 3.3, this means that we divided for 2 or for 1, instead then 3, when respectively, one or two bands were not present.

We stress that this method and the redshifts obtained using it constitute only an intermediate step toward the final redshifts. The redshifts used in our analysis are given by a combination with those resulting from the SED fitting.

### 3.5 Redshift computation methods: comparison and final photometric redshifts

Our final redshifts are the combination of the results obtained using the SED fitting described in the section 3.2 and the flux-redshift relation (F-z) described in the section 3.4. In this section we describe the simple method that we used to combine the two techniques. We will show how the precision of our method is higher than that obtained from the two methods considered separately. We also present another mathematically justified technique that could be used to combine the results, showing that the precision is again lower than that obtained with our method. Finally we compare our precision with that obtained using a technique presented in literature.

Our redshift estimator ( $z_{\text{photo-1}}$ ) is a simple weighted mean between the redshifts resulting from the SED fitting and from the F-z relation. For the two methods, we used fixed weights of  $W_1=2/3$  and  $W_2=1/3$  respectively. In mathematical terms:

$$z_{\text{photo-1}} = W_1 z_{\text{hyperz}} + W_2 z_{F-z} \quad (3.7)$$

where  $z_{\text{hyperz}}$  is the redshift given by the SED fitting and  $z_{F-z}$  is that derived from the F-z relation. The method here described is integrated with an outlier detection and correction technique that we describe in section 3.6. The redshift distribution that we obtain is reported in figure 3.3. The limits and the characteristics of our analysis on the optical-based redshifts are specified in table 3.4. These characteristics and limits can be compared with those in table 4.2 and relative to the IR-based redshifts, computed in the extended and not optically covered area.

In the figures 3.5 and 3.6 we compare, for the COSMOS and the SEP field respectively, the spectroscopic and the photometric redshifts that we obtained with the different techniques. Since we derived our method for the  $24\mu\text{m}$  selected sources, we highlighted these sources. The large data set of spectroscopic and photometric data allows to use the COSMOS field as a test bench. With the photometric data we computed the F-z relation described in section 3.4. The

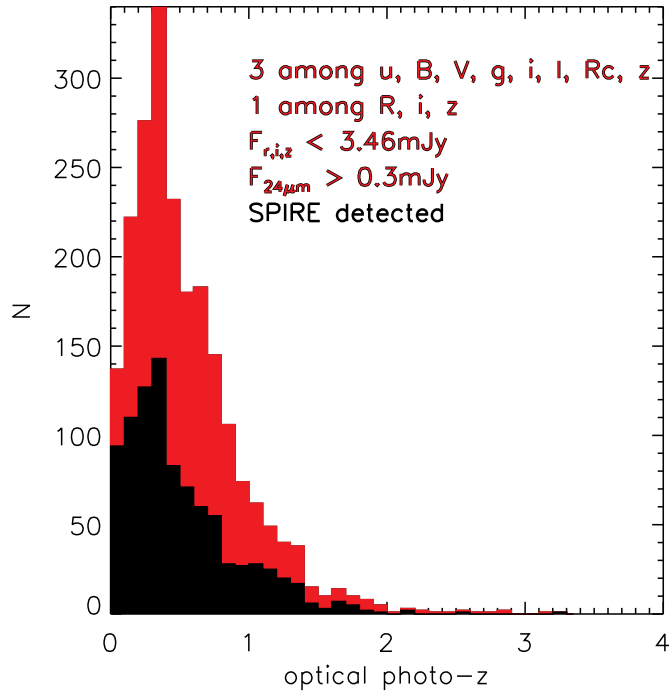


Figure 3.3: *Distribution of the optically derived redshifts, in the SEP field, for the 1934 sources described in table 3.4. In Black, the sources detected also in one of the SPIRE channels, in red the SPIRE undetected. The redshifts were computed combining the results of the SED fitting and the relation between optical fluxes and redshifts calibrated using COSMOS field data.*

precision of the redshifts derived from that relation can now be checked using spectroscopic redshifts<sup>2</sup>.

Observing the upper panels of the figures, we note that at  $z_{\text{spec}} < 1$ , the hyperz output is usually more precise than the redshift derived from the F-z relation. This is not surprising, since we expect the F-z relation to give supplementary information on the redshift of a source, and not a more precise result for itself. At the same time, however, the hyperz output shows an higher tax of outlier sources: for a not negligible fraction of sources the SED fitting gives completely wrong results. The redshift computed from the F-z relation is less precise for the majority of the sources but basically without outliers (among the FIR-selected sources). This fact has important consequences when we consider the probability distribution functions as explained below. The same characteristic can also be exploited to identify the outliers (see section 3.6).

In the lower panels of the figures 3.5 and 3.6 we show, on the left, the precision of the combination method  $z_{\text{photo-1}}$  that we used. The correspondency with the spectroscopic redshifts has to be studied only for the MIPS detected sources, but for informative purposes, we also show the behaviour of the other galaxies. We can see that no outliers are present in the COSMOS MIPS selected sample, while few of them are visible in the SEP filed. This is a

<sup>2</sup>In the COSMOS field, we used a similar set of photometric bands; the only main difference is that in the SEP filed we can use two i bands: i-VST and I-CTIO, while in COSMOS only the Subaru i+ band is available

AREA COVERED	central $\sim 1deg^2$
OPTICAL bands	- detection necessary in at least 3 bands among u, B, V, g, i, I, R <sub>c</sub> , z - detection in one band among R <sub>c</sub> , i, z (to compute $F_{r,i,z}$ )
$F_{r,i,z}$ (see equation 3.3)	< 3.46 mJy (see equation 3.6)
J-VISTA	not necessary, used in the SED fitting (1567/2171 sources)
H-VISTA	not necessary, used in the SED fitting (1549/2171 sources)
K-VISTA	not necessary, used in the SED fitting (1139/2171 sources)
IRAC 1 (3.6 $\mu$ m)	required in both SED fitting and $F_{I1-z}$ relation
IRAC 2 (4.5 $\mu$ m)	not necessary, used in the SED fitting (2159/2171 sources)
WISE W3 (11 $\mu$ m)	not used (1906/2171 sources)
MIPS 24 $\mu$ m	necessary with $F_{24}>0.3mJy$
MIPS 70 $\mu$ m	not used (102/2171 sources)
SPIRE 250 $\mu$ m	not necessary, used in the SED fitting (813/2171)
SPIRE 350 $\mu$ m	not necessary, used in the SED fitting (896/2171)
SPIRE 500 $\mu$ m	not necessary, used in the SED fitting (738/2171)
This table refers to the 2171 IRAC-1 detected sources with:	
- an optical detection in at least 3 bands among u, B, V, g, i, I, R <sub>c</sub> , z;	
- an optical detection in at least one band among R <sub>c</sub> , i, z;	
- a flux $F_{r,i,z} < 3.46mJy$ ;	
- a MIPS 24 $\mu$ m detection $F_{24} > 0.3mJy$ ;	

Table 3.4: *Limits and characteristics of the analysis in the computation of the optical-based photometric redshifts. This table can be compared with the table 4.2 referring to the IR-based redshifts.*

consequence of the particular selection of the spectroscopic sources adopted in the SEP filed. We will discuss this topic in the section 3.6

The second combination analyzed here,  $z_{photo-2}$ , is the result of the mathematical combination between the probability distribution functions (PDF) given by the SED fitting and by the F-z relation. Also in this case we applied the same outlier treatment reserved to the  $z_{photo-1}$  solutions. Even if this method has probably more mathematical justification than the previous one, more precise results are obtained with the simplified  $z_{photo-1}$  combination method (see table 3.5). This can be visually appreciated comparing the bottom-right with the bottom-left panels of the figures 3.5 and 3.6. Hyperz can compute, for each source, a function that describes the probability of a redshift solution. This function depends on the set of filters used, on the flux uncertainties, on the set of template SEDs and on the number of possible steps that the SED fitting procedure can explore for each hyperz output parameter. As already explained however, this PDF, hereafter  $PDF_{hyperz}$  does not take into account the total flux observed for the source considered. To introduce this dependency we proceeded as follows.

Fixed the “super-flux”, (equation 3.3), we assume a gaussian distribution of the data in the  $[\log(z + 1)]^{1/2}$  axis. This is the original probability distribution function  $PDF'_{F-z}$  associated to the data in the F-z relation. The real distribution of the data in the super-flux versus  $[\log(z + 1)]^{1/2}$  plane is shown, for five bins of flux, in figure 3.2. We used the vertical dispersion  $\langle \sigma_{V_z} \rangle = 0.04$  to define the width of the  $PDF'_{F-z}$ .  $PDF_{hyperz}$  and  $PDF'_{F-z}$  can't be directly combined, since they are defined in different dimensions (they are, respectively, probability functions of  $z$  and  $[\log(z + 1)]^{1/2}$ ). We then converted the gaussian  $PDF'_{F-z}$  in the correspondent  $PDF_{F-z}$  defined in  $z$ . At this point, the combined PDF is simply given by the product of the two PDFs:

$$PDF(z) = PDF_{F-z}(z) \cdot PDF_{hyperz}(z) \quad (3.8)$$

Method	$\langle \frac{z-z_{\text{spec}}}{1+z_{\text{spec}}} \rangle$ (median)		$\langle  \frac{z-z_{\text{spec}}}{1+z_{\text{spec}}}  \rangle$		$\sigma \left( \frac{z-z_{\text{spec}}}{1+z_{\text{spec}}} \right)$	
	COSMOS	SEP	COSMOS	SEP	COSMOS	SEP
A - Hyperz output	-0.068	-0.036	0.251	0.183	0.392	0.318
B - From optical Flux ( $z_{F-z}$ )	0.006	-0.047	0.145	0.158	0.120	0.127
<b>C - Weighted mean <math>A \oplus B</math></b> ( $z_{\text{photo}-1}$ )	<b>-0.039</b>	<b>-0.049</b>	<b>0.112</b>	<b>0.118</b>	<b>0.089</b>	<b>0.089</b>
D - PDFs combination $A \oplus B$ ( $z_{\text{photo}-2}$ )	-0.040	-0.049	0.121	0.149	0.104	0.117
E - Krone-Martins et al. (2014) method	0.015	-0.068	0.160	0.200	0.161	0.136

NOTE:

The uncertainties here reported can be applied to the 2171 IRAC-1 detected sources in the SEP fields with:

- an optical detection in at least 3 bands among u, B, V, g, i, I, R<sub>c</sub>, z;
- an optical detection in at least one band among R<sub>c</sub>, i, z;
- a flux  $F_{r,i,z} < 3.46\text{mJy}$ ;
- a MIPS  $24\mu\text{m}$  detection  $F_{24} > 0.3\text{mJy}$ ;

Table 3.5: Precision computed using the methods analyzed in section 3.5. The Precisions are computed on the MIPS  $24\mu\text{m}$  detected sources ( $F_{24\mu\text{m}} > 0.3\text{mJy}$ ), with at least three optical detections, a flux  $F_{r,i,z} < 3.46\text{mJy}$  and an high fidelity spectroscopic redshift (150 sources in the SEP field, 342 in COSMOS). To compute the precision of the Krone-Martins et al. (2014) method in the COSMOS field, we eliminated 5 sources with  $|z - z_{\text{spec}}| / (1 + z_{\text{spec}}) > 3$ , in order to mitigate the effects of the outliers in the precision computation. The other methods didn't need the same treatment.

In figure 3.4 we reported 9 examples that explain this technique. We represent the  $\text{PDF}_{\text{hyperz}}$  with a black area, the  $\text{PDF}_{F-z}$  in orange and the resulting PDF in red. As we discussed before, the redshift given by the F-z relation is usually less precise than that derived with the SED fitting but, at the same time, it is more robust against the outliers problem. For this reason, when the  $\text{PDF}_{\text{hyperz}}$  shows a degeneracy between high and low redshift solutions, the multiplication for  $\text{PDF}_{F-z}$  increases the probability of the PDF's peaks close to the spectroscopic solution, eventually eliminating the outliers problem without the need for a dedicated correction method like the one described in section 3.6. In all the other cases, the shape of the  $\text{PDF}_{\text{hyperz}}$  is not dramatically modified by the multiplication for  $\text{PDF}_{F-z}$ , so that the final result is only blandly modified or even equal to the hyperz output.

The precision of the various methods described so far is summarized in table 3.5, where we computed the values of  $\langle (z - z_{\text{spec}}) / (1 + z_{\text{spec}}) \rangle$  and the corresponding scatter  $\sigma_{(z - z_{\text{spec}}) / (1 + z_{\text{spec}})}$  for each method. We limited the calculation of the precision to the sources with fluxes smaller than  $F_{r,i,z}(z_{F-z} = 0) = 0.00346\text{Jy}$ , detected at  $24\mu\text{m}$  ( $F_{24\mu\text{m}} > 0.3\text{mJy}$ ) and characterized by an high fidelity spectroscopic redshift (155 sources in the SEP field and 342 in COSMOS).

Besides the analysis here described, we also compared our final results with the ones computed as described in Krone-Martins et al. (2014). This method represents an attempt to derive photometric redshifts using an analytical combination of the magnitudes in three optical bands. The equation used in that work is derived using an automatic procedure performed using the *EUREQUA*<sup>3</sup> software. This code is able to scan a large set of possible parameters combinations in order to find the one that better describes the correlation between one selected parameter and the other ones involved (in this case redshift versus fluxes and colors combinations). We analyze this method separately from the other four, since it explicitly considers both the color indexes and the total optical flux, as we tried to do with the techniques

<sup>3</sup><http://www.nutonian.com/products/eureqa/>

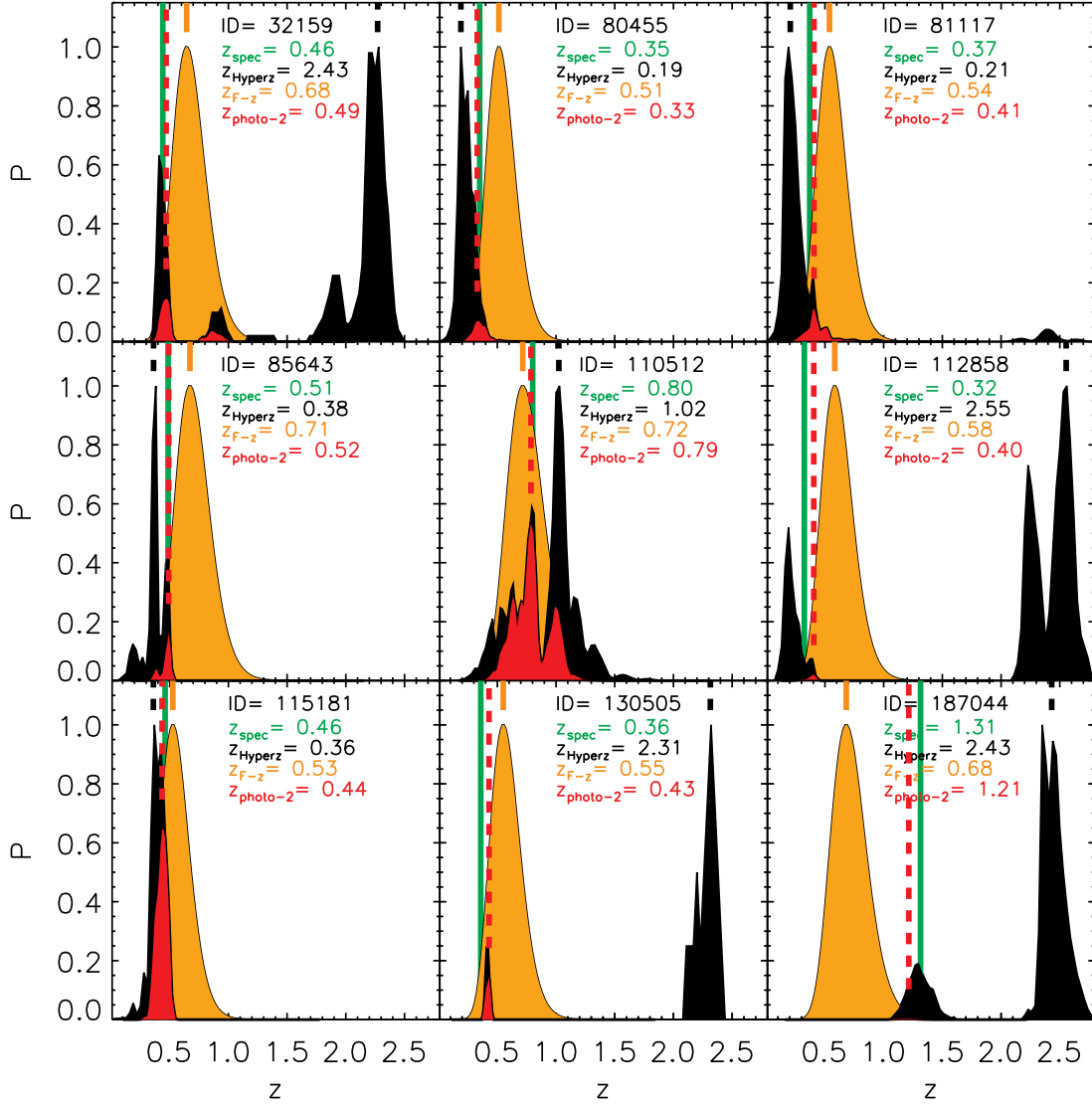


Figure 3.4: Probability distribution functions resulting from different techniques, using the COSMOS data. In black, the  $PDF_{\text{hyperz}}$  given by the SED fitting. In orange, the  $PDF_{F-z}$  resulting from the  $F-z$  relation. In red, the final resulting PDF. We also highlighted, with vertical dashed lines expressed in the same color code, the values of redshift obtained with the different methods. The continuous green line represent the spectroscopic referent redshift.

described above. This method is also a semi-independent result that can be considered as a check test for the SEP filed results, where we only have few spectroscopic sources (and above  $z=1$  only peculiar quasars). In Krone-Martins et al. (2014), the redshift ( $z < 1$ ) is computed using the following equation:

$$z_{\text{Krone-Martins}} = \frac{0.4436r - 8.261}{24.4 + (g - r)^2(g - i)^2(r - i)^2 - g} + 0.5152(r - i) \quad (3.9)$$

where  $g$ ,  $r$  and  $i$  represent the AB magnitudes in the corresponding bands. Using similar photometric bands (Subaru  $g+$ ,  $r+$  and  $i+$  in COSMOS,  $g$ -VST,  $R_c$ -WFI and  $i$ -VST in SEP),

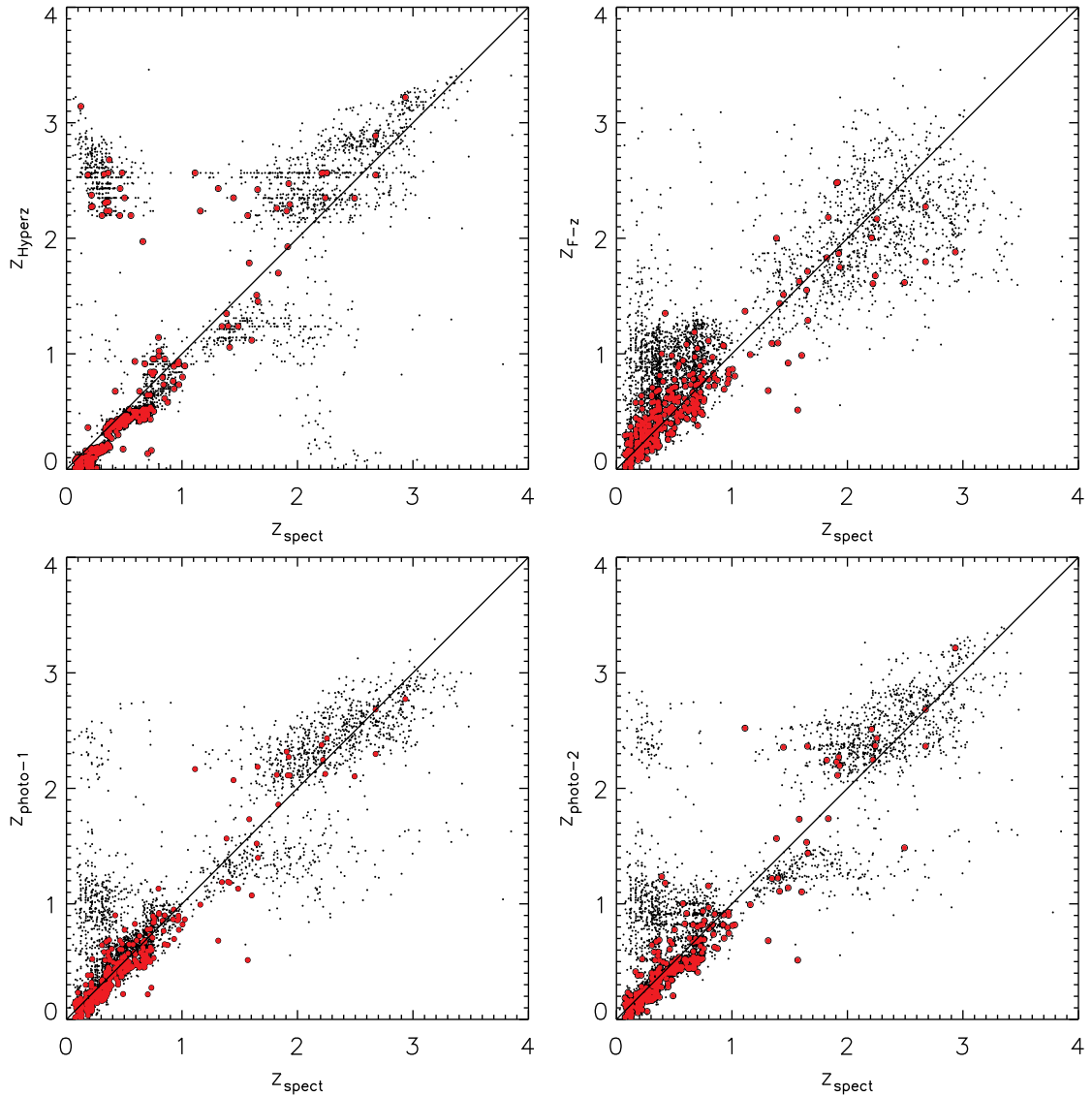


Figure 3.5: *COSMOS* field: comparison between spectroscopic redshifts and hyperz output redshifts (**up left**), redshift obtained from optical fluxes (**up right**), the redshift combination method we used, based on a weighted mean of the results (**bottom left**), alternative combination method through a combination of the probability distribution functions (**bottom right**).

we computed the resulting redshifts and their precisions in the two fields (see table 3.5). The comparison between our final photometric redshifts and the redshift computed using the Krone-Martins et al. (2014) method are shown in figure 3.7.

### 3.6 Outliers treatment

As previously observed, for the majority of the MIPS 24 detected sources below  $z_{\text{spec}}=1$ , the redshift computed using the F-z relation is subject to an higher uncertainty when compared with the results of the SED fitting. However there exists a certain amount of sources for which

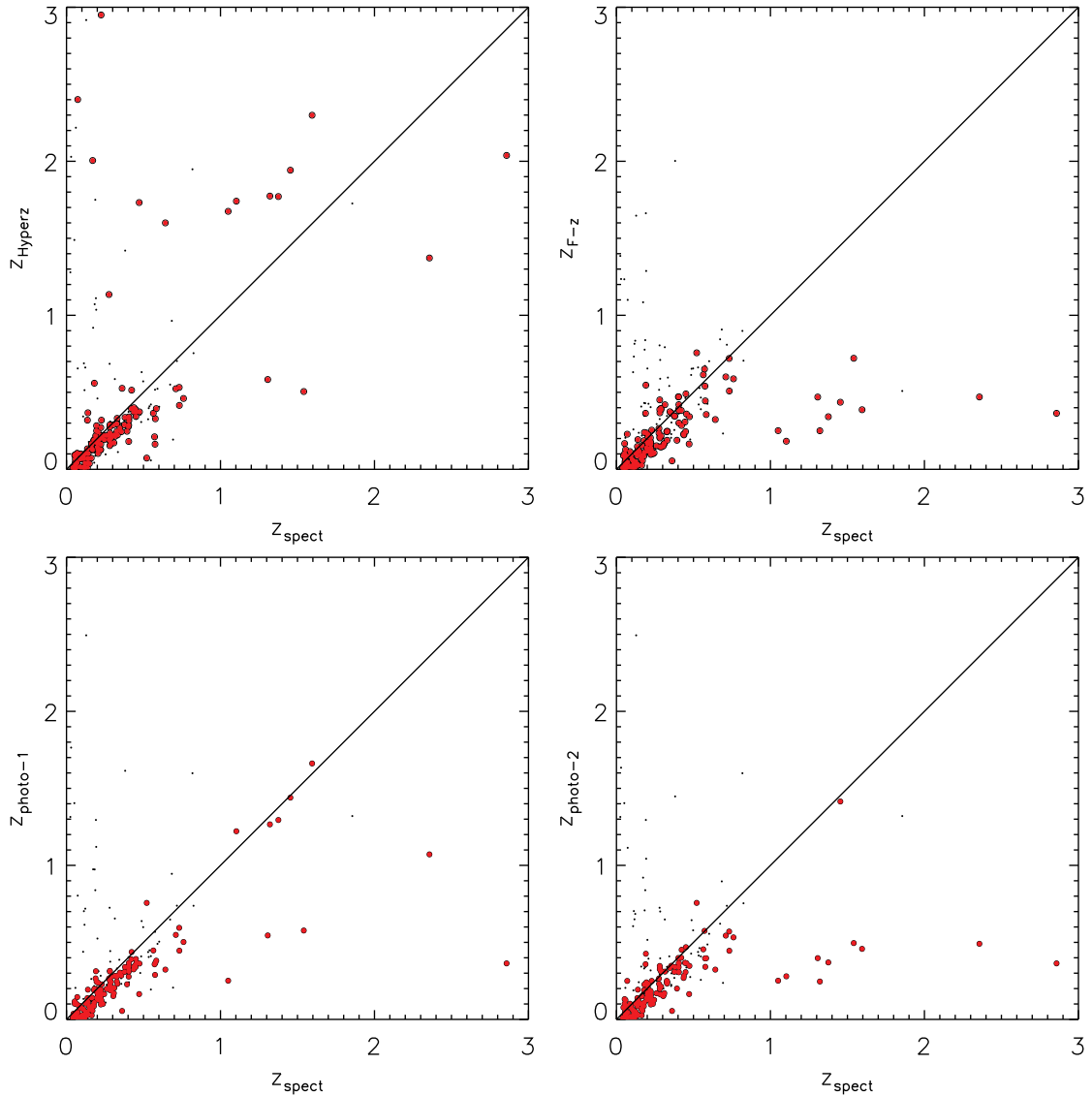


Figure 3.6: *SEP* field: comparison between spectroscopic redshifts and hyperz output redshifts (**up left**), redshift obtained from optical fluxes (**up right**), the redshift combination method we used, based on a weighted mean of the results (**bottom left**), alternative combination method through a combination of the probability distribution functions (**bottom right**).

the redshift solution from the SED fitting catastrophically fails (outliers). This problem is not present if we consider the redshift computed using the total optical flux. When considering the COSMOS data, the previous statement remains true also at  $z_{spec} > 1$ . Using the *SEP* spectroscopic data, instead, we observe 10 sources located above  $z_{spec} = 1$ , with a wrong redshift estimation from both the SED fitting and the F-z relation. We treated this kind of sources in a separate way, when considering the outlier correction. In this section we describe how we identified and corrected the outliers.

Because of the explained peculiarities of  $z_{hyperz}$  and  $z_{F-z}$ , it is possible to identify a possible outlier even without knowing the spectroscopic redshift. This can be done simply comparing the results of the two methods. Basically, when the  $z_{hyperz}$  resulting from the SED fitting

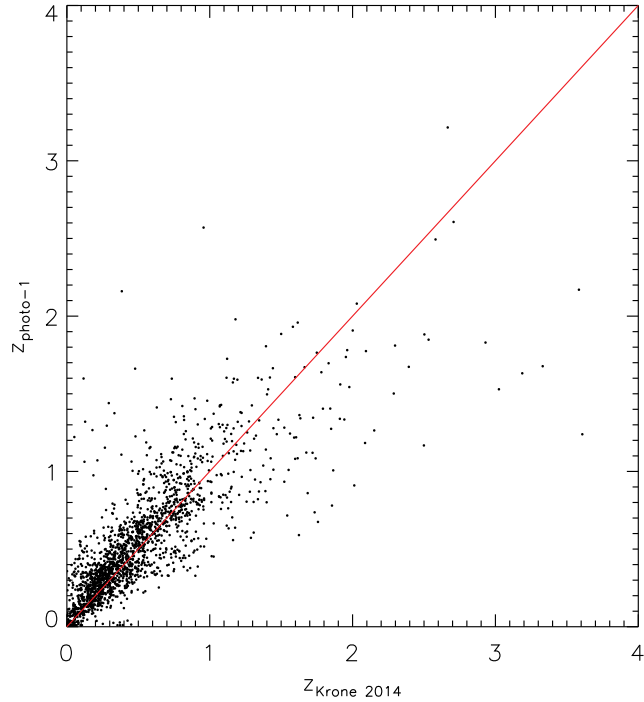


Figure 3.7: *SEP* field: comparison between redshifts computed as in Krone-Martins et al. (2014) and our final photometric redshifts. All the sources are MIPS  $24\mu\text{m}$  selected.

looks very different from the  $z_{\text{F-z}}$  obtained using the F-z relation, there is a high probability that the SED fitting method failed. In these cases the usually less precise  $z_{\text{F-z}}$  estimation has a higher probability to be closer to the real spectroscopic redshift than  $z_{\text{hyperz}}$ . Consequently we set the following rule:

$$\begin{cases} \left| \frac{z_{\text{hyperz}} - z_{\text{F-z}}}{z_{\text{F-z}}} \right| \leq 0.9 \rightarrow z = z_{\text{hyperz}} \oplus z_{\text{F-z}} \\ \left| \frac{z_{\text{hyperz}} - z_{\text{F-z}}}{z_{\text{F-z}}} \right| > 0.9 \rightarrow z = z_{\text{F-z}} \end{cases} \quad (3.10)$$

where  $z_{\text{hyperz}} \oplus z_{\text{F-z}}$  represents one of the combination methods described in the section 3.5.

In the *SEP* field, with the exceptions of the two sources located at  $z_{\text{spec}} > 2$ , all the other spectroscopic sources with redshift  $z_{\text{spec}} > 1$  were selected for being most likely quasars. They show a spectra with a strong MgII emission line at  $\lambda_{\text{MgII}} = 2798\text{\AA}$ . For these sources, the huge non-stellar source of optical luminosity increases the total flux observed, undermining the normal behaviour of the F-z relation. In these cases, the difference between the results given by the SED fitting and by the F-z relation is above the threshold that we set, but the outlier correction would not give the correct result, since both methods are wrong. We found instead that, in these cases, the standard treatment (equation 3.7) still gives better results. In the complete sample, we identified some of these sources using a modified version of the diagnostic method presented in Fadda & Rodighiero (2014). Using only the fluxes in the AKARI N3 and N4 bands, we identified the ‘‘apparent’’ outliers as those sources with  $|(z_{\text{hyperz}} - z_{\text{F-z}})/(z_{\text{F-z}})| > 0.9$  and  $\log(F_{\text{N4}}/F_{\text{N3}}) > 0.2$ . For these ‘‘apparent’’ outliers we applied

the normal procedure expressed in equation 3.7 (that means no outlier correction). In figure 3.8 we show the comparison between the redshifts computed using the total optical fluxes ( $z_{F-z}$ ) and the hyperz output. The outliers are represented by red dots, while the big black dots are the sources that we identified as “apparent” outliers, characterized by  $\log(F_{N4}/F_{N3}) > 0.2$ . The only apparent outliers identified with the method just described resulted the already spectroscopically identified quasars, that were selected and spectroscopically adjoined to the complete sample, just for their nature.

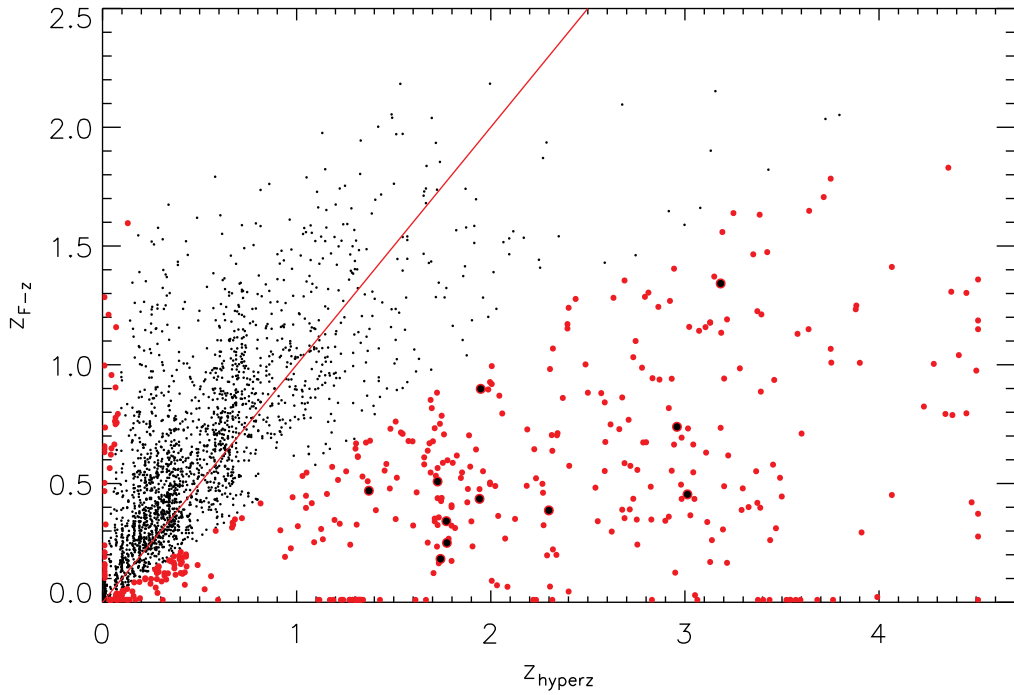


Figure 3.8: *SEP* field: comparison between redshifts computed using total optical fluxes ( $z_{F-z}$ ) and hyperz output. All the sources represented here are detected in the MIPS  $24\mu$  band, above  $0.3mJy$ . With bigger red dots, we represent the identified outliers, for which we will consider the  $z_{F-z}$  as best solution. The big black dots are the identified “apparent” outliers that we found (and for which we used the standard procedure (equation 3.7) to determine the redshift).

## Chapter 4

# Infrared–based photometric redshifts in the extended area

The optically covered area is limited to the central squared degree of the IRAC survey in the SEP field. The redshift estimated for the sources optically covered is discussed in the previous chapters. Without information in any of the optical bands, for the sources in the extended remaining area we can't compute reliable photometric redshifts. Here we describe the multiple-step method that we used to estimate an indicative value of redshift for the SPIRE detected sources in the remaining not optically covered area. We tested the technique both on the SEP field and on the Lockman field, where we can access a similar set of IR data, together with spectroscopic and photometric redshifts. Since the method described in this section is based on a particular SPIRE selection dependent relation between the IRAC fluxes and the redshifts, we limited our analysis to the SPIRE sources detected above  $10\sigma$  (51.6mJy).

The photometric redshift determination proceeds with the following three steps (justified in detail below): first, we use Hyperz (Bolzonella et al. 2000) to obtain a redshift probability function (PDF) for all sources; second, we derived an alternative estimate of the redshift using the IRAC-ch.1 flux as an indicator; finally we computed the weighted average of the two redshifts.

As previously stated, here and in the following analysis, we use the original IRAC SE-extracted fluxes, without considering the offsets calculated as described in section 3.3 and reported in table 3.3. We instead consider the offsets on the VISTA J, H and Ks bands. We made this choice since the offsets were computed fitting the Bruzual & Charlot (2003) SSP models, that do not consider the dust that could affect the IRAC bands. Here, one of the steps of the redshift computation is the fit of the empirical Polletta et al. (2007) templated SEDs that do account for the dust contribution.

### 4.1 Hyperz photometric redshifts

We computed a redshift probability curve (z-PDF) for each SPIRE detected source with  $F_{250} > 51.6\text{mJy}$  ( $10\sigma$ ), using the *hyperz* software (Bolzonella et al. 2000).

We fitted our photometric data, using the empirically derived spectral energy distributions (SED) by (Polletta et al. 2007, P07), together with 6 new templates presented in Gruppioni et al. (2008). These SEDs cover the full wavelength range from UV to the far-IR. We fitted the

SEDs to our photometric data in the following bands: J, H,  $K_S$  from VISTA, IRAC–ch1 and ch–2, WISE W3 ( $11.56\mu\text{m}$ ), MIPS–24 and  $70\mu\text{m}$ , SPIRE 250, 350 and  $500\mu\text{m}$ . We consider  $A_V$  in the range between 0.9 and 3.9, and apply reddening according to Calzetti et al. (2000).

In order to perform the fit, the errors associated to the fluxes in the different bands were not the real uncertainties derived from the photometry. They were instead selected to balance both the real associated errors and the contribution of each filter in the determination of the redshifts. The associated uncertainties have to be considered as a measure of the reliability of both the fluxes in each band and the templates used to fit the data. Moreover, some parts of a templated SED, or some color indexes are more tightly related to the real redshift. The relative importance of each of the bands in our set was empirically determined through an iterative process. In this phase, our goal is not the description of our sources through a precise SED. Instead, we are trying to estimate a reliable probability distribution function for the redshifts. Even if theoretically the two things would have to coincide, practically they are not. For example, the optical part of the best fitting SED could be completely wrong, but since it is not sampled by the data, this result is not unexpected. We will use the PDFs as described below, discarding the SEDs found through the SED fitting. The uncertainties that we associated to the data (in magnitudes) were: 0.05 for VISTA J, 0.1 for VISTA H and  $K_S$ , 0.2 for IRAC 1, 0.3 for IRAC 2, 0.4 for WISE W3, MIPS 24 and MIPS 70, 0.3 for SPIRE 250 and 350 and 0.8 for SPIRE 500. The combination of uncertainties was chosen using the Lockman field data as a test bench. In the Lockman field, we could assess a similar set of data with comparable depths. We refined our method using an iterative process. We compared, at each iteration, our redshifts with the available photometric and spectroscopic ones Rowan-Robinson et al. (2013). Finally, we applied this technique to the SEP field data, checking again the precision of our results, comparing them with the photometric redshifts that we computed as described in section 3 and with the spectroscopic redshifts from Sedgwick et al. (in prep.).

For each source, *hyperz* provides a redshift probability distribution function (PDF). The primary solution given by *hyperz* corresponds to the highest peak  $P(z_1)$  in the PDF. The existence of other probability peaks  $P(z_2)$  with a not negligible importance is however possible. We then proceeded computing the weighted mean of the two most probable solutions:

$$z = \frac{z_1 P(z_1) + z_2 P(z_2)}{P(z_1) + P(z_2)} \quad (4.1)$$

We didn't consider the solutions with null probabilities reported in the *hyperz* output. For these sources we only referred to the relation explained in section 4.2 to compute the redshifts. We usually observe well defined single-peak solutions only for bright sources at  $z < 0.5$ , where an higher number of detections in the different filters are available and with a more precise photometry. At higher redshifts, and when less filters have a detection, broader PDFs are observed, with multiple peaks. If one of the peaks is strongly dominant, the weighted mean has a limited impact on the resulting redshift. If, otherwise, multiple peaks with similar heights are present, the overall shape of the PDF better is better taken into account by the weighted mean. In Figure 4.1 we can observe three typical examples of PDFs.

The method described is mostly based on the role played by the dust in the mid and far infrared. The peak of the thermal emission is located at about  $100\mu\text{m}$  R.F. (Kirkpatrick et al. 2012) and its position is influenced by both the temperature of the dust and by the redshift of the galaxy. For this reason, a certain level of degeneracy has to be kept into account. In the mid-IR, the peak of the stellar emission is sampled by the IRAC bands and by the J,

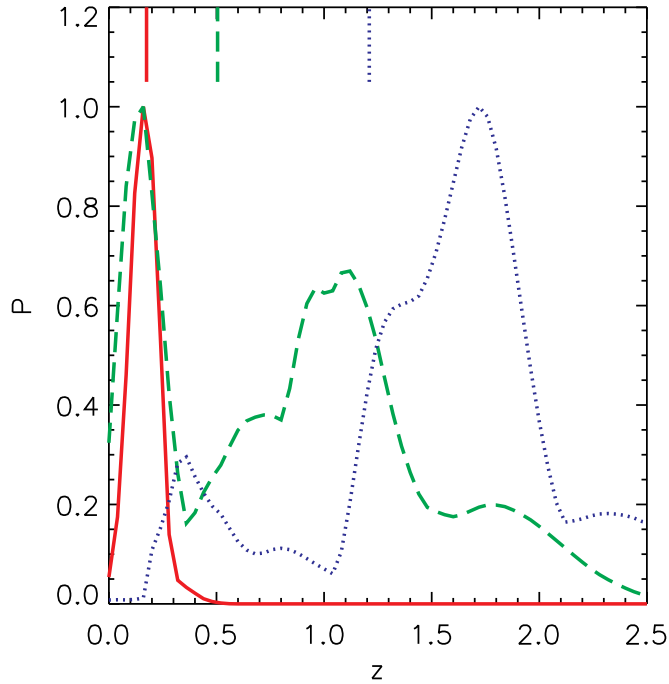


Figure 4.1: Normalized probability functions (PDFs), resulting from the  $\chi^2$  minimization procedure, for three Lockman sources. The real spectroscopic redshift values (vertical lines) are also reported. The continue red line rapresents a well defined single peak redshift solution; this is the typical PDF for  $z < 0.5$  sources, where the photometry is more precise and more bands are available. The measured spectroscopic redshift is almost coincident with the only peak of the PDF. The dashed green and pointed blue lines represent multiple peak PDFs. In these cases the first peak of the PDF doesn't correspond to the spectroscopic redshift measure. The overall shape of the probability curve has to be kept into account.

H and K VISTA bands. This adjoin information to the SED shape and then to the possible redshift. In Pearson et al. (2013), for comparison, they use only the SPIRE fluxes to constrain the position of the peak of the dust emission. Fitting these fluxes with far-IR double black body component SEDs, they obtain lower precisions, as described in section 4.3

## 4.2 IRAC1 versus $z$ relation

The redshifts calculated through the SED fitting were improved using the existing correlation between IRAC-ch1 fluxes and redshifts observed for the SPIRE selected sources (this is similar to what found in Cowie et al. 1996, for the  $K$ -band, without far-IR selection). We measured the correlation between I1 flux and redshift in the Lockman field for sources characterized by  $F_{250\mu m} > 55 \text{ mJy}$ . We exploited the same relation in the SEP field for sources with a similar cut in  $F_{250\mu m}$  ( $51.6, 10\sigma$  cut). The relation is shown in Figure 4.2, for photometric and spectroscopic redshifts, in the Lockman field (taken from Rowan-Robinson et al. 2013). The relation between IRAC fluxes and redshifts arises due to the combined effects of *first*, the selection of the galaxies in the SPIRE  $250\mu m$  channel; *second*, the observed correlation

between the stellar-mass  $M^*$  (probed by IRAC channels) and the SFR (probed by the SPIRE channels)<sup>1</sup>; *third*, the normalization dependency of the  $M^*$ -SFR relation with the redshift. In other words, selecting the sources above a fixed observed  $F_{250\mu m}$  flux, we are considering an inferior limit in luminosity  $L_{250\mu m}$  at  $\sim 250\mu m$  and then a corresponding limit in SFR, that increases with the redshift of the sources. The superior limits in luminosity  $L_{250\mu m}$  and SFR are instead physically determined. As the inferior limit, also the physical superior limit in SFR increases with the redshift, as described for example in Sargent et al. (2012). The variation of the inferior and superior SFR limits is coherent: both of them increase their values with the redshift. The consequence is that, at any redshift, given the limit in  $F_{250\mu m}$ , we can assess only a restricted range of SFRs and a correspondent limited range of  $M^*$  (for the  $M^*$ -SFR relation), that means a limited range of  $\sim 3.6\mu m$  luminosity. Since at any redshift we sample a limited range of  $\sim 3.6\mu m$  luminosity, the relation between  $F_{3.6\mu m}$  and redshift arises naturally. We computed the best-fit relation between redshift and IRAC-ch1 flux for galaxies with 152 spectroscopic and 433 accurate photometric redshifts in the Lockman field as  $\log(z) = a \times \log(I1[Jy]) + b$ , with  $a = -0.673$  and  $b = -2.859$ . The best-fit is shown in Figure 4.2 with a solid line. The galaxies in the Lockman field have similar  $F_{250\mu m}$  as our sources in the SEP, so we applied the relation to our galaxies without any changes. A similar relation can also be observed in the COSMOS field, using for the *Herschel*-PACS ( $100\mu m$ ) fluxes to select the galaxies in the far-IR. The calibration of this relation, however, does depend on the inferior limit in the far-IR and on the band used for the selection. For this reason we only exploited the Lockman data, where we could use an identical far-IR selection band with a similar inferior limit in flux.

### 4.3 Final IR-based redshifts and reliability

We computed the final IR-based redshifts as the “weighted” mean of the two estimates explained above (i.e.,  $z_{\text{final}} = W_{\chi}z_{\chi} + W_{I_1}z_{I_1}$ ). By weighted we mean that we give a different weight to the two determinations. The weights were optimized using the galaxies in the Lockman field, and are  $W_{\chi} = 0.7$  and  $W_{I_1} = 0.3$ . As it can be noted,  $W_{\chi}$  and  $W_{I_1}$  are similar to the weights  $W_1=2/3$  and  $W_2=1/3$  of equation 3.7 that we used to compute the optical-based redshifts, as described in section 3. In that case we exploited a similar technique that combined the *hyperz* outputs with an estimation of the redshift derived from the optical flux. The distribution of the redshifts computed as described in this section, for the  $250\mu m$  sources detected above  $10\sigma$  on the whole 7 square degrees, is shown in Figure 4.3. 700 on 730 SPIRE sources in the  $10\sigma$  sample are detected at  $24\mu m$ . Two of the 30 MIPS undetected sources are located in the area not covered by the MIPS survey. These two sources are detected in the WISE band at  $22\mu m$ . With a visual inspection we found that the remaining 28 sources are real IRAC and SPIRE detections with a faint or absent counterpart at  $24\mu m$ . The precision of our final IR based redshifts is reported in table 4.1. All the sources that we could use to compute the precision where MIPS detected.

In order to assess the precision of the redshifts that we computed in the SEP field, we applied the same technique, using the same photometric bands, at similar depths, in the Lockman-SWIRE field, where reliable spectroscopic and photometric redshifts are available in the revised catalog of Rowan-Robinson et al. (2013). As in the SEP field, the catalog is based on the IRAC  $3.6\mu m$  detections and the  $4.5\mu m$ , MIPS  $24\mu m$  and  $70\mu m$  fluxes are also available

---

<sup>1</sup>See for example Brinchmann et al. (2004); Noeske et al. (2007a); Daddi et al. (2007)

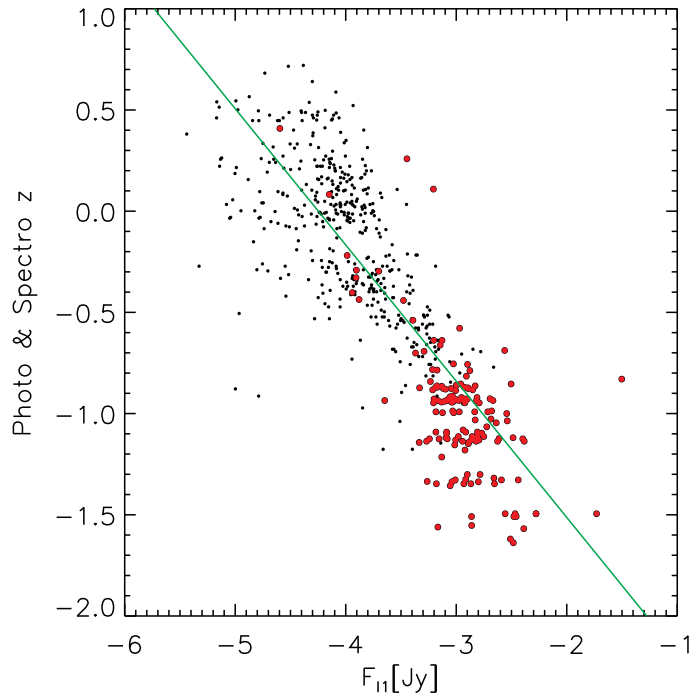


Figure 4.2: *Linear relation between IRAC 1 fluxes and redshifts as computed using the Lockman field data. The redshift values considered here are both spectroscopically (152 red dots) and photometrically (433 black points) derived (Rowan-Robinson et al. 2013).*

in the same Rowan-Robinson et al. (2013) catalog. We found the nearest SPIRE 250, 350 and  $500\mu\text{m}$  counterpart from the public cross correlated catalog for the same field (Oliver et al. 2012). Both for the Lockman and for the SEP field, the SPIRE 250 catalogs are cut at the same level ( $\sim 50\text{mJy}$ ), that correspond to about  $10\sigma$  level in SEP ( $1\sigma=5.16\text{mJy}$ ) and  $20\sigma$  in Lockman ( $1\sigma=2.72\text{mJy}$ ). In Lockman, we considered only sources with both IRAC and SPIRE detections, as we did in the SEP field. We found the nearest SWIRE (W3) and 2MASS (instead of VISTA) J, H and  $K_S$  counterpart from the all-sky public catalog (Wright et al. 2010).

In Figure ?? we show the comparison between the photometric redshifts that we computed with the technique described above and the photometric and spectroscopic redshift presented in Rowan-Robinson et al. (2013). In Figure 4.5 we show the same comparison in the SEP field. For each source, we calculated the precision  $\Delta z/(1+z)$ , where  $\Delta z$  is the difference between our redshifts and the available photometric or spectroscopic redshifts  $z$ . In table 4.1 we report the values of  $\langle \Delta z/(1+z) \rangle$ ,  $\sigma_{\Delta z/(1+z)}$ ,  $\langle |\Delta z|/(1+z) \rangle$  computed for all the three steps of the technique applied (primary solution of the SED fitting, averaged solutions and combination with the  $z$ -I1 relation). The improvement of the precision is visible when passing from the simple *hyperz* output to our final estimation, resulting from the multi-step technique described. This improvement can be noted both in the Lockman and in the SEP field. In the SEP field, the computed precision is higher than in the Lockman field. This is probably due to the presence of a deeper survey in the J, H and  $K_s$  bands in the SEP field, where we can

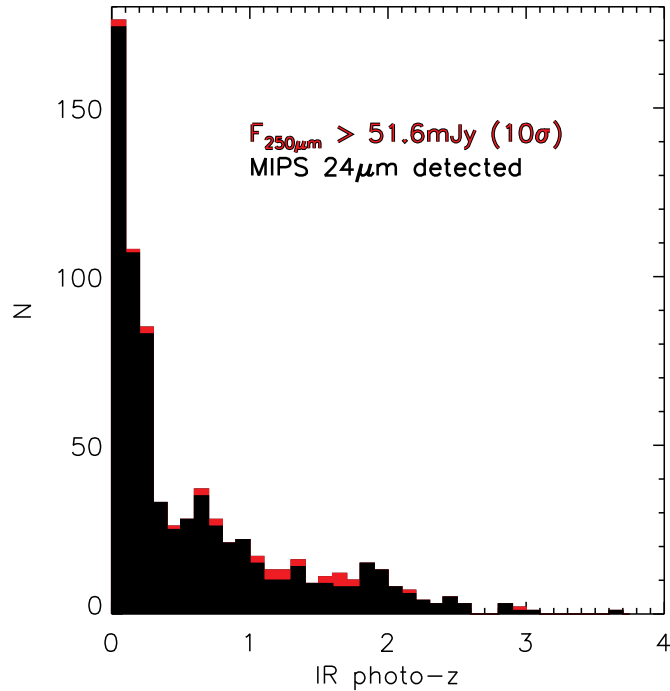


Figure 4.3: Distribution of the IR derived redshifts in the SEP field. In Black, the SPIRE sources detected also in the MIPS 24μm channel, in red the undetected. The redshifts were computed combining the results of the SED fitting and the relation between I1 fluxes and redshifts calibrated using Lockman field data.

exploit the VISTA data. The precision that we estimated for our complete sample, combining both the Lockman and the SEP data is  $\sigma\left(\frac{z-z_{\text{spec}}}{1+z_{\text{spec}}}\right)=0.08\div 0.29$ , where the first datum refers to the comparison with the spectroscopic sample, while the second one to the photometric one. Above  $z=0.5$  the estimated precision is instead  $\sigma\left(\frac{z-z_{\text{spec}}}{1+z_{\text{spec}}}\right)=0.20\div 0.38$ .

When only IR photometric data are available, other possible techniques can be used. For example, in Pearson et al. (2013) they exploit only the SPIRE fluxes to fit a set of double component black bodies. The precision  $\Delta z/(1+z)$  (RMS) obtained in that work is  $=0.26$  for sources above  $z=0.5$ .

The limits and the characteristics of our analysis on the IR-based redshifts are specified in table 4.2. These characteristics and limits can be compared with those in table 3.4 and relative to the optical-based redshifts, computed in the optically covered area (1 deg<sup>2</sup>).

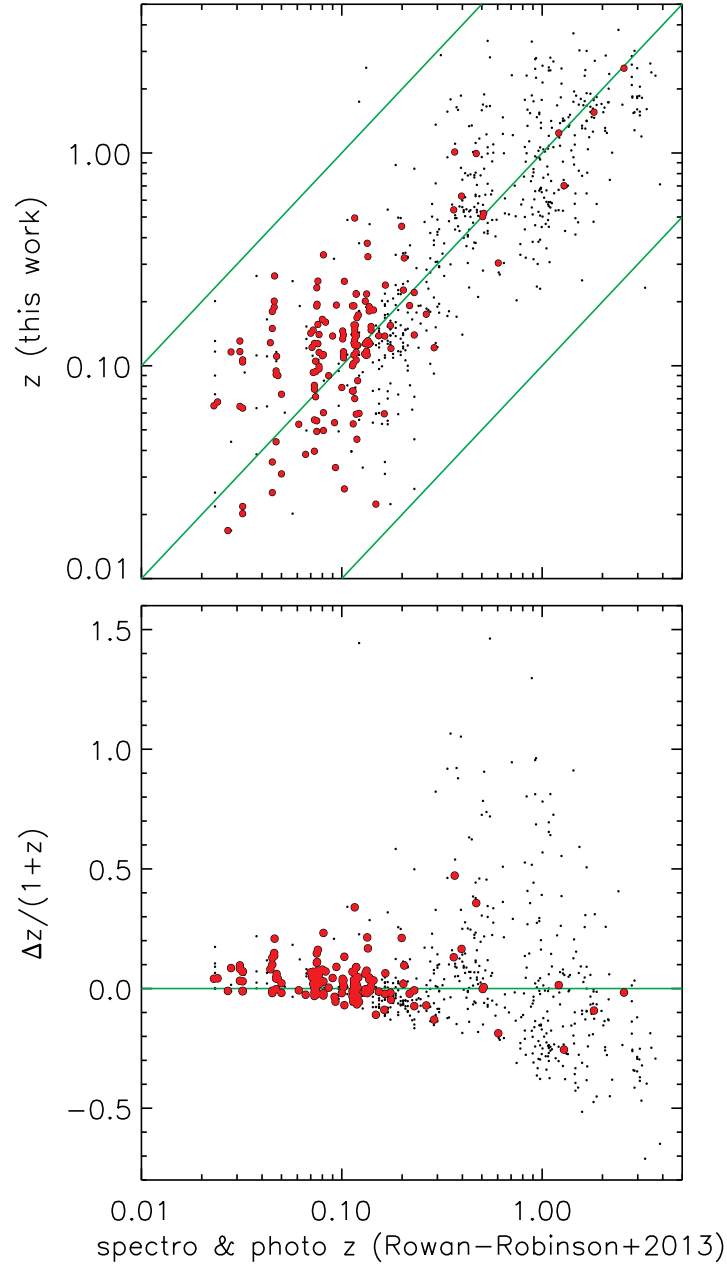


Figure 4.4: *Redshift precision in the Lockman field. Top panel: comparison of the redshifts computed combining the SED fitting and the  $I1$ - $z$  relation with the photometric (black points) and spectroscopic (red crosses) redshifts from Rowan-Robinson et al. (2013). The  $\pm 1$  dex levels are reported in green. Low panel: precision  $\Delta z/(1+z)$  for our photometric redshifts, when compared with photometric (black points) and spectroscopic (red crosses) redshifts from Rowan-Robinson et al. (2013).*

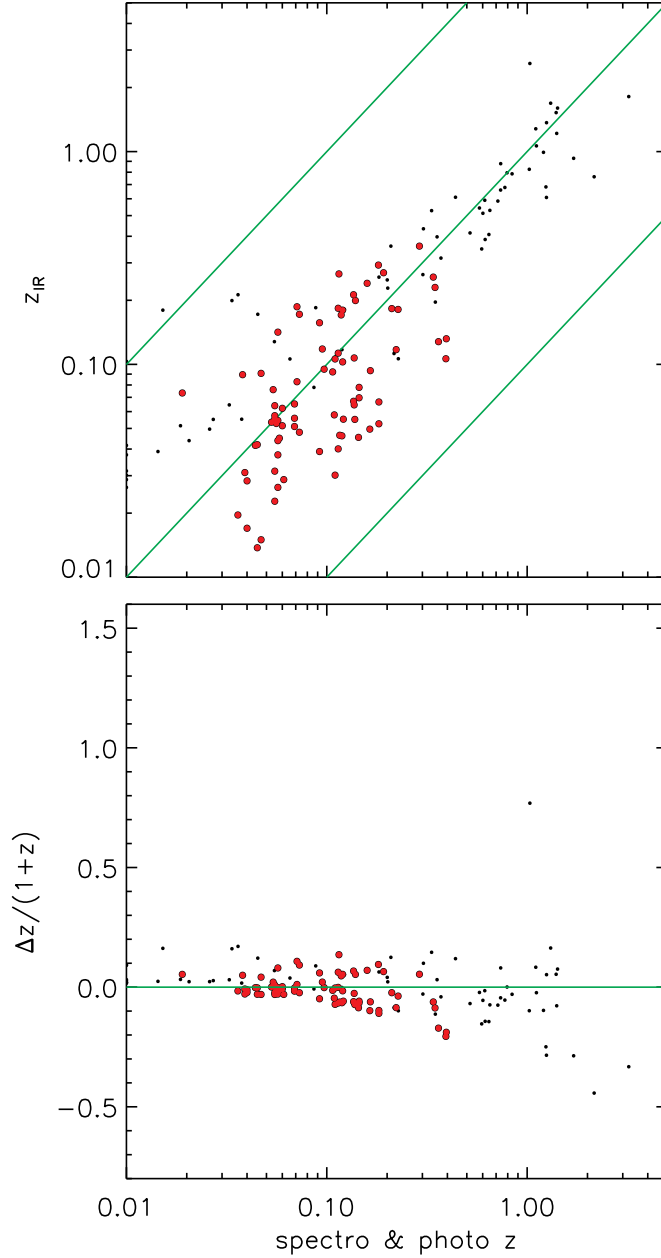


Figure 4.5: Redshift precision in the SEP field. **Top panel:** comparison of the redshifts computed combining the SED fitting and the  $I1-z$  relation with the photometric (black points) and spectroscopic (red circles) redshifts. The photometric redshifts used for the comparison are the optically derived estimations described in section 3, while the spectroscopic redshifts are from Sedgwick et al. in preparation. The  $\pm 1$  dex levels are reported in green. **Low panel:** precision  $\Delta z/(1+z)$  for our final redshift, when compared with photometric (black points) and spectroscopic (red circles) redshifts from Rowan-Robinson et al. (2013).

Method	$\langle \frac{z-z_{\text{spec}}}{1+z_{\text{spec}}} \rangle$ (median)	$\langle  \frac{z-z_{\text{spec}}}{1+z_{\text{spec}}}  \rangle$	$\sigma \left( \frac{z-z_{\text{spec}}}{1+z_{\text{spec}}} \right)$
All – Lockman			
Hyperz (1 <sup>st</sup> PDF peak)	-0.032(535) ÷ 0.005(134)	0.08(535) ÷ 0.23(134)	0.36(535) ÷ 0.14(134)
Weighted PDF peaks	-0.019(535) ÷ 0.014(134)	0.21(535) ÷ 0.081(134)	0.34(535) ÷ 0.12(134)
<b>Final <math>z_{\text{IR}}</math></b>	<b>-0.012(548) ÷ 0.018(151)</b>	<b>0.19(548) ÷ 0.06(151)</b>	<b>0.31(548) ÷ 0.09(151)</b>
$z > 0.5$ – Lockman			
Hyperz (1 <sup>st</sup> PDF peak)	0.13(236) ÷ 0.36(10)	0.33(236) ÷ 0.36(10)	0.44(236) ÷ 0.29(10)
Weighted PDF peaks	0.086(284) ÷ 0.206(12)	0.31(284) ÷ 0.24(12)	0.42(284) ÷ 0.20(12)
<b>Final <math>z_{\text{IR}}</math></b>	<b>0.042(276) ÷ 0.014(10)</b>	<b>0.29(276) ÷ 0.15(10)</b>	<b>0.40(276) ÷ 0.20(10)</b>
All – SEP			
Hyperz (1 <sup>st</sup> PDF peak)	-0.039(46) ÷ 0.019(25)	0.19(46) ÷ 0.33(25)	0.29(46) ÷ 0.50(25)
Weighted PDF peaks	-0.021(38) ÷ -0.036(14)	0.13(38) ÷ 0.06(14)	0.19(38) ÷ 0.06(14)
<b>Final <math>z_{\text{IR}}</math></b>	<b>0.021(67) ÷ -0.013(79)</b>	<b>0.10(67) ÷ 0.05(79)</b>	<b>0.15(67) ÷ 0.06(79)</b>
$z > 0.5$ – SEP			
Hyperz (1 <sup>st</sup> PDF peak)	0.026(22) ÷ 0.79(8)	0.24(22) ÷ 0.88(8)	0.36(22) ÷ 0.43(8)
Weighted PDF peaks	-0.006(21) ÷ -(0)	0.16(21) ÷ -(0)	0.23(21) ÷ -(0)
<b>Final <math>z_{\text{IR}}</math></b>	<b>-0.030(27) ÷ -(0)</b>	<b>0.14(27) ÷ -(0)</b>	<b>0.21(27) ÷ -(0)</b>
Average Lockman and SEP (All)			
<b>Final <math>z_{\text{IR}}</math></b>	<b>-0,008(615) ÷ 0,007(230)</b>	<b>0,18(615) ÷ 0.06(230)</b>	<b>0,29(615) ÷ 0,08(230)</b>
Average Lockman and SEP ( $z > 0.5$ )			
<b>Final <math>z_{\text{IR}}</math></b>	<b>0,036(304) ÷ 0.014(10)</b>	<b>0,28(304) ÷ 0.15(10)</b>	<b>0,38(304) ÷ 0.20(10)</b>
NOTE: The uncertainties here reported can be applied to the 730 IRAC-1 detected sources in the SEP field, with a SPIRE 250 $\mu\text{m}$ detection above the 10 $\sigma$ level (51.6mJy).			

Table 4.1: Redshifts precision computed in the Lockman field exploiting the different techniques described and used as consecutive steps to compute our final redshifts using the IR bands (Final  $z_{\text{IR}}$ ). We report the precision computed for the sources with photometric and with spectroscopic redshifts (respectively before and after the ÷ symbol). The precision is computed on the whole sample and for the sources with redshift (our)  $z > 0.5$  when present. The expected redshift reliability in the SEP field is highlighted. The number of sources available for each comparison is shown in parenthesis. The improvement of the precision is visible, from the first technique to the final  $z$ , both in the whole sample and in the  $z > 0.5$  sample, in the Lockman and in the SEP field.

AREA COVERED	$\sim 7\text{deg}^2$
OPTICAL bands	not necessary, not used
J-VISTA	not necessary, used in the SED fitting (485/730 sources)
H-VISTA	not necessary, used in the SED fitting (486/730 sources)
K-VISTA	not necessary, used in the SED fitting (390/730 sources)
IRAC 1 (3.6 $\mu\text{m}$ )	required in both SED fitting and $F_{\text{IR}}-z$ relation
IRAC 2 (4.5 $\mu\text{m}$ )	not necessary, used in the SED fitting (719/730 sources)
WISE W3 (11 $\mu\text{m}$ )	not necessary, used in the SED fitting (654/730 sources)
MIPS 24 $\mu\text{m}$	not necessary, used in the SED fitting (700/730 sources)
MIPS 70 $\mu\text{m}$	not necessary, used in the SED fitting (345/730 sources)
SPIRE 250 $\mu\text{m}$	required, with $F_{250} > 51.6\text{mJy}$ (10 $\sigma$ ), in both SED fitting and $F_{\text{IR}}-z$ relation
SPIRE 350 $\mu\text{m}$	not necessary, used in the SED fitting (729/730 sources)
SPIRE 500 $\mu\text{m}$	not necessary, used in the SED fitting (716/730 sources)
This table refers to the 730 IRAC-1 detected sources, with a SPIRE 250 $\mu\text{m}$ detection above the 10 $\sigma$ level (51.6mJy).	

Table 4.2: Limits and characteristics of the analysis relative to the IR-based photometric redshifts. This table can be compared with the table 3.4 referring to the optical-based redshifts.



## Chapter 5

# Multiwavelength analysis through SED fitting

### 5.1 Sample selection

The goal of our analysis is to measure the contribution of star formation and AGN activity to the galaxy IR spectra. We also want to study the two mechanisms in relation with the main sequence of star forming galaxies. In order to perform our multiwavelength analysis, and in particular to compute reliable physical quantities using the observed fluxes, we selected a sample of sources from our multiwavelength catalog described in Chapter 2. The selection applied is quite complex and the justification of each single criterium is reported here below. Basically what we want to obtain is a sample of galaxies with reliable photometric redshifts and with a good spectral coverage, especially at those wavelengths dominated or interested by the phenomena that we want to study: stellar masses (optical), AGN activity (mid-IR) and SFR (far-IR).

In Section 3 and 4 we computed photometric redshifts for two different samples of sources in the SEP field. We made those computations combining more redshift indicators (fluxes and colors) but, in both cases, involving an SED fitting technique. In the central optically covered area, we computed the best fitting SEDs using only the optical-to-IRAC photometric fluxes and using SEDs derived from the Bruzual & Charlot (2003) single stellar population models (SSP). These last ones describe only the stellar emission and they are very useful when computing redshifts and stellar masses. However, in order to describe photometric data at wavelengths longer than those of the IRAC channels 1 and 2 (i.e.  $\lambda \gtrsim 5\mu\text{m}$ ) it becomes necessary to keep into consideration the dust emission due to star formation activity (SF) and/or to the dusty torus surrounding the central regions of active galactic nuclei (AGNs). This can be achieved, for example, using empirical templates like those described in Polletta et al. (2007) and a fitting code like *hyperz* (Bolzonella et al. 2000), or considering independent templates for the stellar and the dusty components, and a more complex code like *Magphys* (da Cunha et al. 2008). In any case, finding a SED able to represent the real source spectra, from the u band to the far-IR, requires both a reliable redshift value and a good spectral coverage in terms of number of photometric data per units of  $\lambda$ . This is particularly important for those spectral regions more influenced by the physical phenomena under analysis.

While the deep MIPS and SPIRE observations cover the whole IRAC-SEP field, the important optical observations cover only the central square degree (see Figure 2.2). In the

analysis described in Chapters 3 and 4, we computed reliable redshifts for both the optically covered and for the extended (not optically covered) area, as demonstrated by the precisions reported in Tables 3.5 and 4.1. For the IR based redshifts, the importance of the VISTA J, H and Ks bands, together with the two IRAC channels plays an important role.

A good optical coverage still remains fundamental when computing stellar masses ( $M^*$ ), dust extinctions ( $A_V$ ) and the SED in general. Indeed, we computed reliable IR-based redshift values, using a combination of different techniques, but the SED fitting alone, without optical data, would not give neither precise redshift estimates (see “Hyperz 1<sup>st</sup> PDF peak” precisions in Table 4.1) nor, consequently, a good SED description. This limits the possibility of a precise multiwavelength analysis on single sources to the central optically covered area of the IRAC-SEP field.

In order to apply the combined technique that we used to compute optical-based redshifts, some requirements are needed. These are summarized in Table 3.4. First of all, at least 3 optical detections are necessary (among the CTIO-u, B, V, I, VST-i, g, z and WFI- $R_C$  bands). Using less than 3 optical bands would compromise the reliability of the redshift estimation. Even having an independent and precise redshift estimation (i.e. spectroscopic), but a poor optical coverage, as stated before, the reliabilities of SEDs, stellar masses and extinctions would be very low. Three optical bands in particular are very important for our redshift estimations. In our analysis, fluxes in the WFI- $R_C$ , VST-i and VST-z bands are combined as described in Section 3.4 in order to obtain a redshift tracer ( $F_{i,r,z}$ ). This further restricts our study to the sources with at least a detection in one of these “special” bands. This requirement is not so restrictive and does not reduce significantly the number of sources, since all the three bands are located close to the stellar emission peak, with a good depth and covering the whole optical area. When a source is detected in at least 3 optical bands, there is an high probability that one of them is among the “special” three. In our multiwavelength catalog, without considering other constraints, this probability is 99.7% (24914 on a total of 24989 sources with at least three optical detections). In order to use the combination of WFI- $R_C$ , VST-i and VST-z bands as a redshift tracer, high flux sources have to be removed, since our method is valid through  $F_{R,i,z} < 3.46\text{mJy}$  (see equation 3.6). This limit, again, is not highly restrictive and it allows to remove stars and very local and possibly saturated galaxies. In our catalog, 712 upon 24989 (2.8%) are removed for this only restriction (1.5% among the SPIRE selected). For the redshift computation, our combined technique requires a MIPS-24 $\mu\text{m}$  detection above 0.3mJy. This constraint allows to limit the dispersion of the Flux-redshift relation that we used (see Figure 3.1). In our original catalog, among 8500 sources with both a MIPS and SPIRE detection, only 5.9% of them have a MIPS flux smaller than 0.3mJy.

The previous restrictions were needed in order to obtain precise redshift estimations, as described in Chapter 3. Our analysis is however limited to an even smaller sample since the MIPS and SPIRE detections are fundamental to constrain the peak of the dust emission. For this reason we included only the sources detected in both these two bands (with  $F_{24\mu\text{m}} > 0.3\text{mJy}$ ). Moreover, since we want to study the infrared AGN and star formation properties, constraining the spectrum at the mid-IR wavelengths (i.e. where the maximum AGN torus emission is located) becomes fundamental. This can be done using the *Akari*-IRC and the WISE bands, but for the reasons explained below, we didn’t limit our analysis to *Akari* or WISE detected sources. The whole sample is however covered by the *Akari* or WISE surveys. In order to avoid redundancies with the deeper IRAC bands, we do not consider the *Akari*-N3 and N4 bands and the *WISE*-W1 and W2 filters. For the same reason, we do not consider

*Akari*-L24 and *WISE*-W4, since we expect higher precisions using the MIPS detections at  $24\mu\text{m}$ . For the other mid-IR bands, the intersection between the *Akari* coverage and the optically covered area is even smaller than the central square degree (see Figure 2.2) while, in the other hand, the *WISE* bands cover the whole field with a depth and a detection rate similar or higher than that reached by the *Akari* bands (see Table 2.7). In our selection we included all the sources in the optically covered area since the lack in the *Akari* mid-IR coverage ( $7$ ,  $11$  and  $15\mu\text{m}$ ) is compensated by the *WISE* W3 band ( $11\mu\text{m}$ ). In this area, sources covered by the mid-IR, among  $4.5$  and  $24\mu\text{m}$ , but undetected in any of these bands, are also included in our analysis. We made this choice since in this spectral region the AGN IR emission is particularly important. If the mid-IR undetected sources are not included in the analysis, this would create a bias, since the sources with a prominent AGN emission would be considered with an higher probability in our sample. On the other hand, the AGN emission for these sources is not well constrained like for the mid-IR detected. After applying all the criteria above, this problem is however limited to 64 sources on a total of 916 ( $\sim 7\%$ ).

After applying the SED fitting technique, we rejected 71 unreliable fits, mostly presenting a bad agreement between fluxes and the best fit SED found. From this sample of 845 sources we further selected 826 galaxies with a redshift  $z < 1.5$ .

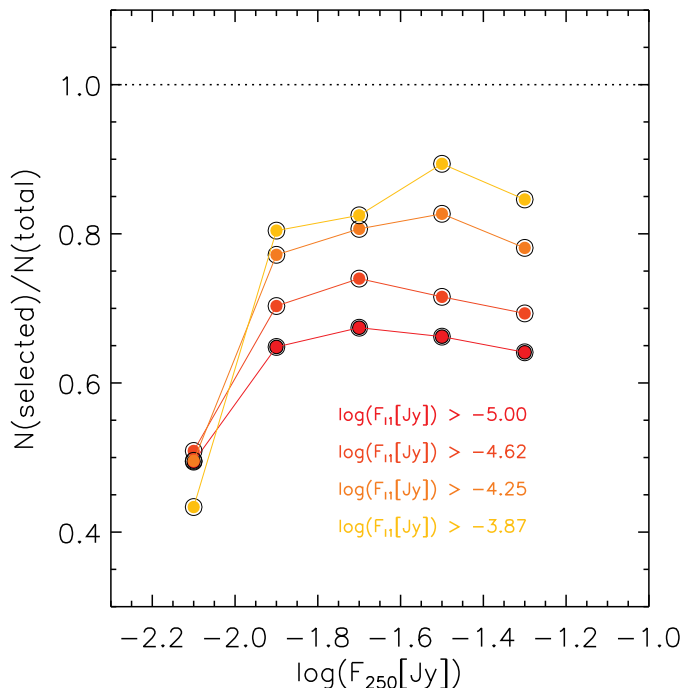


Figure 5.1: Fraction of MIPS+SPIRE sources considered in our analysis as a function of both the SPIRE flux and the IRAC-1 minimum flux. In each flux bin, above  $F_{250} \approx 10\mu\text{Jy}$ , and above the IRAC-1 90% completeness level ( $\sim 10^{-5}\text{Jy}$ ), this fraction is greater than the 65–70% and increases with the IRAC minimum flux.

Every selection that we applied corresponds to a selection of sources on the basis of their physical properties. For example, given that the stellar emission has a peak in correspondence of the IRAC wavelengths, the selection based on the IRAC flux corresponds to a stellar mass

$M^*$  selection, i.e. at a given redshift, only the most stellar-massive galaxies are observed. For similar reasons, the SPIRE selection corresponds to a selection in SFR, given that the maximum far-IR emission due to the dust is located at these wavelength. In this sense, the SPIRE and IRAC selections independently select different kind of physical mechanisms. As for the IRAC bands, the optical selection that we applied can be assimilated to a selection in  $M^*$ , while the required MIPS-24 $\mu$ m detection correspond to a SFR selection, as for the SPIRE ones. In Figure 5.1, we show the fraction of MIPS+SPIRE sources considered in our sample as a function of both the SPIRE flux and the IRAC-1 minimum flux. In each flux bin, above  $F_{250} \sim 10 \mu\text{Jy}$ , and above the IRAC-1 90% completeness level ( $\sim 10^{-5} \text{Jy}$ ), this fraction is greater than the 65-70% and increases with the IRAC minimum flux.

From our multiwavelength catalog (see Section 2) we selected a sample of sources using the set of criteria described above. Here below we summarize the selections criteria applied and the number of sources entering in the data sample after each selection.

- IRAC detections: **255232**
- In the optically covered area: **41563**
- With a MIPS-24 $\mu$ m detection ( $F_{24} > 0.3 \text{mJy}$ ): **3376**
- With a SPIRE detection: **1429**
- With at least three optical detections: **939**
- With one detection among WFI-R, VST-i and VST-z bands: **934**
- With  $F_{r,i,z} < 3.46 \text{mJy}$ : **916**
- With a reliable SED fit: **845**

Upon the 1429 sources with a detection IRAC+MIPS+SPIRE, 934 (65%) are optically selected. With the following selections, bright ( $F_{r,i,z} < 3.46 \text{mJy}$ ) or random sources (bad fits) are eliminated from the sample and do not affect the completeness of our sample.

## 5.2 SED fitting

We performed an SED-fitting analysis on the 845 sources of our sample. We used the photometric redshifts computed as described in section 3 and the spectroscopic ones (Sedgwick et al. in preparation) when available. A total of 112 spectroscopic redshifts are available below  $z=1.5$ . We fit our photometric data using a version of the original MAGPHYS code 4 (DC08 da Cunha et al. 2008), modified as described in (BE13 Berta et al. 2013). For our analysis, the main advantage of using the BE13 version is the possibility to consider the contribution of an AGN component to the total emission. In this section we describe the properties of the two codes and how they perform an SED fitting technique. We also describe the particular set of parameters used for our elaboration.

### 5.2.1 The DC08 MAGPHYS version

The DC08 MAGPHYS version allows to fit photometric data from the UV to the far-IR and sub-mm wavelengths. In general, the approach is similar to that adopted by other similar codes in literature: the differences between the photometric data and the modelized SEDs are used to compute the  $\chi^2$  value. The smaller  $\chi^2$  corresponds to the best fit. However, differently from other codes (e.g. *hyperz* Bolzonella et al. 2000), MAGPHYS is able to perform a physically autoconsistent fit of the stellar emission in the optical and the dust emission in the FIR. In particular, the energy absorbed in the optical/UV is directly converted into IR emission.

The best fit to the integrated stellar emission is found among the library of template models of (BC03 Bruzual & Charlot 2003). The SEDs derived from BC03 models, are the result of the integrated emission of single stellar populations (SSPs) of stars with ages between  $10^5$  and  $10^{10}$  yrs and with a Chabrier (2003) IMF (see equations 1.4 and 1.5). Different star formation histories (SFH), dust contents and metallicities are considered in order to cover the whole parameters' space.

Beside the stellar emission, one important quantity is represented by the dust extinction. In an unresolved galaxy like those in our sample, this is the result of the cumulative absorption due to molecular clouds and to the diffuse interstellar medium (ISM). The extinction model applied is in the form of Charlot & Fall (2000). The extinction curve and the total energy absorbed represent an ideal “bridge” connecting the modelization of the UV/optical wavelength range, with the modelization of the far-IR spectrum, where the same reprocessed energy is emitted.

The models describing the dust emission in the mid and far-IR keep into account three main components: the PAH emission (3–12 $\mu$ m), the mid-IR continuum, due to an hot dust component (130–250 K), and the far-IR black body like component, due to warm (30–60 K) and cold (15–25 K) dust components.

Before the fit, MAGPHYS builds up a large library of spectral models. Given the large set of parameters and the grid of possible values that they can assume, about  $\sim 10^4 \div 10^5$  models are built for the stellar emission and a similar amount for the dust emission. At the end the physical constraint regarding the UV/optical absorption and the IR re-emission, limits the real amount of models used to a  $\sim 30\%$  of the original ones (i.e.  $\sim 10^9$  models). Only at this point, each stars+dust spectral model is compared to the observational data in order to find the best fitting SED. Using a Bayesian approach, MAGPHYS also computes a probability distribution function (PDF) for each single parameter considered in the fit. This allows to assess the reliability of the parameters resulting from the fit.

The original MAGPHYS version described so far does not consider any AGN contribution to the total emission. The AGN emission can however contribute in a significative way to the total emission of the galaxy. This is indeed what we want estimate with our analysis. For this reason, we used a modified version of the original MAGPHYS version able to account for this additional component

### 5.2.2 The BE13 MAGPHYS version

Differently from the original MAGPHYS code, **the BE13 MAGPHYS version** does consider the AGN contribution to the total emission. Also the normalization approach is modified in this MAGPHYS version: in order to find the best AGN description in the optical range,

the best fit to the stellar emission is not found before the fit of the IR. On the contrary, the stellar emission is free to vary in the range of possible values together with the additional AGN emission. Again, the UV/optical absorption is considered to compute the IR emission, but this time, the additive AGN torus emission in the mid and far-IR is also considered.

The AGN spectral models are taken from the Fritz et al. (2006); Feltre et al. (2012) libraries. The complete library includes  $\sim 2400$  models that consider ten different lines of sight from face-on to edge-on inclinations. The spectral emission includes both the contribution from the central engine and the dusty torus. The accretion disk optical/UV emission is modeled using a broken power law:

$$\lambda L_{\lambda} \propto \lambda^{\alpha} \quad (5.1)$$

with  $\alpha=1.2$  between  $\lambda = 0.001\mu\text{m}$  and  $0.03\mu\text{m}$  (Hubeny et al. 2000),  $\alpha=0$  between  $0.03\mu\text{m}$  and  $0.125\mu\text{m}$  (Zheng et al. 1997), and  $\alpha=-1$  between  $0.125\mu\text{m}$  and  $20\mu\text{m}$  (Hatziminaoglou et al. 2008). In the far-IR wavelengths, the dust emission is modeled through a black body emission in the Rayleigh-Jeans regime. The torus models are identified by six different parameters: 1) ratio between the physical inner and the outer radi ( $R_{\text{out}}/R_{\text{in}}$ ), 2) opening angle  $\Theta$ , 3)  $9.7\mu\text{m}$  optical depth in the equatorial plane ( $\tau_{9.7}$ ), 4) radial slope of the density profile ( $\beta$ ) 5) height slope of the density profile ( $\gamma$ ) 6) inclination with the line of sight ( $\theta$ ). Each AGN model is univocally associated to a bolometric correction that allow to compute, from the 1-1000 $\mu\text{m}$  emission, the torus unprocessed bolometric luminosity due to the accretion disk ( $L_{\text{acc}}$ ). This luminosity is not really bolometric, since it accounts for the energy emitted by the central engine in the range between  $10^{-3}$  to  $10^3\mu\text{m}$ , corresponding to  $10^{-1}$  to  $10^{-7}$  KeV. This means that the X-ray emission is considered negligible in terms of fraction of energy emitted, accounting for the  $\sim 4\%$  of the total budget. This assumption relies on the large bolometric correction needed to convert X-ray emission to bolometric luminosity ( $20\div 30$ ) found in literature (Risaliti & Elvis 2004; Pozzi et al. 2007; Hopkins et al. 2007b; Vasudevan & Fabian 2009; Lusso et al. 2012). The bolometric correction derives from the radiative transfer in a smooth dusty structure irradiated by the accretion disk. The importance of the accretion disk bolometric luminosity,  $L_{\text{acc}}$ , is that it can be directly related to the black hole accretion rate (BHAR).

As stated before, the original DC08 MAGPHYS version uses a library of  $\sim 10^9$  models and an high resolution in the parameters variability. The SED fitting technique is then highly time consuming, especially when the additional AGN component is adjoined as in the BE13 version. For this reason, similarly to what is done in Delvecchio et al. (2014), we use the restricted grid of models and parameters described in Berta et al. (2013). The reduced library uniformly spans the original parameters' grid reducing its resolution without introducing biases. Some extreme parameters are also eliminated from the grid of possibilities: the largest  $9.7\mu\text{m}$  optical depth  $\tau_{9.7}$  is rejected (Pier & Krolik 1992), and the highest  $R_{\text{out}}/R_{\text{in}}$  values are also eliminated since no evidence is found for the existence of such geometries Williamson et al. (2002); Tristram et al. (2007, 2009). With the reduced library, only  $10^3$  stellar and  $10^3$  dust models are considered. This limits the possibilities to  $10^6$ , with the further reduction to the 30% of this number when the physical constraint on the energy balance is considered. As demonstrated in Delvecchio et al. (2014) the results obtained using the complete and the reduced library are self-consistent. For the AGN torus, we used a parameters' grid similar to that used in (Hatziminaoglou et al. 2008, 2009; Pozzi et al. 2012; Delvecchio et al. 2014) and summarized in table 5.1. The other parameters considered in the SEF fitting are summarized in table 5.2

Parameter	range	description
$R_{\text{out}}/R_{\text{in}}$	10 ÷ 100	Ratio between inner and outer radii of the dusty torus
$\Theta$	40° ÷ 140°	Dusty torus opening angle
$\tau_{9.7}$	0.1 ÷ 6	Optical depth at 9.7 $\mu\text{m}$
$\beta$	-1 ÷ -0.5	Radial slope of density profile
$\gamma$	0 ÷ 6	Height slope of density profile
$\theta$	0° ÷ 90°	Torus inclination

Table 5.1: List of parameters correspondent to the different torus SED models used in the SED fitting procedure performed with the Berta et al. (2013) version of MAGPHYS.

MAGPHYS main elaboration	
Parameter	range or value
bands used	CTIO-u, B, V, I, WFI- $R_C$ , VST-g, i, z, VISTA-J, H, Ks, IRAC-1, 2, AKARI-S7, S11, L15, WISE-W3 (11 $\mu\text{m}$ ), MIPS-24, 70, SPIRE-250, 350, 350
Models	BC03
IMF	Chabrier (2003)
Extinction Law	Charlot & Fall (2000)

Table 5.2: Parameters and models used for the MAGPHYS elaboration. For the parameters specific of the torus models, refer to Table 5.1.

### 5.3 Resulting SEDs, physical quantities and reliabilities

In this section we briefly summarize the physical quantities computed through the the SED fitting technique described in section 5.2. We also compute the reliabilities of some crucial physical parameters used in our analysis, such as the stellar mass  $M^*$  and the AGN fraction (i.e. fraction of luminosity due to the AGN) at different wavelengths. For each physical parameter, a probability distribution function (PDF) is computed. In our analysis, we considered the 50% percentiles of these distributions. This is different from considering the value corresponding to the peak of the PDF. In particular, the SED resulting from the fit corresponds to this peak of probability, while the 50% percentile can even correspond to another SED model, although not too different.

#### 5.3.1 SEDs

As explained when describing the BE13 version of the MAGPHYS code, the SEDs resulting from the  $\chi^2$  minimization are the sum of three different components considered separately but with a physical auto-consistent treatment of the energetic balance. The stellar emission dominates the optical wavelengths, whereas the AGNs' dusty tori are responsible for the enhanced mid-IR emission. The combined emission from star forming regions and interstellar medium heated by the star formation referred as "SF" is predominant in the mid and far-IR. For both the AGN and the SF, the absorbed UV and optical light is re-emitted at longer wavelengths. In figures ?? we report six random examples of normal star forming galaxies requiring an additive AGN component or without AGN. In figures from 5.22 to 5.28 we report the SEDs of the identified extreme starburst galaxies in our sample. In these figures, beside

the total emission (black line), the following components are represented: unobscured and obscured stellar emission (blue and orange), AGN emission (green), SF dust emission (cyan) and obscured stellar plus SF emission without AGN component (red).

### 5.3.2 AGN fraction

In our analysis, the AGN fraction ( $f_{\text{AGN}}^{\lambda}$ ) represents the contribution of the AGN to the total luminosity, in a given rest frame wavelength range. In this sense, it has not to be confused with the number of AGN dominated systems at a given luminosity, or SFR. We computed  $f_{\text{AGN}}^{\lambda}$  in 6 bands:  $1\div 2.5\mu\text{m}$ ,  $2.5\div 5\mu\text{m}$ ,  $5\div 10\mu\text{m}$ ,  $10\div 20\mu\text{m}$ ,  $20\div 40\mu\text{m}$ ,  $8\div 1000\mu\text{m}$ . We refer to this last band as “bolometric”. The AGN fraction does not derive from the computation on the best fitting SED components (smallest  $\chi^2$ ), but from the 50% percentile of the probability distribution function (PDF). From the same PDF we derive the AGN fraction uncertainty. In Figure 5.3 and 5.4 we report the precision computed for the calculated AGN fractions. We report the same plot in a linear and in a logarithmic scale in order to highlight the different regimes (above and below 10% of AGN contribution). In the figures, the superior and inferior limits of the error bars correspond to the 75% and the 25% percentiles of the PDFs. We also computed the average values of the superior and inferior error bar limits in AGN fractions bins of width 0.1 (red lines), together with the 25% and 75% percentiles of these values (green lines).

Before going on, it is necessary to clarify that the AGN fraction computed quantifies the relative importance of one mechanism on another. In particular, in all the longer wavelength ranges analyzed ( $\lambda > 5\mu\text{m}$ ), we are considering the relative importance of AGN and star formation. On the other side, at shorter wavelengths ( $1\text{--}5\mu\text{m}$ ), the SF emission become secondary and the light emitted by stars and AGNs dominate the spectrum. In this range, a measure of the AGN fraction quantify the importance of the AGN with respect to (mostly) stellar emission.

### 5.3.3 AGN fraction and the Fadda & Rodighiero (2014) diagnostic

Using a diagram similar to that described in Fadda & Rodighiero (2014), hereafter FR14, we compare our resulting AGN fractions with this dichotomic diagnostic (AGN/other galaxies). The original FR14 diagnostic diagram, similarly to other diagnostic methods presented in literature (e.g. Donley et al. 2012; Lacy et al. 2007), allows to separate AGN dominated systems from other kind of galaxies, using flux ratios at different bands. Given the strong contribution of AGNs to the mid-IR, the IRAC and MIPS bands ( $3.6\text{--}8\mu\text{m}$ , and  $24\mu\text{m}$ ) are usually the most commonly used since they sample that part of the spectrum where the AGN torus emission begin to dominate. However, at the same wavelengths, the highly variable PAH and Silicate emission features also contribute to the total spectrum making difficult to disentangle the AGN from the SF contribution. Moreover, these methods are calibrated using galaxy templates (Polletta et al. 2007, like those of ). This is a major problem since in some areas of these color-color plots, even the original SEDs of AGNs and starbursts are superimposed (Rodighiero et al. 2007). The innovative FR14 diagnostic method overcome these problems summing up mid-IR fluxes before inserting them in a color-color diagram. This is in principle similar to use broader mid-IR filters, less sensible to spectral variabilities than single photometric bands. We used a FR14-type diagnostic diagram (Rodighiero in preparation.) calibrated using Polletta et al. (2007) templates to assess the consistency of

the two methods. The diagnostic calibration is shown in Figure 5.5. The photometric bands involved are the *Akari* N3, N4, S7, L15 and MIPS 24 and different kind of sources can be distinguished in the plane  $\log[(F_{24} + F_{L15})/F_{S7}]$  versus  $\log(F_{N4}/F_{N3})$ .

The comparison between our SED fitting results and the diagnostic method described is shown in Figure 5.6. There, we compare the AGN fraction derived from the SED fitting technique with the positions in the color–color plot resulting from the sources’ fluxes. The comparison is made for all the wavelength ranges in which we computed the AGN fraction:  $1\mu\text{m}\div 2.5\mu\text{m}$ ,  $2.5\mu\text{m}\div 5\mu\text{m}$ ,  $5\mu\text{m}\div 10\mu\text{m}$ ,  $10\mu\text{m}\div 20\mu\text{m}$ ,  $20\mu\text{m}\div 40\mu\text{m}$  and  $8\mu\text{m}\div 1000\mu\text{m}$ . It can be observed that, apart for some contamination, indeed the most AGN dominated sources preferentially occupy the AGN area of the color–color diagnostic diagram. This happens in all the wavelengths ranges considered. The number of sources with all the *Akari* detections needed to be inserted in the diagnostic plot is limited to a small amount. In order to increase this number, when possible, we substituted scaled fluxes computed in other bands close, in wavelength, to the original wavelengths. In particular, when *Akari* N3 or N4 are not present, we use IRAC–1 and 2, while if *Akari* L15 is absent, we use the scaled *Akari* S11 or the WISE W3 band ( $11\mu\text{m}$ ). These substitutions are highlighted in the plots of Figure 5.6 using a green exterior circle instead than the normal black.

### 5.3.4 AGN fraction evolution

We analyzed the evolution of the AGN fraction with redshift. In this particular case we do not limit our study to  $z < 1.5$ . In Figure 5.7 we report the total bolometric ( $8\text{--}1000\mu\text{m}$ ) luminosity distribution, with a color/dimension codification of the AGN fraction computed in the wavelength ranges considered in this analysis. Then we selected from our sample the luminous infrared galaxies (LIRGs,  $L > 10^{11}L_{\odot}$ ) and we studied the redshift evolution of their average AGN fraction. We considered 4 redshift bins:  $0.02 < z < 0.5$ ,  $0.5 < z < 1.0$ ,  $1.0 < z < 1.5$ ,  $1.5 < z$ . The results are reported in Figure 5.8. For all the wavelength ranges considered, we observe an increasing AGN fraction from low to high redshift. This evolution is however less prominent at longer wavelengths.

### 5.3.5 Black hole accretion rate

The black hole accretion rate (BHAR) indicate the velocity with which the central black hole increases its mass and is expressed in units of solar masses per year ( $M_{\odot}/\text{yr}$ ). Differently from the AGN fraction explained above (Section 5.3.2), the BHAR is an absolute measure of black hole activity. In this sense, it does not measure the relative importance or contribution of one physical mechanism on another, but its intrinsic strength. Matter falling into the black hole distributes itself in an accretion disc. This optically thick and geometrically thin disk (Shakura & Sunyaev 1973) is responsible for the AGN emission from the X–ray to the optical wavelengths, due to dissipative processes involving the infalling matter. The luminosity can then be considered a measure of the rate at which matter falls into the black hole.

As described in section 5.2.2, every single AGN model in the library used for the fitting procedure is univocally related to a bolometric correction that allows to transform the  $1\div 1000\mu\text{m}$  AGN infrared emission in a bolometric ( $10^{-3} \div 10^3$ ) AGN luminosity ( $L_{\text{acc}}$ ). Differently from the AGN fraction described in Section 5.3.2, this quantity does not measure the relative importance of AGN and star formation. It is instead an intrinsic measure of how fast the black hole is increasing matter, independently from the SFR of the host galaxy and from its total

FIR ( $8\div 1000\mu\text{m}$  luminosity). Following Mullaney et al. (2012), we compute the BHAR of our sources through the following equation<sup>1</sup> :

$$\text{BHAR} = \frac{(1 - \epsilon) \times L_{\text{acc}}}{\epsilon c^2} \quad (5.2)$$

where  $\epsilon = 0.1$  is the efficiency in the energy production,  $c$  the speed of light (cm/s),  $L_{\text{acc}}$  the bolometric luminosity of the accretion disk (erg/s) and BHAR the black hole accretion rate (g/s).

To obtain the specific black hole accretion rate (sBHAR), it is necessary to divide the BHAR for the total black hole mass  $M_{\text{BH}}$ . This last one, using the simple conversion reported in e.g. Mullaney et al. (2012), can be obtained from the stellar mass of the host galaxy using a constant conversion factor of  $1.5 \times 10^3$ :  $M_{\text{BH}} = M^* \times 1.5 \times 10^{-3}$ .

---

<sup>1</sup>The bolometric luminosity  $L_{\text{BOL}}$  in Mullaney et al. (2012) corresponds to  $L_{\text{acc}}$  in this analysis.

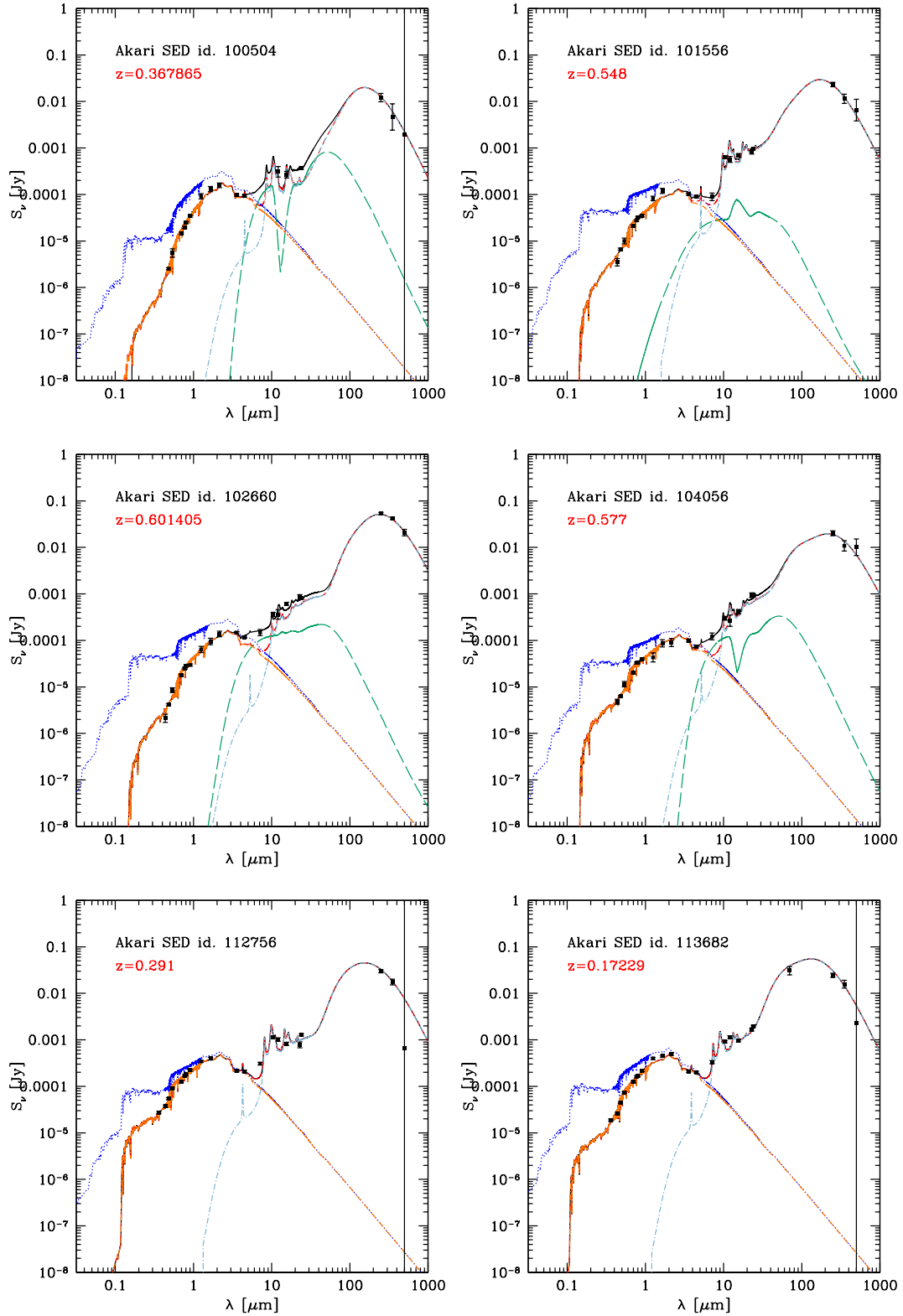


Figure 5.2: SEDs of normal star forming galaxies in our sample ( $0.02 < z < 1.5$ ,  $\log(M^*) > 9$ ). Beside the total emission (black), the following components are represented: unobscured and obscured stellar emission (blue and orange), AGN emission (green), SF dust emission (cyan) and obscured stellar plus SF emission without AGN component (red).

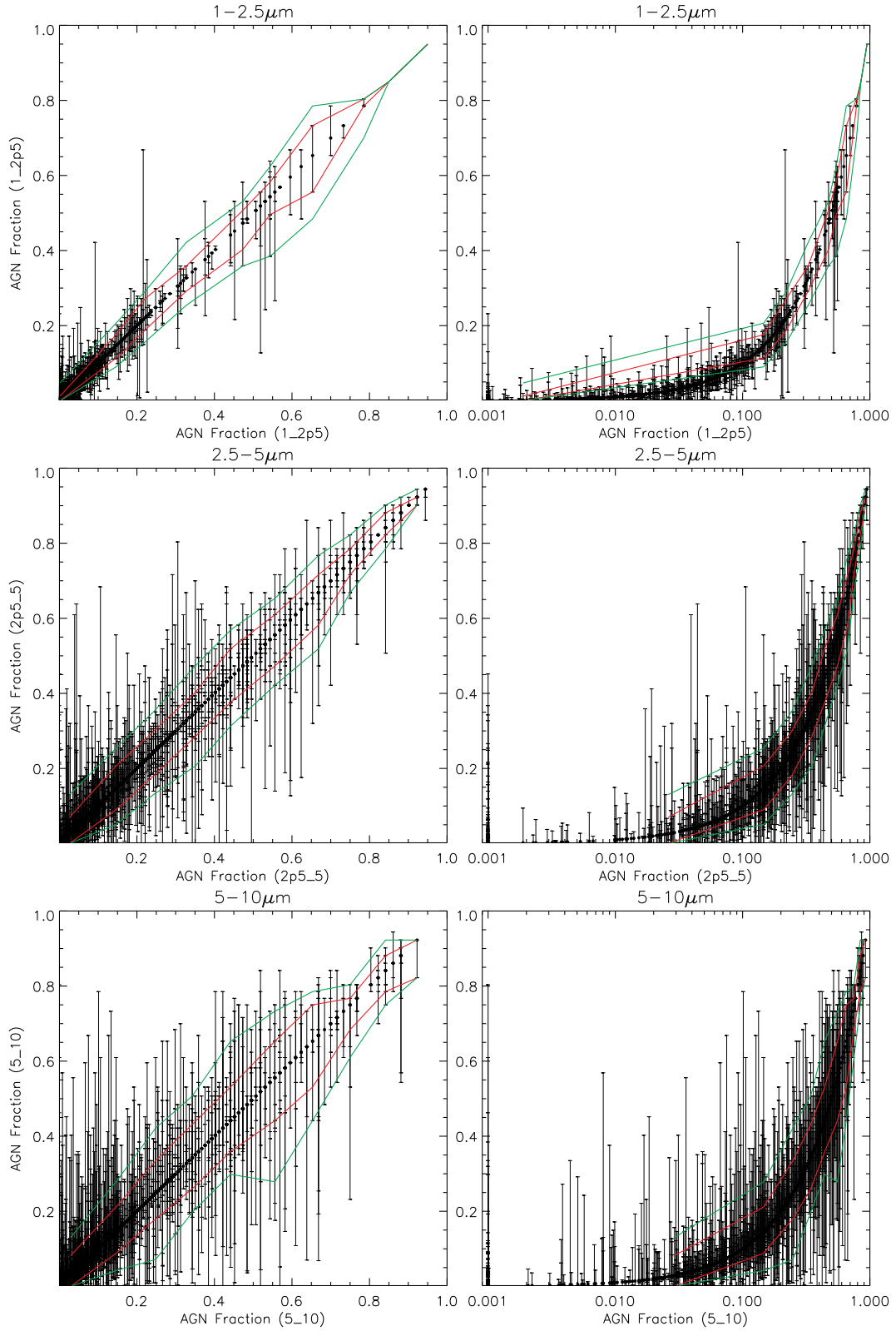


Figure 5.3: AGN fraction uncertainty (25% and 75% percentiles of the PDF) as a function of the AGN fraction computed in logarithmic (left panels) and linear scale (right panels). The AGN fraction and correspondent uncertainty is computed in the  $1\div 2.5\mu\text{m}$  (upper panels),  $2.5\div 5\mu\text{m}$  (middle panels) and  $5\div 10\mu\text{m}$  (lower panels) wavelength ranges. The red lines represent the average values of the superior and inferior error bars, while the green lines are the 25% and 75% percentiles of these values.

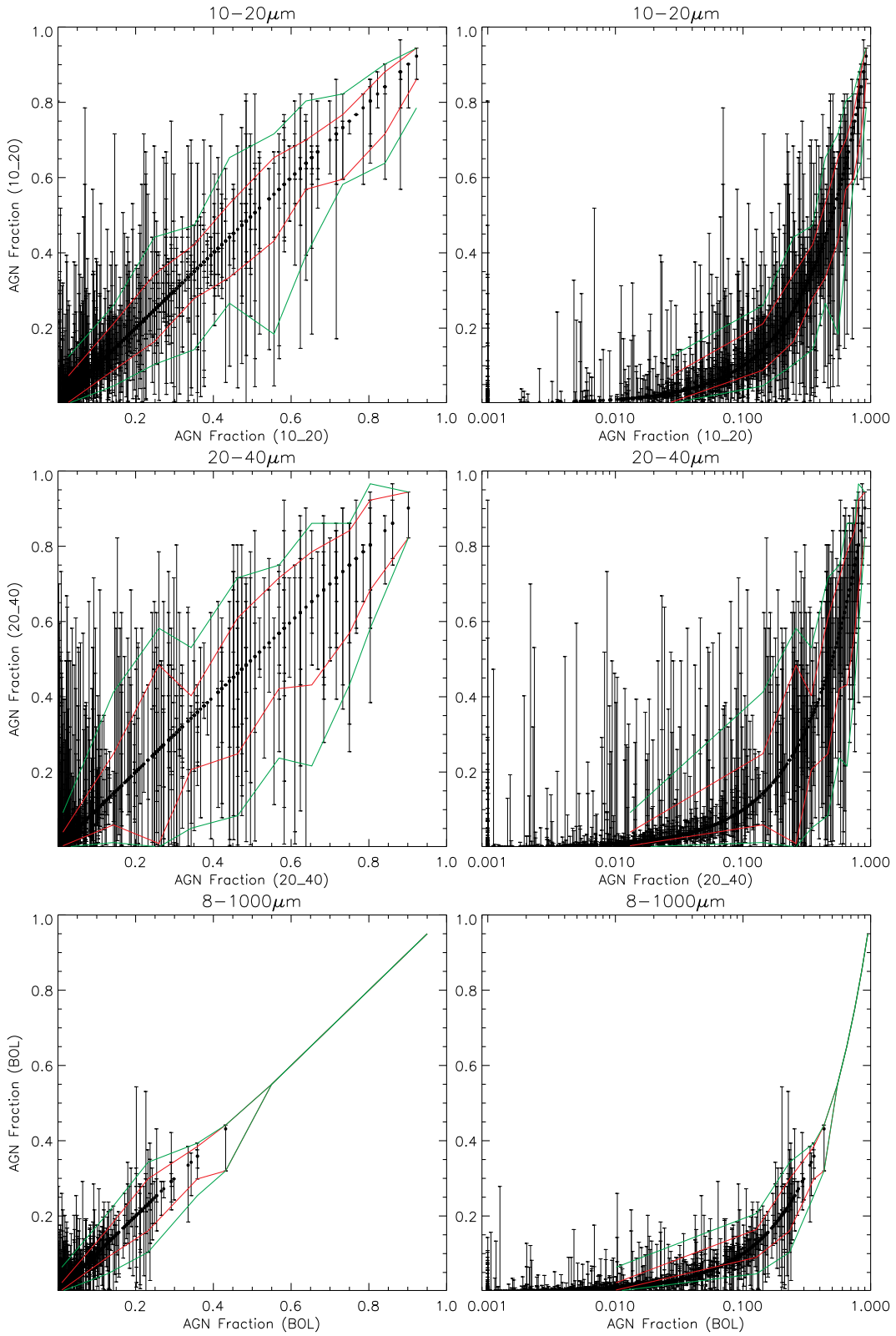


Figure 5.4: AGN fraction uncertainty (25% and 75% percentiles of the PDF) as a function of the AGN fraction computed in logarithmic (left panels) and linear scale (right panels). The AGN fraction and correspondent uncertainty is computed in the 10–20  $\mu\text{m}$  (upper panels), 20–40  $\mu\text{m}$  (middle panels) and 8–1000  $\mu\text{m}$  (lower panels) wavelength ranges. The red lines represent the average values of the superior and inferior error bar limits, while the green lines are the 25% and 75% percentiles of these values. 115

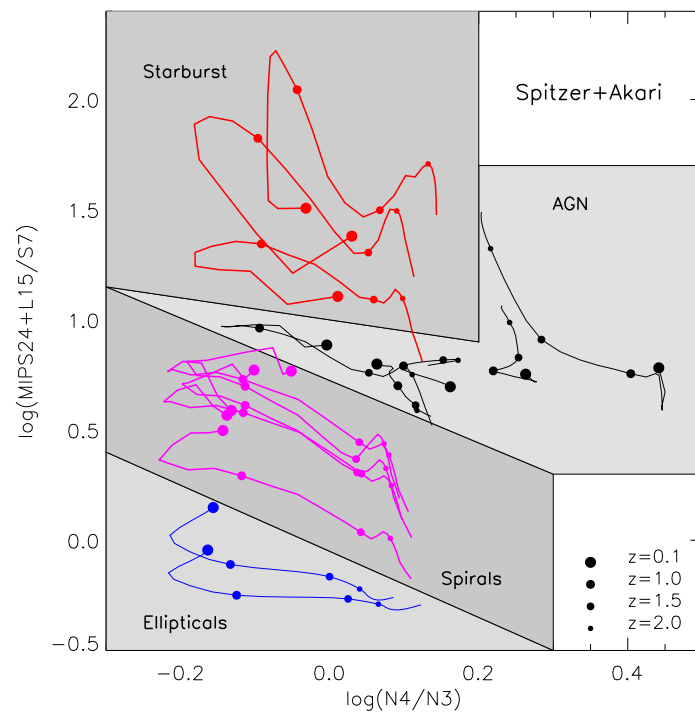


Figure 5.5: Calibration of the FR14-type diagnostic diagram: position of Polletta et al. (2007) templates in the mid-IR color-color plot as a function of type and redshift (Rodighiero in preparation.)

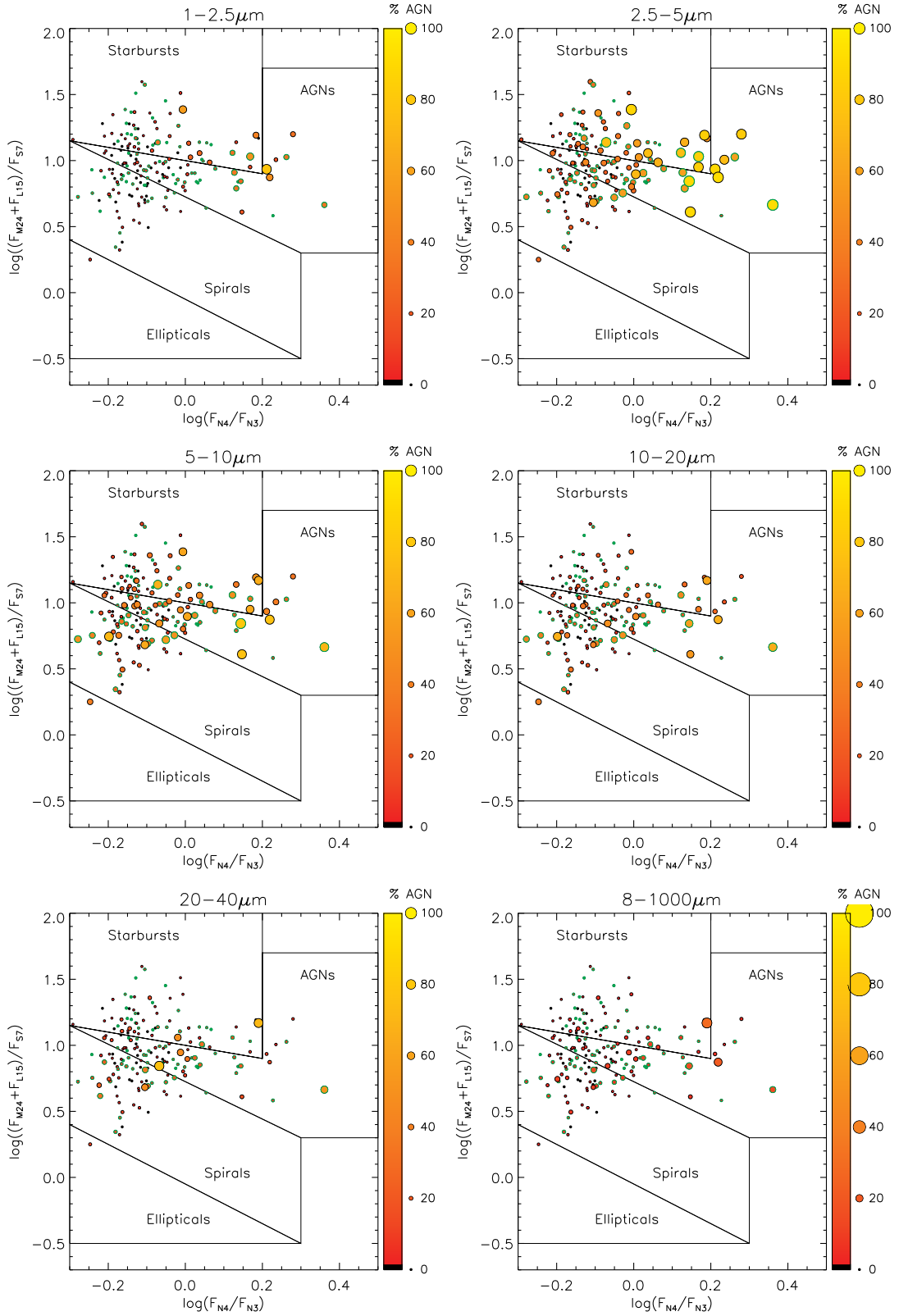


Figure 5.6: Comparison between the FR14-type diagnostic method (Rodighiero in preparation) and our AGN fractions computed between (from high left to low right) 1  $\mu\text{m}$  and 2.5  $\mu\text{m}$ , 2.5 and 5, 5 and 10, 10 and 20, 20 and 40 and in the bolometric band between 8 to 1000  $\mu\text{m}$ .

## Chapter 5: Multiwavelength analysis through SED fitting

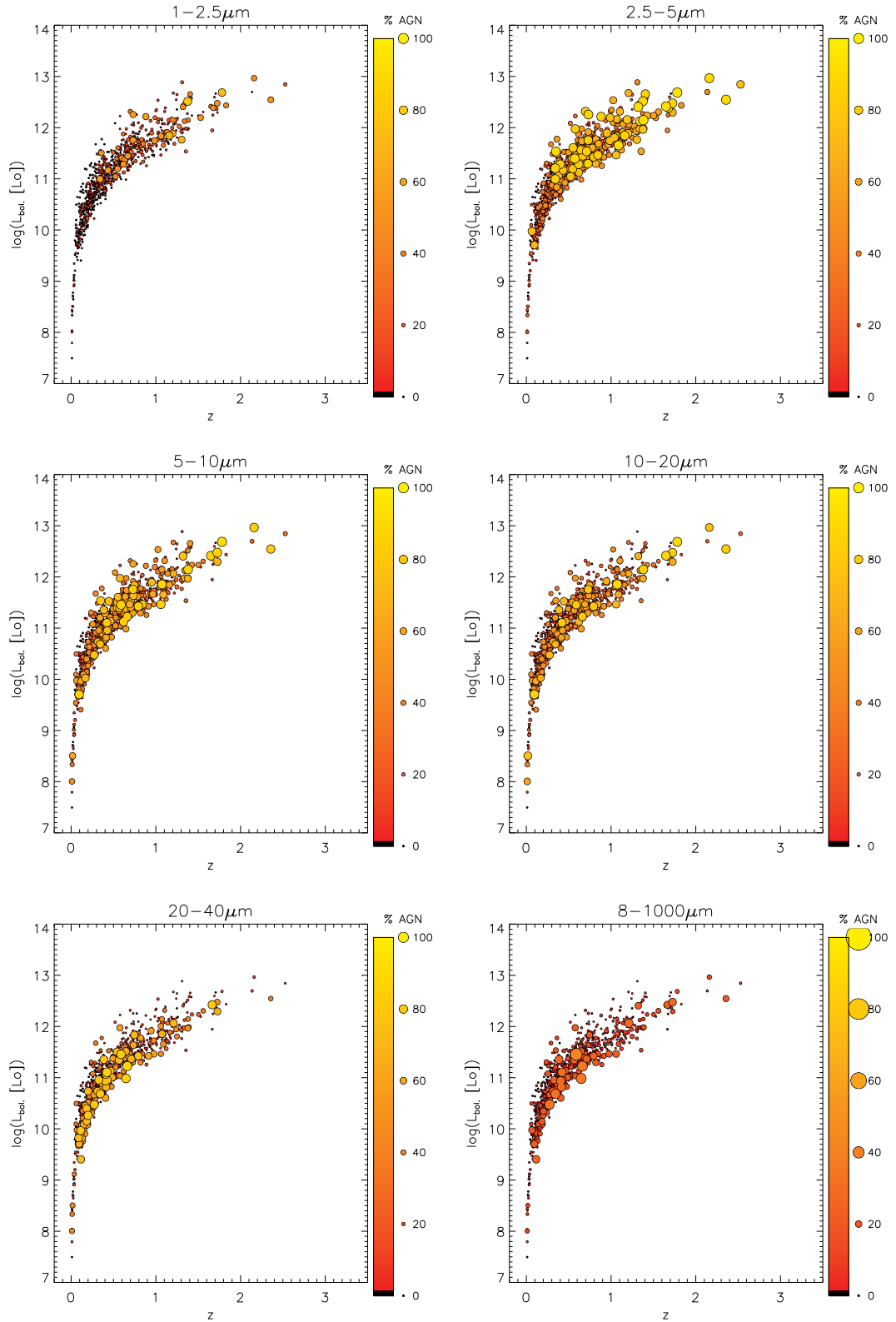


Figure 5.7: Bolometric luminosity ( $L_{8-1000\mu\text{m}}^{\text{SF}+\text{AGN}}$ ) of the sources in our sample. The dimension of the symbols and their brightness depends on the AGN fraction computed in the wavelength ranges (from up left to bottom right): 1  $\mu\text{m}$  and 2.5  $\mu\text{m}$ , 2.5 and 5, 5 and 10, 10 and 20, 20 and 40 and in the bolometric band between 8 to 1000  $\mu\text{m}$

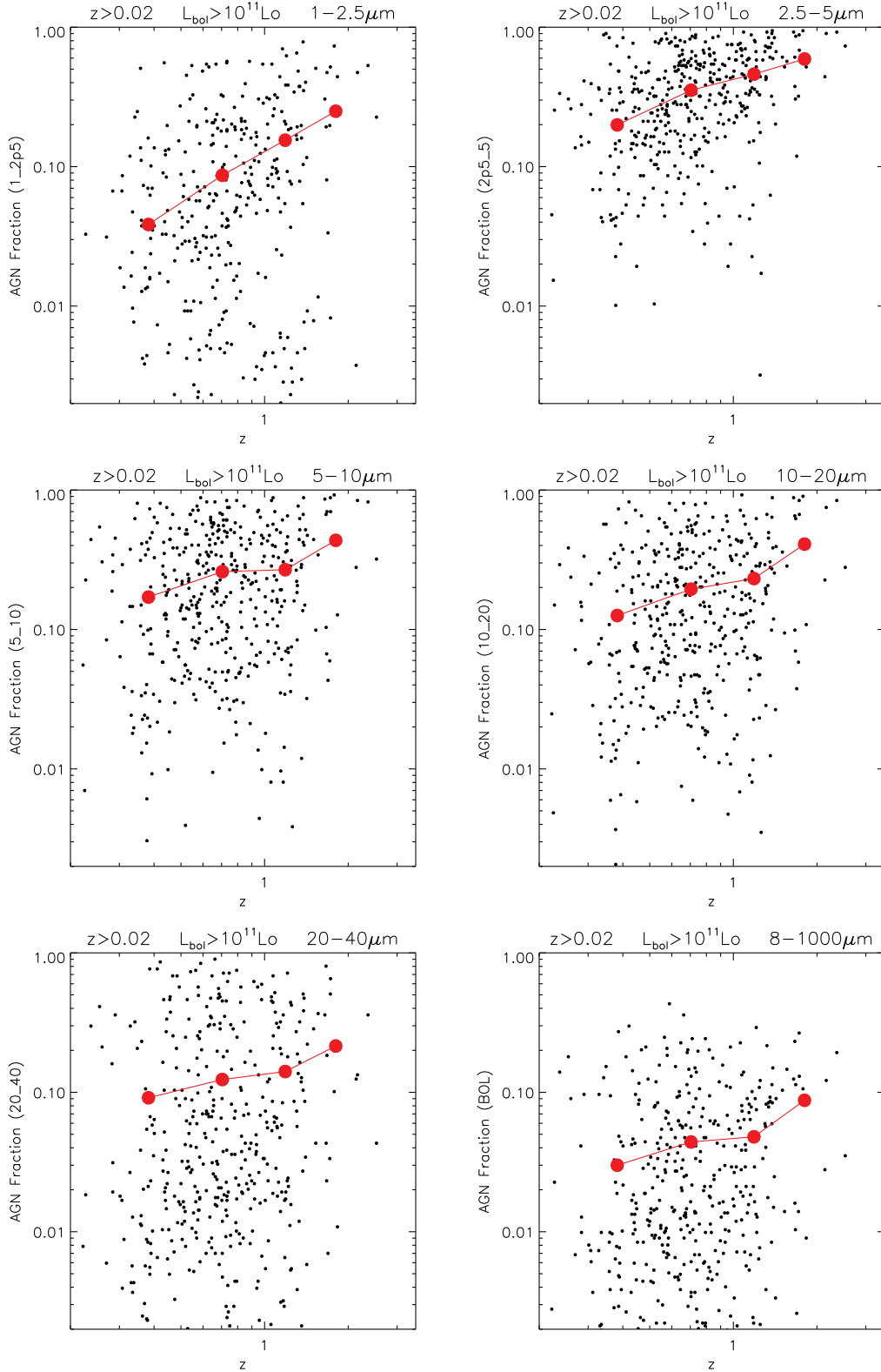


Figure 5.8: Bolometric luminosity ( $L_{8-1000\mu m}^{\text{SF}+\text{AGN}}$ ) of the sources in our sample. The dimension of the symbols and their brightness depends on the AGN fraction computed in the wavelength ranges (from up left to bottom right):  $1\mu m$  and  $2.5\mu m$ ,  $2.5$  and  $5$ ,  $5$  and  $10$  and  $20$ ,  $20$  and  $40$  and in the bolometric band between  $8$  to  $1000\mu m$

### 5.3.6 Stellar mass $M^*$

The stellar mass  $M^*$  (see equation 1.3) derives directly from the BC03 model used to compute the SED. The (BC03, Bruzual & Charlot 2003) simple stellar population models (SSPs) are combined in order reproduce the observed spectra, as described in section 1.1. Using a Chabrier (2003) IMF and leaving the code free to find the most reliable value of metallicity, age and star formation history (SFH), thanks to equations 1.4 and 1.5 it is possible to compute the stellar mass  $M^*$ . As stated before, to estimate  $M^*$  we used the 50% percentile of the PDF derived from the SED fitting technique.

Given the adopted procedure described in section 5.2.2, the AGN emission could possibly influence the mass estimations, in particular when a type 1 AGN is required to find the best fit. Indeed, in these cases, a fraction of optical/UV light is considered as produced by the AGN's engine instead then by stars. This could result in an underestimation of the total stellar mass  $M^*$ . We studied the effects of such possible influence by performing a similar SED fitting technique using a modified version of the *hyperz* code (Bolzonella et al. 2000), called *hyperzmass* with a similar set of stellar templates (BC03) and the same Chabrier (2003) IMF. In this case, the fit is performed considering the stellar component alone and only the photometric data between the u and IRAC-1 bands. The parameters used in this check elaboration are summarized in table 5.3.

<i>Hyperzmass</i> check elaboration	
Parameter	range or value
bands used	CTIO-u, B, V, I, WFI-R <sub>c</sub> , VST-g, i, z, VISTA-J, H, Ks, IRAC-1, 2
Models	BC03 ( $\tau = 0, 0.1, 0.3, 1.0, 2.0, 3.0, 5.0, 10, 15, 30$ )
IMF	Chabrier (2003)
Extinction Law	Calzetti et al. (2000)
extinction range	$A_V = 0.0 \div 3.0$ $\Delta A_V = 0.1$

Table 5.3: Parameters and models used for the *hyperzmass* elaboration. The stellar masses  $M^*_{hyperz}$  computed with this elaboration are used to demonstrate that considering the AGN component in our MAGPHYS elaboration does not create biases, even at high AGN fraction values.

In Figure 5.9, the comparison between stellar masses computed using the *hyperz* code without AGN component and our MAGPHYS masses is shown. The stellar mass is expressed in units of solar masses  $M_\odot$  and the comparison is shown as a function of the AGN fraction computed in different wavelength ranges. It can be noted that  $M^*_{MAGPHYS}$  is a little bit overestimated when compared with  $M^*_{hyperz}$  (or vice versa, *hyperz* underestimates the stellar mass with respect to MAGPHYS). This demonstrates that considering the AGN contribution does not strongly influence the computed stellar mass precision. In Figure 5.10 we show the logarithmic difference between MAGPHYS and *hyperz* stellar masses as a function of redshift, for the three redshift bins considered in our analysis (0–0.5, 0.5–1.0, 1.0–1.5) and as a function of the AGN fraction computed in the 1–2.5 $\mu\text{m}$  range, where the AGN component is expected to influence most the stellar mass computation. No redshift dependency is observed in the three redshift bins, since the average difference (0.16 between  $0 < z < 1.5$ ) remains pretty similar (0.14 between  $0 < z < 0.5$ , 0.2 between  $0.5 < z < 1.0$  and 0.24 between  $1.0 < z < 1.5$ ). At higher AGN fractions, MAGPHYS seems to overestimate stellar masses with respect to *hyperz*, contrary to what would be expected in case of an influence of the AGN component on mass estimation. We divided the sample in two bins with  $f_{AGN}^{1-2.5\mu\text{m}} < 0.10$  and  $f_{AGN}^{1-2.5\mu\text{m}} > 0.10$ . In this case

we observe an average  $\log(M^*)_{MAGPHYS} - \log(M^*)_{hyperz} = 0.14$  at lower  $f_{AGN}^{1-2.5\mu m}$  and 0.24 at higher  $f_{AGN}^{1-2.5\mu m}$ .

### 5.3.7 Star formation rate

One of the quantities that can be computed thanks to the SED fitting technique that we applied is the total bolometric (8-1000 $\mu m$ ) IR luminosity ( $L_{FIR}$ ). In literature, this quantity is commonly used to compute the total star formation rate (SFR) of a galaxy, following Kennicutt (1998). However, not all the FIR luminosity is due to the light emitted by dusty star forming regions or by the interstellar dust heated by young massive stars. The AGN contribution to the FIR luminosity, that we computed as described above, has not to be kept into account in this calculation. Given that:

$$L_{FIR} = L_{FIR}^{SF} + L_{FIR}^{AGN} \quad (5.3)$$

the IR contribution due to the AGN is subtracted from  $L_{FIR}$  before computing the SFR. Moreover, the Kennicutt (1998) equation refers to a Salpeter (1955) IMF. We convert it to the Chabrier (2003) IMF that we are using, subtracting a 0.24 dex correction factor (dividing for 1.7) (e.g. Béthermin et al. 2013):

$$SFR[M_{\odot}/yr] = \frac{1.7 \times 10^{-10} \times L_{FIR}^{SF}[L_{\odot}]}{1.7} \quad (5.4)$$

The specific star formation rate (sSFR) can be simply obtained dividing the SFR for the stellar mass  $M^*$  resulting from the SED fitting technique, as described in section 5.3.6, i.e.  $sSFR = SFR/M^*$ .

### 5.3.8 AGN fraction and main sequence

Once computed the AGN fraction (Section 5.3.2), stellar masses (Section 5.3.6) and SFRs (Section 5.3.7), we studied how the sources of our sample are distributed in the  $M^*$ -SFR space, at different redshifts, as a function of their AGN fraction.

In Figures 5.11 to 5.13 we report the results of this analysis. We compare the position of our sources with the main sequence (MS) as defined, at  $z=1$ , in Elbaz et al. (2007):

$$SFR(z=1) = [M_{\odot}/yr] = 7.2 \times \left( \frac{M^*[M_{\odot}]}{10^{10}} \right)^{0.9} \quad (5.5)$$

The normalization of the MS is redshift dependent. We parametrized this dependency following Sargent et al. (2012), that consider a  $(1+z)^{2.8}$  evolution. Then we obtain:

$$SFR(z) = SFR(z=1) \times \left( \frac{1+z}{2} \right)^{2.8} \quad (5.6)$$

The Elbaz et al. (2007) equation is defined for a Salpeter (1955) IMF and it can be transformed in Chabrier (2003) IMF by dividing  $M^*$  and SFR for a constant factor of  $\sim 1.7$  (e.g. Béthermin et al. 2013). In Figures 5.11 to 5.13, the main sequence is computed for three bins of redshift, using as reference the average redshift in each bin.

We observe that while at shorter wavelengths ( $1 \div 5\mu m$ ) higher AGN fractions seems to favour starburst galaxies, at longer wavelengths the opposite behaviour is observed. This

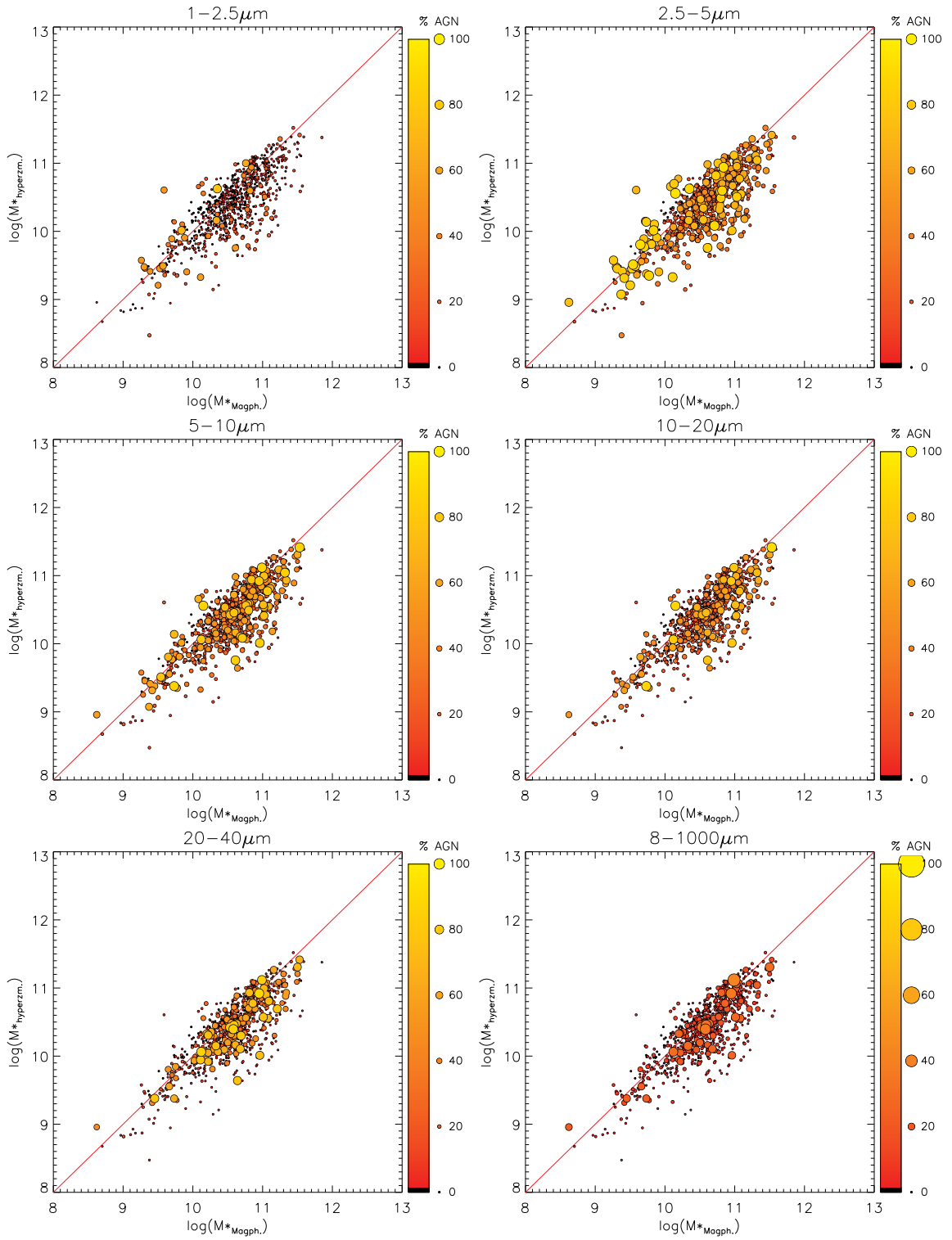


Figure 5.9: Comparison between logarithmic stellar masses (in units of  $M_{\odot}$ ) computed using the hyperz code without AGN component and our MAGPHYS masses. The AGN fraction is computed in the ranges, (from the high left to the low right): 1–2.5  $\mu\text{m}$ , 2.5–5  $\mu\text{m}$ , 5–10  $\mu\text{m}$ , 10–20  $\mu\text{m}$ , 20–40  $\mu\text{m}$ , 8–1000  $\mu\text{m}$ .

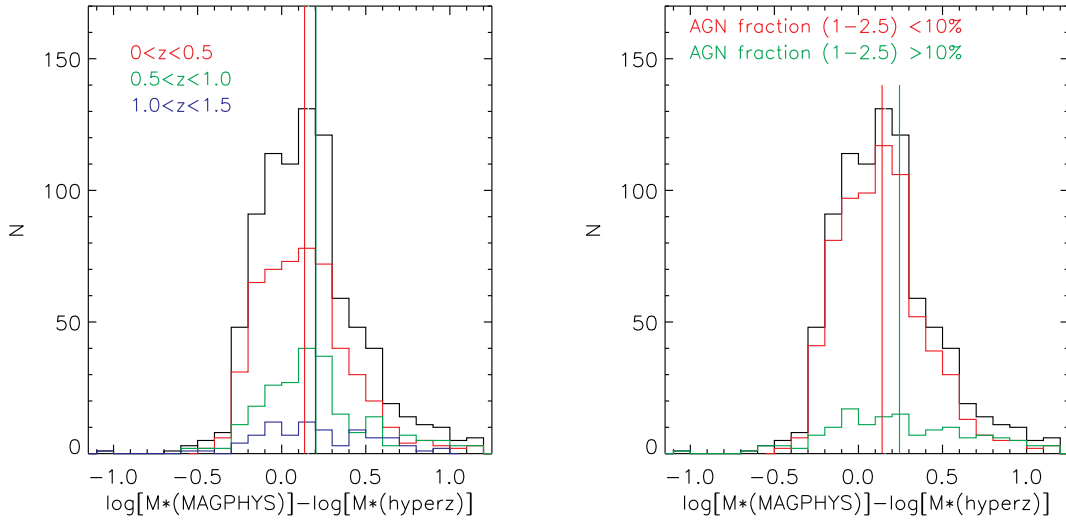


Figure 5.10: *Logarithmic difference between MAGPHYS and hyperz stellar masses ( $M_{\odot}$  units) as a function of redshift and AGN fraction in the range 1-2.5 $\mu\text{m}$ , where it more influence the stellar mass computation. At higher AGN fractions MAGPHYS overestimates stellar masses with respect to hyperz, contrary to what is expected in case of an influence of the AGN component on mass estimation.*

effect is more clearly visible as a transition of the slope of the average relation in Figures 5.14 to 5.16, when passing from shorter to longer wavelengths. In these plots, we divided our data in bins of redshift and stellar mass. For each source, we computed the ratio  $\text{SFR}/\text{SFR}(\text{MS})$  between the measured SFR and the main sequence SFR calculated for a stellar mass and redshift equal to those of the galaxy considered. Then we further divided the sample in five bins of  $\log(\text{SFR}/\text{SFR}(\text{MS}))$  ( $-0.6 \div -0.3$ ,  $-0.3 \div 0.0$ ,  $0.0 \div 0.3$ ,  $0.3 \div 0.6$  and  $>0.6$ ), computing the average values of  $\log(\text{SFR}/\text{SFR}(\text{MS}))$  and AGN fraction for each of the analysed wavelength ranges. In order to increase the statistical meaning, we considered only bins containing more than 5 data points. In these plots, we can observe more quantitatively the trends already seen in figures 5.11 to 5.13.

The observed trends, graphically outlined in the upper panels of Figure 5.17, are not completely unexpected. The AGN fraction measured in a given spectral region quantifies the relative importance of different physical mechanisms. At longer wavelengths ( $\lambda > 5\mu\text{m}$ ) the AGN fraction measures the ratio between nuclear black hole and SF activity. At shorter wavelengths (1-5 $\mu\text{m}$ ) the emission is mostly due to stars and to the AGN itself, when present. In this case, the AGN fraction quantifies the importance of the AGN with respect to the (mostly) stellar emission. Then, to understand the following arguments, one has to keep in mind the difference between observed and intrinsic AGN emission.

Two major factors contribute to create the observed gradients of AGN fraction (Upper panels of Figure 5.17) at different wavelengths:

- A) The data distribution, given the adopted far-IR selection, is flat in the  $M^*$ -SFR space. At low  $M^*$  values we can mostly observe extremely star forming galaxies, while at higher  $M^*$ , we mostly detect MS galaxies. At the shorter wavelengths (1-5 $\mu\text{m}$ ) stellar emission is dominant and directly related to the stellar mass  $M^*$  of the host galaxy. The same AGN emission in a low mass system and in an high  $M^*$  galaxy would result in

very different AGN fractions, that favours, in particular, low mass systems. At the same wavelengths, and considering a given AGN emission, an higher or lower SFR would not change the observed AGN fraction. This situation is represented in the middle left panel of Figure 5.17.

- B) At longer wavelengths, the IR emission due to star formation and to dusty tori dominates ( $5\text{-}1000\mu\text{m}$ ). In this case, when fixing the torus emission, the observed AGN fraction does not change between higher or lower  $M^*$  systems, since the AGN fraction is computed in a spectral region where the stellar emission is negligible. Vice versa, an higher SFR will result in an higher FIR emission and then in a lower AGN fraction. This situation is represented in the middle right panel of Figure 5.17.

Anyway, the two above explanations do not account for the residual observed “gradients” of AGN fraction (bottom panels of Figure 5.17).

At the shorter wavelengths we observe higher AGN fractions at higher SFRs (bottom left panel). At longer wavelengths, we observe higher AGN fractions at higher masses  $M^*$  (bottom right panel). It follows that we have to refuse the unnatural hypothesis of a constant AGN emission in the  $M^*$ -SFR space, in favour of an intrinsically stronger AGN emission at higher SFR (information that we get from shorter wavelengths) and at higher masses (information that we get from longer wavelengths). In the next sections we will analyse the intrinsic AGN emission (i.e. the BH accretion rate), demonstrating that these observations are indeed correct. Malmquist biases do not modify the arguments above.

### 5.3.9 Black hole accretion rate and main sequence

As described in Section 1, the BHAR estimated in the X-ray range shows a relation with stellar masses similar to the main sequence of star forming galaxies, relating SFR and  $M^*$  (Mullaney et al. 2012). At a given mass  $M^*$ , the BHAR also seems to increase at increasing SFRs (Rodighiero et al. 2015). In this section we study the behaviour of the BHAR in the optical-to-FIR spectral range.

Similarly to what we did for the AGN fraction measured at different wavelengths, we studied the intrinsic black hole activity through the measure of the black hole accretion rate and the specific black hole accretion rate (BHAR and sBHAR, see Section 5.3.5).

In the upper panel of Figure 5.18 we report the position of the sources in our sample, in the  $M^*$ -SFR and  $M^*$ -sSFR space. The sBHAR is codified through bigger symbols and brighter colors. The sBHAR shows a behaviour similar to that observed for the AGN fraction computed between 1 and  $2.5\mu\text{m}$  and between  $2.5$  and  $5\mu\text{m}$ . As in that case, at all masses, we observe higher sBHARs at higher SFR/SFR(MS). For comparison, the upper panel of Figure 5.18 can be compared with the two panels of Figure 5.11.

In order to better quantify the observed trend, we divided our sample in bins of stellar mass and redshift, similarly to what we did in section 5.3.8. We studied the sBHAR in 5 bins of  $\log(\text{SFR}/\text{SFR}(\text{MS}))$  ( $-0.6\div-0.3$ ,  $-0.3\div0.0$ ,  $0.0\div0.3$ ,  $0.3\div0.6$  and  $>0.6$ ), computing the average values of  $\log(\text{SFR}/\text{SFR}(\text{MS}))$  and  $\log(\text{sBHAR})$ . We considered only those bins containing 5 data points at least. The results of this analysis are shown in the lower panels of Figure 5.18.

We repeated the same analysis considering the BHAR in place of sBHAR. The results are reported in Figure 5.19. Both the BHAR and the sBHAR increase with the sSFR, as it is observed, using X-ray data by Rodighiero et al. (2015). With our IR-selected data it is more difficult to constrain the BHAR variation as a function of stellar mass, at a given sSFR. This

is particularly difficult in the higher redshift bins. For this reason, in this case, we limited our analysis to  $z < 0.5$ . We divided our  $z < 0.5$  sample in three mass bins, computing the average  $\log(\text{BHAR})$  for the main sequence galaxies ( $-0.3 < \text{SFR}/\text{SFR}(\text{MS}) < 0.6$ ) and for the starburst sources ( $\text{SFR}/\text{SFR}(\text{MS}) > 0.6$ ). Again, we considered only those bins containing a minimum of 5 data points. This constraint limit the off-sequence sample to one only point. The result is shown in Figure 5.20. Our analysis confirms the existence of the “*hidden main sequence of BHAR*” found in Mullaney et al. (2012) at higher redshifts and in the X-ray domain. We also found increasing BHARs at higher  $M^*$  values for main sequence sources. From the fit of our points we obtains  $\text{BHAR} \propto M^{*0.65}$ . This value is in agreement with the slope evolution reported in Mullaney et al. (2012), that find  $\text{BHAR} \propto M^{*1.05}$  at  $z \sim 2$  and  $\text{BHAR} \propto M^{*0.86}$  at  $z \sim 1$ . With a linear interpolation of Mullaney et al. (2012) results, at the average redshift of our sample ( $z \sim 0.26$ ), we would expect a slope of 0.72. This value is in agreement with our result (0.65).

The slope that we observe could be marginally affected by the consequences of selection effects, and then we expect a steeper real slope. This can be understood from the following reasoning. The first point to keep in mind is that the BHAR increases with the sSFR, as we demonstrated with our data and as is shown in Rodighiero et al. (2015). A far-IR data selection, given the main sequence of star forming galaxy, preferentially excludes, among low mass sources, those with a SFR lower then the average. Vice versa, galaxies with low masses and SFRs higher then the average are more easily detected. At higher masses the same problem is less effective. For these reasons, FIR selections shows a MS with slopes flatter then with other selections (e.g. optical). Given the demonstrated relation between BHAR and sSFR, we expect the same effect on the BHAR main sequence.

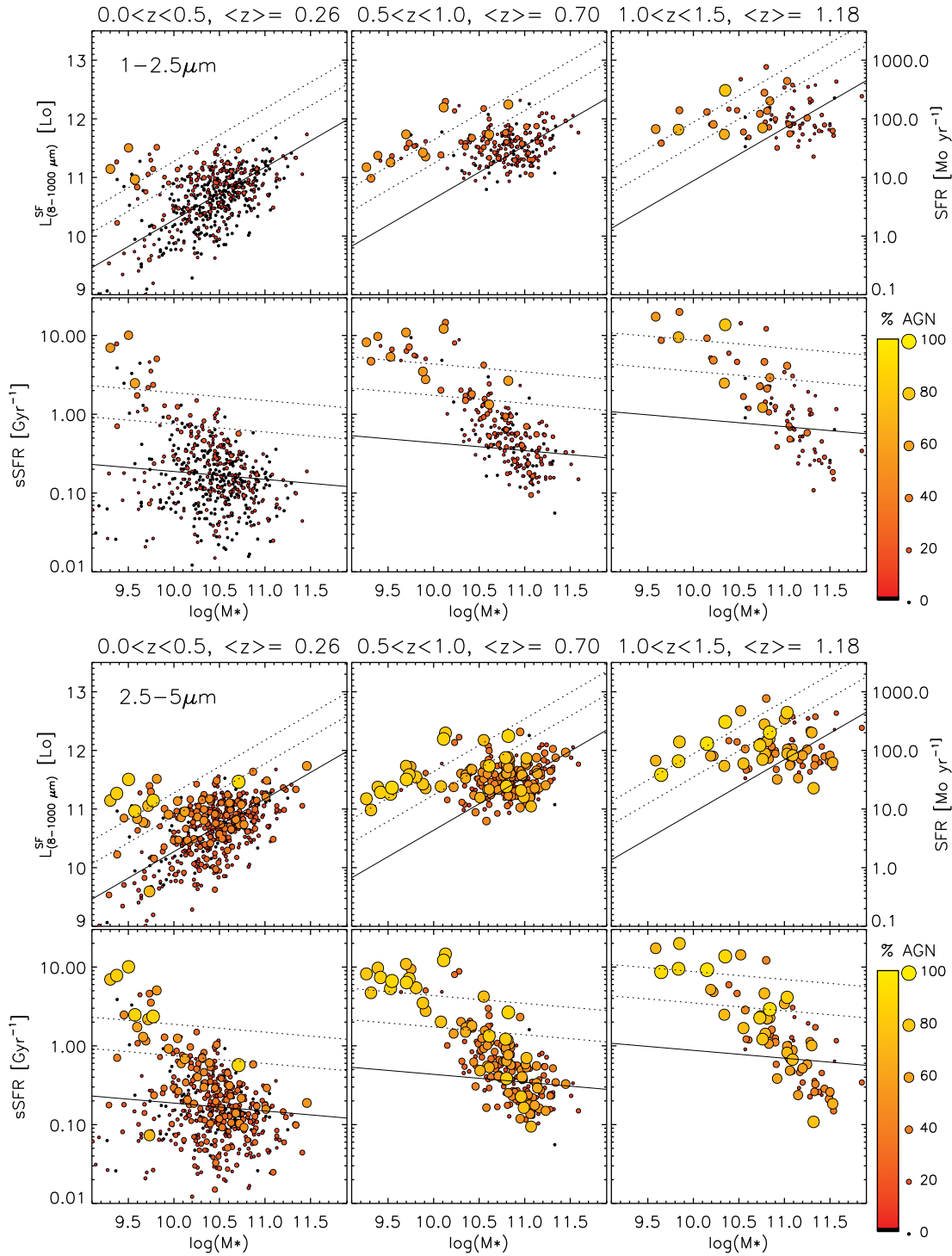


Figure 5.11: AGN fraction and main sequence of star forming galaxies (MS). **Upper six panels:** AGN fraction in the range  $1\div 2.5\mu\text{m}$ . **Lower six panels:** AGN fraction in the range  $2.5\div 5\mu\text{m}$ . In the three upper panels of each image, the distribution of our selected sources is shown in the  $M^*$ -SFR and in the correspondent  $M^*$ - $L_{\text{IR}}^{\text{SF}}$  planes, for three bins of redshift ( $0\div 0.5$ ,  $0.5\div 1.0$ ,  $1.0\div 1.5$ ). In the lower three panels of each image, the sources are shown in the  $M^*$ -sSFR space, for the same redshift bins. The computed AGN fraction is represented with a color scale and with bigger circles corresponding to higher AGN fractions. With a black continue line we indicate the MS in the Elbaz et al. (2007) form and with a Sargent et al. (2012) redshift evolution. Levels of SFR 4 times and 10 times higher are also indicated.

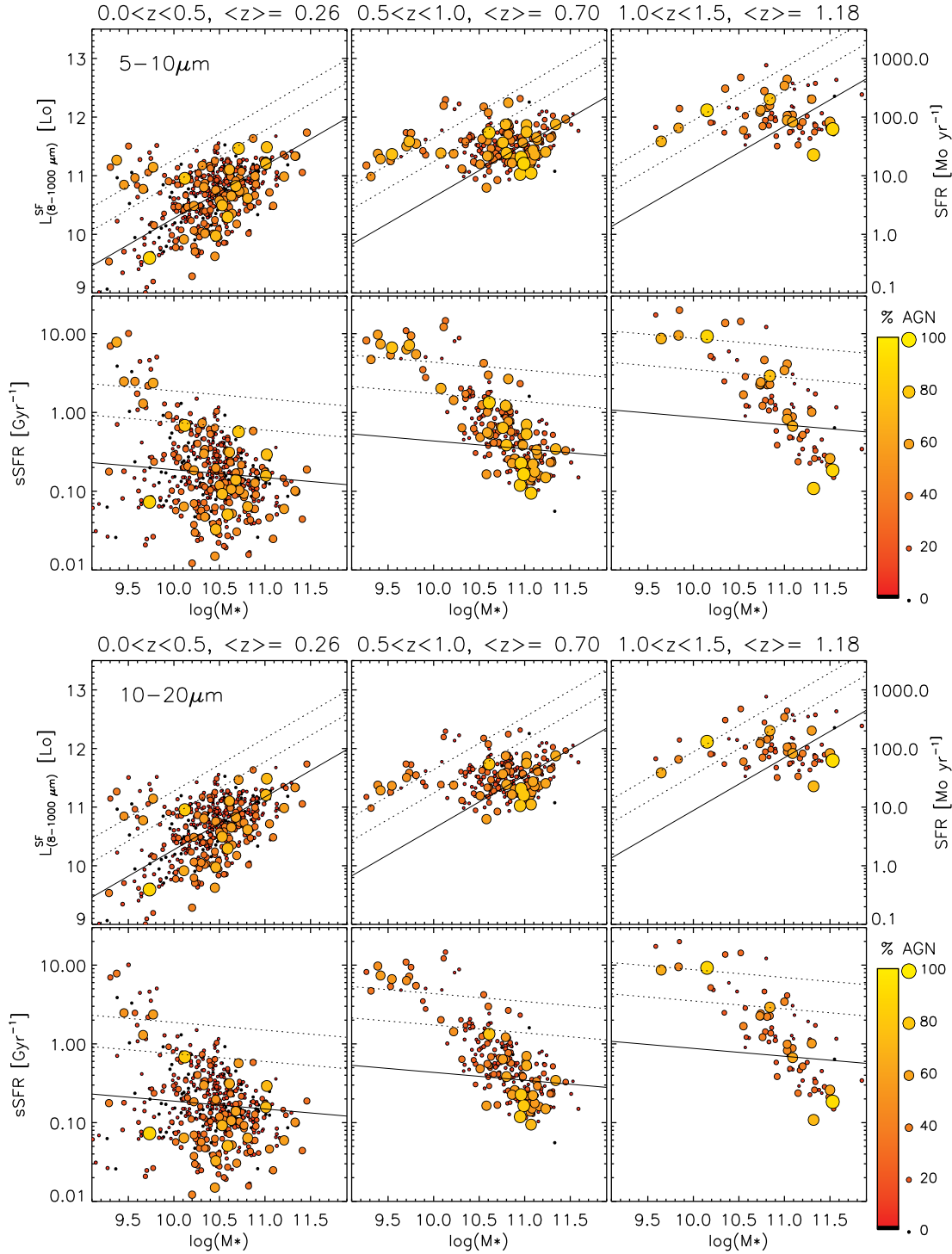


Figure 5.12: AGN fraction and main sequence of star forming galaxies (MS). **Upper six panels:** AGN fraction in the range  $5\div 10\mu\text{m}$ . **Lower six panels:** AGN fraction in the range  $10\div 20\mu\text{m}$ . In the three upper panels of each image, the distribution of our selected sources is shown in the  $M^*$ -SFR and in the correspondent  $M^*$ - $L_{IR}^{SF}$  planes, for three bins of redshift ( $0\div 0.5$ ,  $0.5\div 1.0$ ,  $1.0\div 1.5$ ). In the lower three panels of each image, the sources are shown in the  $M^*$ -sSFR space, for the same redshift bins. The computed AGN fraction is represented with a color scale and with bigger circles corresponding to higher AGN fractions. With a black continue line we indicate the MS in the Elbaz et al. (2007) form and with a Sargent et al. (2012) redshift evolution. Levels of SFR 4 times and 10 times higher are also indicated.

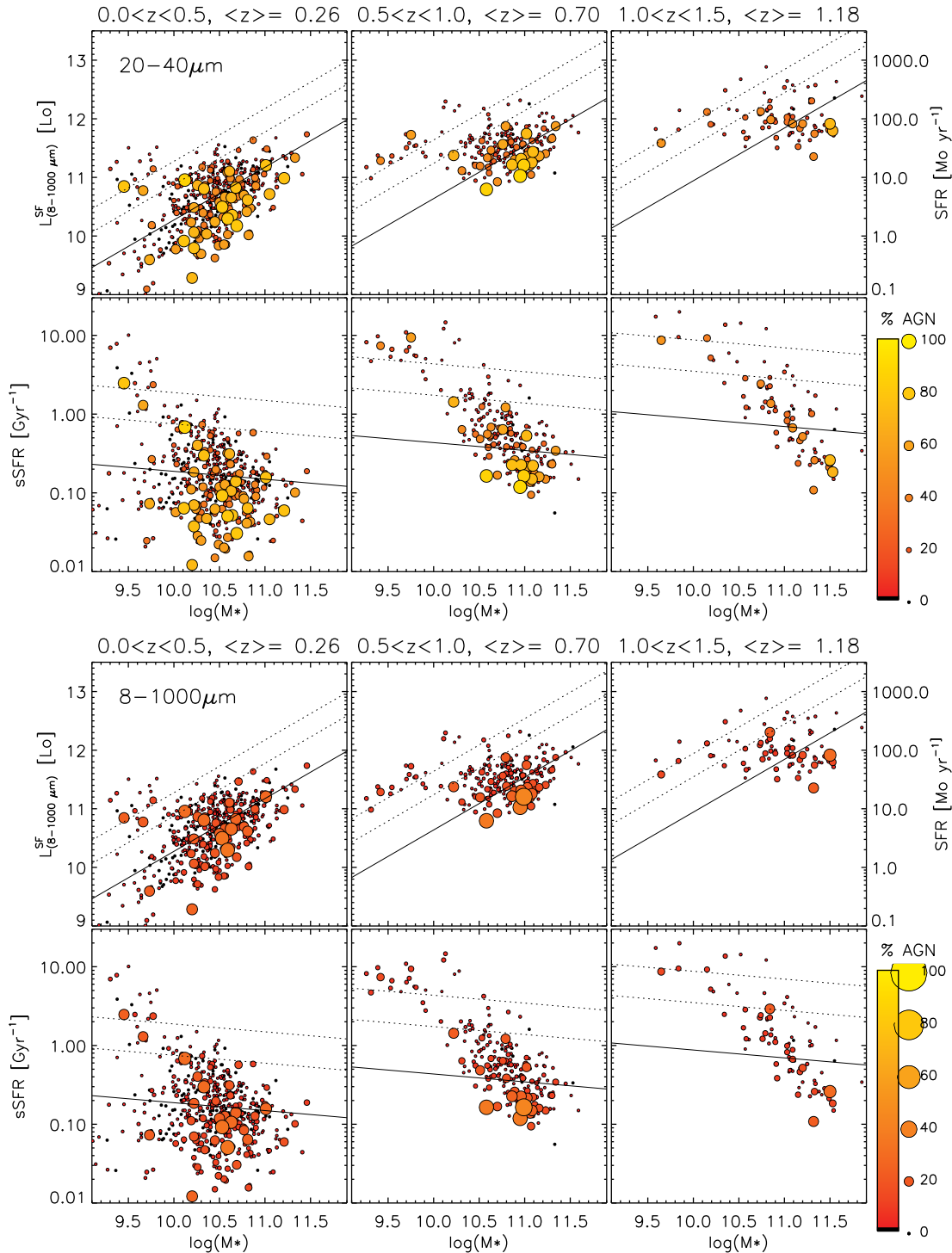


Figure 5.13: AGN fraction and main sequence of star forming galaxies (*MS*). **Upper six panels:** AGN fraction in the range  $20\div 40\mu\text{m}$ . **Lower six panels:** AGN fraction in the range  $8\div 1000\mu\text{m}$ . In the three upper panels of each image, the distribution of our selected sources is shown in the  $M^*$ - $SFR$  and in the correspondent  $M^*$ - $L_{IR}^{SF}$  planes, for three bins of redshift ( $0\div 0.5$ ,  $0.5\div 1.0$ ,  $1.0\div 1.5$ ). In the lower three panels of each image, the sources are shown in the  $M^*$ - $sSFR$  space, for the same redshift bins. The computed AGN fraction is represented with a color scale and with bigger circles corresponding to higher AGN fractions. With a black continue line we indicate the *MS* in the Elbaz et al. (2007) form and with a Sargent et al. (2012) redshift evolution. Levels of *SFR* 4 times and 10 times higher are also indicated.

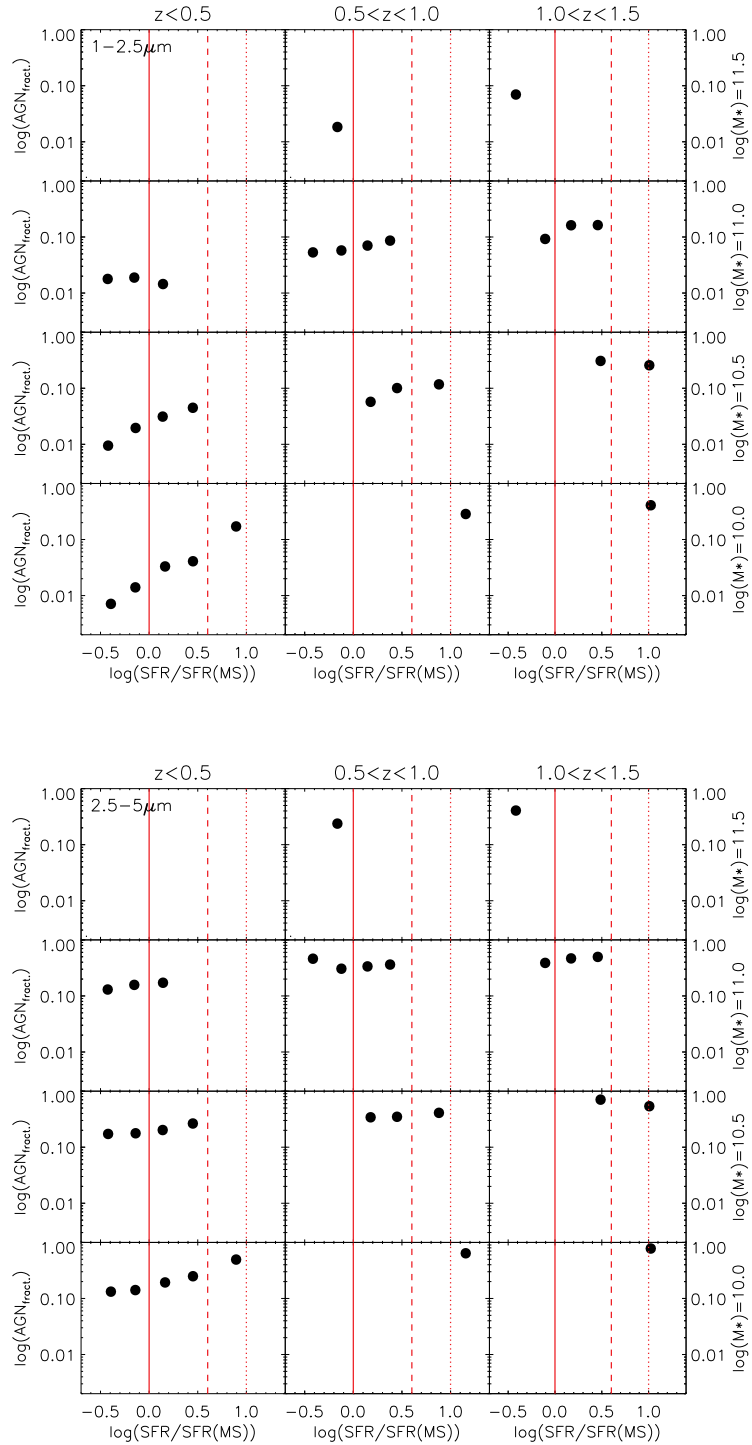


Figure 5.14: AGN fraction as a function of  $SFR/SFR(MS)$  ratio. **Upper six panels:** AGN fraction in the range  $1 \div 2.5 \mu m$ . **Lower six panels:** AGN fraction in the range  $2.5 \div 5 \mu m$ . Only bins with more than 5 data points are shown. The main sequence is shown (continue red line) together with the  $4\times$  and  $10\times$  levels. The AGN fraction at shorter wavelengths increases with  $SFR/SFR(MS)$ , while the opposite behaviour is observed at longer wavelengths (see also Figures 5.15 and 5.16).

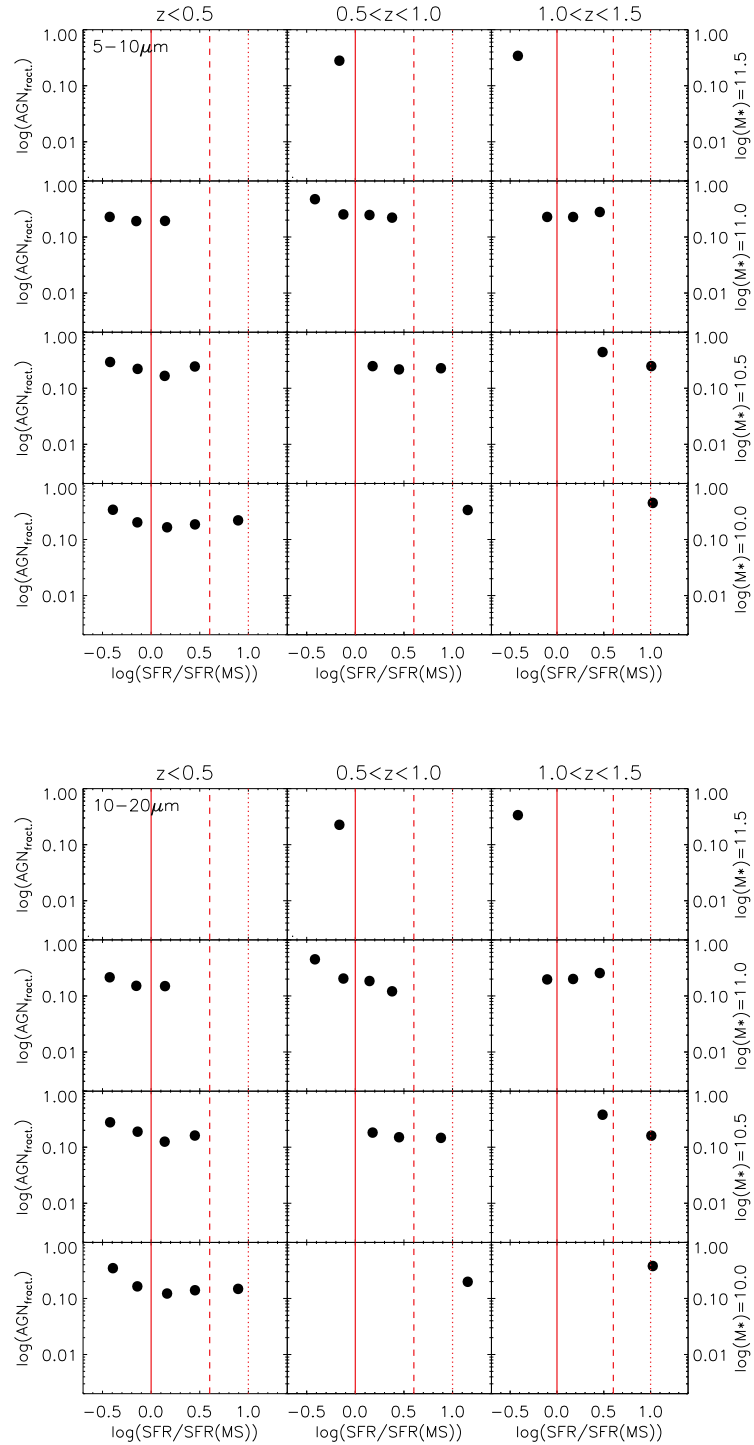


Figure 5.15: AGN fraction as a function of  $SFR/SFR(MS)$  ratio. **Upper six panels:** AGN fraction in the range  $5\div 10\mu m$ . **Lower six panels:** AGN fraction in the range  $10\div 20\mu m$ . Only bins with more than 5 data points are shown. The main sequence is shown (continue red line) together with the  $4\times$  and  $10\times$  levels. The AGN fraction at shorter wavelengths increases with  $SFR/SFR(MS)$ , while the opposite behaviour is observed at longer wavelengths (see also Figures 5.14 and 5.16).

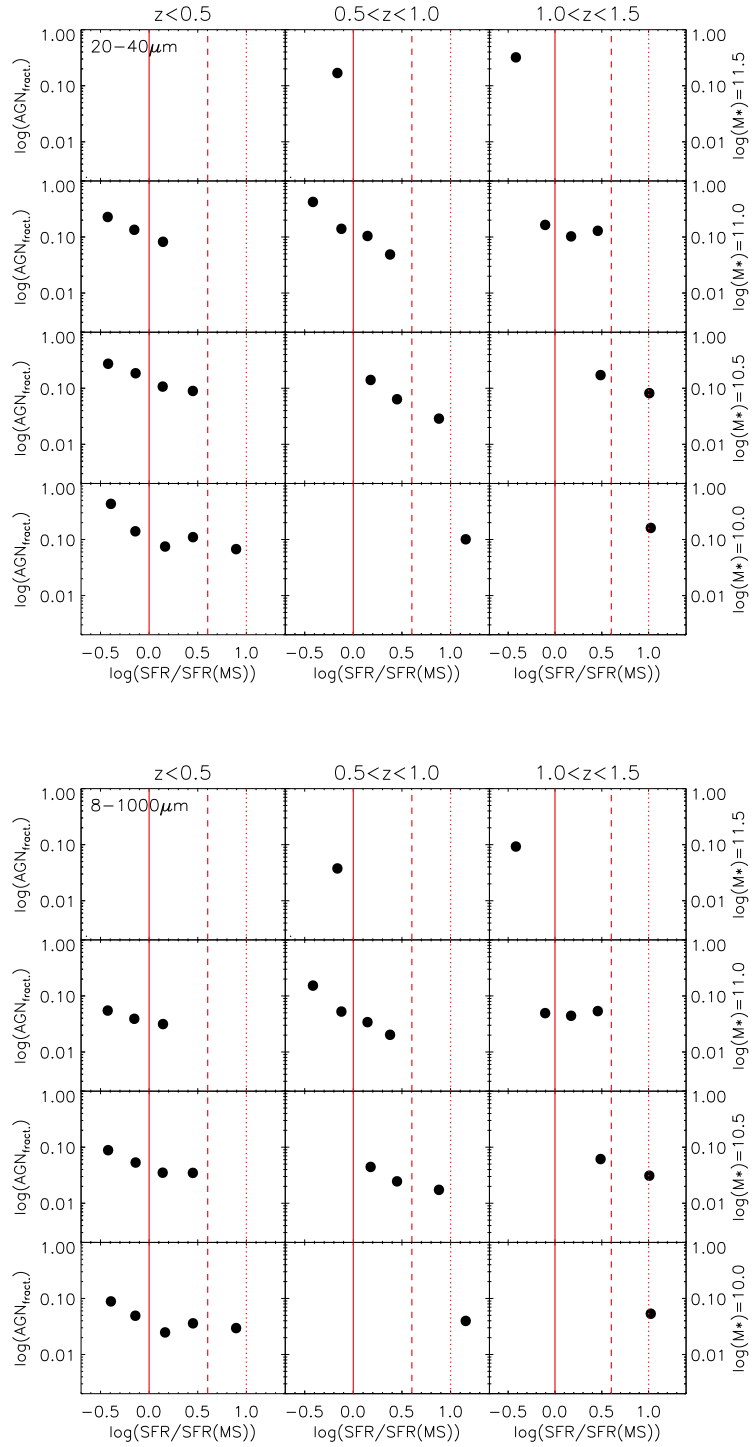


Figure 5.16: AGN fraction as a function of  $SFR/SFR(MS)$  ratio. **Upper six panels:** AGN fraction in the range  $20\div 40\mu m$ . **Lower six panels:** AGN fraction in the range  $8\div 1000\mu m$ . Only bins with more than 5 data points are shown. The main sequence is shown (continue red line) together with the  $4\times$  and  $10\times$  levels. The AGN fraction at shorter wavelengths increases with  $SFR/SFR(MS)$ , while the opposite behaviour is observed at longer wavelengths (see also Figures 5.14 and 5.15).

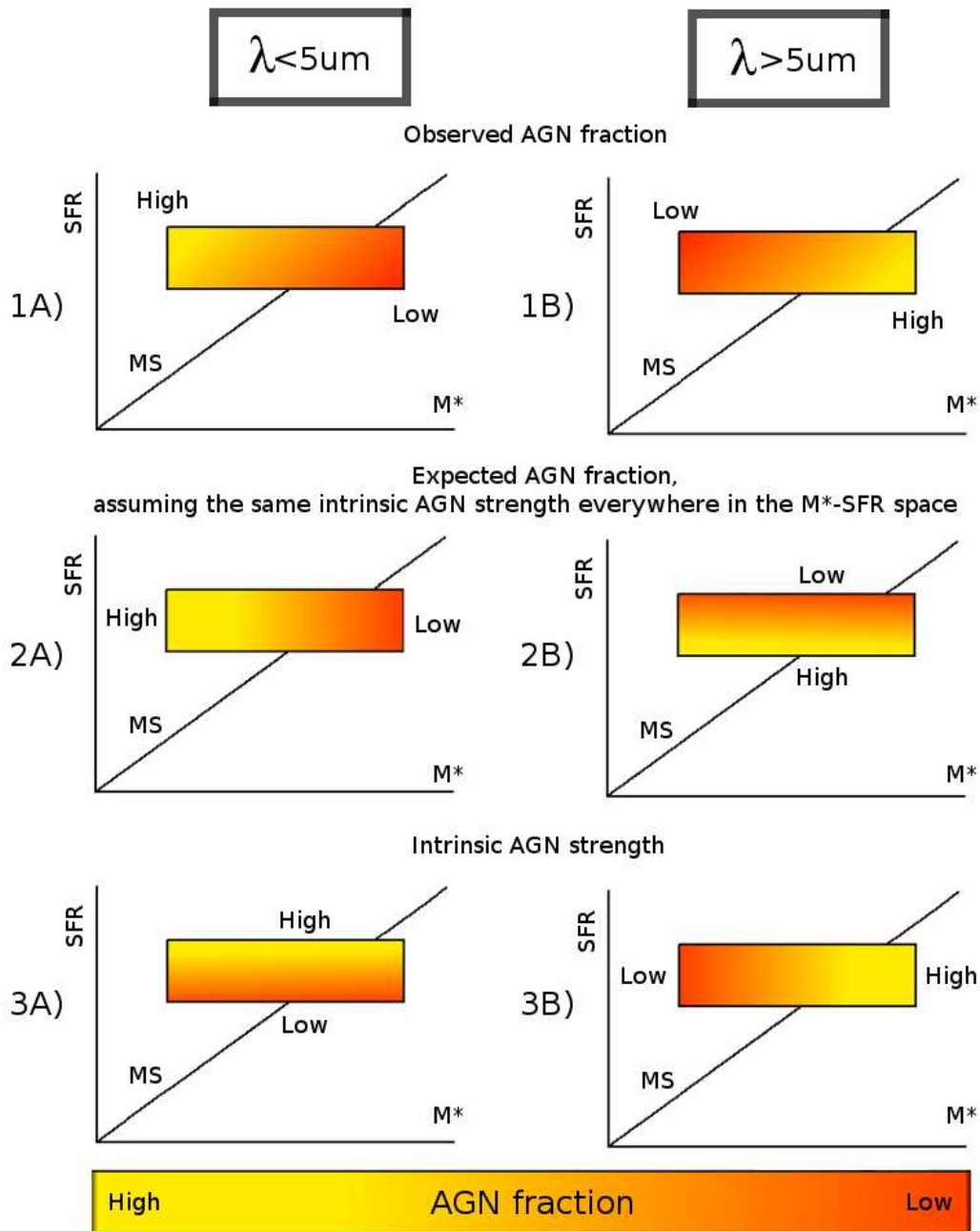


Figure 5.17: Schematic representation of the observed AGN fraction  $f_{\text{AGN}}^{\lambda}$ , at shorter (left panels) and at longer  $\lambda$  (right panels). Higher AGN fractions are represented with brighter colors. The actual observed AGN fraction is represented in the upper panels. If the intrinsic AGN emission was the same everywhere in the  $M^*$ -SFR space, we would expect an AGN fraction distribution like that represented in the middle panels, where  $f_{\text{AGN}}^{\lambda}$  is influenced only by the stellar emission (i.e.  $M^*$ , left panel) at  $\lambda < 5\mu\text{m}$  or by the FIR luminosity due to SF (i.e. SFR, right panel) at  $\lambda > 5\mu\text{m}$ . When we subtract these expected dependencies, a gradient of observed AGN fraction still remains at both short and long wavelengths (lower panels). The residuals have to be ascribed to an intrinsic variation of the AGN emission.

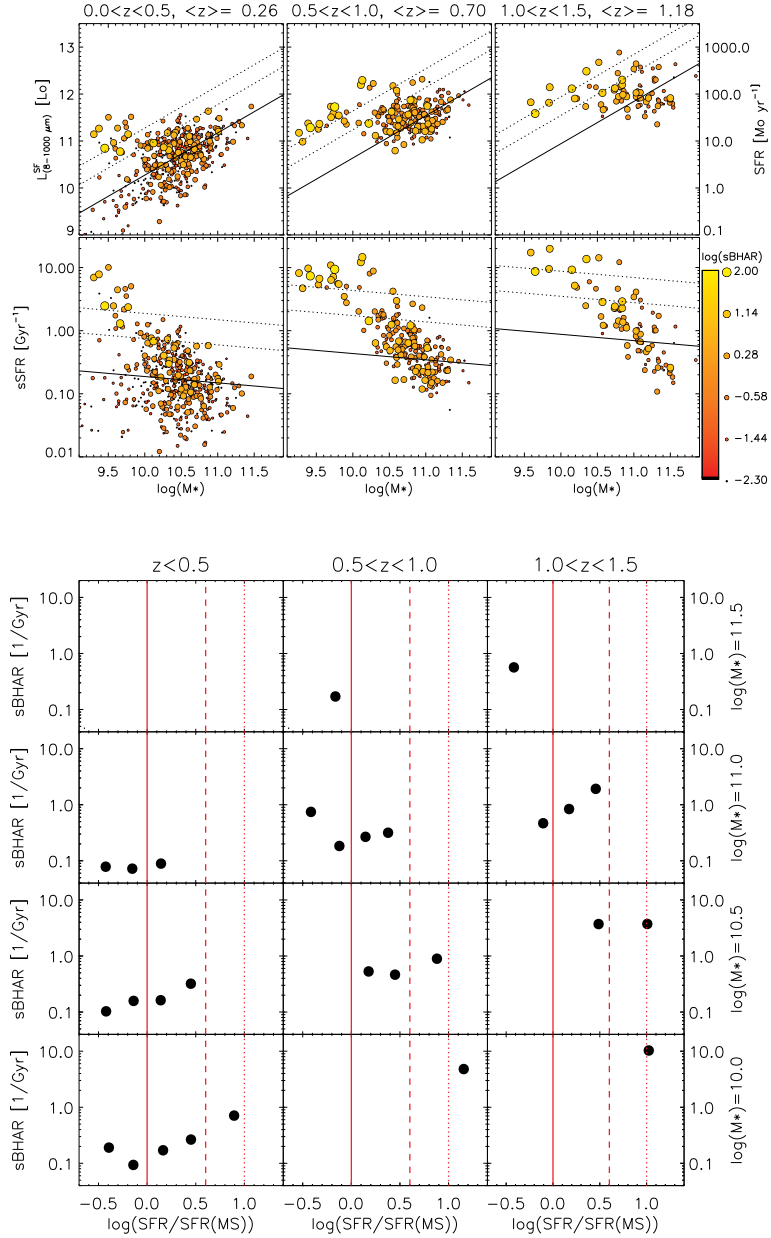


Figure 5.18:  $sBHAR$  and main sequence of star forming galaxies ( $MS$ ). **Upper panels:** position of the sources in the  $M^*$ - $SFR$  and  $M^*$ - $sSFR$  spaces, for three redshift bins. The  $\log(sBHAR)$  is represented with bigger dots and brighter color. **Lower panels:**  $sBHAR$  as a function of the  $SFR/SFR(MS)$  ratio for three redshift bins and four  $M^*$  bins. Only dots representing a minimum of 5 points are reported. The main sequence is shown in both upper and lower panels (continue lines) together with the  $4\times$  and  $10\times$  levels.

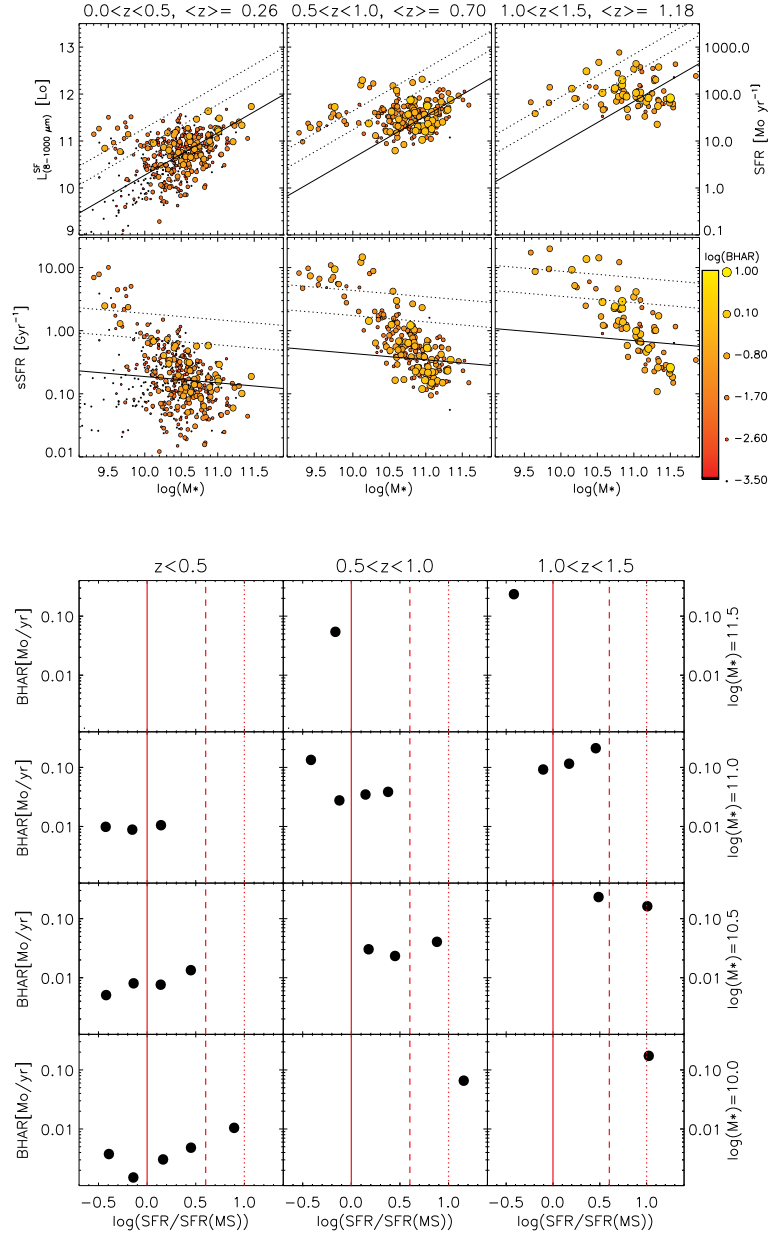


Figure 5.19: *BHAR and main sequence of star forming galaxies (MS). Upper panels: position of the sources in the  $M^*$ -SFR and  $M^*$ -sSFR spaces, for three redshift bins. The  $\log(\text{BHAR})$  is represented with bigger dots and brighter color. Lower panels: BHAR as a function of the SFR/SFR(MS) ratio for three redshift bins and four  $M^*$  bins. Only dots representing a minimum of 5 points are reported. The main sequence is shown in both upper and lower panels (continue lines) together with the  $4\times$  and  $10\times$  levels.*

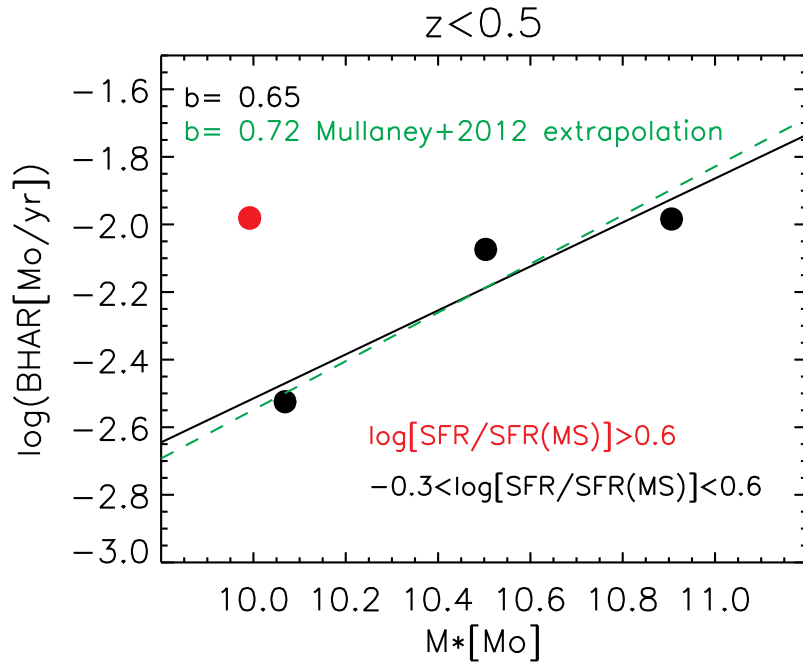


Figure 5.20:  $BHAR$  as a function of  $M^*$  for  $z < 0.5$  galaxies. We divided our sample in main sequence ( $-0.3 < \text{SFR}/\text{SFR}(\text{MS}) < 0.6$ , black dots) and starburst ( $\text{SFR}/\text{SFR}(\text{MS}) > 0.6$ , red dot) galaxies. The slope that we found is 0.65 (black continue line). We also report the extrapolated slope value from Mullaney et al. (2012) at 0.26 (green dashed line).

### 5.3.10 BHAR/SFR ratio and main sequence

In the previous sections we demonstrated that our multiwavelength analysis is in agreement with literature results obtained at X-ray wavelengths. Both the SFR and the BHAR follow a “main sequence” with the stellar mass  $M^*$ . The two “main sequences” observed seems to point toward common underlying secular processes feeding and sustaining both the star formation and the black hole accretion. An even higher correlation between central black hole activity and star formation in the host galaxy is demonstrated by the direct relation between BHAR and sSFR. The correlation between AGN and SF could be direct, in the sense that one of the two drives the behaviour of the other (e.g. feedback), or indirect, meaning that both AGN and SF are triggered by external and common physical mechanisms (e.g. infalling material, merging). Studying the ratio between BHAR and SFR allows to analyze the relative efficiency with which the two mechanisms are triggered. This study was undertaken in Rodighiero et al. (2015) using X-ray data at  $z \sim 2$ . In that work, they divided the sample in two samples: one of “starburst” and the other of main sequence galaxies, finding an higher BHAR/SFR in main sequence with respect to the starbursts.

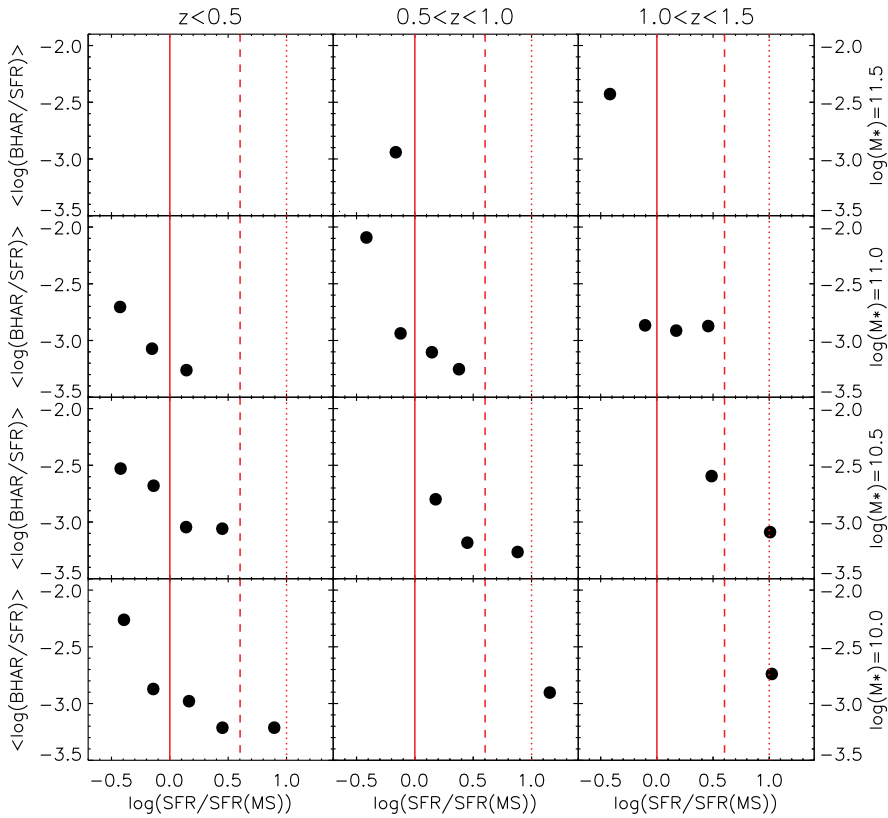


Figure 5.21:  $BHAR/SFR$  as a function of the  $SFR/SFR(MS)$  ratio for three redshift bins and four  $M^*$  bins. Only dots representing a minimum of 5 points are reported. The main sequence is shown (continue line) together with the  $4\times$  and  $10\times$  levels (dashed lines).

As we did when analyzing the AGN fraction, the BHAR and the sBHAR, we consider

three redshift and four mass bins. In each sub-sample, we divide the sources in five bins of SFR/SFR(MS). In each of these bins we computed the BHAR/SFR ratio. The result is reported in Figure 5.21. It is possible to observe that, as in Rodighiero et al. (2015), the BHAR/SFR that we measure is lower at higher sSFR. We also highlight the fact that BHAR/SFR decrease smoothly with the sSFR.

### 5.3.11 Starbursts in our sample

We conclude reporting additional information on the extreme starburst galaxies in our sample. Given their extreme nature, they represent a very peculiar sample of galaxies. Rodighiero et al. (2011) demonstrated their lesser role in the cosmic SFR density (SFRD). While the majority of stars were formed in main sequence galaxies, reserving to the starbursts a secondary role, the relation between this phase and the AGN activity still remains unclear. While major mergers seems to play an important role in triggering their star formation (Sanders & Mirabel 1996), at least in the local universe, it is difficult to clarify if this is the only way in which extreme starbursts are activated or if, for example, they represent a common evolutive phase. In this picture, the role played by the AGN can not be neglected and, nowadays, its co-evolution with the host galaxy is becoming more and more clear. In Table 5.4 we report the most fundamental information concerning the starbursts in our sample. In Figures 5.22 to 5.27 we also report the best fitting SEDs found through the Bertola et al. (2013) MAGPHYS version discussed in Section 5.2. The modeled emissions due to the various mechanisms considered (Stellar emission, star formation, AGN emission) are also represented in the same plots.

Extreme Starbursts						
(SFR/SFR(MS)>10) 0.02<z<1.5 log(M*)> 9						
IRAC ID	RA (J2000)	dec (J2000)	z	log(M*) [M <sub>⊙</sub> ]	SFR [M <sub>⊙</sub> /yr]	log(BHAR) [M <sub>⊙</sub> /yr]
93540	4:43:40.817	-53.833274	0.523	9.312	9.661	-1.524
93985	4:45:54.710	-53.638394	1.206	10.52	473.2	-0.514
94336	4:44:18.363	-53.775588	0.519	10.60	118.9	-0.344
95987	4:45:56.142	-53.621650	0.401	9.372	18.41	-1.384
96302	4:47:15.576	-53.503240	1.062	9.587	66.83	-1.234
105032	4:46:41.319	-53.488889	0.821	9.752	53.09	-0.144
107772	4:43:48.670	-53.720376	1.310	10.80	767.4	-1.074
108870	4:42:29.779	-53.821721	1.191	9.847	139.6	-0.834
109133	4:42:33.060	-53.815344	1.160	9.837	65.31	-0.864
110296	4:42:59.146	-53.770951	0.440	9.747	19.72	-2.314
127316	4:44:23.766	-53.523734	0.651	9.642	21.14	-3.074
130568	4:46:14.199	-53.340599	1.376*	10.35	305.5	-0.064
133020	4:46:46.112	-53.278484	0.698	10.13	197.2	-0.324
138617	4:45:07.024	-53.382780	1.089	9.647	38.46	-0.484
140760	4:41:41.083	-53.658027	0.497	9.812	32.73	-1.834
141955	4:45:20.077	-53.336050	0.578	10.28	167.9	-0.984
142012	4:43:16.269	-53.513013	0.358	9.502	31.99	-1.914
144554	4:44:02.941	-53.427336	0.827	9.787	34.28	-1.814
146500	4:44:56.242	-53.338804	0.571	9.542	23.17	-1.064
147566	4:44:31.734	-53.364736	0.711	9.702	31.99	-1.094
153331	4:45:12.017	-53.265688	0.240	9.377	9.226	no AGN
155133	4:45:49.733	-53.198658	0.327	9.452	6.998	-0.544
158026	4:43:05.548	-53.412453	0.359	9.537	11.35	no AGN
159105	4:44:29.557	-53.283919	0.705	9.912	41.21	-2.284
167321	4:45:22.183	-53.148083	0.728	9.417	19.29	-0.554
167368	4:43:17.680	-53.329187	0.882	10.11	156.7	-0.444
177676	4:41:25.215	-53.408999	0.643	9.807	35.08	-0.944
179292	4:45:47.612	-53.018635	0.938	10.23	136.5	-1.634
183032	4:43:07.082	-53.223500	0.341	9.572	9.226	-1.544
188346	4:43:19.501	-53.162098	0.435	9.302	13.96	-1.554
189340	4:46:57.966	-52.835260	0.547	9.262	14.96	-1.474
189808	4:44:39.589	-53.034318	0.389	9.732	24.83	-2.214
194798	4:44:42.034	-52.992611	0.341	9.772	13.96	-0.964
206481	4:43:04.390	-53.039845	0.598	9.387	23.71	-1.434
215989	4:42:07.879	-53.043764	0.436	9.627	18.84	-1.624
216069	4:45:03.679	-52.789032	0.618	9.527	17.99	-1.534
217366	4:43:19.404	-52.933968	0.552	9.732	38.46	-1.094
218417	4:43:15.207	-52.928593	0.985	9.697	54.33	-1.264

NOTE:

\* Spectroscopic redshift

Table 5.4: (A) Main parameters computed for the starbursts galaxies in our sample ( $SFR/SFR_{MS}(z) > 10$ ). We consider only sources with redshifts in the range  $0.02 < z < 1.5$ . The table will continue with part B.

Extreme Starbursts ( $SFR/SFR_{MS} > 10$ ) $0.02 < z < 1.5$ $\log(M^*) > 9$						
IRAC ID	AGN fraction					
	1-2.5 $\mu m$	2.5-5 $\mu m$	5-10 $\mu m$	10-20 $\mu m$	20-40 $\mu m$	8-1000 $\mu m$
93540	0.452	0.785	0.519	0.351	0.062	0.080
93985	0.092	0.668	0.367	0.285	0.023	0.013
94336	0.0	0.32	0.484	0.367	0.090	0.029
95987	0.136	0.841	0.638	0.376	0.064	0.041
96302	0.543	0.70	0.16	0.127	0.053	0.019
105032	0.0010	0.638	0.452	0.292	0.569	0.094
107772	0.193	0.442	0.084	0.029	0.0040	0.0040
108870	0.385	0.804	0.359	0.16	0.017	0.029
109133	0.70	0.881	0.61	0.452	0.084	0.079
110296	0.122	0.394	0.13	0.077	0.017	0.0060
127316	0.014	0.054	0.0090	0.0070	0.0010	0.0010
130568	0.785	0.902	0.422	0.272	0.104	0.060
133020	0.327	0.822	0.335	0.176	0.065	0.044
138617	0.327	0.923	0.70	0.653	0.519	0.14
140760	0.272	0.556	0.136	0.053	0.016	0.011
141955	0.0020	0.279	0.124	0.047	0.014	0.0070
142012	0.507	0.841	0.313	0.108	0.011	0.0080
144554	0.184	0.432	0.104	0.070	0.038	0.011
146500	0.197	0.902	0.767	0.543	0.176	0.065
147566	0.216	0.861	0.61	0.495	0.18	0.041
153331	0.0	0.0	0.0	0.0	0.0	0.0
155133	0.0	0.462	0.569	0.507	0.785	0.237
158026	0.0	0.0	0.0	0.0	0.0	0.0
159105	0.099	0.248	0.050	0.025	0.0050	0.0040
167321	0.037	0.841	0.61	0.569	0.452	0.15
167368	0.569	0.861	0.442	0.254	0.039	0.058
177676	0.143	0.804	0.582	0.376	0.108	0.058
179292	0.164	0.313	0.054	0.024	0.0040	0.0040
183032	0.596	0.861	0.507	0.272	0.086	0.064
188346	0.556	0.767	0.351	0.237	0.104	0.046
189340	0.531	0.804	0.403	0.221	0.088	0.047
189808	0.024	0.367	0.101	0.070	0.0080	0.0050
194798	0.226	0.881	0.624	0.569	0.32	0.127
206481	0.484	0.785	0.569	0.484	0.070	0.054
215989	0.0	0.146	0.127	0.054	0.052	0.010
216069	0.543	0.841	0.473	0.32	0.073	0.047
217366	0.327	0.822	0.716	0.412	0.067	0.054
218417	0.543	0.75	0.305	0.32	0.092	0.029

Table 5.4: **(B)** Main parameters computed for the starbursts galaxies in our sample ( $SFR/SFR_{MS}(z) > 10$ ). We consider only sources with redshifts in the range  $0.02 < z < 1.5$ .

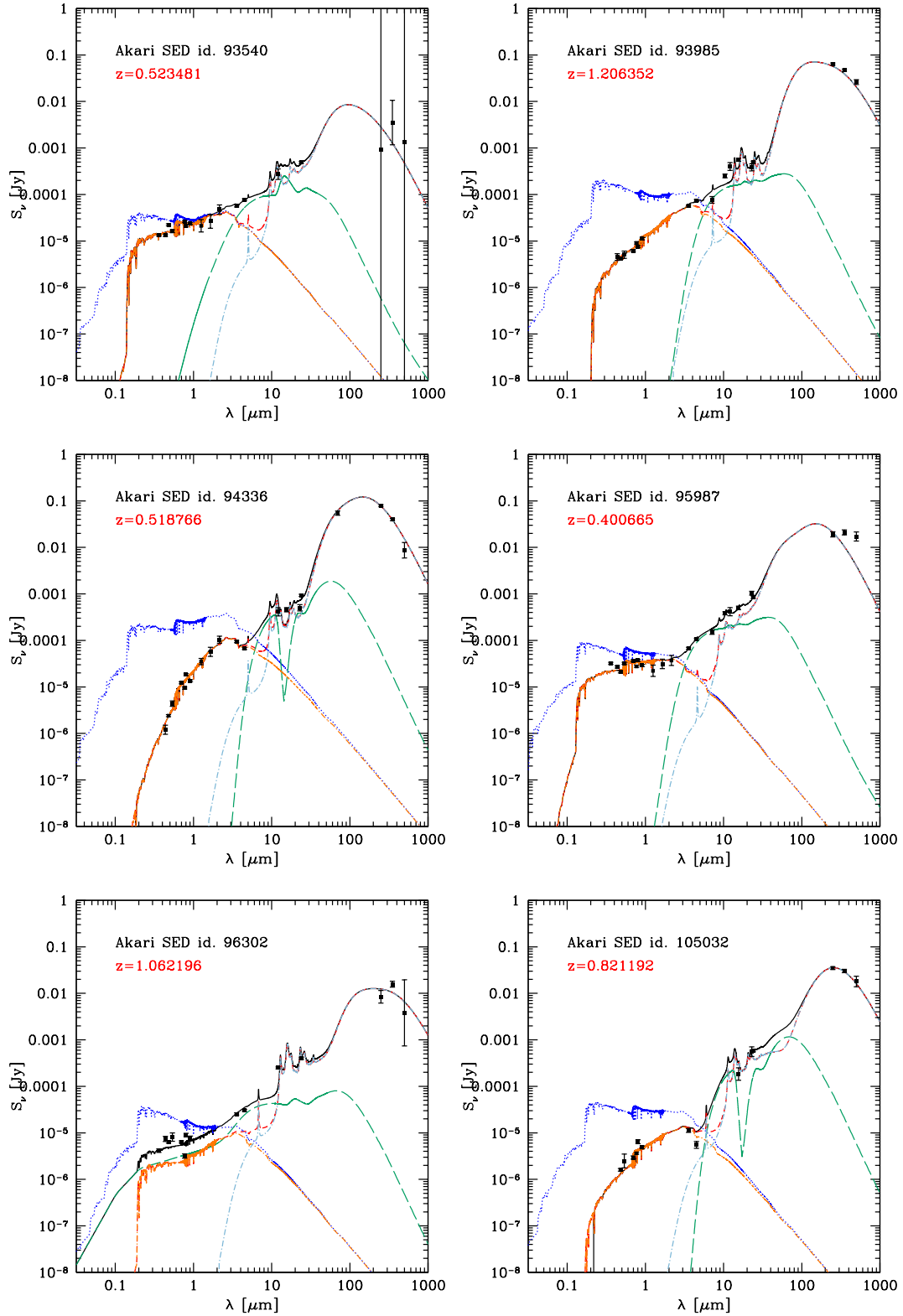


Figure 5.22: SEDs of starburst galaxies in our sample ( $0.02 < z < 1.5$ ,  $\log(M^*) > 9$ ). Beside the total emission (black), the following components are represented: unobscured stellar emission (blue and orange), obscured stellar (green), SF dust emission (cyan) and obscured stellar plus SF emission without AGN component (red).

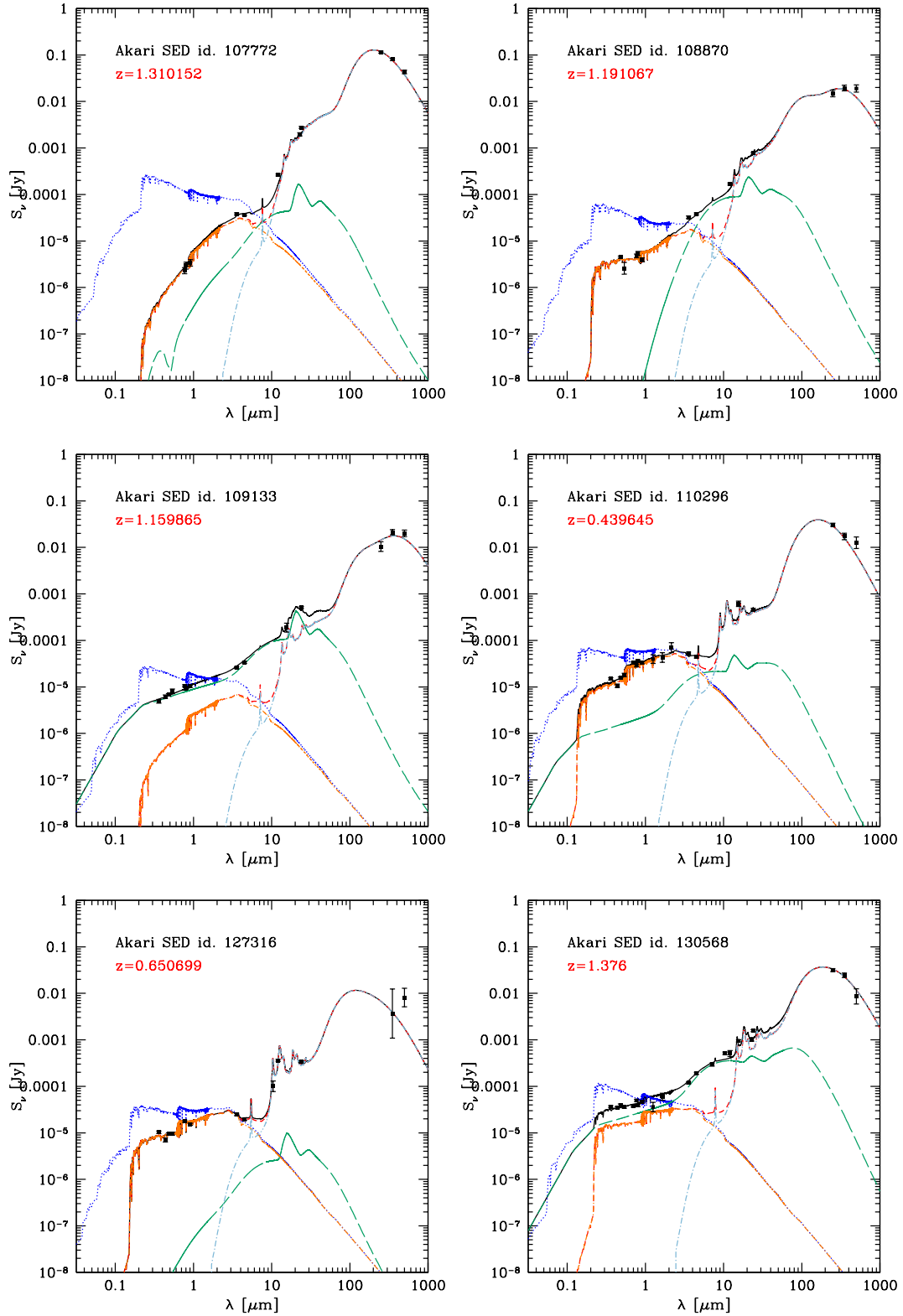


Figure 5.23: SEDs of starburst galaxies in our sample ( $0.02 < z < 1.5$ ,  $\log(M^*) > 9$ ). Beside the total emission (black), the following components are represented: unobscured and obscured stellar emission (blue and orange), AGN emission (green), SF dust emission (cyan) and obscured stellar plus SF emission without AGN component (red).

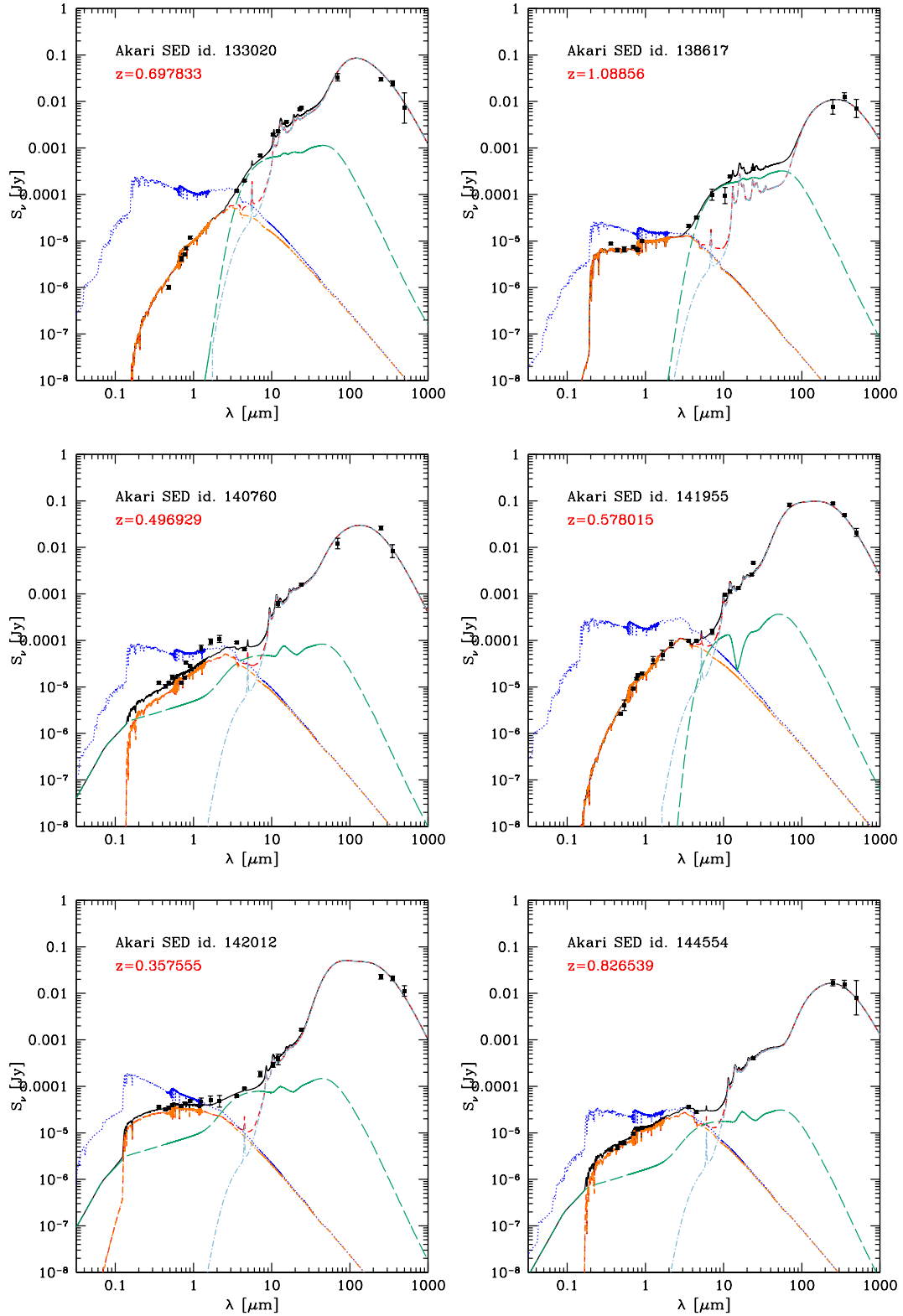


Figure 5.24: SEDs of starburst galaxies in our sample ( $0.02 < z < 1.5$ ,  $\log(M^*) > 9$ ). Beside the total emission (black), the following components are represented: unobscured and obscured stellar emission (blue and orange), AGN emission (green), SF dust emission (cyan) and obscured stellar plus SF emission without AGN component (red).

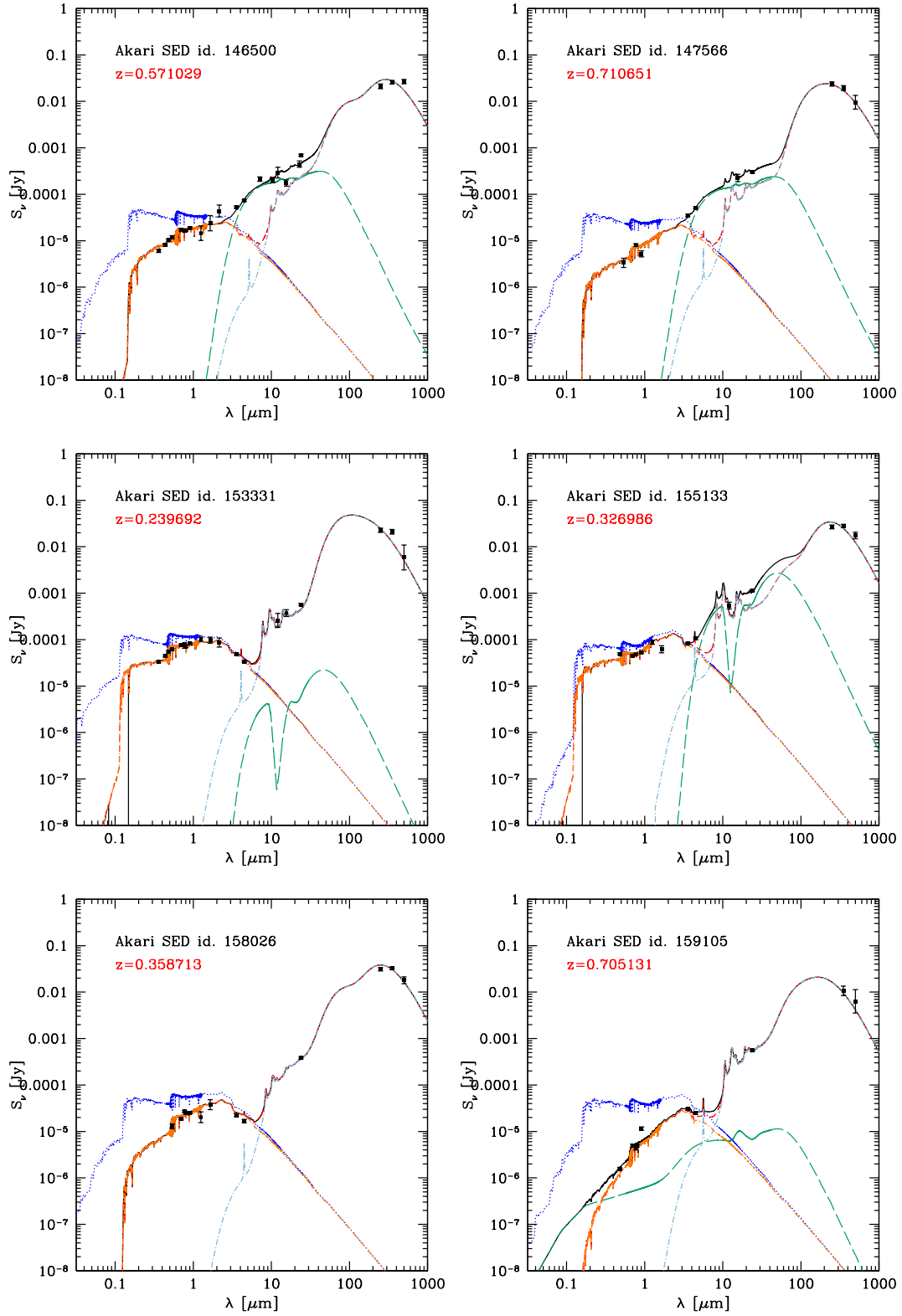


Figure 5.25: SEDs of starburst galaxies in our sample ( $0.02 < z < 1.5$ ,  $\log(M^*) > 9$ ).

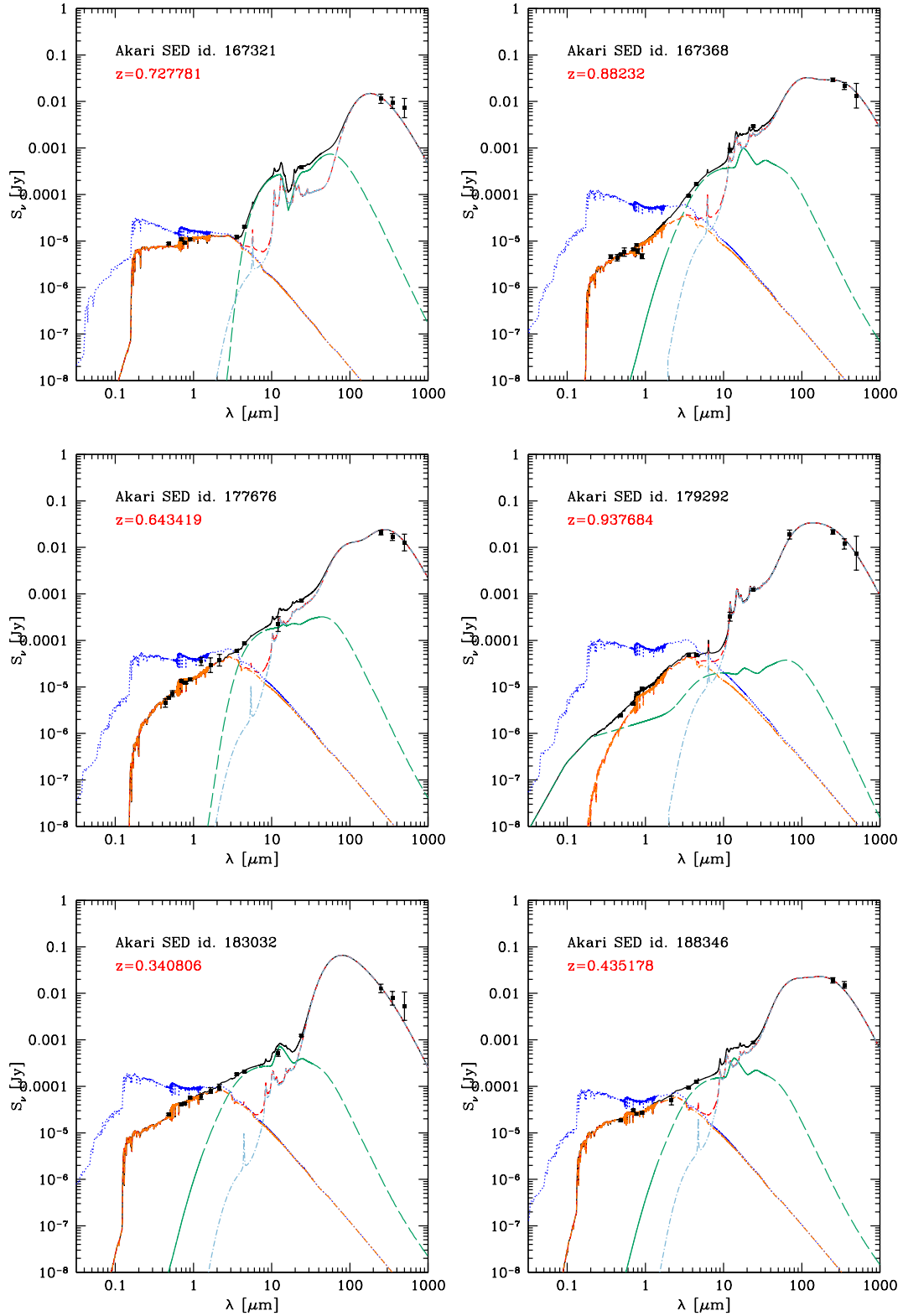


Figure 5.26: SEDs of starburst galaxies in our sample ( $0.02 < z < 1.5$ ,  $\log(M^*) > 9$ ). Beside the total emission (black), the following components are represented: unobscured and obscured stellar emission (blue and orange), AGN emission (green), SF dust emission (cyan) and obscured stellar plus SF emission without AGN component (red).

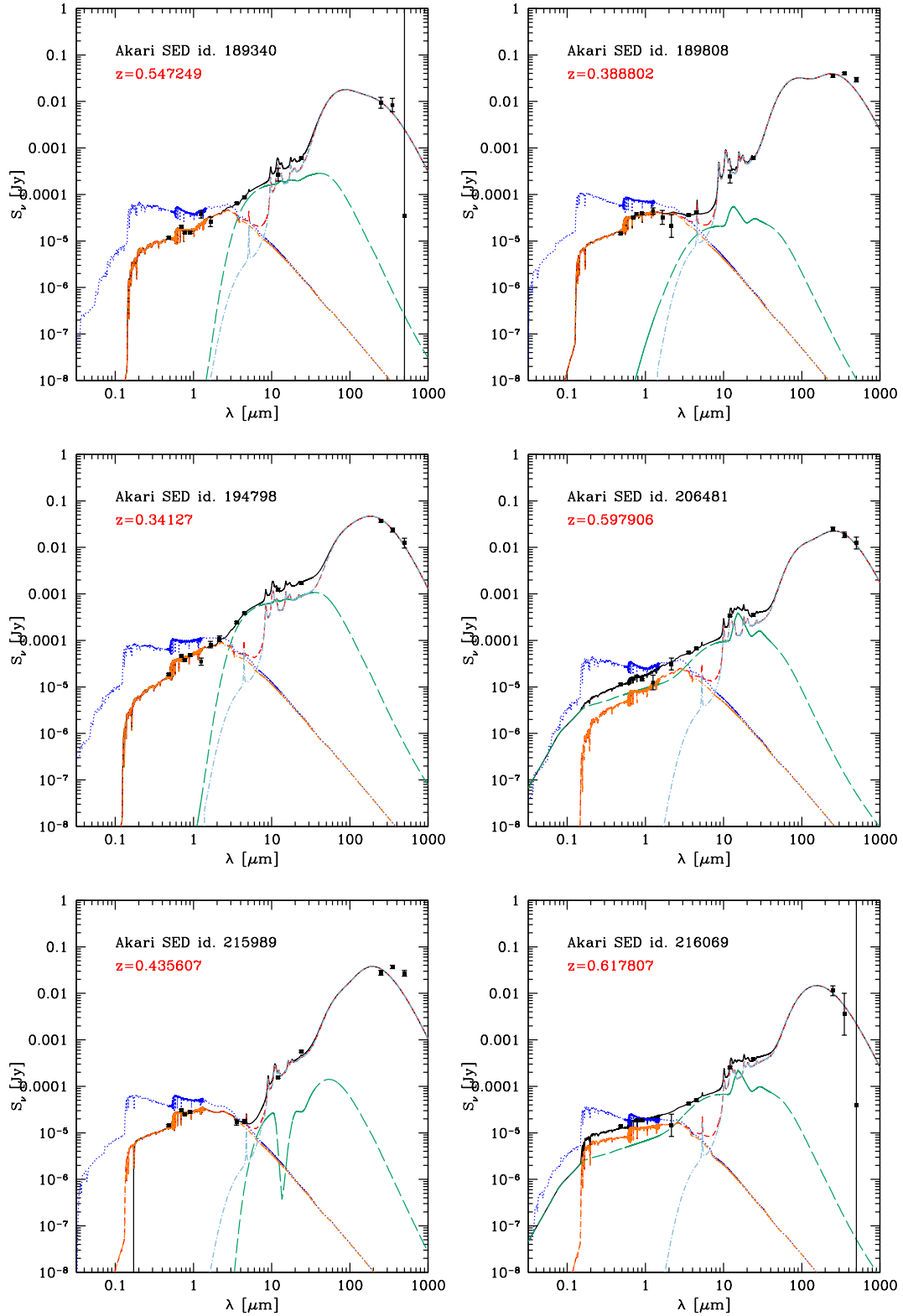


Figure 5.27: *SEDs of starburst galaxies in our sample ( $0.02 < z < 1.5$ ,  $\log(M^*) > 9$ ). Beside the total emission (black), the following components are represented: unobscured and obscured stellar emission (blue and orange), AGN emission (green), SF dust emission (cyan) and obscured stellar plus SF emission without AGN component (red).*

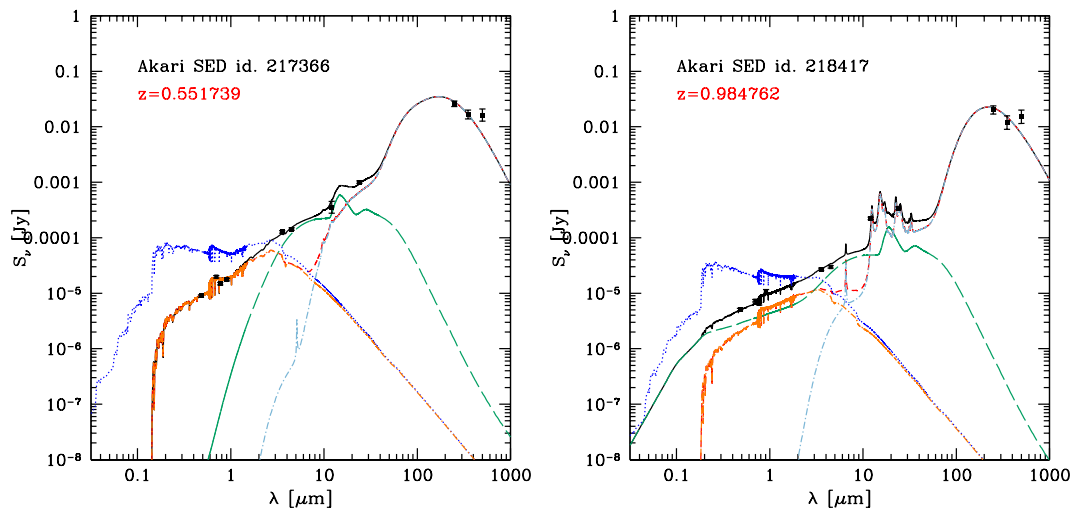


Figure 5.28: *SEDs of starburst galaxies in our sample ( $0.02 < z < 1.5$ ,  $\log(M^*) > 9$ ). Beside the total emission (black), the following components are represented: unobscured and obscured stellar emission (blue and orange), AGN emission (green), SF dust emission (cyan) and obscured stellar plus SF emission without AGN component (red).*

## Chapter 6

# Discussion and conclusions

Thanks to the high sensitivity and high angular resolution of the *Herschel* and *Spitzer* space observatories, a large number of infrared surveys were carried out in the last few years. The precise instruments on board of these space telescopes, such as the Spectral and Photometric Imaging Receiver (SPIRE–*Herschel*), the Infrared Array Camera (IRAC–*Spitzer*) and the Multiband Imaging Photometer (MIPS–*Spitzer*), allowed to obtain substantial information about the galaxy evolution history. Residing in dusty regions, both star formation and AGN activity are hidden at wavelengths shorter than the mid-IR spectral range. The nature and the strength of these phenomena can however be unveiled in the IR spectral region, where the light absorbed at shorter wavelengths is re-emitted as thermal radiation. In order to obtain useful information from these two fundamental space observatories, however, observations carried out in the mid and far IR need to be complemented with multi-wavelength observations covering the largest wavelength range as possible. For example, computing reliable photometric redshifts is almost impossible without a good optical coverage. Moreover, given the relative importance of the AGN torus emission in the mid-IR and the PAH and Silicate features around  $\sim 10\mu\text{m}$ , in order to better constrain the AGN incidence, the spectral coverage between the IRAC ( $4.5\mu\text{m}$ ) and MIPS ( $24\mu\text{m}$ ) band become fundamental. In this sense, *Akari*–IRC observations can be considered crucial.

In this thesis we contributed to the study of active galaxies in three ways. First, we reduced a large set of raw optical data in 5 different bands. These images were taken in the south ecliptic pole (SEP area) and are a fundamental complement of the following analysis. We do not discuss the data reduction, but the images obtained are however fundamental to obtain the results here discussed. Second, we created a database of multiwavelength observations, taken in the same field, in the context of the Spitzer IRAC–MIPS Extragalactic Survey (SIMES) and the Akari deep field south (ADFS). The catalog spectral coverage spans from the optical to the far-IR wavelengths and represents, for this reason, a fundamental tool for galaxy evolution studies. The catalog described is already available for the scientific community and still in evolution with further additional observations. Our third contribution is represented by the multiwavelength analysis that we carried out on the active galaxies of our sample. After computing reliable photometric redshifts, we studied the relationship between AGNs and host galaxies using a multiwavelength approach. We studied the relative emission of each physical mechanism (stars, AGN, star formation) besides their intrinsic strength.

## Multi-wavelength catalog

We built a multiwavelength catalog of sources detected in the South Ecliptic Pole field (SEP). The catalog is based on the IRAC-1 ( $3.6\mu\text{m}$ ) identifications above the  $3\sigma$  S/N level. IRAC sources were identified in the images and their fluxes were computed as described in section 2.1. We merged this catalog with optical data that we personally reduced. The description of the reduction process is not included in this thesis but resulted fundamental, since provided us with crucial data that we used to compute reliable redshifts (see Section 3) and stellar masses. VST (g, i, z) and VISTA (J, H, Ks) measures are also included in our final catalog. We cross correlated our IRAC detections with the *Herschel*-SPIRE and *Spitzer*-MIPS public catalogs. The *Akari* mid-IR fluxes that we directly extracted from the images are included in the multi-wavelength catalog. These observations allowed us to probe the spectral region dominated by the AGN emission, constraining the strength of such mechanisms in the host galaxies.

## Multi-wavelength analysis

From the catalog, we selected a sub-sample of FIR detected galaxies on which we performed a multi-wavelength analysis through an approach similar to that described in Berta et al. (2013). For each of the selected sources, the spectral coverage includes optical bands, mid and far-IR measures. This allows to compute reliable SEDs from the  $\chi^2$  minimization. Each SED is the result of the combined emission of three physical mechanisms: stellar populations total emission, black hole accretion and star formation.

We quantified the AGN fraction (i.e. fraction of emission due to the AGN) at different wavelengths. We compared the values obtained with the “dichotomic” diagnostic method described in Fadda & Rodighiero (2014) finding good agreement at all the wavelengths considered, meaning that the majority of our AGN dominated sources ( $f_{\text{AGN}}^\lambda > 50\%$ ) are located inside the AGN area of this diagnostic diagram or close to the border defining the AGN area itself.

We explored the contribution of the AGN emission in different positions of the  $M^*$ -SFR space finding that, when considering shorter wavelengths, AGN dominated sources prevail among the starbursts, while at longer wavelengths, higher AGN fractions are found along the  $M^*$ -SFR main sequence. This effect would be expected even if the AGN emission was identical in all the regions of the  $M^*$ -SFR space since:

1) At short wavelengths ( $\lambda < 5\mu\text{m}$ ) the AGN fraction measures the relative AGN/ $M^*$  contribution. Then, the same AGN emission at lower masses  $M^*$  results in higher AGN fractions.

2) At longer wavelengths ( $\lambda > 5\mu\text{m}$ ) the AGN fraction measures the relative AGN/SFR contribution. Then, the same AGN emission at lower SFRs results in higher AGN fractions.

These effects are however enhanced by the different AGN strength observed in different regions of the  $M^*$ -SFR space. We quantified the real AGN importance through the black hole accretion rate (BHAR), that we estimated from the intrinsic (unobscured) AGN emission  $L_{\text{acc}}$ , univocally determined by both the AGN model used to fit the data and its normalization. We observe that at all the redshifts explored in our analysis, the BHAR increases with the sSFR of the sources. In the first redshift bin ( $z \sim 0.26$ ) we could also estimate the dependence of the BHAR from the stellar mass  $M^*$  finding increasing BHARs with increasing stellar masses.

From our data, the relation can be represented with a law in the form:  $\text{BHAR} \propto M^{*0.65}$ , that is very similar to what is expected extrapolating at  $z=0.26$  the results of Mullaney et al. (2012), obtained in the X-ray regime.

Sources in the  $M^*$ -BHAR space seem to imitate their behaviour in the  $M^*$ -SFR space. This analogy is however limited to the general behaviour, since:

A) The slopes of the  $M^*$ -SFR and  $M^*$ -BHAR relations are different. In particular while the  $M^*$ -SFR relation scales with the redshift without a sensible slope variation, the slope of the  $M^*$ -BHAR relation seems to change with  $z$ .

B) The ratio between the BHAR and the SFR decreases at higher sSFR, meaning that in a linear representation, at a given stellar mass  $M^*$ ,  $\text{BHAR} \propto \text{SFR}^\alpha$ , with  $0 < \alpha < 1$ .

## Future perspective

The SEP field is a cosmological field still lacking coverage in many important bands, when compared with other widely studied fields, such as COSMOS or GOODS. Optical observations are particularly important in order to complete the coverage of the whole extended area. We limited our multiwavelength analysis to the central square degree mostly for this reason. Images taken in complementary optical bands are already under reduction and will allow to increase the detection rate in the optically covered area, enlarging our data sample and the precision of the best fitting SEDs. In general, a wider spectral coverage of the SEP is expected in the near future. Merging our catalog with the *Herschel*-PACS observations, available in the SEP field, would provide a full coverage of the dust emission peak. Radio and X-ray observations are fundamental to complete the study of AGNs in this field. Wider and deeper spectroscopic surveys would allow for SED fitting analysis with higher precisions. In this perspective, the SEP field will be covered by the *Euclid* observatory in the next future. This will allow to obtain precise spectroscopic redshifts for thousand of SF galaxies. The galaxies in our SFR selected sample will probably be prime targets for ALMA followup.

We based our study on a far IR (SFR) selected sample of galaxies. Including a mass selected sample of galaxies in our analysis will allow to explore the  $M^*$ -SFR and  $M^*$ -BHAR main sequences at lower  $M^*$ , SFRs and BHARs values, increasing our understanding of the relations among these parameters both at low and high redshifts.



# Bibliography

- Alexander, D. M., Smail, I., Bauer, F. E., et al. 2005, *Nature*, 434, 738
- Antonucci, R. 1993, *ARA&A*, 31, 473
- Antonucci, R. R. J. 1984, *ApJ*, 278, 499
- Antonucci, R. R. J. & Miller, J. S. 1985, *ApJ*, 297, 621
- Arav, N., Barlow, T. A., Laor, A., Sargent, W. L. W., & Blandford, R. D. 1998, *MNRAS*, 297, 990
- Barger, A. J., Cowie, L. L., Sanders, D. B., et al. 1998, *Nature*, 394, 248
- Beckmann, V. & Shrader, C. R. 2012, *Active Galactic Nuclei*
- Berta, S., Lutz, D., Santini, P., et al. 2013, *A&A*, 551, A100
- Bertin, E. & Arnouts, S. 1996, *A&AS*, 117, 393
- B  thermin, M., Wang, L., Dor  , O., et al. 2013, *A&A*, 557, A66
- Bolzonella, M., Miralles, J., & Pell  , R. 2000, *A&A*, 363, 476
- Booth, C. M. & Schaye, J. 2009, *MNRAS*, 398, 53
- Bower, R. G., Benson, A. J., Malbon, R., et al. 2006, *MNRAS*, 370, 645
- Brinchmann, J., Charlot, S., White, S. D. M., et al. 2004, *MNRAS*, 351, 1151
- Bruzual, G. & Charlot, S. 2003, *MNRAS*, 344, 1000
- Bryant, P. M. & Scoville, N. Z. 1999, *AJ*, 117, 2632
- Calzetti, D., Armus, L., Bohlin, R. C., et al. 2000, *ApJ*, 533, 682
- Cano-D  az, M., Maiolino, R., Marconi, A., et al. 2012, *A&A*, 537, L8
- Chabrier, G. 2003, *PASP*, 115, 763
- Charlot, S. & Fall, S. M. 2000, *ApJ*, 539, 718
- Clavel, J., Wamsteker, W., & Glass, I. S. 1989, *ApJ*, 337, 236
- Clements, D. L., Bendo, G., Pearson, C., et al. 2011, *MNRAS*, 411, 373

## Chapter 6: BIBLIOGRAPHY

---

- Condon, J. J. 1992, *ARA&A*, 30, 575
- Conroy, C., Gunn, J. E., & White, M. 2009, *ApJ*, 699, 486
- Cowie, L. L., Songaila, A., Hu, E. M., & Cohen, J. G. 1996, *AJ*, 112, 839
- Croton, D. J., Springel, V., White, S. D. M., et al. 2006, *MNRAS*, 365, 11
- da Cunha, E., Charlot, S., & Elbaz, D. 2008, *MNRAS*, 388, 1595
- Daddi, E., Cimatti, A., Renzini, A., et al. 2004, *ApJ*, 617, 746
- Daddi, E., Dickinson, M., Chary, R., et al. 2005, *ApJ*, 631, L13
- Daddi, E., Dickinson, M., Morrison, G., et al. 2007, *ApJ*, 670, 156
- Daddi, E., Elbaz, D., Walter, F., et al. 2010, *ApJ*, 714, L118
- Dekel, A. & Birnboim, Y. 2006, *MNRAS*, 368, 2
- Dekel, A., Birnboim, Y., Engel, G., et al. 2009, *Nature*, 457, 451
- Delvecchio, I., Gruppioni, C., Pozzi, F., et al. 2014, *MNRAS*, 439, 2736
- Dickinson, M., Papovich, C., Ferguson, H. C., & Budavári, T. 2003, *ApJ*, 587, 25
- Diolaiti, E., Bendinelli, O., Bonaccini, D., et al. 2000, *A&AS*, 147, 335
- Domínguez Sánchez, H., Mignoli, M., Pozzi, F., et al. 2012, *MNRAS*, 426, 330
- Donley, J. L., Koekemoer, A. M., Brusa, M., et al. 2012, *ApJ*, 748, 142
- Downes, D. & Solomon, P. M. 1998, *ApJ*, 507, 615
- Dunne, L., Ivison, R. J., Maddox, S., et al. 2009, *MNRAS*, 394, 3
- Elbaz, D., Daddi, E., Le Borgne, D., et al. 2007, *A&A*, 468, 33
- Elbaz, D., Dickinson, M., Hwang, H. S., et al. 2011, *A&A*, 533, A119
- Elbaz, D., Hwang, H. S., Magnelli, B., et al. 2010, *A&A*, 518, L29
- Engelbracht, C. W., Gordon, K. D., Rieke, G. H., et al. 2005, *ApJ*, 628, L29
- Engelbracht, C. W., Rieke, G. H., Gordon, K. D., et al. 2008, *ApJ*, 678, 804
- Erb, D. K., Steidel, C. C., Shapley, A. E., et al. 2006, *ApJ*, 647, 128
- Fadda, D. & Rodighiero, G. 2014, *MNRAS*, 444, L95
- Farrah, D., Afonso, J., Efstathiou, A., et al. 2003, *MNRAS*, 343, 585
- Farrah, D., Urrutia, T., Lacy, M., et al. 2012, *ApJ*, 745, 178
- Fath, E. A. 1909, *Lick Observatory Bulletin*, 5, 71
- Fazio, G. G., Ashby, M. L. N., Barmby, P., et al. 2004, *ApJS*, 154, 39

- Feltre, A., Hatziminaoglou, E., Fritz, J., & Franceschini, A. 2012, *MNRAS*, 426, 120
- Feltre, A., Hatziminaoglou, E., Hernán-Caballero, A., et al. 2013, *MNRAS*, 434, 2426
- Franceschini, A., Rodighiero, G., Cassata, P., et al. 2006, *A&A*, 453, 397
- Fritz, J., Franceschini, A., & Hatziminaoglou, E. 2006, *MNRAS*, 366, 767
- Genzel, R., Lutz, D., Sturm, E., et al. 1998, *ApJ*, 498, 579
- Genzel, R., Tacconi, L. J., Gracia-Carpio, J., et al. 2010, *MNRAS*, 407, 2091
- Grado, A., Capaccioli, M., Limatola, L., & Getman, F. 2012, *Memorie della Societa Astronomica Italiana Supplementi*, 19, 362
- Graham, A. W. & Driver, S. P. 2005, *PASA*, 22, 118
- Granato, G. L., Silva, L., Danese, L., de Zotti, G., & Bressan, A. 2004, in *Multiwavelength AGN Surveys*, ed. R. Mújica & R. Maiolino, 379–384
- Grupponi, C., Pozzi, F., Polletta, M., et al. 2008, *ApJ*, 684, 136
- Haardt, F. & Maraschi, L. 1993, *ApJ*, 413, 507
- Häring-Neumayer, N., Cappellari, M., Rix, H.-W., et al. 2006, *ApJ*, 643, 226
- Harwit, M. & Pacini, F. 1975, *ApJ*, 200, L127
- Hatziminaoglou, E., Fritz, J., Franceschini, A., et al. 2008, *MNRAS*, 386, 1252
- Hatziminaoglou, E., Fritz, J., & Jarrett, T. H. 2009, *MNRAS*, 399, 1206
- Hewett, P. C., Warren, S. J., Leggett, S. K., & Hodgkin, S. T. 2006, *MNRAS*, 367, 454
- Hopkins, A. M. & Beacom, J. F. 2006, *ApJ*, 651, 142
- Hopkins, P. F., Hernquist, L., Cox, T. J., & Kereš, D. 2008, *ApJS*, 175, 356
- Hopkins, P. F., Hernquist, L., Cox, T. J., Robertson, B., & Krause, E. 2007a, *ApJ*, 669, 67
- Hopkins, P. F., Richards, G. T., & Hernquist, L. 2007b, *ApJ*, 654, 731
- Hubeny, I., Agol, E., Blaes, O., & Krolik, J. H. 2000, *ApJ*, 533, 710
- Hughes, D. H., Serjeant, S., Dunlop, J., et al. 1998, *Nature*, 394, 241
- Ishibashi, W. & Courvoisier, T. J.-L. 2011, *A&A*, 525, A118
- Jarrett, T. H., Cohen, M., Masci, F., et al. 2011, *ApJ*, 735, 112
- Karim, A., Schinnerer, E., Martínez-Sansigre, A., et al. 2011, *ApJ*, 730, 61
- Kellermann, K. I., Sramek, R. A., Schmidt, M., Green, R. F., & Shaffer, D. B. 1994, *AJ*, 108, 1163
- Kennicutt, R. C. & Evans, N. J. 2012, *ARA&A*, 50, 531

## Chapter 6: BIBLIOGRAPHY

---

- Kennicutt, Jr., R. C. 1998, *ARA&A*, 36, 189
- Kirkpatrick, A., Pope, A., Alexander, D. M., et al. 2012, *ApJ*, 759, 139
- Kormendy, J. & Ho, L. C. 2013, *ARA&A*, 51, 511
- Krolik, J. H. 1999, *Nature*, 398, 678
- Kron, R. G. 1980, *ApJS*, 43, 305
- Krone-Martins, A., Ishida, E. E. O., & de Souza, R. S. 2014, *MNRAS*, 443, L34
- Kroupa, P. 2001, *MNRAS*, 322, 231
- Lacy, M., Petric, A. O., Sajina, A., et al. 2007, *AJ*, 133, 186
- Lilly, S. J., Carollo, C. M., Pipino, A., Renzini, A., & Peng, Y. 2013, *ApJ*, 772, 119
- Lilly, S. J., Le Fevre, O., Hammer, F., & Crampton, D. 1996, *ApJ*, 460, L1
- Lusso, E., Comastri, A., Simmons, B. D., et al. 2012, *MNRAS*, 425, 623
- Madau, P. & Dickinson, M. 2014, *ARA&A*, 52, 415
- Madau, P., Ferguson, H. C., Dickinson, M. E., et al. 1996, *MNRAS*, 283, 1388
- Madau, P., Pozzetti, L., & Dickinson, M. 1998, *ApJ*, 498, 106
- Magdis, G. E., Daddi, E., Béthermin, M., et al. 2012, *ApJ*, 760, 6
- Magnelli, B., Elbaz, D., Chary, R. R., et al. 2009, *A&A*, 496, 57
- Magnelli, B., Elbaz, D., Chary, R. R., et al. 2011, *A&A*, 528, A35
- Maraston, C. 2005, *MNRAS*, 362, 799
- Maraston, C., Strömbäck, G., Thomas, D., Wake, D. A., & Nichol, R. C. 2009, *MNRAS*, 394, L107
- Marconi, A. & Hunt, L. K. 2003, *ApJ*, 589, L21
- Marconi, A., Pastorini, G., Pacini, F., et al. 2006, *A&A*, 448, 921
- Matsuhara, H., Wada, T., Matsuura, S., et al. 2006, *PASJ*, 58, 673
- Matsuura, S., Shirahata, M., Kawada, M., et al. 2011, *ApJ*, 737, 2
- McMahon, R. G., Banerji, M., Gonzalez, E., et al. 2013, *The Messenger*, 154, 35
- Merloni, A. & Heinz, S. 2008, *MNRAS*, 388, 1011
- Meurer, G. R., Heckman, T. M., & Calzetti, D. 1999, *ApJ*, 521, 64
- Mignoli, M., Cimatti, A., Zamorani, G., et al. 2005, *A&A*, 437, 883
- Miyoshi, M., Moran, J., Herrnstein, J., et al. 1995, *Nature*, 373, 127

- Moustakas, J., Kennicutt, Jr., R. C., & Tremonti, C. A. 2006, *ApJ*, 642, 775
- Mullaney, J. R., Daddi, E., Béthermin, M., et al. 2012, *ApJ*, 753, L30
- Noeske, K. G., Faber, S. M., Weiner, B. J., et al. 2007a, *ApJ*, 660, L47
- Noeske, K. G., Weiner, B. J., Faber, S. M., et al. 2007b, *ApJ*, 660, L43
- Nordon, R., Lutz, D., Shao, L., et al. 2010, *A&A*, 518, L24
- Oliver, S. J., Bock, J., Altieri, B., et al. 2012, *MNRAS*, 424, 1614
- Onaka, T., Matsuhara, H., Wada, T., et al. 2007, *PASJ*, 59, 401
- Osterbrock, D. E. 1981, *ApJ*, 249, 462
- Padmanabhan, T. 2002, *Theoretical Astrophysics - Volume 3, Galaxies and Cosmology*
- Page, M. J., Symeonidis, M., Vieira, J. D., et al. 2012, *Nature*, 485, 213
- Pannella, M., Carilli, C. L., Daddi, E., et al. 2009, *ApJ*, 698, L116
- Papovich, C., Rudnick, G., Le Floch, E., et al. 2007, *ApJ*, 668, 45
- Pearson, E. A., Eales, S., Dunne, L., et al. 2013, *ArXiv e-prints*
- Peng, Y.-j., Lilly, S. J., Kovač, K., et al. 2010, *ApJ*, 721, 193
- Peng, Y.-j., Lilly, S. J., Renzini, A., & Carollo, M. 2012, *ApJ*, 757, 4
- Peng, Y.-j., Lilly, S. J., Renzini, A., & Carollo, M. 2014, *ApJ*, 790, 95
- Peterson, B. M. 1997, *The Observatory*, 117, 314
- Petrosian, V. 1976, *ApJ*, 209, L1
- Pier, E. A. & Krolik, J. H. 1992, *ApJ*, 401, 99
- Polletta, M., Tajer, M., Maraschi, L., et al. 2007, *ApJ*, 663, 81
- Pope, E. C. D., Mendel, J. T., & Shabala, S. S. 2012, *MNRAS*, 419, 50
- Pozzi, F., Vignali, C., Comastri, A., et al. 2007, *A&A*, 468, 603
- Pozzi, F., Vignali, C., Gruppioni, C., et al. 2012, *MNRAS*, 423, 1909
- Reach, W. T., Megeath, S. T., Cohen, M., et al. 2005, *PASP*, 117, 978
- Reddy, N., Dickinson, M., Elbaz, D., et al. 2012a, *ApJ*, 744, 154
- Reddy, N. A., Pettini, M., Steidel, C. C., et al. 2012b, *ApJ*, 754, 25
- Reddy, N. A., Steidel, C. C., Fadda, D., et al. 2006, *ApJ*, 644, 792
- Renzini, A. 2009, *MNRAS*, 398, L58
- Rieke, G. H. & Lebofsky, M. J. 1979, *ARA&A*, 17, 477

## Chapter 6: BIBLIOGRAPHY

---

- Risaliti, G. & Elvis, M. 2004, in *Astrophysics and Space Science Library*, Vol. 308, *Supermassive Black Holes in the Distant Universe*, ed. A. J. Barger, 187
- Rodighiero, G., Brusa, M., Daddi, E., et al. 2015, *ArXiv e-prints*
- Rodighiero, G., Daddi, E., Baronchelli, I., et al. 2011, *ApJ*, 739, L40
- Rodighiero, G., Gruppioni, C., Civano, F., et al. 2007, *MNRAS*, 376, 416
- Rodighiero, G., Renzini, A., Daddi, E., et al. 2014, *MNRAS*, 443, 19
- Rodighiero, G., Vaccari, M., Franceschini, A., et al. 2010, *A&A*, 515, A8
- Rowan-Robinson, M. 1977, *ApJ*, 213, 635
- Rowan-Robinson, M., Gonzalez-Solares, E., Vaccari, M., & Marchetti, L. 2013, *MNRAS*, 428, 1958
- Rudnick, G., Rix, H.-W., Franx, M., et al. 2003, *ApJ*, 599, 847
- Salpeter, E. E. 1955, *ApJ*, 121, 161
- Sanders, D. B. & Mirabel, I. F. 1996, *ARA&A*, 34, 749
- Sanders, D. B., Soifer, B. T., Elias, J. H., et al. 1988, *ApJ*, 325, 74
- Santini, P., Fontana, A., Grazian, A., et al. 2009, *A&A*, 504, 751
- Santini, P., Fontana, A., Grazian, A., et al. 2012, *A&A*, 538, A33
- Sargent, M. T., Béthermin, M., Daddi, E., & Elbaz, D. 2012, *ApJ*, 747, L31
- Schweitzer, M., Lutz, D., Sturm, E., et al. 2006, *ApJ*, 649, 79
- Sérsic, J. L. 1963, *Boletin de la Asociacion Argentina de Astronomia La Plata Argentina*, 6, 99
- Shakura, N. I. & Sunyaev, R. A. 1973, *A&A*, 24, 337
- Shi, Y., Helou, G., Armus, L., Stierwalt, S., & Dale, D. 2013, *ApJ*, 764, 28
- Shields, G. A. 1978, *Nature*, 272, 706
- Shupe, D. L., Rowan-Robinson, M., Lonsdale, C. J., et al. 2008, *AJ*, 135, 1050
- Skrutskie, M. F., Cutri, R. M., Stiening, R., et al. 2006, *AJ*, 131, 1163
- Smail, I., Ivison, R. J., & Blain, A. W. 1997, *ApJ*, 490, L5
- Smith, J. D. T., Draine, B. T., Dale, D. A., et al. 2007, *ApJ*, 656, 770
- Springel, V., Di Matteo, T., & Hernquist, L. 2005, *MNRAS*, 361, 776
- Stringer, M., Cole, S., Frenk, C. S., & Stark, D. P. 2011, *MNRAS*, 414, 1927

- Surace, J. A., Shupe, D. L., Fang, F., et al. 2005, in Bulletin of the American Astronomical Society, Vol. 37, American Astronomical Society Meeting Abstracts, 1246
- Trenti, M. & Stiavelli, M. 2008, ApJ, 676, 767
- Tristram, K. R. W., Meisenheimer, K., Jaffe, W., et al. 2007, A&A, 474, 837
- Tristram, K. R. W., Raban, D., Meisenheimer, K., et al. 2009, A&A, 502, 67
- Urry, C. M. & Padovani, P. 1995, PASP, 107, 803
- Vasudevan, R. V. & Fabian, A. C. 2009, MNRAS, 392, 1124
- Veilleux, S. & Osterbrock, D. E. 1987, ApJS, 63, 295
- Weedman, D. W., Feldman, F. R., Balzano, V. A., et al. 1981, ApJ, 248, 105
- Whitaker, K. E., van Dokkum, P. G., Brammer, G., & Franx, M. 2012, ApJ, 754, L29
- Williamson, R. A., Hurst, W., & Jeffe, M. 2002, in ESA Special Publication, Vol. 515, Space Applications for Heritage Conservation, ed. B. Warmbein, 15
- Worsley, M. A., Fabian, A. C., Bauer, F. E., et al. 2005, MNRAS, 357, 1281
- Wright, E. L., Eisenhardt, P. R. M., Mainzer, A. K., et al. 2010, AJ, 140, 1868
- Yun, M. S., Reddy, N. A., & Condon, J. J. 2001, ApJ, 554, 803
- Zacharias, N., Monet, D. G., Levine, S. E., et al. 2005, VizieR Online Data Catalog, 1297, 0
- Zheng, W., Kriss, G. A., Telfer, R. C., Grimes, J. P., & Davidsen, A. F. 1997, ApJ, 475, 469